UNIVERSITY OF NAPLES FEDERICO II

DEPARTMENT OF INDUSTRIAL ENGINEERING
AEROSPACE SECTION

Ph.D. COURSE
IN INDUSTRIAL ENGINEERING
XXIX CYCLE

Infrared thermography to monitoring mechanical tests on composite materials: Experimental procedure and data analysis

Simone Boccardi

Research Supervisors:

Prof. Ing. Giovanni M. Carlomagno

Dr. Ing. Carosena Meola

The Chairman of the Ph.D. School:

Prof. Ing. Michele Grassi

2017

"Nil tam difficile est, quin
quaerendo investigari possit"

(Publio Terenzio)

Contents

Introduction 1

Chapter 1 Composite materials 3

Introduction 3

1.1. Some basics of composite materials 4
1.2. The matrices 5
1.2.1. Polymer types 5
1.3. Reinforcement for polymer-based composites 6
1.3.1. Glass fibres 7
1.3.2. Carbon fibres 8
1.3.3. Natural fibres 9
1.3.4. . Woven fabric architectures 10
1.4. Main types of deficiency in composites 10
1.4.1. Manufacturing defects. 11
1.4.2. In-service failures 12
1.4.2.1. Some hints on failure mechanisms 13

References to Chapter 1 15

Chapter 2 Infrared thermography 18

Nomenclature 18

Introduction 20

2.1. Some basics 20
2.2. Real objects radiation 22
2.2.1. Effects of interposed atmosphere 24
2.3. Infrared devices. 25
2.3.1. Thermal detectors 26
2.3.2. Photon Detectors 26
2.3.3. QWIP detectors technology 27
2.3.4. Detector performance 28
2.4. IR Image generation 30
2.4.1. Problems affecting infrared images 31
2.5. Calibration 32
2.6. Applications 33

References to Chapter 2 33

Chapter 3 Infrared cameras, temporal noise and Reference Area Method 37

Nomenclature 37

Introduction 38

3.1. Characterization of QWIP SC6000 temporal noise 38
3.2. SC6000 camera electronic architecture and image construction 41
3.3. Black body monitoring with other detector types 43
3.4. The Reference Area Method 46
3.5. Application of the Reference Area Method to a real surface 51
3.6. Some effects of the Reference Area Method 58
3.7. Practical applications 60

References to chapter 3 60

Chapter 4 Cyclic bending tests 61

Nomenclature 61

Introduction 62

4.1. Some theoretical considerations 62
4.2. Some preliminary tests 65
4.3. New Investigation 68
4.3.1. Test setup and procedure 68
4.3.2. Description of specimens 71
4.4. Data post-processing 73
4.4.1. Description of the Area Method 73
4.4.2. Description of the Whole Width Method 77
4.5. Qualitative evaluation of ΔT on the rear specimen surface 78
4.6. Influence of the bending frequency 79
4.7. The effects of the matrix on ΔT values in thermoplastic specimens 83
4.8. A comparison between epoxy/resin and PP matrices in glass reinforced specimens 88
4.9. The influence of fibres in thermoplastic matrix based specimens 89
4.10. Some bending coupled effects 90
4.10.1. Some considerations about the heating up effects 92
4.10.2. The influence of bending frequency on the heating up effect 93
4.11. Some remarks to Chapter 4 95

References to chapter 4 95

Chapter 5 Impact tests 98

Nomenclature 98

Introduction 100

5.1. Description of specimens 100
5.2. Conventional procedure for assessing impact resistance of new composite materials 102
5.2.1. Lock-in thermography: test setup and procedure 103
5.2.2. PAUT test setup 104
5.2.3. Some results of LT inspection 105
5.2.4. Comparison of LT and PAUT results 107
5.3. The added value of online monitoring 109
5.4. Preliminary tests of impact monitoring 110
5.5. New investigation 114
5.5.1. Test setup and experimental procedure 114
5.5.2. Interpretation of infrared images recorded during impact tests 115
5.6. Analysis of impact dynamics 119
5.6.1. ΔT evolution under impact 119
5.6.2. Quantitative analysis of results 120
5.6.3. ΔT and Δt as clues of the impact damage 128
5.7. Measurement of Impact-Damaged Area 129
5.7.1. Estimation of the impact damage along horizontal and vertical directions 131
5.8. Methods of warm area measurement 138
5.8.1. Description of the R method 139
5.8.2. Comparison of the R method with the Otsu's method. 141
5.8.3. Limitations of the R method and introduction of noise correction. 143
5.8.4. Some results obtained with the NCR method 146
5.9. Problems and future improvement of the NCR method 154
5.10. A summary to Chapter 5 155

References to Chapter 5 156

Conclusions 160

Acknowledgments 162

Introduction

Composite materials are increasingly used in an ever wider number of application fields such as in the transport industry, in civil infrastructures, in chemical equipments, as well in the fabrication of many objects for use in daily life Their success is mainly due to their high strength-to-weight ratio, easy formability, and other properties that make them preferable to metals and other conventional engineering materials. Then, the efforts are driven ever more towards the creation of materials of superior characteristics by changing something in the matrix ingredients and/or by arranging the fibres in particular ways, Besides the many advantages, there are also some disadvantages due to their tendency to include defects during fabrication and their susceptibility to impact damage, at least for those including a brittle matrix. Often, especially under impact at low energy, important damage may occur inside the material thickness, without any surface sign, which may entail considerable loss in strength, and possibly leading to catastrophic in-service failures. Moreover, impact damaging of composites is a very complex mechanism involving matrix cracking, surface buckling, delamination, fibre shear-out and fibre rupture, which are difficult to simulate numerically and represent one of the major design concerns.

To get the best during the design phase, a lot of information about the material's properties and its intended in-service performance should be available. This is practically impossible and then, once a new material is created, it has to be subjected to many tests involving non-destructive evaluation, chemical tests, mechanical tests, etc. Amongst them, especially for materials designed for aerospace components, assessing the impact resistance is a primary requirement. This feature is assessed through specific impact tests, which are intended to identify the energy that has caused delamination of a given extension, the peak force, contact duration and other parameters. In particular, some tests consist in impacting the laminate at a given energy, evaluating (in a non-destructive way) the induced damage extension and go on to increasing impact energies until the preset delamination has been reached. This is a long way on.

In recent years, at the University of Naples Federico II, it has been demonstrated that the use of an infrared imaging device, to monitor the surface of the laminate precisely during the impact, may be advantageous to get information on the extension of the occurred delamination. In fact, the damage caused by the impact is related to the thermal signatures that develop, and can be visualized on-line, on the laminate surface opposite to the impact. This approach appeared sudden fast and advantageous. However, the evaluation of the extension of the delamination from the acquired thermal images requires *ad hoc* post-processing of such thermal images.

The objective of this dissertation is to go on and to understand more through tests on many types of composites and by developing specific post-processing procedures. In reality, the project is wider including monitoring of composites during either impact, or cyclic bending tests. The latter is involved with the measurement of very small temperature variations coupled with thermoelastic effects, at the edge of the instrument resolution and strongly affected by the instrument temporal noise. This noise, at least for the QWIP detector, is mainly constituted by random jumps, which may completely disrupt the harmonic temperature variation coupled with cyclic bending.

Then, the attention of this thesis is focused on two types of tests: cyclic bending and impact tests, dealing with the temporal detector noise. The innovative idea is to reduce, or eliminate, the temporal noise through the use of a reference unloaded specimen.

The work is organized in five chapters.
Chapter 1 deals with a brief description of composite materials, involving the main types of matrix and/or reinforcement. A section is dedicated to the description of the main types of defects which may arise during manufacturing and/or in service. Particular attention is given to the impact damage, which is of great concern within the industrial community.
Chapter 2 supplies some general hints on infrared thermography, infrared detectors and their characteristics. The QWIP detector is more deeply described since is largely used during this work.
Chapter 3 is entirely devoted to the description of temporal noise correction with the developed Reference Area Method. This correction approach, which is firstly experimentally investigated with the help of a blackbody, is further implemented with either cyclic bending tests, or impact tests.
Chapter 4 is concerned with cyclic bending tests, which are performed on a single cantilever beam configuration by means of a prototype machine suitably conceived and realised for the purpose. Tests are carried out by changing the bending frequency, from 0.05 Hz up to 4 Hz, and the bending configuration to perform bending in one direction, or in two directions. These cyclic bending tests are performed with two purposes. One is to validate the Reference Area Method for correction of the instrument temporal noise described in Chapter 3. The second one is to verify the possibility to get, in a simple and fast way, information, which may be useful for the characterization of new composite materials.
Chapter 5 is concerned with impact tests, which are carried out by means of a modified Charpy pendulum, which allows enough room for positioning of the infrared camera to view the side opposite to the impacted one. Tests are carried out by considering different types of composites and different impact energies. The acquired sequences of thermal images are post-processed with specific routines developed in the Matlab environment and aimed at extracting the desired information. In particular, a method is developed to outline and evaluate the extension of the impact damaged area, which can be of utmost importance to the aerospace industry.
The described activities have been carried out within a cooperation between the Department of Industrial Engineering, the Department of Chemical, Materials and Production Engineering and two research Centres, namely: the National Council of Research (CNR), in particular, the Institute for Polymers, Composites and Biomaterials of CNR, and the Regional Centre for Energy, Materials, Electronics and Industrial design (CRdC Tecnologie).

Chapter 1

Composite materials

Introduction

The Aerospace Industry has traditionally represented the engineering sector which has promoted development and application of advanced materials. For aerospace applications, the large number of requirements makes finding an appropriate material particularly challenging. An 'ideal material' should have the following properties: high strength, high stiffness, high toughness, low weight, environmental resistance, high temperature capability, easy processing, and low cost. In particular, weight/resistance ratio has always been a factor of great concern in aircraft technology.

At the beginning of the last century, during the pioneering phase, when aluminium was not yet available at reasonable prices, wood (a composite material provided by the natural world) was the cheapest and most readily available substance to be easily tailored into the desired shape and strong enough to withstand flight loads. It was just with a wood-and-fabric biplane that the Wright brothers made the first flight on 17 December, 1903, achieving the first milestone in the aviation era. A second important step in aeronautics was the so-called structural revolution of 1930s, when wood was replaced by metal, mostly aluminium; such a revolution was marked by the Boeing 247D and the Douglas DC-3, even if, already in 1915, an all-metal construction was pioneered by Hugo Junkers, driven by military purposes. Composites were first introduced in military aviation in 1960 and, about 10 years later, also in the civil aviation. Initially, the use of composites was confined to the fabrication of secondary wing and tail components, such as rudder and wing trailing edge panels involving directional reinforcement [1,2].

The limiting factors of composites that initially discouraged their widespread application, especially in civil airframes, were the stringent safety requirements, which collided with the limited experience within composites, and their high production costs.

A revolutionary exploitation of composites took place in the 2000s with the production of two big airplanes, the Airbus A380 and the Boeing Dreamliner; in fact, in both of these airplanes, composites have been extensively deployed in the primary load-carrying structure with fuel saving and reduced CO_2 emission [3]. They were followed by the A400, which is made almost entirely of composites.

The success in the aircraft industry has paved nowadays the way to composite materials to an ever more wide number of application fields (Fig. 1.1) such as transport industry involving also automotive and naval, civil infrastructures, chemical equipments, as well the fabrication of many objects for use in daily life [4].

To this regard in the last years, an increasing attention from both the industrial and academic communities has been devoted also to composites based on thermoplastic matrix because of their many advantages, compared with their thermoset counterparts, in terms of: potential recyclability after life-cycle, chemical and environmental resistance, reduced moisture absorption and, usually, faster production as well as reduced processes costs [5].

Actually the thermoplastic composite materials, especially those reinforced with natural fibres, are finding an increasing use, mostly in automotive and aircraft industries, for non-structural applications.

Fig. 1.1 Some examples of composite materials applications: (a) 787 Fuselage section; (b) Car body; (c) bike frame.

Besides their many advantages, composites pose also some problems in terms of establishing duration and fatigue-life criteria. In fact, the duration of a metallic component is dependent on the possible formation of cracks and their growth. Metal fracture mechanics is often adequate to predict the size of critical flaws and, as a consequence, to establish rejection/acceptance criteria on the basis of the designer requirements. On the contrary, composites are largely inhomogeneous and behave in a complex way which is difficult to be completely understood also in consideration of the multitude of items (articles) that can be created, e.g., by simply changing the ply alignment and stacking sequence. A main weakness of at least thermoset-matrix based composites is their susceptibility to low energy impact [6].

1.1 Some basics of composite materials.

The idea of composite materials can be found in nature; an example is wood, which is made of a lignin matrix reinforced with cellulose fibres. Indeed, a composite material is made of two or more basic substances that can be combined to obtain a new material, i.e., the composite material, having a unique combination of properties with respect to its original constituents. This definition is the most general and includes also metal alloys, plastic co-polymers, minerals, and wood.
However, the term composite is more widely used as an abbreviation to indicate fibre-reinforced composite materials which differ from the above definition being the constituent materials different at molecular level and mechanically separable. In the present work, the term *composite materials* is used to indicate fibre-reinforced composite materials.
The composites are generally made of a fibrous, or particulate, substance (*reinforce*) mixed within a *matrix* to form a relatively homogeneous material. The reinforcement provides most of the mechanical properties of the resultant material, like strength and stiffness.
The matrix performs several critical functions, including maintaining the reinforcement-like fibres in the proper orientation and location, protecting them from abrasion and environmental effects, helping to transfer stresses among fibres, avoiding the propagation of fractures, and also contributing to electrical conductivity as well to thermal stability [4].

1.2 The matrices.

Several materials can be used as matrix and they include: polymers, cement, ceramics and metals. Polymer-matrix and cement-matrix are the mostly used.
Cement matrix are widely exploited in civil engineering, especially as concrete products in which sand, stones and steel act as reinforcement, embedded in the form of particles, or metal rods, (reinforced concrete).
Ceramic matrix are particularly appreciated for their resistance to environmental effects like corrosion and exposure to high temperature but they are extremely brittle. They are used in applications where thermal protection is compulsory, especially in the aerospace field where matrices of silicon carbide (SiC) are widely used [7].
Metal matrix are used in applications where high mechanical performances like enhanced specific strength and stiffness, low density and high-temperature strength are demanded; aluminium alloys, titanium and magnesium are the mostly employed [8].
Polymer matrix, thanks to their relative low-processing cost and weight, are the mostly used in aircraft industry but they are finding ever larger application also in automotive and sport industries, as well as to fabricate daily life objects. Polymer composites involving different types of polymers and fibres are investigated in the next chapters.

1.2.1 Polymer types

The term polymer indicates a large molecule constituted of a long chain of reiterating units (small molecules called *monomers*, or '*mers'*), bonded together through a so-called polymerization chemical reaction. Polymerization requires at least two reaction points, or functional groups, for each monomer. There are two types of polymerization: condensation polymerization and addition polymerization. In the first, the chain development is accompanied by elimination of relatively small molecules such as H_2O or CH_3OH; in the second, monomers react to form a polymer without formation of by products, but, to get polymerization, the addition of catalysts is needed [9].
Owing to their behaviour under heating or cooling, polymers can be grouped into two categories: *thermosets* and *thermoplastics*. Thermosets, before polymerization, behave like low-viscosity resin, which gradually cures at a relatively low temperature (20-200°C) and cannot be reprocessed by reheating. In a fully cured state, thermoset molecules are cross-linked and permanently insoluble and infusible. These types of polymers are also known as cross-linked polymers. Thermosets include unsaturated epoxies, polyesters and phenolics. Cured epoxy resins are reasonably stable to chemical attack and are excellent adhesives having low shrinkage during curing (polymerization) and no emission of volatile gases. Because of these characteristics, which result in a material with high mechanical properties and high corrosion resistance (coupled with a quite simple curing process), they are the most popular amongst composite matrices. In contrast, epoxies are quite expensive, cannot be stored for a long time and so are mainly used in high technology applications. It is worth noting that, polyester resins are quite easily accessible, cheaper and used in a wide range of fields. Liquid polyesters can be stored at room temperature for months, sometimes even years, and with the mere addition of a catalyst can cure within a short time; the cured polyester can be rigid, or flexible, as the case may be, and transparent. They are mainly used in the automotive and naval fields. Phenolics represent the first truly synthetic plastic (commercialized since 1905)

obtained combining formaldehyde and phenol. They are water and solvent resistant, can be used as an electrical insulator (they were extensively used in circuit boards), but are generally brittle even if they can be strengthened, to a certain extent, by fillers. Nowadays, they have been practically superseded by modern plastics such as epoxy or polyester resins.
Thermoplastics are composed of chainlike molecules, and may be high-viscosity resins with varying degrees of crystallinity; a number of them can be dissolved in certain liquids and they soften, or melt, upon heating above their melting temperature (100-400 °C) for additional processing. Some types of thermoplastic resins include polypropylene (PP), polyvinylchloride, polyether imide (PEI), polyether ether ketone (PEEK), polystyrene and polyphenylene sulfide (PPS). Thermoplastic matrices have recently become of great interest for their ductility and high-processing speed, as well as for the greater choice of manufacturing techniques. In fact, their processing can be selected by the scale and rate of production required and by the size of the component. In addition, thermoplastic composites can be easily repaired because transition to the softened phase can be accomplished any number of times by heating them up.
Due to the high strength/lightweight requirement, thermoset matrices (especially epoxy) are generally preferred for aeronautical high technology applications, even if the use of thermoplastics and natural fibres is significantly increasing in the last years for daily life applications [4].
In Table 1.1, the most important mechanical characteristics of some polymers used as matrix are collected.

MATRIX	**Density** (g/cm^3)	**Elastic modulus** (GPa)	**Traction resistance** (MPa)	**Breaking deformation** (%)
Epoxy	1.1 - 1.4	2.75 - 4.10	55 - 130	1.5 - 8
Polyester	1.1 - 1.4	2.1 - 3.8	20 - 103.5	1 - 5
Phenolic	1.2-1.35	2.0-3.5	20-40	1.2-2.5
PP	0.90	1.2-1.6	25-35	40-70
LDPE	0.92	0.18-0.22	20-28	200-400
PEEK	1.30 - 1.32	3.2	100	50
PPS	1.36	3.3	83	2-20
PEI	1.27	3	105	60
PLA	1.24	3.4-3.8	50-60	2-5

Table 1.1. Most important polymer types used as matrix.

1.3 Reinforcement for polymer-based composites

Long small-diameter fibres are mostly used in the fabrication of composites because, a material with a fibrous shape entails small and scarce defects and fibres can be oriented along the main tensile stresses. Besides in a material with a fibrous shape, defects are present with a smaller size and in a lower percentage and consequently the strength increases. In addition, small-diameter fibres have greater flexibility and are more amenable to fabrication processes. High-performance composites are generally made from *continuous fibres* (Fig. 1.2), but there are many applications for which the requirements are less demanding and in these cases *short fibres* can be used in an aligned array, or with a random orientation. In Table 1.2, the mostly used fibres, with their mechanical characteristics, are listed.

FIBRES	Density (g/cm^3)	Elasticity modulus (GPa)	Traction resistance (GPa)	Specific Modulus (10^7 m^2/s^2)
E Glass	2.54	72.4	3.45	2.85
S Glass	2.49	86.2	4.58	3.46
Carbon HS	1.76	230	3.53	13
Carbon HM	1.87	405	3.10	21.7
Carbon UHM	2.15	572	1.86	29.2
Aramid	1.45	130	3.55	9.0
Boron	2.7	393	3.10	14.5
Aluminium	2.78	70	0.40	2.52
Steel	7.85	210	0.60	2.68
Jute	1.4	20	0.5	1.42

Table 1.2. Some of the mostly used reinforcement fibres

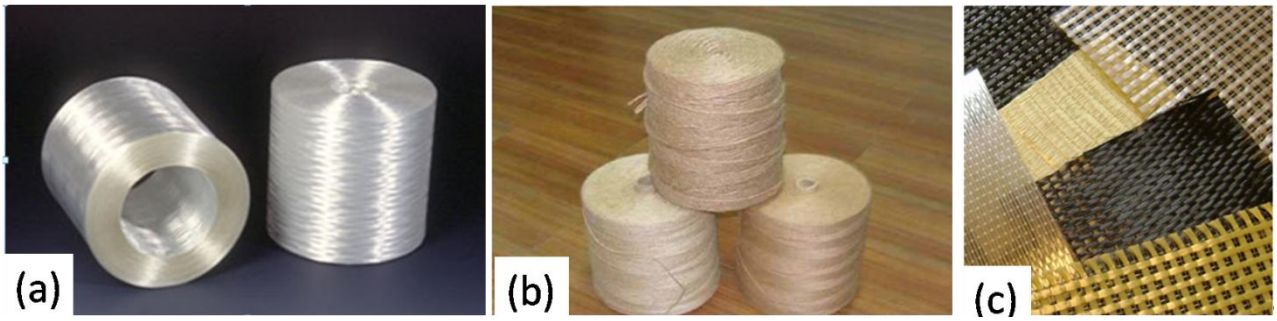

Fig. 1.2. Some fibres in different formats: (a)glass fibres rowing; (b) Jute fibres rowing (c) fabrics of several kinds of fibres.

1.3.1 Glass fibres

Fibreglass was first discovered in 1893 and made commercially available in 1936; it was first used as insulating material in electrical, thermal and acoustic applications. Then, it achieved a great popularity during the 1950s when it was considered as a good substitute to asbestos fibres, whose health hazards were becoming apparent. Today, fibreglass is the dominant reinforcement in composite construction, accounting for about 90% of worldwide consumption. This is simply because it has good strength-to-weight characteristics, can be easily processed and sold at a low price. Glass filaments are relatively easily produced by extruding molten glass, which is obtained by blending quarry products (sand, kaolin, limestone, colemanite) at about 1600 °C; then, the formed liquid is passed through micro-fine bushings and simultaneously cooled to produce the fibre filaments of diameter generally ranging between 5 and 24 μm. The filaments are drawn together into a strand (closely associated), or roving (more loosely associated), and coated with a '*size*', or *binder*; so as to provide filament cohesion and to minimize degradation of filament strength that would otherwise be caused by filament-to-filament abrasion. The size may be temporary, as in the form of a starch-oil emulsion that is subsequently removed by heating and replaced with a glass-to-resin coupling agent known as a *finish*. On the other hand, the size may be a compatible treatment that performs several necessary functions during the subsequent forming operation and which, during impregnation, acts as a coupling agent to the resin being reinforced [10].

By varying the 'recipe' (i.e., by adding chemicals to silica sand), different types of glass can be produced:

- A-glass (alkali glass) has good chemical resistance, but lower electrical properties.
- C-glass (chemical glass) has very high chemical resistance.
- E-glass (electrical glass) is an excellent insulator and resists attacks from water.
- R-, S- and T-glass (structural glass) are optimized for mechanical properties; the different letter identifies the manufacturer's trade name for equivalent fibres.
- D-glass (dielectric glass) has the best electrical properties but lacks in mechanical properties when compared to electrical and structural glass.
- M-glass (modulus) has high stiffness.

Electrical and structural glasses are, by far, the most common types used in composites because of their good combination of chemical resistance, mechanical properties and insulating properties. In particular, E-glass looks more attractive from the cost point of view, while structural glass offers better mechanical performance [4].

1.3.2 Carbon fibres

Carbon has the highest strength and highest price of all reinforcement fibres today available for composites. These fibres were produced in the United Kingdom in the early 1960s, even if Edison had much earlier used them in lighting lamps. The most common method of making long carbon fibres is the oxidation and thermal pyrolysis of an organic precursor, poly-acrylonitrile (PAN). Through heating at correct conditions (2500-3000 °C), the non-carbon constituents evaporate away with a resulting material having a 93-95% carbon content. Of course, the properties of carbon fibres depend on the raw material and the manufacturing process; in fact, the relative amount of exposure at high temperatures results in greater, orless, graphitization of the fibres. Higher degrees of graphitization usually result in a stiffer fibre (higher modulus) with greater electrical and thermal conductivity values.
The size, or thickness, of carbon tows is measured in 'k' or thousands of filaments. A 3k tow contains 3000 filaments while a 12k has 12,000. Carbon fibres exhibit: substantially better strength and stiffness values than all the others types for fibre reinforcement, outstanding temperature performance and high electrical and thermal conductivities. Impact, or damage tolerance, of pure carbon composite products can range from relatively low to higher depending on the processing method. Despite that, when weight of a composite product is important, carbon fibres represent the best reinforcement to be used because of the significant advantages retained by them:

- high stiffness-to-weight ratio
- high strength
- corrosion resistant
- fatigue resistant
- high-energy absorption on impact
- tailored material properties.

First of all, it has to be mentioned that carbon fibres are very light, resulting in lightweight structures. Furthermore, one can chose between stiff, or strong, fibres depending on the composite part being produced.
Another major advantage is that their thermal expansion is practically zero; this means that unlike metals, which expand when heated, carbon fibres remain in their basic form with remarkable benefits in specific projects where thermal stability is required. Moreover, the material can resist very high temperatures (1000 °C), being essentially limited only by the matrix. If properly designed and conceived, carbon fibre composite structures do not suffer any fatigue issues. Finally, carbon fibres are permeable to X-ray and do not corrode, which is a huge concern with metals. The material also has some disadvantages that need to be taken into consideration when planning a project. For instance, carbon fibres are fairly expensive compared to other reinforcements even if their price is steadily decreasing due to the progress of production technology. Moreover, carbon fibre is an electric conductor and, as such, can reflect radio waves, which can be a disadvantage in some cases. In addition, carbon fibres are brittle and material breakage can create debris, which can fly in multiple directions with safety implications.
Finally, handling of carbon fibres may be difficult requiring specific protection. The material size must be appropriately chosen since it must provide consistent handling, without swelling residues on the processing equipment and without obstacles to the penetration of resin into the fibre bundle.
Owing to the different commercial carbon fibre surface features (i.e., smooth, striated, round or kidney shaped), a different blend of physical characteristics, optimized for the fibre shape and surface texture, is required. Size materials must also be compatible with the resin matrix; this includes solubility in and/or reactivity with the formulated resin. This allows the resin to better penetrate the fibre bundle and interact with the fibre surface [4].

1.3.3 Natural fibres

Natural fibres are grouped into three types: seed hair, bast fibres, and leaf fibres, depending upon the source. Some examples are cotton (seed hairs), ramie, jute, and flax (bast fibres), and sisal and abaca (leaf fibres). Of these fibres, jute, ramie, flax, and sisal are the most commonly used fibres for polymer composites. Natural fibres in the form of wood flour have also been often used for preparation of natural fibre composites.
Natural fibres themselves are cellulose fibre reinforced materials as they consist of microfibrils in an amorphous matrix of lignin and hemicellulose. These fibres consist of several fibrils that run all along the length of the fibre. The hydrogen bonds and other linkages provide the necessary strength and stiffness to the fibres. The chemical composition of natural fibres varies depending upon the type of fibre. Primarily, fibres contain cellulose, hemicellulose, pectin, and lignin. The properties of each constituent contribute to the overall properties of the fibre. Hemicellulose is responsible for the biodegradation, moisture absorption, and thermal degradation of the fibre as it shows least resistance, whereas lignin is thermally stable but is subjected to UV degradation. The percentage composition of each of these components varies for different fibres. Generally, the fibres contain 60–80% cellulose, 5–20% lignin, and up to 20% moisture [11,12].

1.3.4 Woven fabric architectures

The reinforcing medium can be produced also in the form of a woven fabric by directly interlacing either separate bundles of fibres, or tows, thus combining warp (0 degree) and weft (90 degree) in a regular pattern, or weave, style. The woven fabric architecture (Fig. 1.3) should be chosen with a compromise between ease of handling during manufacture, drapeability (the ability to form the fabric into a three-dimensional geometry) and mechanical performance [13]. For example, the compact plain weave (Fig. 1.3a), in which each warp fibre passes alternately under and over each weft fibre, is highly stable during handling, due to the intertwined weave structure, but it is the most difficult of the weaves to drape. In addition, it produces a composite with reduced in-plane strength and stiffness because of the high level of fibre crimp; the latter is a misalignment of fibres from the plane of the fabric, which produces resin-rich areas of limited performance benefits. Superior wet out and drape is seen in the twill weave (Fig. 1.3b) where one or more warp fibres alternately weave over and under two or more weft fibres in a regular repeated manner with the visual effect of a straight or broken diagonal 'rib' to the fabric. Twill weaves also have reduced crimp, a smoother surface and slightly higher mechanical properties over the plain weave, with only a small reduction in stability.

Satin weaves (Fig. 1.3c) are fundamentally twill weaves modified to produce fewer intersections of warp and weft. The 'harness' number used in their designation (typically 4, 5 and 8) is the total number of fibres crossed and passed under, before the fibre repeats the pattern. In particular, a 5-harness satin weave is one of the most drapeable examples, with a weave pattern of reduced intertwining, and produces improved in-plane mechanical properties at the expense of stable handling. In addition, the asymmetry needs to be considered in satin weaves since one face of the fabric has fibres running predominantly in the warp direction while the other face has fibres running predominantly in the weft direction [4].

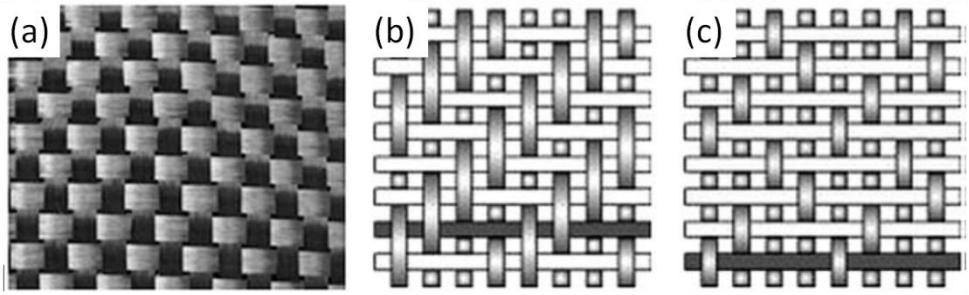

Fig. 1.3 Some woven fabric types. (a) Plain, (b) twill and (c) satin.

1.4 Main types of deficiency in composites

Being composites made of two or more basic materials and manufactured through complex processes involving temperature, pressure, chemical reaction etc., it may be expected that the final product can be affected by anomalies. Moreover, the in-service life of the component could be responsible for defect creation and/or degradation of the composite. In the following discussion, the defects that are mostly present in composites will be grouped into two categories: manufacturing defects and in-service failures [4].

1.4.1 Manufacturing defects

Several different types of defects may occur during fabrication of composites, the most common being: fibre/play misalignment, broken fibres, resin or transversal ply cracks, voids, porosity, slag inclusions, non-uniform fibre/resin volume ratio, disbonded interlaminar regions, kissing bonds, incorrect cure and mechanical damage around machined holes and/or cuts.
The effective performance of a fibre is a function of its correct alignment with the stress/strain direction. In fact, in the presence of fibre misalignment, the loading of the fibre may change from straight tension/compression to shear loading of the weaker interface. This may result in a considerable drop of the composite mechanical properties [14].
Slag inclusions such as dirt and debris, which may inadvertently contaminate the matrix or act as local stress concentrators, leading to delamination either during the manufacturing process, or later when the composite is in service.
The strength of a carbon-fibre-reinforced polymer (CFRP) component is strongly dependent on the volume percentage of resin with respect to fibres. In fact, the presence of regions of fibres unsupported by the matrix can induce local stress concentration (notch effect), with a consequent severe degradation of strength and stiffness during the component's in-service life [15].
Amongst the procedures that allow composite production, the most important is probably the resin curing one. This process has to be optimized in order to get appropriate components responding to the structural design requirements. In fact, resin curing is dependent on the temperature rate increase, the temperature and duration of the curing plateau, the time at which pressure is applied and the post-curing temperature and pressure. If something unexpected occurs in the process, the typical consequence could be incomplete or inappropriate chemical reactions, uneven wetting of the fibres, incorrect fibre volume ratio as well as formation of local matrix-rich pockets, or matrix-starved regions. Moreover, the vacuum pressure, if not suitable, could affect the degassing of contaminants with only partial removal of the gases developing during chemical reactions. This may induce formation of voids (or porosity) within the matrix, between the plies or at the fibre/matrix interface. The detrimental effects of porosity have been known since 1978 when it was found that there was a decrease of the interlaminar shear strength by about 7% for each 1% of voids up to a total void content of about 4% [16]. The decrease of other properties for the first 1% of voids is reported as high as 30% (flexural strength), 9% (torsional shear), 8% (impact strength) and 3% (tensile properties).
The just described defects are the mostly recurrent ones; but, there are also some defects that are peculiar to specific manufacturing processes. In particular, composites fabricated with pre-impregnated layers may entail some specific defects due to the improper storage of pre-pregs, like:

- out-of-date resin because of exposure to ambient temperature (higher than that required for correct storage);
- wrinkled surface because of an uneven positioning, which may result in resin-rich regions within the laminate;
- accumulation of debris, resulting in slag inclusions;
- broken, or damaged, fibre tows, resulting in reduced strength of the laminate.

During processing in autoclave, some defects can occur in the laminate, mainly related to imperfectly cured resin regions due to incorrect pressure/temperature reached values. Besides, lack

of bonding between layers, due to non-uniform pressure on the whole surface, may also occur. Typical drawbacks of the resin transfer moulding (RTM) process are: formation of porosity due to the volatilization of dissolved gases in the resin, mechanical entrapment of gas bubbles or a possible evaporation of mould-release agents. The void formation can be influenced by many factors, such as resin properties, moulding temperature, injection pressure and external pressure during curing. Of course, whatever the type of defect, it may result in slight, or severe, variations of the material properties with, in turn, a reduction of the predicted component life. In fact, these variations may act as sites for the initiation of fatigue damage, or may facilitate the growth of a fatigue crack during cyclic loading.
A comprehensive assessment of the quality of a composite material prior to putting it into service is therefore as important as the monitoring of the levels of damage accumulated in a composite structure during service [17]. This justifies the increasing attention toward development of:

- effective non-destructive evaluation methods able to discover defects at an incipient stage;
- aerospace design procedures aimed at achieving zero-growth thresholds for any type of defect.

Theoretically, many defects may be avoided and the overall quality of a component may be increased with the implementation of particular procedures and the use of specific instrumentation. As an example, the use of computer-controlled tape-laying machines may assure construction of a pre-preg stack for autoclaving to very high standards of quality and repeatability. Similarly, errors of control in pressing can be avoided to some extent by the use of automated autoclaves with pressure-temperature cycles. These cycles must be carefully programmed from detailed chemical knowledge of the gelation and viscosity characteristics of the type of resin in use [17]. Of course, this entails extra costs that remain an industrial decision.
A challenging question may arise concerning the real consequences of the presence of a defect. As stated by Harris [17] in his comprehensive book, a few isolated spherical pores, a micron, or so, in diameter, can have no effect on any physical property, and may not therefore affect the tensile or flexural mechanical performance of a composite. But a distribution of innocuous-looking pores can markedly reduce the interlaminar shear strength of a material and, by providing sites for accumulation of moisture, may also decay the electrical or dielectric performance of the material.
A minor delamination between plies in a complex laminate may have no effect on the tensile strength of the material, but such defect is frequently injurious to the compression performance of laminates and, as previously indicated, can rapidly grow to eventually damage the composite under cyclic-loading conditions. Therefore, to avoid unpredictable failure, it is important to use the most effective non-destructive defects detection techniques and then establish the critical size with a case-by-case approach, owing to the specific type of composite and the specific service conditions for the given application [4].

1.4.2 In-service failures

The in-service failure of composite aircraft structures is primarily caused by impact strikes [18]. The weakness of composites, at least those based on a thermoset matrix, to impacts is well known, especially to low-velocity/energies that may cause subsurface damage in the form of delamination, cracks, as well as fibre breakage without appreciable surface signs. In fact, other than a small dent,

these impacts show no, or little visual evidence on the external surface as to the extent of the delaminated area [19]. In particular, delamination in CFRP laminates reduces the strength, particularly the compression strength, of the structure; if undetected and unrepaired, it may result in reduction of ultimate load capability, or even inability to withstand design limit load in service life [20,21]. Conversely, high velocity impact is accompanied by little structural response [21] and can be identified with the naked eye. For safety issues, when impact damage occurs to an aircraft structure, the latter must be able to 'withstand reasonable loads without failure or excessive structural deformation' for the 'operational life of the aircraft' or 'until the damage is detected' [22]. Of course, for design purposes, it is of great importance to have knowledge of the failure mechanisms.

1.4.2.1. Some hints on failure mechanisms

In the Griffith model [23], the fracture of homogeneous materials like metals is based on the stress-intensity factor, K, and the associated strain-energy release rate, G, which is mainly related to the material fracture toughness (material resistance to crack propagation) [17]. In real fibre composites, the micro-structural inhomogeneity and anisotropy cause the failure process to be very complex with also a combination of micro-failure events, which can often give rise to high levels of fracture energy. In fact, unlike homogeneous materials, composites have crack-stopper ability inherent in both types of interfaces at a microscopic level (between fibres and matrix) and at a macroscopic level (between separate laminas). This gives rise to complex fracture mechanisms involving breaking of fibres and matrix, delamination between fibres and matrix, and a combination of crack deviations along interfaces (at both micro- and macroscopic levels).

In practice, the fracturing of a composite is driven by three factors: the matrix, the reinforcement and the interface; it is important to consider the types of matrix and fibres, their mutual volumes and the type of bonds in between them, meaning the curing process. Then, the toughness of a composite is derived from many sources, and the relative magnitudes of the separate contributions depend not only on the characteristics of the components but also on the manner in which they interact. Thus, there is no simple recipe for predicting the toughness of all composites [17]. It follows that the procedures based on classical fracture mechanics cannot be simply applied for design purposes of composites. When fibres are incorporated into a matrix of any kind, the separate phases may be able to contribute in an additive fashion their individual levels of toughness to the composite, or they may not, depending on the kind of interaction that occurs and on the level of constraint that is set up as a result of their different properties [17]; so, it is rather difficult, or even impossible, to predict the way a composite will fail. This justifies the huge amount of literature on the subject [6, 19, 24-47].

Since the introduction of composites in aircraft construction, one main interest of the scientific community was to establish the delamination threshold load (DTL) under impact [24]. However, notwithstanding the huge amount of available data coming from both numerical simulation and experimental testing, a methodology to unambiguously establish the DTL has still not been completely achieved. This is because the DTL depends on many factors, in primis, the effective material mechanical characteristics as well as the geometry of the target [25,26] and of the impactor [27]. The high variability of mechanical properties of composites derives also from the amount of porosity that is induced by manufacturing processes and that is practically unavoidable [48]; the

voids content can be reduced but not completely suppressed. Perhaps this is the reason why composite materials display a large variety of damaging ways under impact. In fact, as reported by Abrate [28], some impacts produce plastic deformations in a small zone surrounding the impact point, while others involve deformations of the entire structure. In some cases, a major portion of the impact energy is transferred to the impacted plate, and in other cases, most of the energy is returned to the impactor. In some circumstances, the indentation absorbs a significant amount of the impact energy so that it must be adequately modelled in the analysis; in other cases, the effects of indentation are practically negligible. It must also be considered that mainly in the aircraft industry there is the habit to quantify impact threats in terms of impact energy, but, as observed by Olsson et al. [47], this is not completely correct since a small mass and a large mass impactor may entail, at the same impact energy, completely different responses. A contribution to solve this drawback was given by Meola and Carlomagno [49] who proposed a relationship that links the damaged area to the impact energy and the impactor dimension; this result was achieved while using infrared thermography to investigate the response of composites to impact events [49,50].

Owing to the available literature within the last thirty years, it comes up that the prediction of the impact response of composites to low energy impact has been widely addressed from analytical, numerical and experimental approaches, but it is still an open question. This because the results available in literature are generally restricted to particular cases, while new composite materials are continuously developed, which require ad hoc testing. The problem seems of no solution considering the many parameters involved (type of material, laminate thickness, testing machine, boundary conditions, etc.) and complexity of the coupled physical phenomena, which make difficult modelling as well the high costs involved with experimental tests.

As an important observation, the evaluation of new materials is generally performed owing to criteria based on energy and force, or on a multiple parameters configuration [45]. The energy based criterion involves damage maps, which are plots of damage area vs. impact energy or dissipated energy, and Compression After Impact (CAI) curves, which are plots of the static residual strength vs. impact or dissipated energy. The force criterion relies on the peak force recorded during an impact event. The multiple parameters approach includes many tests in sequence to get information about the most important parameters that characterize the impact behaviour of a structure and practically includes both energy and force criteria. Amongst others, a main factor of interest is the damage extension vs. the impact energy. Often, this feature is assessed through specific impact tests, which are intended to identify the energy that has caused delamination of a given extension. More specifically, such tests consist of impacting the laminate at a given energy, evaluating, in a non-destructive way, the induced damage extension and go on to increasing impact energies until the preset delamination has been reached. This is a long way on and often not very accurate since the presence of very thin delamination is difficult to be discovered with the available non-destructive testing techniques (NDT). In fact, it may happen that two layers of a thermoset matrix based composite, which were separated by the impact, recommit themselves very tightly, even if delaminated, once the impacting object went away and the surface has recovered its undeformed configuration. It is also worth considering that, depending on the composite architecture, delamination may propagate along tortuous pathways, which may complicate the situation.

In recent years, at the University of Naples Federico II, it has been demonstrated that it is possible to monitor the surface of the laminate directly during the impact with an infrared imaging device [51] to get information on the extension of the occurred delamination [49,50]. In particular, they

proved that, with an infrared imaging device, it is possible to visualize the thermal effects that develop under low-energy impact, and which may supply information about initiation and propagation of the impact damage. By considering that during an impact event kinetic energy passes from the impactor nose to the target, and that such energy is in part dissipated as heat, the detection of thermal signatures developing under impact may be important for the comprehension of failure modes. In fact, any form of damage (delamination and/or fibre breakage) is generally accompanied by heat dissipation, which manifests itself through the appearance of hot spots/areas over the material surface. In this regard, the use of infrared thermography has to be considered as beneficial and unique.

Amongst the objectives of this dissertation, one is to go on that subject and to understand more through tests on many types of composites and by developing post-processing procedures to evaluate the extension of the occurred damage. This topic will be addressed in Chapter 5.

Another objective within composites is to investigate their behaviour under cyclic bending to search for any likely information, which may be easily derived through monitoring with an infrared camera and which may be helpful to characterize novel composite materials.

References to Chapter 1

[1]. R. Shütze, Aircraft wings. US Patent 5496002; 1996.

[2]. M. Piening, A. Pabsch, C. Sigle, Structural element of high unidirectional rigidity.US Patent 6355337; 2002.

[3]. P.M. Peeters, J. Middel, A. Hoolhorst, Fuel efficiency of commercial aircraft. An overview of historical and future trends. Retrieved at <http://www.transportenvironment.org/docs/Publications/2005pubs/2005-12_nlr_aviation_fuel_efficiency.pdf>.

[4]. C. Meola, S. Boccardi, G.M. Carlomagno, Infrared Thermography in the Evaluation of Aerospace Composite Materials, Elsevie & Woodhead publishing ISBN 978-1-78242-171-9, 2016

[5]. M.C. Collier, D.G. Baird, Separation of a thermotropic liquid crystalline polymer from polypropylene composites. Polym Compos, 20, 423–35, 1999.

[6]. T.W. Shyr, Y.H. Pan, Impact resistance and damage characteristics of composite laminates. Compos Struct, 62, 193–203, 2003.

[7]. D.J Landini, R.L.K. Matsumoto, D.M. Domanski, Processing of Sic/Sic Ceramic Matrix Composites by Use of Colloidal Carbon Black, US 0035024 A1, 2006.

[8]. K.U. Kainer, Metal Matrix Composites. Custom-made Materials for Automotive and Aerospace Engineering, Wiley-VCH, 2006.

[9]. M.A. Masuelli, Introduction of fibre-reinforced polymers polymers and composites: concepts, properties and processes, in: M. Masuelli (Ed.), Fibre Reinforced Polymers - the Technology Applied for Concrete Repair, InTech, 2013, ISBN 978-953-51-0938-9, http://dx.doi.org/10.5772/54629.

[10]. A.C. Long (Ed.), Design and Manufacture of Textile Composites, Woodhead Publishing and CRC Press LLC, 2005, ISBN 9781855737440.

[11]. H. Ku, H. Wang, N. Pattarachaiyakoop, M. Trada, A review on the tensile properties of natural fibre reinforced polymer composites, Composites Part B, 42, 856-873, 2011.

[12]. D. Nabi Saheb, J. P. Jog, Natural Fibre Polymer Composite: A Review, Advances in Polymer Technology, 18 (4), 352-363, 1999.

[13]. C.M. Pastore, D.W. Whyte, H. Soebruto, F.K. Ko, Design and analysis of multi axial warp knit fabrics for composites, J. Ind. Fabrics, 5 (14) 4-14, 1986.

[14]. J. Summerscales, Manufacturing defects in fibre reinforced plastics composites, Insight, 36 (12) 936-942, 1994.

[15]. H.T. Yoshida, T. Ogasa, R. Hayashi, Statistical approach to the relationship between ILSS and void content of CFRP, Comput. Sci. Tech. 25 (1) 3-18, 1986.

[16]. N.C.W. Judd, W.W. Wright, Voids and their effects on the mechanical properties of composites - an appraisal, SAMPE J. 14 (1) 10-14, 1978.
[17]. B. Harris, Engineering Composite Materials, The Institute of Materials (IOM), London, 1999. ISBN:1861250320, 9781861250322.
[18]. Civil Aviation Authority Safety Regulation Group, Reliability of Damage Detection in Advanced Composite Aircraft Structures Paper 2013/03, 2013.
[19]. M.S. Sohn, X.Z. Hua, J.K. Kimb, L. Walker, Impact damage characterisation of carbon fibre/epoxy composites with multilayer reinforcement, Composites: Part B, 31, 681-691, 2000.
[20]. Transportation Safety Board of Canada, Assessment of the Response from Transport Canada to Aviation Safety Recommendation A06-05 Inspection Program of Rudder Assembly, 2007.
[21]. P.E. Irving, C. Soutis, Polymer Composites in the Aerospace Industry, Woodhead Publishing Series in Composites Science and Engineering, ISBN 978-0-85709-523-7, 2014.
[22]. European Aviation Safety Agency, Certification Specifications for Large Aeroplanes CS-25, Amendment 5, 2008.
[23]. A.A. Griffith, The phenomena of rupture and flow in solids, Philos. Trans. R. Soc. Lond. Ser. A 221, 163-198, 1920.
[24]. D.J. Elder, R.S. Thomson, M.Q. Nguyen, M.L. Scott, Review of delamination predictive methods for low speed impact of composite laminates, Compos. Struct. 66, 677-683, 2004.
[25]. G.A. Schoeppner, S. Abrate, Delamination threshold loads for low velocity impact on composite laminates, Composites: Part A, 31, 903-915, 2000.
[26]. W.J. Cantwell, Geometrical effects in the low velocity impact response of GFRP, Compos. Sci. Technol. 67, 1900-1908, 2007.
[27]. T. Mitrevski, I.H. Marshall, R. Thomson, R. Jones, B. Whittingham, The effect of impactor shape on the impact response of composite laminates, Compos. Struct. 67, 139-148, 2005.
[28]. S. Abrate, Modeling of impacts on composite structures, Compos. Struct. 51, 129-138, 2001.
[29]. W.J. Cantwell, J. Morton, Detection of impact damage in CFRP laminates. Compos Struct, 3, 241–57, 1985.
[30]. K.N. Shivakumar, W. Elber, W. Illg, Prediction of Impact force and duration due to low-velocity impact on circular composite laminates. J Appl Mech, 52, 674–80, 1985.
[31]. P. Sjo¨blom, T. Hartness, T.M. Corbell, On low velocity impact testing of composite materials. J Compos Mater, 22 (1), 30–52, 1988.
[32]. G.A.O. Davies, X. Zhang, Impact damage prediction in carbon composite structure. Int J Impact Eng, 16 (1), 149–70, 1994.
[33]. D. Delfosse, A. Poursartip, Energy-based approach to impact damage in CFRP. Compos Part A, 28A, 647–55, 1997.
[34]. G. Zhou, Effect of impact damage on the residual compressive strength of glass–fibre reinforced polyester (GFRP) laminates. Compos Struct, 35, 171–81, 1996.
[35]. D. Liu, B.B. Raju, X. Dang, Size effects on impact response of composite laminates. Int J Impact Eng, 21(10), 837–54, 1998.
[36]. C.F. Li, N. Hu, J.G. Cheng, H. Fukunaga, H. Sekine, Low velocity impact induced damage of continuous fibre-reinforced composite laminates. Part II. Verification and numerical investigation. Compos Part A, 33, 1063–72, 2002.
[37]. G. Belingardi, R. Vadori, Low velocity impact tests of laminate glass-fibre-epoxy matrix composite material plates. Int J Impact Eng, 27, 213–29, 2002.
[38]. T. Mitrevski, I.H. Marshall, R.S. Thomson, R. Jones. Low-velocity impacts on preloaded GFRP specimens with various impactor shapes. Composite Structures, 76, 209–217, 2006.
[39]. G. Caprino , V. Lopresto , C. Scarponi, G. Briotti. Infuence of material thickness on the response of carbon-fabric/epoxy panels to low velocity impact. Comp. Sci. Technol. 59. 2279-2286, 1999.
[40]. W.C. Jackson, C.C. Poe, The use of impact force as a scale parameter for the impact response of composite laminates. J Compos Technol Res, 15/4, 282–9, 1993.
[41]. A.T. Nettles, M.J. Douglas. A comparison of quasi-static indentation to low-velocity impact, NASA TP-2000-210481, Aug.; 2003.
[42]. G. Caprino, V. Lopresto, The significance of indentation in the inspection of carbon fibre-reinforced plastic panels damaged by low velocity impact. Compos Sci Tech, 60, 1003–12, 2000.
[43]. G. Caprino, A. Langella, V. Lopresto, Indentation and penetration of carbon fibre reinforced plastic laminates. Compos Part B, 34(4), 319–25, 2003.

[44]. J.N. Baucoma, M.A. Zikryb. Low-velocity impact damage progression in woven E-glass composite systems. Composites: Part A, 36, 658–664, 2005.
[45]. P. Feraboli, K.T. Kedward, A new composite structure impact performance assessment program, Comp. Sci. Technol. 66, 1336–1347, 2006.
[46]. V. Lopresto, C. Leone, I. De Iorio. Mechanical characterisation of basalt fibre reinforced plastic. Composites: Part B 42, 717-7123, 2011.
[47]. R. Olsson, M.V. Donadon, B.G. Falzon, Delamination threshold load for dynamic impact on plates, Int. J. Solids Struct. 43, 3124-3141. 2006.
[48]. L. Liu, B.M. Zhang, D.F. Wang, Z.J. Wu, Effects of cure cycles on void content and mechanical properties of composite laminates, Compos. Struct. 73, 303-309, 2006.
[49]. C. Meola, G.M. Carlomagno, Impact damage in GFRP: new insights with infrared thermography, Composites: Part A 41, 1839-1847, 2010.
[50]. C. Meola, G.M. Carlomagno, F. Ricci, V. Lopresto, G. Caprino, Investigation of impact damage in composites with infrared thermography, in: P. Mazal (Ed.), Proceedings of 6th NDT in Progress, Prague (Czech Republic), 2011, pp. 175-182.
[51]. C. Meola, G.M. Carlomagno, Infrared thermography to impact-driven thermal effects, Applied Physics A, 96, 759-762, 2009.

Chapter 2

Infrared thermography

Nomenclature

A,B,C	Constants that accounts for the surface and atmosphere characteristics.
A_{det}	Detector active area
A_{e}	Electrical area
A_o	Optical Area.
c	Speed of light
D^*	Detectivity.
d_w	Wien's displacement constant ($d_w \cong 2898$ μm K)
E_a	Fraction of E_{Tot} Energy emitted by the atmosphere
E_d	Detected radiationE_b Total hemispherical radiation intensity
E_ε	Fraction of E_{Tot} emitted by the generic object
E_g	Energy gap from the valence band and conduction band
$E_{\lambda b}$	Monochromatic (spectral) radiation intensity
E_{mc}	Incident Radiation.
E_{ph}	Photon energy
E_ρ	Fraction of E_{Tot} reflected by the generic object
E_{Tot}	Total energy detected by the IR camera.
f_{ph}	Photon Frequency
h	Planck's constant (h = 6.6 x 10^{-34} J s)
I_{inc}	Incident energy over a surface.
I_{out}	Reflected energy over a surface.
k_b	Boltzmann's constant (k_b = 1.38 x 10^{-23} J/K)
N_L	rms noise level.
N_{out}	Noise output.
R_v	Responsivity
S_{out}	Signal output.
T	Absolute temperature
$1/f$	Flicker noise or pink noise

Greek Symbols

α	Total absorptance
α_λ	Monochromatic absorptance
β	Angle formed by the I_{out} direction and the surface normal direction
γ	Angle formed by the I_{inc} direction and the surface normal direction.
Δf	Noise bandwidth
ΔS_m	Signal measured for the temperature ΔT
ΔT	Temperature difference.
ε	Emissivity coefficient.
ε_λ	Monochromatic emissivity coefficient.

η_q	Quantum efficiency.
λ	Wavelength
λ_c	Cut-off wavelength.
λ_{max}	Wavelength at which is emitted the maximum radiation intensity of monochromatic (spectral) radiation intensity $E_{\lambda b.}$
ρ	Total reflectance coefficient.
ρ_λ	Monochromatic reflectance coefficient
σ	Stefan Boltzmann constant (σ = 5.67 x 10^{-8} W/m^2 K^4)
τ	Total transmittance
τ_λ	Monochromatic transmittance
Φ_b	Photon flux density (also called dark current).

Introduction

Infrared thermography (IRT) is a discipline that relies on physical principles, theoretical basis and practical approaches. Essentially, it includes an IR detecting device to sense the thermal energy that is radiated from objects in the IR band; such energy, with the aid of specific software and basic relationships, is transformed into a video signal and, finally, into the object surface temperature map. Naturally, this is a simplified description; in reality, the way the final temperature map is accomplished is a rather complex procedure that involves many disciplines like electromagnetism, electronics, signal treatments, heat transfer, etc. IRT is being used in a broad number of application fields and for many different purposes; definitely, any process that is temperature dependent may benefit from the use of an IR device. Indeed, an IR imaging device should be considered as a precious partner to consult for diagnostics and preventative purposes, for understanding of complex fluid dynamics phenomena, or for material characterization and procedures assessment, which can help improve design and fabrication of products. IRT may accompany the entire life of a product, since it may be used to control the manufacturing process (online process control), to non-destructively assess the final product integrity and to monitor the component in service.
Besides, IRT can be usefully exploited in all the applications in which the temperature in a key parameter like: medicine, veterinary, electrics, electronics, video surveillance, astronomy, and many other industrial fields [1-57]. Of course, for the success of any application, it is most important to choose the most adequate IR camera and test procedure, as well image processing and data analysis for the specific use required.

2.1 Some basics

Infrared thermography is based on the physical evidence that any body at temperature above 0 K emits thermal radiation, due to molecular and atomic agitation associated with the internal energy of the material. The radiant energy is carried by photons, generally regarded as a discrete particle having zero mass, no electric charge, indefinitely long lifetime and moving in vacuum at the speed of light $c \cong 3 \times 10^8$ m/s. Each photon has energy E_{ph}, which is equal to its frequency f_{ph} multiplied the *Planck's constant* ($h = 6.6 \times 10^{-34}$ J s); such energy can be expressed, according to Einstein, in terms of :

$$E_{ph} = hf_{ph} = h\frac{c}{\lambda} \tag{2.1}$$

which states that the energy is inversely proportional to the wavelength λ of the considered radiation, i.e., the higher the energy, the shorter the wavelength. The electromagnetic spectrum is shown in Fig. 2.1.
From Fig. 2.1 it is possible to see the location of the IR band in terms of wavelength, or frequency, and the extension of the thermal region, which embraces the entire IR and visible bands, as well as the upper part of the ultraviolet band.
In order to formulate simple general laws for thermal radiation, it is useful to introduce a conceptual body, usually called a *black body*, which has the property of being a perfect emitter and absorber of radiation. A black body is thus able to absorb all the incident radiation, regardless of its wavelength

and direction, and is the body that, for a fixed temperature and wavelength, emits the maximum possible amount of radiation.

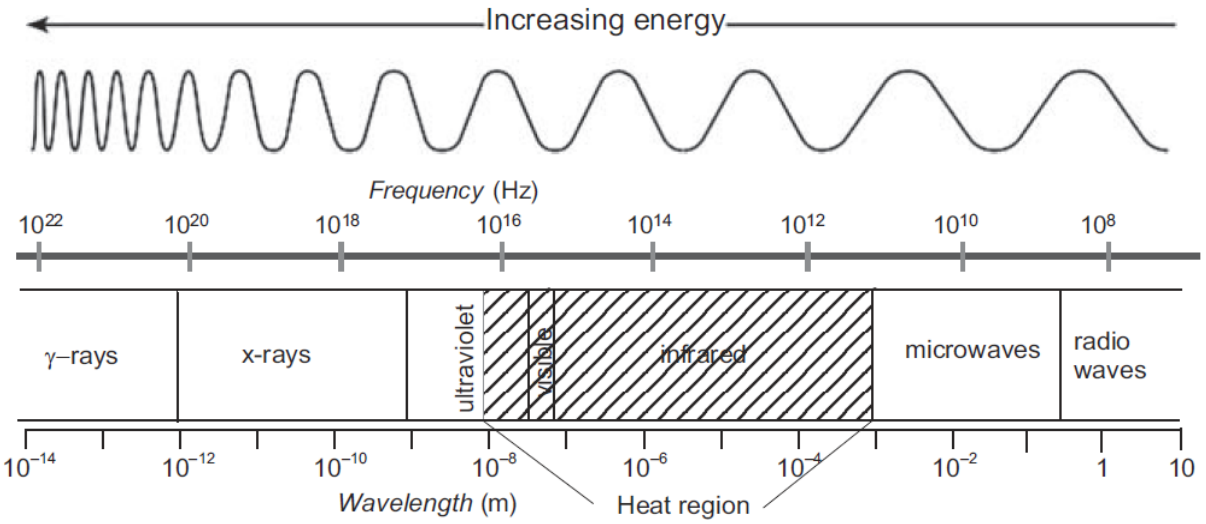

Fig. 2.1. Representation of the electromagnetic spectrum (wave not to scale).

The *Planck's law* describes the spectral distribution of the radiation from a black body:

$$E_{\lambda b} = \frac{2\pi hc^2}{\lambda^5\left(e^{\frac{hc}{\lambda k_b T}}-1\right)} \tag{2.2}$$

where: $E_{\lambda b}$ is the black body monochromatic (spectral) radiation intensity, k_b is Boltzmann's constant (k_b = 1.38 x 10^{-23} J/K) and T is the absolute temperature of the black body (K). Planck's law is plotted in Fig. 2.2. for several absolute temperature values in the range 200-6000K. For each curve, $E_{\lambda b}$ starts from zero for λ= 0, then increases rapidly up to a maximum and, finally, decreases toward zero again at very long wavelength values. As can be seen, the higher the temperature, the shorter the wavelength at which the maximum occurs and the higher the temperature, the higher the energy emitted by the black body.
In particular, by differentiating Planck's law Eq. (2.2) with respect to λ and setting to 0 the derivative function it is possible to evaluate, for a given temperature, the value of λ_{max} at which is emitted the maximum radiation intensity. The values of λ_{max} follows the *Wien's displacement law*:

$$\lambda_{max} = \frac{d_w}{T} \tag{2.3}$$

The symbol d_w is the Wien's displacement constant, which is approximately equal to 2898 μm K. Practically, at ambient temperature (about 300K), the radiation peak lies in the far IR at about 10 μm. The sun radiation (about 6000K) peaks at about 0.5 μm in the visible light spectrum (Fig. 2.2). Conversely, at the temperature of liquid nitrogen (77K) the maximum radiation intensity occurs at about 38 μm, in the extreme IR wavelength.

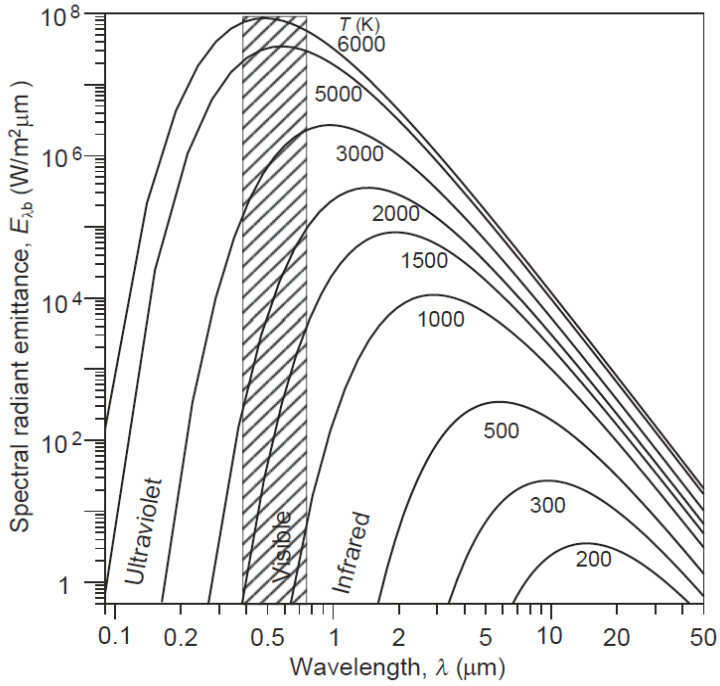

Fig. 2.2. Black body emissive power against wavelength (Planck's law).

By integrating Planck's law over the entire spectrum ($\lambda \in [\ 0\ ,\ \infty]$, the total hemispherical radiation intensity emitted by a black body (*Stefan Boltzmann's law*) can be obtained:

$$E_b = \sigma T^4 \tag{2.4}$$

where σ is the Stefan Boltzmann constant (σ = 5.67 x 10^{-8} W/m^2 K^4).
It has to be pointed out that a real object generally emits only a part E_λ of the radiation emitted by a black body at the same temperature and at the same wavelength $E_{\lambda b}$.

2.2 Real objects radiation

A generic real object may have a different ability to absorb (emit), reflect and transmit energy with respect to the black body owing to its bulk material nature and surface finishing. This ability is generally described through the relationship:

$$\alpha + \rho + \tau = 1 \tag{2.5}$$

which links the *total absorptance* α to the *total reflectance* ρ and to the *total transmittance* τ. For a black body Eq.(2.5) simplifies as α = 1 because the black body does not reflect, nor transmit, energy. Moreover, for real bodies α, ρ and τ are, in general, not constant but depend on the wavelength λ (spectral dependence);so that, more specifically, Eq.(2.5) becomes:

$$\alpha_\lambda + \rho_\lambda + \tau_\lambda = 1 \tag{2.6}$$

It has to be observed that a surface may exhibit selective behaviour not only with respect to the wavelength but also with respect to the direction of the propagating energy since the energy, absorbed by a surface, may come mostly from certain directions.
By considering a generic wavelength λ, it is possible to demonstrate through the *Kirchoff's law* that, at thermodynamic equilibrium, the energy released by a surface is equal to the absorbed one:

$$\alpha_\lambda = \varepsilon_\lambda \tag{2.7}$$

where ε_λ indicates the *emissivity coefficient*, which represents the fraction of the energy emitted by a real body with respect to that emitted by the black body at the same temperature:

$$\varepsilon_\lambda = \frac{E_\lambda}{E_{\lambda b}} \tag{2.8}$$

In other words, Eq.(2.7) states that, for a body at constant temperature, the rate at which it absorbs energy is equal to the rate at which it emits energy; otherwise the object would warm, or cool, in contrast with the assertion of thermodynamic equilibrium. It is general habit to use the symbol ε without reference to the wavelength.
For some non black body objects, the emissivity does not vary with the wavelength; these objects are called *grey*bodies. A comparison between the spectral radiant emittance of a black body, a grey body and a real body, all at the same temperature, is shown in Fig. 2.3 [58].

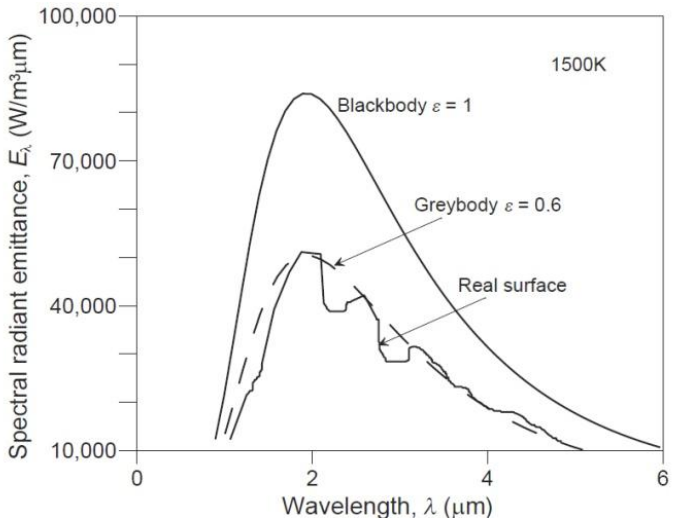

Fig. 2.3. Emissive power for black, grey and real surfaces.

The radiation curve of a greybody is identical to that of a black body except that it is scaled down for the radiated power by the factor ε. Conversely, the radiation distribution of a real object depends on the wavelength. The knowledge of the thermal emissivity is essential for accurate temperature measurements with an IR imaging system. The values of many of the most common materials are generously listed in the literature. However, these values are not at all useful when dealing with an IR system because of the following reasons:

- The values of emissivity are reported in the tables without any additional explanation about the direction and the wavelength.

- Tables present in literature include terms like: polished, cast, rolled, oxidized, heavily oxidized etc that does not allow to uniquely identify the real surface under consideration.

Thus, the emissivity values reported in the tables does not allow to get accurate temperature measurements. The better way is to directly measure the emissivity with the same IR camera according to the standards [59]. This procedure consists simply in comparing the radiation emitted by the material sample and that emitted by a black body at the same temperature. As last observation to perform accurate thermographic measurements, it is preferable to work with high-emissivity surfaces; to this end, it is possible to increase the surface emissivity of highly polished metals, or reflectors, with deposition of thin films of dull paint or grease.
To allow for successful measurements with an IR imaging device, the object must be opaque (non transparent) in the IR wavelength band and must have high emissivity. For an opaque material and taking into account Eq. (2.7.), Eq. (2.6.) reverts to:

$$\varepsilon + \rho = 1 \tag{2.9}$$

According to Eq. 2.9, all real surfaces reflect part of the incident radiation coming from the surroundings that bounces off the target. Both ρ and ε depend on the considered material, surface finishing and wavelength of the incident radiation.
A surface may reflect the incident radiation in two modes: *specular* and *diffuse*. When a surface is very smooth and highly polished, almost all of the incident energy I_{inc} is thrown out of the surface as I_{out} in a single direction, with the incident angle γ equal to the exit one β . In the case of rough surfaces the incident energy I_{inc} is reflected almost uniformly in all directions .
The emissivity does not depend only on the bulk material and surface finishing but also on the direction. In fact a real surface does not emit the same radiation in all directions; for non metallic materials, the maximum emission generally occurs in the direction normal to the radiating surface and decreases, becoming null for a direction parallel to that surface. Practically, a curved surface must be subdivided into at least three sectors to obtain reliable temperature measurements [49].

2.2.1 Effects of interposed atmosphere

For accurate temperature measurements with an IR system, reflections should be removed, or kept small ($\rho << 1$). Owing to Fig. 2.4, the total energy detected by the IR camera E_{Tot} includes the energy emitted by the object E_{ε}, the reflected energy coming from the surroundings E_{ρ} and the energy emitted by the atmosphere E_a and it can be written as:

$$E_{Tot} = \mathrm{A}E_{\varepsilon} + \mathrm{B}E_{\rho} + \mathrm{C}E_a \tag{2.10}$$

where A, B and C are constants that account for the characteristics of the object surface and of the atmosphere between the object and the camera. In particular, before reaching the detector, the radiation emitted by a body passes through the atmosphere and it may be affected by its absorption and emission, which must be taken into account. In most cases, the absorptance of the interposed atmosphere can be neglected.

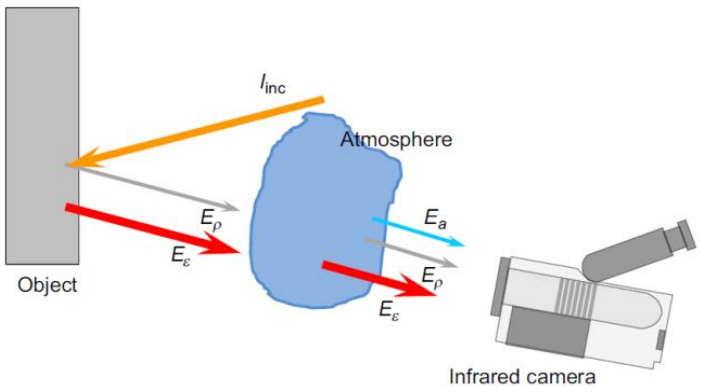

Fig. 2.4. Components of energy reaching the infrared camera.

As a final point, to perform measurements of temperature starting from thermal radiation, it is important to know exactly how much energy is emitted by the object and is captured by the IR detector; it is worth noting that E_ρ can be measured and accounted for.
Normal atmosphere consists of a mixture of gases that absorbs IR radiation in several wavelength intervals and their combined effects determine the atmosphere transmittance with the wavelength (Fig. 2.5) [60].

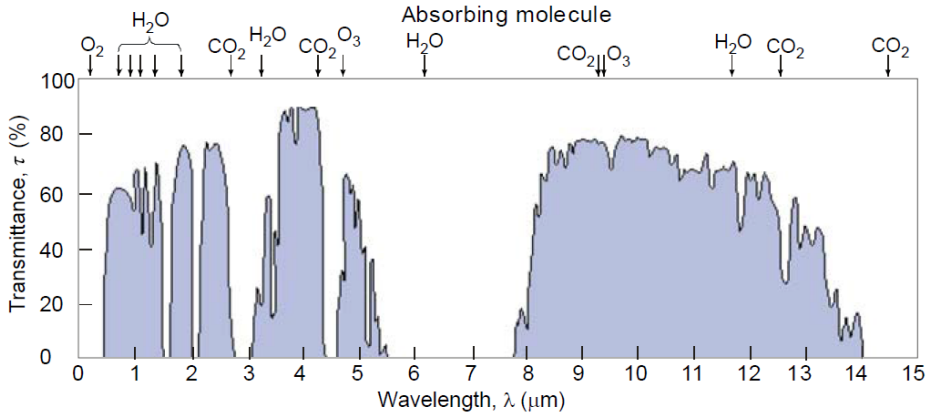

Fig. 2.5. Atmosphere composition and transmittance(1 km thick layer).

The presence of aerosols (salt particles, water droplets, dust, pollution) contributes to atmospheric absorption but their main effect is scattering (Mie scattering), i.e., a redistribution of the radiation into all directions with loss in the travelling direction of the wave from source to detector. In any case, the scattering phenomenon is stronger in the visible region and in the IR region close to the visible one. The atmosphere emits its own radiation (Eq. 2.10), but this contribution becomes important for large distances between the object and the IR camera and for measurements of a low-temperature object. It is not simple to evaluate the atmosphere emission and attenuation; an easy and convenient way is to account for them through calibration of the IR system.

2.3 Infrared devices

Infrared devices perform measurements in three main IR bands [61]:

- *Short Wave Infrared* SWIR (0.8 - 2 μm).

- *Middle Wave Infrared* MWIR (2 - 5.5 μm).
- *Long Wave Infrared* LWIR (8 - 14 μm).

The detector is the kernel of any IR device; it absorbs the IR energy emitted by the object and produce electrical signals proportional to the amount of incident radiation falling on it. The actual in use infrared imager are based on the focal plane array (FPA) technology. The overall performance of an IR imaging system is conventionally expressed through several parameters:

- *Thermal sensitivity*- is expressed through the equivalent random noise level.
- *Frame rate*- is the number of images per unit time.
- *Image resolution*- is the number of independent measurement data points the image is composed of.
- *Dynamic range or intensity resolution* - is the number of intensity levels, which allows for fine temperature differences.

The detectors mostly used for IR technology can be grouped into two main categories: *thermal* and *quantum* (or *photon*) detectors.

2.3.1 Thermal detectors

These detectors are also called energy detectors, or photon absorbers, because they absorb the incident energy and warm up; their temperature changes are measured through the variation of a temperature-dependent property of the material such as the electrical resistance. The main advantage is their response at room temperature and over a large band of the IR spectrum. The main disadvantage is their relatively slow response time (of the order of milliseconds), which makes them not suitable for high frequency events. Examples of detectors that belong to this family are: thermopiles, bolometers, pyroelectric detectors and microcantilevers.
The microbolometer technology is based on the resistance change with temperature of a resistor element and is the mostly employed in handheld IR systems. Basically, a microbolometer consists of two platinum strips, covered with lampblack; one strip is shielded from the radiation and the other one is exposed to it. The two strips form two branches of a Wheatstone bridge; the resistance in the circuit varies when the strip, which is exposed to IR radiation, heats up and changes its electrical resistance. Nowadays, advances in silicon micromachining have led to the microbolometer technology, which includes a grid of vanadium oxide, or amorphous silicon heat sensors, atop a porous silicon bridge as thermal insulator and a mechanical supporting structure. The microbolometer grid is commonly found in different sizes: 160 x 120, 320 x 240, 640 x 512 and 1024 x 1024 arrays.

2.3.2 Photon Detectors.

Photon or quantum detectors generate free electrical carriers in response to photon absorption. Their main advantage is a very short response time (of the order of microseconds). While a disadvantage is the need of cooling them down to cryogenic temperature to avoid excessive dark current. In fact, electrons can be excited from the valence to the conduction band by photons having an energy E_{ph}

that is larger than the energy gap E_g between the bands. There exists a wavelength λ_c named cut-off wavelength beyond which no emission occurs. The value of E_g varies from semiconductor to semiconductor and tends to increase as temperature increases (cut-off wavelength decreases). Thus, the detector must be maintained at low temperature.
Different cooling methods were developed through the history of infrared thermography. The current mostly used method involves a Stirling pump that operates by cyclic compression and expansion of the working fluid (generally helium gas). In modern cooled cameras, the detector focal plane assembly is generally tightly attached to the cold side of a Stirling cooler to allow for conductive heat exchange. The Stirling system removes heat from the cold finger and dissipates it at the warm side. It has relatively low efficiency but it is adequate for cooling of the IR camera detector and allows operation of the camera for a long time and in complex placements.
There are four main types of photon detectors: *photovoltaic* (PV), *photoconductive*, *photo-emissive* and *quantum well* IR photodetector (QWIP). In particular, the PV and photoconductive types may be intrinsic or extrinsic. The structure of a PV intrinsic (electromotive force generation) is based on a p-n junction device (two dissimilar materials), which, under IR radiation, generates photocurrents. These detectors are generally fabricated from silicon (Si), germanium (Ge), gallium arsenide (GaAs), indium antimonide (InSb), indium gallium arsenide (InGaAs) and mercury cadmium telluride (HgCdTe) (also called MCT).
In PV intrinsic detectors, the incident radiation, with energy greater than or equal to the energy band-gap of the semiconductor, generates majority electrical carriers. The electric conductivity of the material is improved; there is an internal photoelectric effect. Common materials are lead sulfide (PbS), lead selenide (PbSe) and MCT (HgCdTe). Extrinsic detectors are similar to intrinsic detectors. The difference lies in the fact that carriers are excited from the impurity levels and not over the band-gap of the basic material; this is achieved by doping the semiconductor material. The most-used materials are silicon and germanium doped with impurities such as boron, arsenic and gallium. The spectral response of these detectors can be controlled by the doping level. Photo-emissive detectors are bi-materials involving a metal layer superimposed to a semiconductor layer; a typical example is platinum silicide (PtSi) on silicon (Si). The process, which is also called external photoelectric effect, consists of the emission of carriers from the metal into the semiconductor under photon absorption. The main advantage is a more uniform response since the response depends on the characteristics of the metal. However, since the photon absorption is proportional to the square of the wavelength, this type of detector is more indicated for long wavelengths.
The QWIP generally consists of layers of thin gallium arsenide alternated to layers of aluminium gallium arsenide (AlGaAs). The basic principle is similar to that of extrinsic detectors with the peculiarity that the dopants are concentrated in microscopic regions and create the quantum wells. The radiation is absorbed by the entire quantum well, not only by a single doping atom, and thus the absorption is increased (so is the response) with respect to extrinsic detectors.

2.3.3. QWIP detectors technology

The Quantum Well Infrared Photodetector (QWIP) is a semiconductor device which is generally made of layers of thin gallium arsenide (GaAs) alternated to layers of aluminium gallium arsenide (AlGaAs). These quantum well devices have a number of potential advantages, including the use of

standard manufacturing techniques based on mature GaAs growth and processing technologies, highly uniform and well-controlled molecular beam epitaxy growth on GaAs wafers greater than 6 in., high yield and thus low cost, more thermal stability, and extrinsic radiation hardness [62]. Conversely, QWIPs present some problems: low quantum efficiency (η_q< 50%, typical ≅ 20%), lower operating temperature, high dark currents, complex light coupling schemes, narrow spectral response that limits sensitivity in low-background conditions. As a fabrication drawback, photons normally impinging are not absorbed (do not produce excitation) and so roughed surfaces are needed to scatter photons inside the detector. The major source of noise in QWIPs is the dark current (i.e., the current that flows through a biased detector in the dark with no photons impinging on it). As reported by Rogalski [63], at low temperature (<40 K) the dark current is mostly caused by defect related direct tunnelling, while in the medium range between 40 and 70 K the thermally assisted tunnelling dominates. At temperature above 70 K, the dark current is mostly dominated by classic thermionic emission (i.e., heat-induced flow of charge carriers) of ground state electrons directly out of the well into the continuum. The choice of the detector operating temperature is performed as a compromise between reducing the dark current and improving the sensitivity since the two parameters are correlated. Generally, the choice falls on the value of 70 K opting for high sensitivity. From a practical standpoint, QWIPs are suited for large arrays (640 x 512 pixels) formats, low frame rates and large integration time.

2.3.4 Detector performance

The performance of a detector is evaluated through three parameters: *responsivity* R_v, *noise equivalent power* (NEP) and *detectivity D**. The responsivity R_v is a measure of the signal output S_{out} (voltage, or current) per incident radiation E_{mc} over the active area of the detector A_{det}:

$$R_v = \frac{S_{out}}{E_{mc} A_{det}} \tag{2.11}$$

The active area is determined as the ratio $A_{det} = A_o/A_e$ between the optical area A_o and the actual electrical area A_e. The NEP defines the intrinsic noise level of the detector, or better the detection limit of the detector. It can be expressed by:

$$\mathrm{NEP} = \frac{N_{out}}{R_v \sqrt{\Delta f}} \tag{2.12}$$

with N_{out} the noise output and Δf the noise bandwidth. The detectivity *D** defines the resolving power of the detector and is expressed in terms of the signal-to-noise ratio (*Sout/Nout*) with respect to the incident power:

$$D^* = \frac{\sqrt{A_{det}}}{NEP} \tag{2.13}$$

The noise that affects detection of IR radiation is of different types and comes from several sources [63]. One major noise source is the electronic circuitry, which gives rise to two different types of

noise. One is thermal noise, also known as Johnson noise [64], or Johnson-Nyquist noise, which refers to fluctuations in the electrical signal induced by thermal motion of free electrons in a resistive element [65]. Thermal noise is important for thermal detectors while it is generally negligible for photon detectors for which the detection limit is evaluated by accounting for the background radiation. The other type of noise linked to the electronic circuitry is shot noise, first described by Schottky in 1918 and often also named Schottky noise. From a general point of view, since electrons share the particle-wave duality with photons, shot noise applies to both. As a definition, shot noise is due to the fluctuations of the number of independent charge carriers crossing a boundary (electrons in an electronic circuit, or photons in an optical device). It is a random process following Poisson statistics (for which the mean squared fluctuation of the number of emission events is equal to the average count (N) and the signal-to-noise ratio (SNR) takes the expression:

$$\mathrm{SNR} = \sqrt{\mathrm{N}} \tag{2.14}$$

Of course, shot noise dominates when the finite number of particles that carry energy is small enough. As N increases, the Poisson distribution approaches the Gaussian one and shot noise becomes insignificant. Shot noise is independent of frequency (white noise), but, unlike thermal noise, it is also independent of temperature, meaning it cannot be eliminated by lowering the sensor temperature. Generally, shot noise dominates at high frequency and is linearly proportional to the current [66]. At low frequency (below 10 kHz), another type of noise dominates, which is related to time dependent fluctuations; this noise is called flicker noise, or 1/*f*, or pink noise, and, in contrast to the white noise (thermal and shot), is frequency dependent. Flicker noise occurs in virtually all electronic components, as well as in many other physical items in everyday life from the earth's rotation to undersea currents [67,68]. There are two major theoretical hypotheses to its origin. One refers to the fluctuation of the number of carriers caused by capture and emission of carriers into trap centres close to the substrate/dielectric interface. The second hypothesis accounts for fluctuations of the mobility of free carriers, since it is believed to be due to microscopic defects in the semiconductor material.

As described in literature, when the area of the device is small, or the number of defects in the device reduces to one or two, flicker noise becomes burst noise. This type of noise also got the name of popcorn noise because the sound it makes when played over a speaker resembles the sound of popcorn popping. Burst noise is described to look, on an oscilloscope, like a square wave of constant magnitude but with random pulse widths. Recently this noise was also referred to as random telegraph signal (RTS). In particular, Kleinpenning [69] showed that RTS noise exists with devices with a small number of carriers, where a single electron can be captured by a single trapping centre. RTS noise is present in sub-micrometer MOS transistors and in bipolar junction transistors with defected crystal lattice, as well as in modern SiGe transistors. This type of noise is a function of temperature, induced mechanical stress and radiation, and has significant effects at low frequency (typically $f < 1$ kHz). It is described to manifest as a sudden step, or jump, in base current on bipolar transistors, or a step in threshold voltage for FETs. Bursts can happen several times a second or, in some rare cases, may take minutes to occur. They are believed to be caused by charge traps or microscopic defects in the semiconductor material.

In IR detectors, noise comes from two main sources: the IR detector itself with its circuits and the background fluctuations. The first contribution is generally negligible with respect to the second

one and then the detection limit is evaluated by accounting only for the background radiation. This contribution is called *background limited IR photodetection* (BLIP). PV detectors are characterized by a $\sqrt{2}$ higher BLIP; in fact, the relationship for a PV detector is:

$$D^*_{BLIP_{pv}} = \frac{\lambda}{hc}\frac{\sqrt{\eta_q}}{\sqrt{2\Phi_b}} \tag{2.15}$$

while for a photoconductive is:

$$D^*_{BLIP_{pc}} = \frac{\lambda}{2hc}\frac{\sqrt{\eta_q}}{\sqrt{\Phi_b}} \tag{2.16}$$

Φ_b being the background photon flux density (also called dark current). The value of Φ_b received by the detector depends on its responsivity to the wavelengths contained in the radiant source and on its field of view of the background.
A relevant parameter for IR systems is the noise equivalent temperature difference; it can be defined as the temperature change, for incident radiation, that gives an output signal equal to the rms noise level N_L:

$$\mathrm{NETD} = N_L \frac{\Delta T}{\Delta S_m} \tag{2.17}$$

where ΔS_m is the signal measured for the temperature difference ΔT. In other words the NETD can be considered as the amount of scene temperature difference that equals the internal noise. The NETD can be improved by increasing the size of the detecting elements but, increasing the IFOV would degrade the spatial resolution.

2.4 IR Image generation

A typical FPA can be described as a two-dimensional matrix of *n* columns by *m* rows of individual cells, or pixels, with each pixel (detector) having micrometre-size dimensions. The interface circuit (or driving circuit) of each cell, which converts the current from each photodiode to a voltage at each pixel, is referred to as a readout integrated circuit (ROIC) unit cell. A control circuit is also needed to synchronize the operation of the unit cells and converts the output of the IR pixels to a stream of bits [70]. The main function of an ROIC is transforming the small diode incremental current, generated by IR radiation, into a relatively large measurable output voltage; this is commonly done by integrating the photocurrent in a capacitor during a fixed period of time. There are two integration modes: the asynchronous integrate while read (AIWR) and the asynchronous integrate then read (AITR). In the AIWR mode, the camera is able to integrate scene signals while simultaneously reading out the previous frame. This mode allows for semi-independent control of the camera's frame rate and integration time snapshots taken per second; the integration time is the length of time that each snapshot actually views the scene. However, the time required to read out all of the pixels limits the maximum frame rate; the selection of a smaller window size allows the

maximum frame rate to increase The AITR mode is used in some radiometric cameras coupled with specific calibrated windows [60,71]
The integration process is controlled by the Frame Synchronization (FSYNC) clock pulse. The rising edge of the FSYNC clock pulse marks the beginning of the frame time; this is followed immediately by a sequence of line synchronization (LSYNC) clock pulses that produce a readout sequence. Each time the switch is closed, the capacitor discharges and when the switch is open the integration starts again. The rate at which this switch is operated is called the sampling rate; such sample & hold circuit acts in a sinusoidal fashion. The FSYNC clock remains high until the readout sequence has been completed. The integration time occurs after the readout time, resulting in a frame time that is approximately.
Two main signals that are used for time synchronization of the circuit are line synchronization (LSYNC) and frame synchronization (FSYNC), which along with the master clock (CLK), multiplex the provided array of the unit cell voltages to a serial stream, sequentially. The master clock is the highest frequency clock and provides a reference for pixel readout; the other clocks (FSYNC and LSYNC) are integral numbers of CLK periods. In particular, the LSYNC controls the readout synchronization of each individual line of the array, while the FSYNC marks the beginning of the frame time. Starting from the first cell of the first row, the outputs of all cells in the row go to the column multiplexer. With each clock pulse, the multiplexer connects the output of one of the cells in the first row to the output stage. After multiplexing the last cell in the row, the LSYNC pulse triggers the row shift register and the second line is selected (the column shift register is also reset). Similar to the first row, each column will again be selected sequentially by the clock pulse. At the end of the frame, the FSYNC pulse resets both row and column shift registers and the pointer returns to its initial position to start a new frame. The LSYNC and FSYNC pulses are generated based on the ROIC operation mode (integrate-while read or integrate-then-read). More specifically, in any case, the rising edge of the FSYNC triggers the beginning of the frame, but it is followed by a sequence of LSYNC signals for every line change in the AIWR mode making the frame time approximately equal to the read time. Conversely, in the AITR, the FSYNC signal remains high until the end of the readout sequence, and the integration starts just after the readout, resulting in a frame time that is approximately equal to the readout time plus the integration time [70].

2.4.1 Problems affecting infrared images

Every pixel in the sensor array is acting like a single element detector with its own thermal response curve (offset and gain). This means that if we put in front of the camera an object with a uniform temperature distribution, we would like to see each pixel of the array giving out the same signal, in terms of digital level, or grey level or colour level. Instead, a raw image may appear affected by non-uniformity and may be almost unusable without the due software corrections. Common effects are:

- Fixed pattern noise is due to spatial intensity values observed either as a grid like pattern or as a striping pattern laid on the top of the true image. It is due to the pixel reading procedure in the IR cameras that implement FPA.

- Bad pixels, defined as anomalous pixels that can be distinguished in dead pixels, permanently dark, and hot pixels, permanently white. A map of dead pixels is generally known from the FPA manufacturer.
- Vignetting, which appears as a darkening of the image corners while the centre remains brighter. It is related to the gap between the temperature of the scene and the temperature of the lens.
- Different offset and gain of the pixels, which is almost unavoidable in the detector production process.

All these effects deteriorate the image quality, hence, to get a good image out of a FPA detector, it is necessary to go through the characterization of each array pixels. This process is the so-called "*Nonuniformity Correction*" mapping (NUC).
This is part of the calibration procedure and in the microbolometer camera is factory prepared and stored in the camera memory. For laboratory systems instead, this process can be either stored in the camera memory or performed by the user according to the working conditions. The procedure consists of placing in front of the camera two homogeneous black bodies, one at low temperature and another one at higher temperature. All the image pixels are scanned by the software and checked one by one for offset, gain and wrong response. Gain and offset values are identified and then stored in file maps corresponding to the image size. The non responding pixels are instead stored in another file map; the bad pixels will be replaced by the neighbours. Once calculated, these maps will be applied on the fly to the raw image at camera scanning speed. Another problem may be the camera's ambient temperature drift, or better the radiation caused by the heating and cooling of the camera itself, mainly of the internal electronic circuitry. Any swings in camera internal temperature caused by changes in environment, or the heating and cooling of camera electronics, will affect the radiation intensity at the detector. This is called parasitic radiation and can cause inaccuracies in the camera output, especially with thermographically calibrated cameras. Certain IR cameras have internal sensors that monitor changes in camera temperature and send feedback to the camera processor. The camera output is then corrected for any parasitic radiation effects; this functionality is commonly referred to as ambient drift compensation [72].

2.5 Calibration

As already said, the core of the camera is the infrared detector, which absorbs the IR energy emitted by the object (whose surface temperature is to be measured) and converts it into electric voltage or current. Every object emits energy proportional to its surface temperature. However, the energy really detected (by the infrared detector) depends on the emissivity coefficient ε of the surface under measurement and on the environment. In fact, a bright surface (low ε value) not only emits less energy than a blackbody but also reflects part of the incident energy coming from the surroundings (Fig.2.4). A fraction of such reflected energy falls in the detector optical pathway and is added to the effective energy emitted by the object surface under measurement. Furthermore, the infrared radiation measured by the detector can be affected by atmospheric damping. In fact, a fraction of energy is absorbed by the atmosphere between the object and the camera; such a fraction becomes important in presence of low-transmittance atmosphere. To take into account these factors, calibration of the system by using a reference blackbody and by simulating real atmospheric operating conditions has to be performed [17]. The calibration function:

$$E_d = \varepsilon \frac{A}{e^{B/T - C}} \quad (2.18)$$

relays the real amount of detected energy E_d to the blackbody temperature T through the calibration constants A, B and C which take into account spurious quantities of energy from, or to, the environment.

2.6 Applications

As already said at the beginning of this chapter, infrared thermography can be used in a wide range of applications which are linked to thermal aspects, or in which the temperature is a parameter of interest. Indeed, there is availability of a wide selection of infrared devices, which differentiate for weight, dimensions, shape, performance and of course costs to fulfil with desires of users in a vast variety of applications. However, within composite materials, infrared thermography has been used mainly for non-destructive evaluation purposes to discover either manufacturing defects, or artificially created defects, or impact damage. Different techniques have been developed: pulse, long, or step pulse, lock-in, pulse phase, ultrasound lock-in, etc. With regard to the impact damage, infrared thermography can also be used to monitor impact tests and get information helpful for understanding the impact damaging mechanisms, as also said at the end of chapter 1. This work is intended to pursue this objective with the obtained results being described in chapter 5.

References to Chapter 2

[1] M.P. Connolly, The measurement of porosity in composite materials using infrared thermography. J. Reinf. Plast. Compos. 11, 1367–1375, 1992.

[2] D. Wu, A. Salerno, U. Malter, R. Aoki, R. Kochendörfer, P.K. Kächele, G. Busse, Inspection of aircraft structural components using lockin-thermography. Quantitative infrared thermography, QIRT, 96, 251-256, 1996.

[3] M.P. Luong Fatigue limit evaluation of metals using an infrared thermographic technique. Mech. Mater. 28, 155–163, 1998.

[4] E. Grinzato, V. Vavilov, T. Kauppinen, Quantitative infrared thermography in buildings. Energy Build. 29, 1–9, 1998.

[5] V. Vavilov, D. Almond, G. Busse, E. Grinzato, J. Krapez, X. Maldague, S. Marinetti, W. Peng, V. Shirayev, D. Wu, Infrared thermographic detection and characterisation of impact damage in carbon fibre composites: Results of the round robin test. Proceedings of the Eurotherm Seminar; Lodz, Poland. September 1998; pp. 7–10.

[6] V. P. Vavilov, S. Marinetti, E. Grinzato, P. Bison, Thermal tomography characterization and pulse-phase thermography of impact damage in CFRP, or why end users are still reluctant about practical use of transient IR thermography. In Aerospace/Defense Sensing and Controls. International Society for Optics and Photonics, 275-281, 1998.

[7] G. La Rosa, A. Risitano, Thermographic methodology for rapid determination of the fatigue limit of materials and mechanical components. Int. J. Fatigue. 22, 65–73, 2000.

[8] X. Maldague, Applications of infrared thermography in nondestructive evaluation. Trends Opt. Nondestruc. Test. 591–609, 2000.

[9] X. Maldague Theory and Practice of Infrared Technology for Nondestructive Testing. Wiley; New York, NY, USA: 2001.

[10] S.M. Shepard Advances in pulsed thermography Proc. SPIE 4360, Thermosense XXIII, 511 (March 23, 2001); doi:10.1117/12.421032.

[11] E. Grinzato, P. Bison, S. Marinetti, Monitoring of ancient buildings by the thermal method. J. Cultural Herit. 3, 21–29, 2002.

[12] C. Ibarra-Castanedo, F. Galmiche, A. Darabi, M. Pilla, M. Klein, A. Ziadi, S. Vallerand, J.F. Pelletier, X.P. Maldague, Thermographic nondestructive evaluation: Overview of recent progress. Proc. SPIE 5073. 2003 doi: 10.1117/12.485699.
[13] N.P. Avdelidis, B. Hawtin, D. Almond, Transient thermography in the assessment of defects of aircraft composites. NDT& Int. 36, 433–439, 2003.
[14] S. M. Shepard, Advances in thermographic NDT. Proceedings of the AeroSense 2003. International Society for Optics and Photonics; Orlando, FL, USA. 21 April 2003; pp. 882–887.
[15] C. Meola, G.M. Carlomagno, A. Squillace, G. Giorleo, The use of infrared thermography for nondestructive evaluation of joints. Infrared Phys. Technol. 46, 93–99, 2004.
[16] N.P. Avdelidis, D.P. Almond, A. Dobbinson, B. Hawtin, C. Ibarra-Castanedo, X. Maldague, Aircraft composites assessment by means of transient thermal NDT. Progr. Aerosp. Sci. 40, 143–162, 2004.
[17] C. Meola, G.M. Carlomagno, Recent advances in the use of infrared thermography. Meas. Sci. Technol. 15, R27-54, 2004.
[18] V.P. Vavilov, D.A. Nesteruk. Detecting water in aviation honeycomb structures: The quantitative approach. Quant. InfraRed Thermogr. J. 1, 173–184, 2004.
[19] B. Wiecek, Review on thermal image processing for passive and active thermography. Proceedings of the 27th Annual International Conference of the IEEE Engineering in Medicine and Biology; Shanghai, China. 1–4 September 2005; pp. 686–689.
[20] M. Stewart, J. Webster, A. Schaefer, N. Cook, S. Scott, Infrared thermography as a non-invasive tool to study animal welfare. Anim. Welf. 14, 319–325, 2005.
[21] A.R. Al-Kassir, J. Fernandez, F. Tinaut, F. Castro, Thermographic study of energetic installations. Appl. Therm. Eng. 25, 183–190, 2005.
[22] C. Ibarra-Castanedo, M. Genest, J.M. Piau, S. Guibert, A. Bendada, X.P. Maldague, C. Chen. Ultrasonic and Advanced Methods for Nondestructive Testing and Material Characterization. In: Chen C.H., editor. Active Infrared Thermography Techniques for the Non-Destructive Testing of Materials. World Scientific; Singapore, 2007. pp. 325–348.
[23] S.M. Shepard, Flash thermography of aerospace composites, in: Proceedings of the 4th Pan American Conference for NDT, Buenos Aires, Argentina, October 2007. papers 132.
[24] R. Usamentiaga, D.F. García, J. Molleda. Real-time adaptive method for noise filtering of a stream of thermographic line scans based on spatial overlapping and edge detection. J. Electron. Imaging. 17, 033012, 2008;.
[25] E.K. Ng, A review of thermography as promising non-invasive detection modality for breast tumor. Int. J. Therm. Sci. 48, 849–859, 2009.
[26] C. Maierhofer, M. Roellig. Active thermography for the characterization of surfaces and interfaces of historic masonry structures. Proceedings of the 7th International Symposium on Non-destructive Testing in Civil Engineering (NDTCE); Nantes, France. 30 June–3 July 2009.
[27] C. Meola, G.M. Carlomagno. Recent Advances in Non-Destructive Inspection. Nova Science Publisher Inc; New York, NY, USA: 2010.
[28] G.M. Carlomagno, G. Cardone, Infrared thermography for convective heat transfer measurements, Experiments in Fluids, 49, 1187-1218, 2010.
[29] M. Vollmer, K.P. Möllmann, Infrared Thermal Imaging: Fundamentals, Research and Applications. Wiley; Weinheim, Germany: 2011.
[30] G. Mayr, B. Plank, J. Sekelja, G. Hendorfer, Active thermography as a quantitative method for non-destructive evaluation of porous carbon fiber reinforced polymers. NDT & Int. 44, 537–543, 2011.
[31] C. Ibarra-Castanedo, N.P. Avdelidis, E. Grinzato, P.G. Bison, S. Marinetti, C.C. Plescanu, X.P. Maldague, Delamination detection and impact damage assessment of GLARE by active thermography. International Journal of Materials and Product Technology, 41(1-4), 5-16, 2011.
[32] B. Lahiri, S. Bagavathiappan, T. Jayakumar, J. Philip, Medical applications of infrared thermography: A review. Infrared Phys. Technol. 55, 221–235, 2012.
[33] R. Usamentiaga, P. Venegas, J. Guerediaga, L. Vega, I. López, Non-destructive inspection of drilled holes in reinforced honeycomb sandwich panels using active thermography. Infrared Phys. Technol. 55, 491–498, 2012.
[34] C. Meola, Infrared Thermography: Recent Advances and Future Trends. Bentham Science; New York, NY, USA: 2012.

[35] U. Galietti, D. Palumbo, G. Calia, M. Pellegrini, Non destructive evaluation of composite materials with new thermal methods. In 15th European Conference on Composite Materials: Composites at Venice, ECCM (pp. 24-28), 2012.
[36] C. Ibarra-Castanedo, J.R. Tarpani, X.P. Maldague, Nondestructive testing with thermography. Eur. J. Phys. 34, S91, 2013.
[37] X. Guo, V. Vavilov, Crack detection in aluminum parts by using ultrasound-excited infrared thermography. Infrared Phys. Technol. 61, 149–156, 2013.
[38] S. Bagavathiappan, B. Lahiri, T. Saravanan, J. Philip, T. Jayakumar, Infrared thermography for condition monitoring—A review. Infrared Phys. Technol. 60, 35–55, 2013.
[39] T. Astarita, G.M. Carlomagno, Infrared Thermography for Thermo-Fluid-Dynamics, Springer-Verlag, Berlin-Heidelberg, 224 pages, 2013.
[40] C. Maierhofer, P. Myrach, M. Reischel, H. Steinfurth, M. Röllig, M. Kunert, Characterizing damage in CFRP structures using flash thermography in reflection and transmission configurations. Compos. Part B Eng. 57, 35–46, 2014.
[41] D. Palumbo, U. Galietti, Characterisation of steel welded joints by infrared thermographic methods, Quantitative InfraRed Thermography Journal 11 (1), 29-42, 2014.
[42] D. Palumbo, F. Ancona, U. Galietti, Quantitative damage evaluation of composite materials with microwave thermographic technique: feasibility and new data analysis, Meccanica 50 (2), 443-459, 2015.
[43] R. Marani, D. Palumbo, U. Galietti, E. Stella, T. D'Orazio, Automatic detection of subsurface defects in composite materials using thermography and unsupervised machine learning. In Intelligent Systems (IS), 2016 IEEE 8th International Conference on (pp. 516-521). IEEE, 2016.
[44] D. Palumbo, R. De Finis, P.G. Demelio, U. Galietti, A new rapid thermographic method to assess the fatigue limit in GFRP composites Composites Part B: Engineering 103, 60-67, 2016.
[45] L.M. Serio, D. Palumbo, U. Galietti, L.A.C. De Filippis, A.D. Ludovico, Monitoring of the friction stir welding process by means of thermography Nondestructive Testing and Evaluation 31 (4), 371-383, 2016.
[46] D. Palumbo, U. Galietti, Mechanical Behaviour of Stainless Steels under Dynamic Loading: An Investigation with Thermal Methods R De Finis, Journal of Imaging 2 (4), 32, 2016.
[47] C. Maierhofer, P. Myrach, R. Krankenhagen, M. Röllig, H. Steinfurth, Detection and Characterization of Defects in Isotropic and Anisotropic Structures Using Lockin Thermography, J. Imaging 2015, 1(1), 220-248; doi:10.3390/jimaging1010220
[48] C. Meola, S. Boccardi, G.M. Carlomagno, An Excursus on Infrared Thermography Imaging, J. Imaging 2016, 2(4), 36; doi:10.3390/jimaging2040036.
[49] C. Meola, S. Boccardi, G.M. Carlomagno, Infrared Thermography in the Evaluation of AerospaceComposite Materials, Elsevier& Woodhead publishing ISBN 978-1-78242-171-9, 2016.
[50] C. Meola, S. Boccardi, G.M. Carlomagno, N.D. Boffa, F. Ricci, G. Simeoli, P. Russo, Characterization with infrared thermography, Compositi Magazine, 39, 25-29, 2016.
[51] C. Bonavolontà, C. Aramo, M. Valentino, G. Pepe, S. De Nicola, G. Carotenuto, A. Longo, M. Palomba, S. Boccardi, C. Meola, Graphene–polymer coating for the realization of strain sensors, Beilstein J. Nanotechnology, 8, 21–27, 2017.
[52] C. Bonavolontà, C. Camerlingo, G. Carotenuto, S De Nicola, A. Longo, C. Meola, S. Boccardi, M. Palomba, G.P. Pepe, M. Valentino, Characterization of piezoresistive properties of graphene-supported polymer coating for strain sensor applications, Sensors and Actuators A: Physical, 252, 26-34, 2016.
[53] L. Maio, M. Liberini, D. Campanella, A. Astarita, S. Esposito, S. Boccardi, C. Meola, Infrared thermography for monitoring heat generation in a linear friction welding process of Ti6Al4V alloy, Infrared Phys. Technol, 81, 325-338, 2017.
[54] C. Meola, G.M. Carlomagno, S. Boccardi, G. Simeoli, D. Acierno, P. Russo, Infrared Thermography to Monitor Thermoplastic-matrix Composites Under Load, Proc. 11th ECNDT, Prague (Czech Republic), 10p,. 2014.
[55] C. Meola, S. Boccardi, G.M. Carlomagno, G. Simeoli, P. Russo, Learning More on Thermoplastic Composites with Infrared Thermography, Proc. 19th WCNDT, Munich (Germany),8p., 2016.
[56] S. Boccardi, N.D. Boffa, G.M. Carlomagno, C. Meola, F. Ricci, Visualization of impact damaging of carbon/epoxy panels. Proc. AIP Conf. TOP & Composites Ischia (Italy), 4p., 2016.

[57] C. Meola, S. Boccardi, G.M. Carlomagno, N.D. Boffa, E. Monaco, F. Ricci, Experimental Investigation of Impact Damaging of Carbon Fibre Reinforced Composites, Proc. 19th WCNDT, Munich (Germany), 8p., 2016.
[58] F. Kreith, R.M. Manglik, M.S. Bohn Principles of Heat Transfer 7th Edition, 2009.
[59] ASTM E1933-14, Standard Test Methods for Measuring and Compensating for Emissivity Using Infrared Imaging Radiometers, American Society for Testing and Materials, Pennsylvania, USA, 2014.
[60] Flir Systems SC6000 Manual.
[61] European Standards (EN 16714, part 1 to 3), 2016.
[62] A. Rogalski, Competitive technologies of third generation infrared photon detectors, Opto-Electron. Rev. 14, 87–101, 2006.
[63] A. Rogalski, Infrared detectors: status and trends, Prog. Quantum Electron. 27, 59–210, 2003.
[64] J.B. Johnson, Thermal agitation of electricity in conductors, Am. Phys. Soc. 32, 97, 1928.
[65] E.L. Dereniak, D.G. Crowe, Optical Radiation Detectors, John Wiley & Sons, pp. 39-40, 1984.
[66] C. Beenakker, C. Schönenberge, Quantum shot noise, Phys. Today 56, 37-42, 2003.
[67] P. Dutta, P.M. Horn, Low-frequency fluctuations in solids: 1/f noise, Rev. Mod. Phys. 53, 497-516, 1981.
[68] A.A. Balandin, Noise and Fluctuations Control in Electronic Devices, American Scientific Publishers, Los Angeles, 2002.
[69] T.G.M. Kleinpenning, On 1/f noise and random telegraph noise in very small electronic devices, Physica B 164.
[70] M. Singh, M. Sadana, S. Sachdev, G. Pratap, Development of miniature Stirling cryocooler technology for infrared focal plane array, Def. Sci. J. 63 (6) 571-580, 2013.
[71] N.Y. Aziz, R.F. Cannata, G.T. Kincaid, R.J. Hansen, J.L. Heath, W.J. Parrish, S.M. Petronio, J.T. Woolaway, Standardized high performance 640 by 512 readout integrated circuit for infrared applications, in: Proc. SPIE 3698, Infrared Technology and Applications XXV, vol. 766, July 26, 1999, http://dx.doi.org/10.1117/12.354577.
[72] http://www.flir.com/uploadedFiles/Thermography/MMC/Brochures/T559243/T559243_APAC.pdf , (accessed on August 2014).

Chapter 3

Infrared cameras, temporal noise and Reference Area Method

Nomenclature

A	Measuring Area.
A_i	Generic Measuring Area.
A_R	Reference Area.
A_{Ri}	Generic Reference Area.
F_R	Infrared camera frame rate.
i	Row index.
j	Column index.
m	Generic number of pixels along a column.
n	Generic number of pixels along a row.
T	Temperature
t	Image index in the sequence or time.

Greek Symbols

ΔT_C	Corrected ΔT_R values.
ΔT_N	Temporal noise evaluated in the reference area.
ΔT_R	Raw Temperature difference.
ε	Emissivity coefficient.
μ	ΔT mean values over time relative to a specific signal.
$\mu(t)$	ΔT signal mean value evaluated amongst several signals at time t.
σ	ΔT standard deviation over time relative to a specific signal.
$\sigma(t)$	ΔT signal standard deviation evaluated amongst several signals at time t.

Introduction

The accuracy of measurement performed with infrared thermography depends on many factors involving amongst others the instrument performance and the thermographer's skill. Of course, the magnitude of temperature differences to be measured is of great concern.
In fact, some limitations may arise when attempting to measure temperature variations that are very small, in particular, at the edge of the instrument resolution. In this regard, a difficult task is to perceive the temperature variations that are related to thermoelastic effects, e.g., developing under relatively low loads. This is because of the presence of the detector noise; practically, the amplitude of the signal to be measured may fall within the noise amplitude. In particular, some detectors may exhibit random jumping noise that may mask the temperature variations to be measured. However, some of the detector temporal noise may be accounted for and eliminated in a simple and effective way with the use of a reference area.
This chapter is entirely devoted to the investigation of the temporal noise exhibited by several types of infrared camera and the effectiveness of the Reference Area Method [1,2]. To this end, measurements are carried out by considering either a black body, or real surfaces. In particular, the temporal noise characterizing the infrared camera SC6000 equipped with the QWIP detector will be analyzed more deeply being this camera the one mainly used within the applications reported in this thesis. Indeed, this is the infrared camera available at the Gasdynamics Laboratoy where research activities have been carried out; the others infrared cameras have been kindly provided by Flir systems for a limited time period.

3.1 Characterization of QWIP SC6000 temporal noise.

The SC6000 QWIP LW is a radiometric cooled infrared camera developed by Flir Systems for Research & Development (R&D). Its principal characteristics are listed below:

- Detector QWIP working in the 8-9.2 μm electromagnetic band.
- Cooling system: Linear Stirling cycle engine.
- Maximal spatial resolution of 640x480 pixels.
- Pixel size 25 μm.
- Integration time 9 μs to full frame rate.
- Operating temperature -40+55 °C.
- Dynamic range 14 bit.
- NETD < 35 mK.
- Lens focal length 50 mm.

To try to characterize the SC6000 infrared camera temporal noise some specific tests are carried out. In particular, the infrared camera is positioned to look at a blackbody (Fig. 3.1) that is maintained at constant temperature being connected at a thermostatic bath. Of course, care was put to wait that steady state conditions were reached for both infrared camera and thermostatic bath. Two temperature values are considered: ambient temperature of about 25 °C and 30 °C; thermal images in time sequence are acquired. by changing the frame rate from 1 up to 100 Hz. The use of the blackbody assures getting free of any effects linked to emissivity variations and reflections from the ambient.

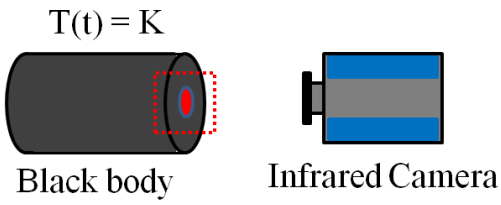

Fig. 3.1. Test setup.

Then, the acquired sequences of thermal images are post-processed by using either the software available within the infrared camera package (Flir Researcher, ResearchIR), or proper routines developed in the Matlab environment. Firstly, sequences of ΔT images are created according to:

$$\Delta T(i,j,t) = T(i,j,t) - T(i,j,0) \tag{3.1}$$

where i,j and t are the row, column and frame number respectively in the sequence and t=0 indicates the first frame. Some ΔT plots versus time taken with varying the frame rate F_R are reported in Fig. 3.2; in particular, each ΔT plot is obtained as average over at least 100 pixels. Being the black body kept at constant temperature the measured ΔT over time should be perfectly equal to zero for each pixel in the image, while as it is possible to see in Fig. 3.2. some irregularities are present over time in the recorded signal.

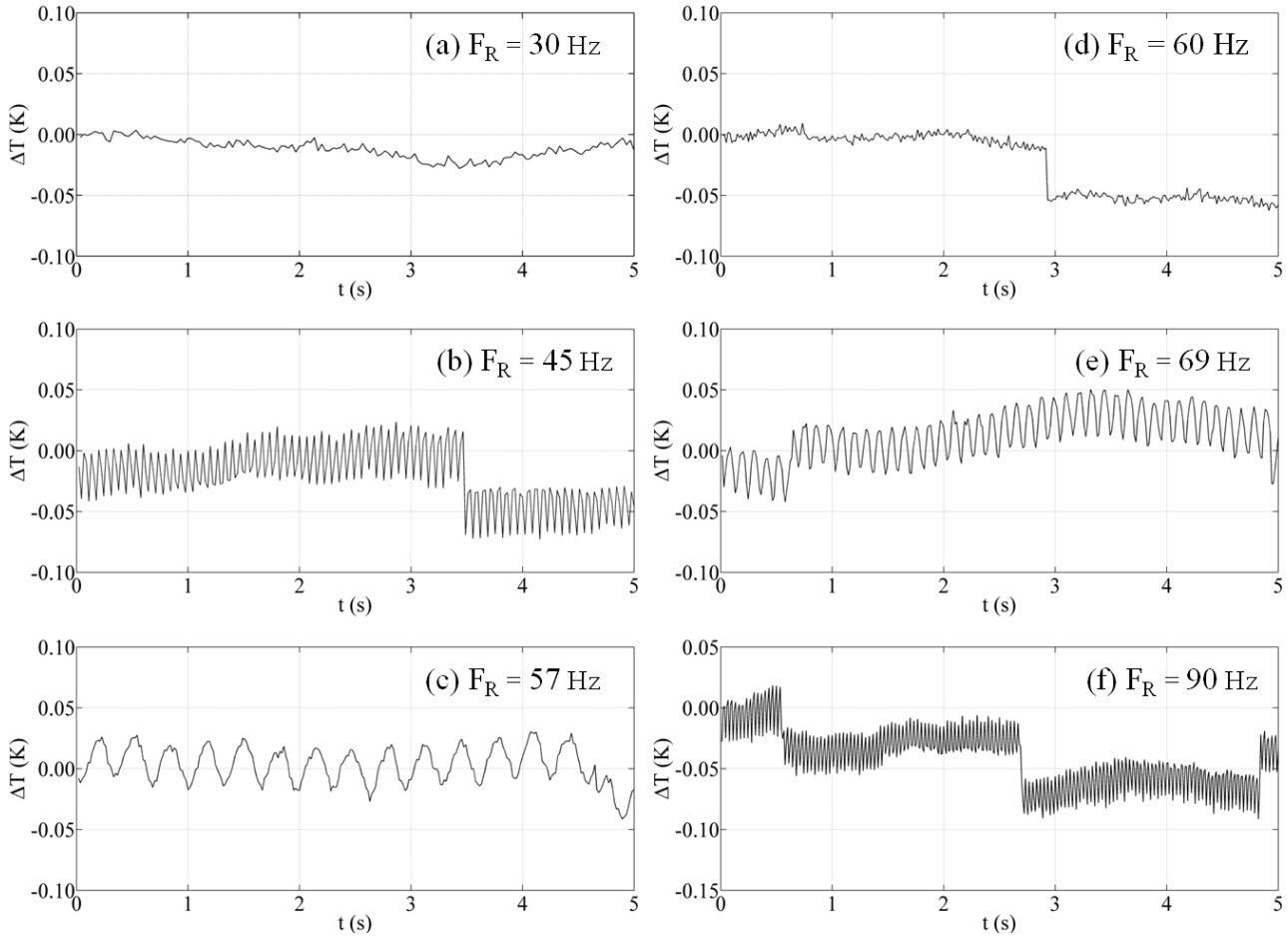

Fig. 3.2. ΔT over time taken with the FlirSC6000 camera from a black body at ambient temperature for varying the frame rate.

Moreover, it can be noticed that the ΔT irregularities depend on the chosen frame rate.
To allow for a direct comparison, all plots are represented with the same scale for both x (5 s) and y (0.2 K, total amplitude) axes. In general, by considering also ΔT plots not shown herein, an almost spiky sinusoidal pattern is often observed with random abrupt jumps which resembles the RTS signal illustrated by Pavelka et al. [3] (see Fig. 14 of ref [3]).for UG = 0.66 V. This would mean that the observed ΔT variations are mainly linked to the burst noise of the detector. On the other hand, the QWIP detector suffers from dark current effects; of course, these manifest mostly as burst noise.
For some frame rate values, like 60 Hz (Fig. 3.2d) and all submultiples of 60, the ΔT plot losses the sinusoidal distribution, while it retains the jumping fashion. To characterize the sinusoidal patter, each ΔT sequence is subjected also to frequency analysis; some results are shown in Fig. 3.3. As can be seen, a frequency-variable peak is observed to appear at certain frame rate values. More specifically, such a peak shows dependence, in terms of frequency and amplitude, on the frame rate, within the acquisition time interval; it is not present for F_R = 30 Hz, 60 Hz and for other frame rate values submultiples of 60.

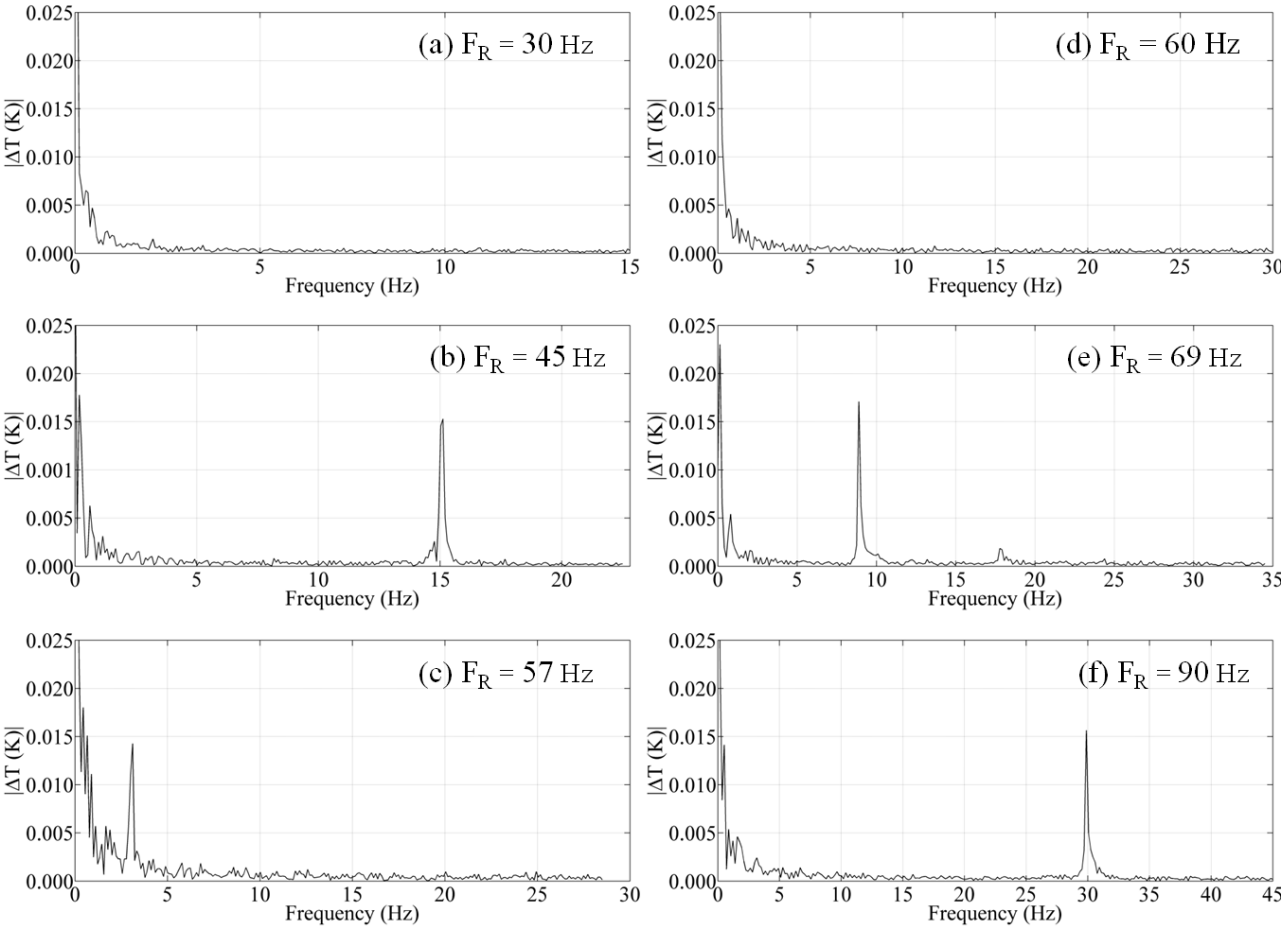

Fig. 3.3. Frequency spectrum for some frame rate values of thermal image sequences taken with SC6000.

One may notice that this peak (about 15 mK) occurs at a frequency which either summed, or subtracted, to the considered F_R value leads to 60. The sinusoidal trend may be eliminated by performing frequency correction. In particular starting from the raw signal spectrum it is possible to identify and delete the peak relative to the sinusoidal pattern and then use the Fourier inverse transform in order to reconstruct the signal over time without sinusoidal pattern (Fig. 3.4).

However, the frequency correction does not eliminate the alternate jump effect which, as already discussed, is due to the random detector noise and some random environmental disturbance. This effect can be eliminated only through correction by the use of an unloaded reference area.
It is very difficult to reduce the other sources of temporal noise from the signal spectrum without compromising the physical information because they are not characterized by a specific value or interval of frequencies.
The signal irregularities were also suspected to be introduced by the used camera data acquisition software ThermaCAM(R) ResearcherTM 2.10. Then, to get accomplished with the signal behaviour it is necessary to have a look at the camera electronic architecture and image construction [2].

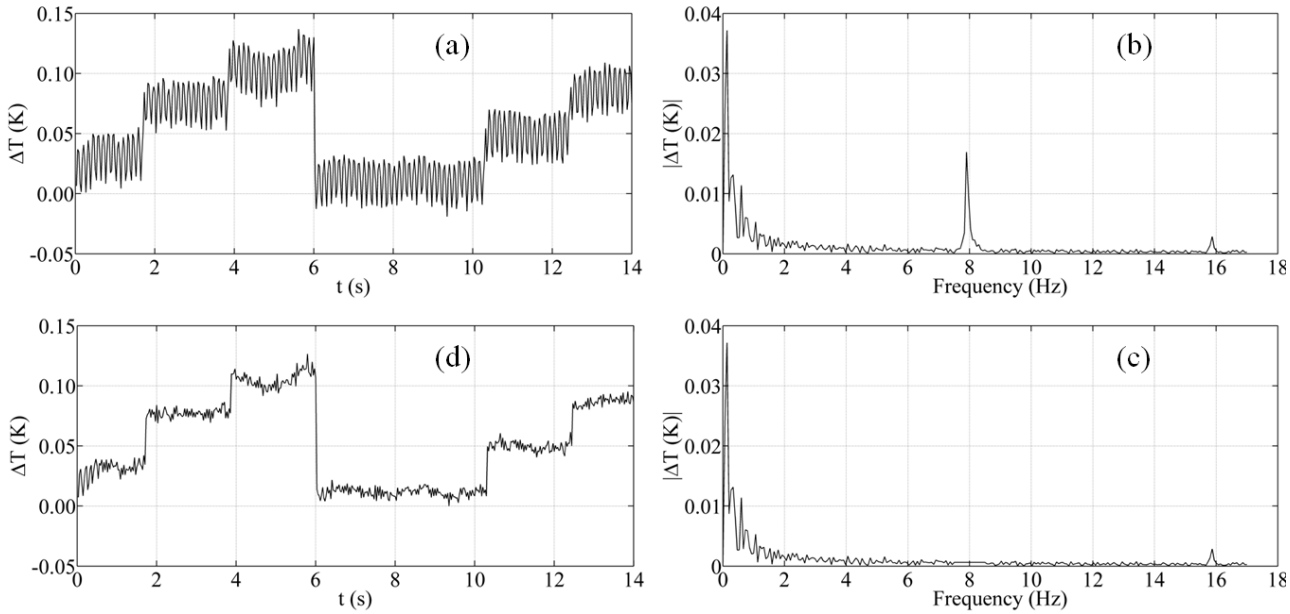

Fig. 3.4. Example of sinusoidal pattern elimination for a frame rate of 34 Hz: (a) Original Signal, (b) Original signal spectrum and identification of sinusoidal pattern frequency, (c) Signal spectrum without sinusoidal pattern frequency, (d) Reconstructed temporal signal.

3.2 SC6000 camera: electronic architecture and image construction.

The main components of an infrared imaging system are the detector and the readout circuit. The detector focal plane assembly, in the cooled camera, is tightly attached to the cold side of the Stirling cooler to allow conductive heat exchange. The QWIP SC6000 camera is equipped with a Stirling-cycle linear cryogenic cooler that is thermally coupled to the FPA via a cold finger. The Stirling process removes heat from the cold finger and dissipates it at the warm side; it has relatively low efficiency, but is adequate for cooling the IR camera detector. The cooler uses helium as the working gas which is compressed by axial movement of a piston; the latter generates an axial thrust, due to its inherent inertia, which in turn generates high vibrations and electromagnetic noise in the cold region. The vibration export may cause line-of sight-jitter, low frequency noise, high frequency microphones, etc. [4]. In addition, there are thermal losses in the regenerator, which assume great importance in small capacity coolers [5].
As already described in Chapter 2, a typical FPA can be described as a two-dimensional matrix of *n* columns by *m* rows of individual cells, or pixels, with each pixel (detector) having micrometer size

dimensions. The interface circuit (or driving circuit) of each cell, which converts the current from each photodiode to a voltage, is referred to as ROIC (readout integrated circuit) Unit Cell. A control circuit is also needed to synchronize the operation of the unit cell which converts the output of the IR pixels to a stream of bits [5]. The main function of a ROIC is transforming the small diode incremental current, generated by infrared radiation, into a relatively large measurable output voltage, which is commonly done by integrating the photocurrent in a capacitor during a fixed period of time. In particular, the standard integrated circuit ISC9803 of the LWIR QWIP SC6000 is a 640 x 512 large format array with 25 μm pixel pitch and direct injection with up to 11 million electron well capacity. The detector signal is integrated onto a capacitive trans-impedance amplifier that includes two selectable capacitors and an anti-blooming transistor. In details, the detector current flows through the input gate transistor and charges up the integration capacitor. The voltage of the integration capacitor is sampled and multiplexed to the column amplifier (the column amplifier is multiplexed to two output channels).

The anti-bloom gate keeps the input circuit from saturating, acting as global offset for the output signal on top of a fixed background, or leakage current [6].

The standard mode of camera operation is the Asynchronous Integrate While Read (AIWR) mode, meaning the camera is able to integrate scene signal while simultaneously reading out the previous frame. This mode allows for semi-independent control of the camera's frame rate and integration time. The frame rate is the number of snapshots taken per second and the integration time is the length of time that each snapshot actually views the scene. However, the ThermaCAM(R) ResearcherTM software (herein used) does not allow the user to change integration time as this would affect the factory calibration. In addition, the integration mode used by Researcher is the Asynchronous Integrate Then Read (AITR) [6,7]. In any case, the time required to readout all of the pixels limits the maximum frame rate; the selection of a smaller window size allows the maximum frame rate to increase. There are several fixed window sizes to be used with the ThermaCAM®Researcher^{TM}.

The integration process is controlled by the Frame Synchronization (FSYNC) clock pulse. The rising edge of the FSYNC clock pulse marks the beginning of the frame time; this is followed immediately by a sequence of line synchronization (LSYNC) clock pulses that produce a readout sequence. Each time the switch is closed, the capacitor discharges and when the switch is open the integration starts again. The rate at which this switch is operated is called the sampling rate; such sample & hold circuit acts in a sinusoidal fashion. The FSYNC clock remains high until the readout sequence has been completed. The integration time occurs after the readout time, resulting in a frame time that is approximately equal to the readout time plus the integration time. This results in a lower maximum frame rate and integration time duty cycle for a given window size [7]. Since clock timing and output modes determine the current required to slew and settle internal nodes, power adjustment control is required to allow optimization of operation for the specific application. An adjustment of the on chip master current is also provided to compensate for the temperature of operation.

The detector bias voltage may be either controlled by a control register Digital to Analog Converter in Command Mode or by applying a bias on the Vdet_adj pad when in Default Mode [7].

Then, it can be inferred that the observed ΔT variations may be ascribed to different causes. The dominant one is the RTS noise which has its main source in the presence of defects in the semiconductor material, but it is also driven by temperature related effects (thermionic emission) depending on the Stirling cycle. Other causes have to be ascribed to the readout circuit and the

detector bias control which is a function of the chosen window size and frame rate, as well on the camera ADC which in turn depends on any parasitic radiation due to either internal warming up, or to ambient induced temperature variations. Of course, effects from different sources may sum up, or cancel each other. From a practical point of view, a good practice may be to avoid the frame rate values with presence of frequency peaks (Fig. 3.3) within the recording time, or the number of frames, of interest. However, it has to be noted that for all the observed peaks the amplitude is lower than 0.025 K which practically has no effects on the measurement of enough large temperature variations. On the other hand, they may be easily eliminated through frequency analysis and correction.
In addition, owing to the abrupt jumps (Fig. 3.2), it can be observed that the ΔT amplitude is quite small reaching in the worst cases 0.1 K, which does not affect the measurement of enough large temperature variations. Indeed, in most of the infrared thermography applications this condition is satisfied. Instead, problems may arise when attempting to use the infrared camera in extreme conditions such as in the measurement of very low temperature variations induced by thermo-elastics effects or thermoplastic effects, which is the topic of the next chapters 4 and 5.

3.3 Black body monitoring with other detector types

The behaviour of tree other cameras, the MWIR X6540sc, the MWIR SC6800 and the un-cooled T440, is analyzed by considering the same experimental setup and data analysis procedure already described in section 3.1 for the SC6000 camera.

- The MWIR X6540sc is equipped with InSb detector working in the 1.5–5.1 μm infrared band, cooled by a rotary Stirling cycle engine, with NEDT < 25 mK, spatial resolution 640 x 512 pixels full frame and detector pitch 15 μm; the FlirResearchIR 3.4 MAX is used for camera and image handling and the frame rate is 125 Hz full frame with integration time of 500 ns.
- The MWIR SC6800 is equipped with InSb detector working in the 3–5 μm infrared band, cooled by a rotary Stirling cycle engine, with NEDT < 20 mK, spatial resolution 640 x 512 pixels full frame and detector pitch 25 μm; the FlirResearchIR is used for camera and image handling and the maximum frame rate at full frame is 565 Hz with integration time of 480 ns.
- The hand-held T440 camera is equipped with a bolometer thermal detector, working in the LWIR 8–12μm infrared band, NEDT 45 mK, 320 x 240 pixels, 30 Hz frame rate.

Sequences of thermal images are again acquired by looking at the blackbody by each of the tree infrared cameras and by changing the frame rate from 20 up to 800 Hz for the MWIR X6540sc, from 7.5 up to 970.75 Hz for the SC6800 and from 7.5 up to 30 Hz for the T440. Some of the data obtained with the X6540sc are reported in Fig. 3.5 as plots of ΔT values against time. The first thing that catches eyes is a low-amplitude ΔT randomly distributed without any well recognizable sinusoidal trend and without jumps. Again, frequency analysis of the image sequences is performed with results shown in Fig. 3.6. It is possible to note the appearance of small peaks, randomly distributed at every frame rate, their amplitude being generally lower than 0.005 K.

Some data obtained with the infrared camera SC6800 are shown in Fig. 3.7. Also is this case, the ΔT appears as randomly distributed without any well recognizable sinusoidal trend but differently from the X6540sc it is possible to underline some abrupt jumps having an amplitude of about 0.02 K that occur at the frequencies of 30 and 69 Hz. No jumps are observed at 60 and 656.66 Hz. Again, frequency analysis of the image sequences is performed with results shown in Fig. 3.8. It is possible to note that no significative peaks appear.

As expected, the two infrared cameras equipped with InSb detector show very similar raw signals even if small differences are present. As main differences, some jumps can be distinguished at some frame rate values only for the SC6800, while no jumps are observed for the x6540 camera.

Conversely, unlike the SC6800 camera a small sinusoidal trend is displayed by data recorded with the X6540sc.

Fig. 3.9. shows a plot of ΔT values against time for F_R = 30 Hz taken with the un-cooled T440 camera. It is possible to see random ΔT variations due to the detector noise, which may be ascribed to different sources either internal to the camera, or external. As expected, no frequency peaks are found since the latter are mainly to be ascribed to the noise caused by the dark current which in turn is linked to the Stirling cooler (not present in the T440 camera).

For all the infrared cameras, some temporal noise affects the acquired data which could influence the measurements especially when the ΔT values to be measured are low and at the edge of the instrument resolution. Of course the characteristics of temporal noise and its amplitude depend on the whole infrared camera architecture. It is very simple to notice that the two cooled MW infrared cameras exhibit a reduced temporal noise with respect to both the SC6000 and T440 ones. In particular, no random jumps are recognized in the signals acquired with the two MW infrared cameras equipped with InSb detector.

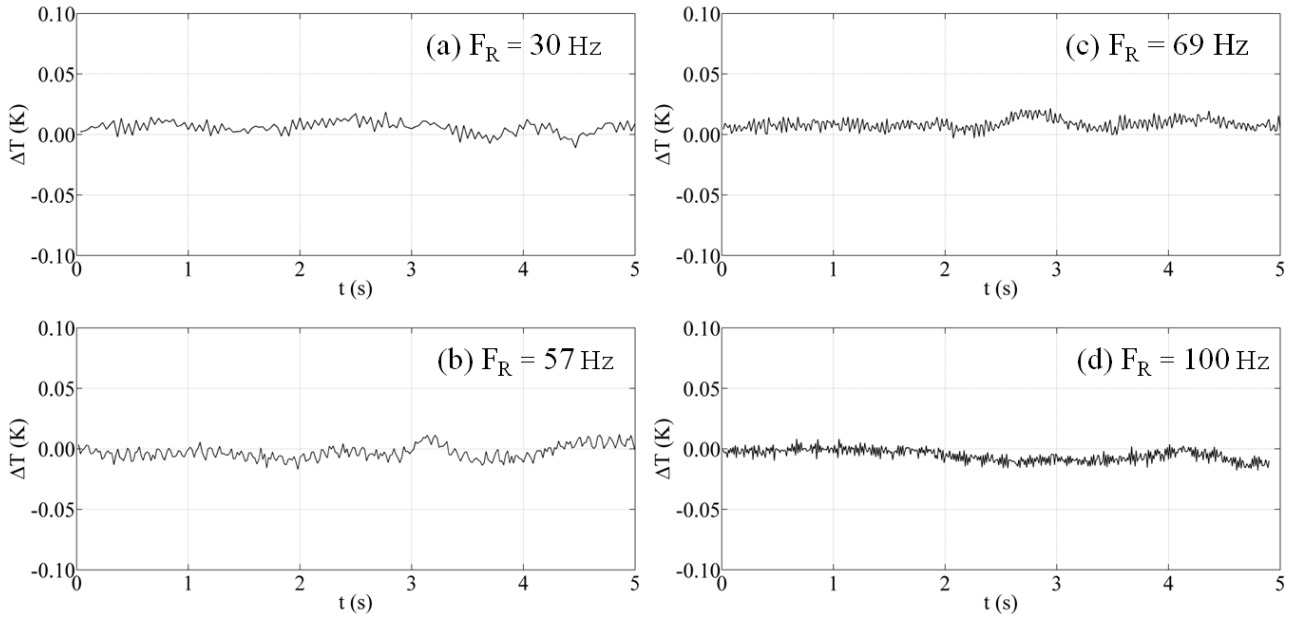

Fig. 3.5. ΔT distribution with time for different frame rate values
for the MWIR X6540sc camera.

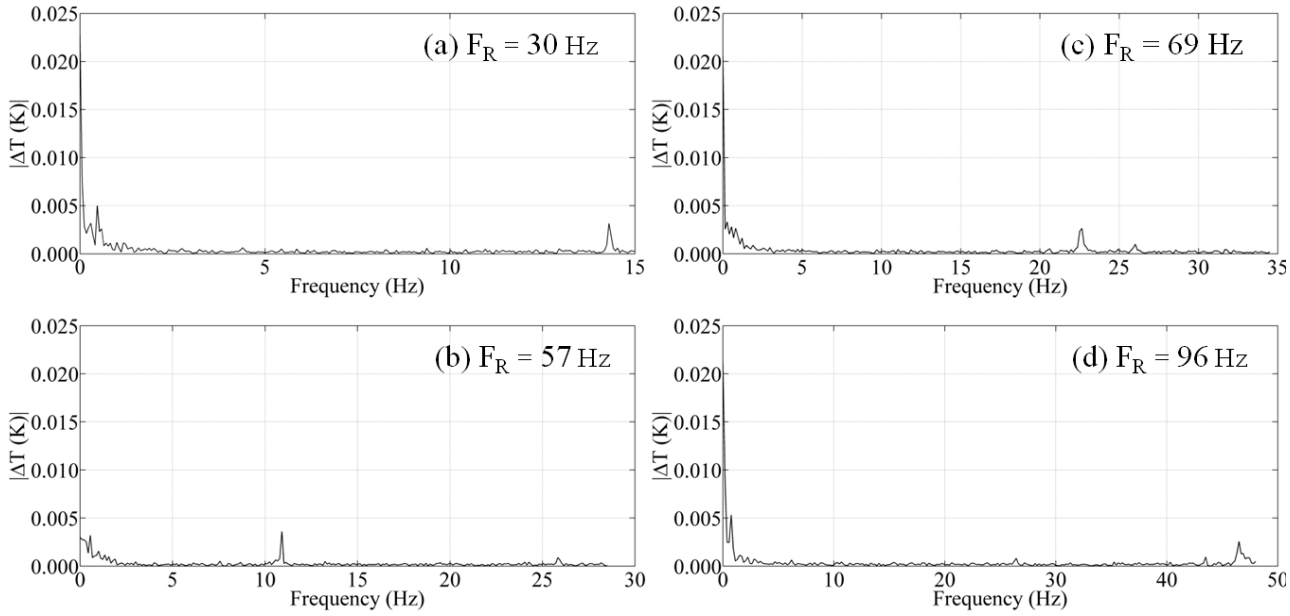

Fig. 3.6. Frequency spectrum of thermal image sequences taken with the MWIR X6540sc camera by varying the frame rate.

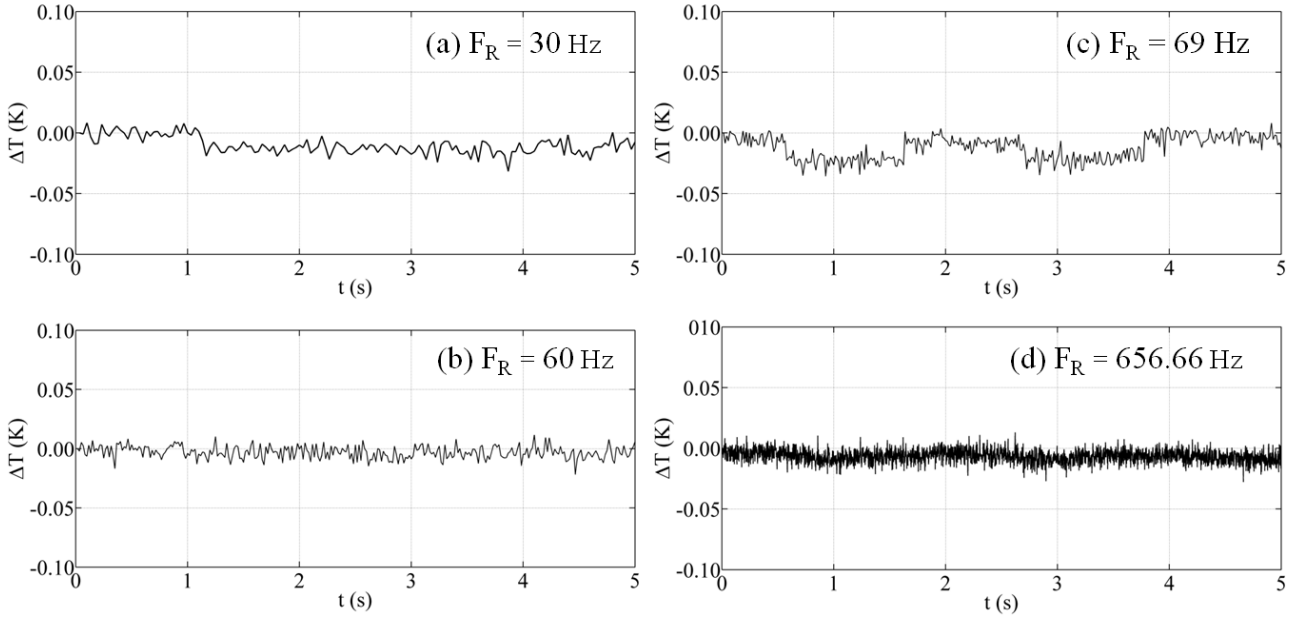

Fig. 3.7. Δ*T* distribution with time for different frame rate values for the MWIR SC6800 camera.

It is worth noting that many factors must be considered when choosing an infrared camera, amongst them, the thermal resolution plays a key role when discrimination of very small temperature variations is required. In this context, it has been found that the InSb detector does not suffer from the dark current noise as does the QWIP one, but it is not able to chase feeble temperature variations [2,8]. Since the temporal noise can be significantly reduced in a simple manner by the Reference Area Method (RAM), a noisy detector can be fruitfully used [1,9].

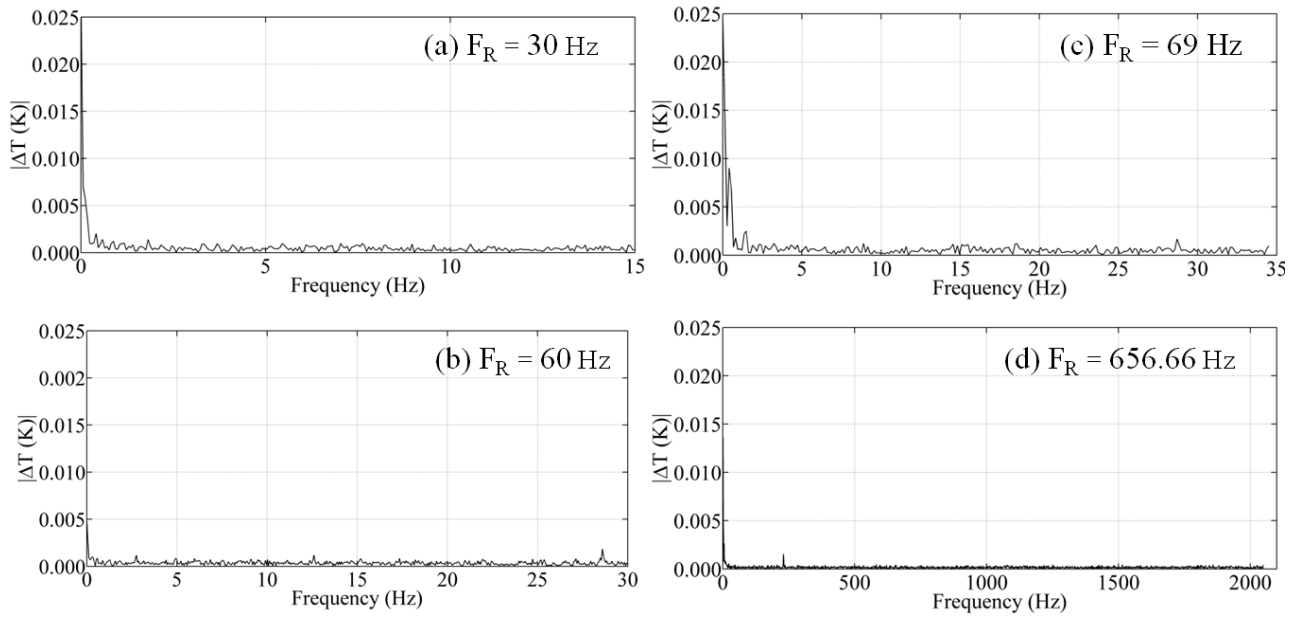

Fig. 3.8. Frequency spectrum of thermal image sequences taken with the MWIR SC6800 camera by varying the frame rate.

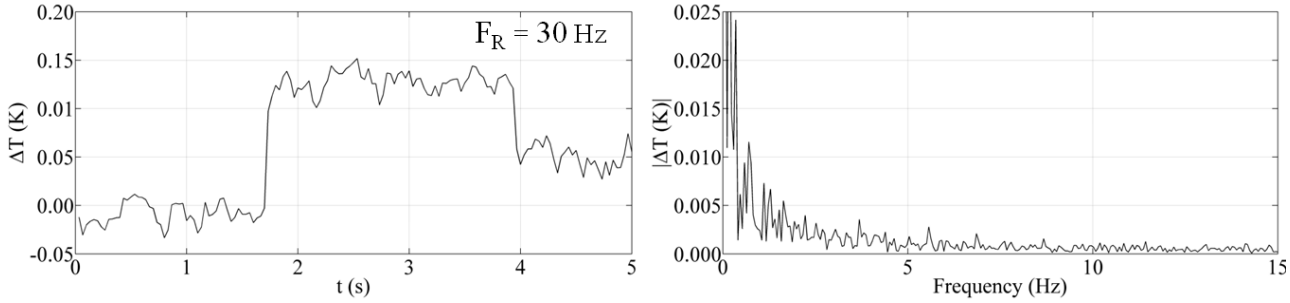

Fig. 3.9. Δ*T* distribution and frequency spectrum for the T440 camera at frame rate of 30 Hz.

3.4 The Reference Area Method

The Reference Area Method basically consists of the detraction from the acquired raw signal ΔT_R of the temporal noise ΔT_N properly measured in a reference area. The reference area is a small portion of space contained in the field of view which is not influenced or affected by the physical phenomenon under investigation during tests. The corrected signal ΔT_C is obtained by subtracting the noise ΔT_N from the raw signal according to:.

$$\Delta T_C(i,j,t) = \Delta T_R(i,j,t) - \Delta T_N(t) \tag{3.2}$$

where *i* and *j* indicate row and column numbers in the image while *t* is the frame number in the sequence. The quantity ΔT_N is the mean value of ΔT evaluated in the reference area of *m* x *n* pixels for each frame in the sequence.

The correction consists in the subtraction, for each value of time *t*, of the noise ΔT_N from all pixels in the image.

The Reference Area Method has been validated trough several experimental tests. As first step, it has been applied to a blackbody with the used test setup sketched in Fig. 3.10.

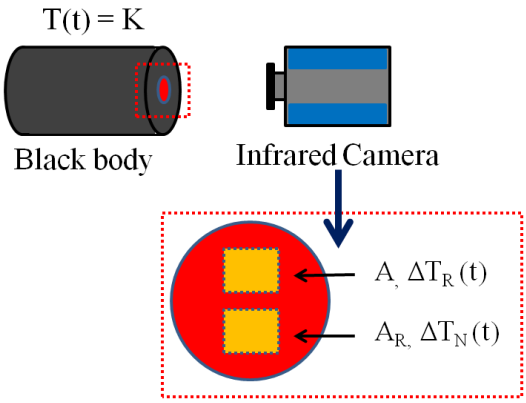

Fig. 3.10. Setup for tests on a blackbody.

In Fig 3.10, A represents the measurements position (an area of m x n pixels) while A_R is the reference Area (an area of m_1 x n_1 pixels). The aim of the test is to measure the mean value of ΔT over time inside the area A for a blackbody, which is kept at constant temperature; this means that the measured ΔT should be zero over time.

The acquired sequences are post-processed following the already described procedure by applying first Eq.(3.1) to create raw sequences of $\Delta T_R\,(i,j,t)$ images. Then, the mean raw value of $\Delta T_R\,(t)$ is evaluated for each frame inside the Area A according to:

$$\Delta T_R(t) = \frac{1}{mxn}\sum_{i,j}\Delta T_R(i,j,t) \tag{3.3}$$

and the mean noise value of $\Delta T_N\,(t)$ is evaluated for each frame inside the Area A_R according to:

$$\Delta T_N(t) = \frac{1}{mxn}\sum_{i,j}\Delta T_N(i,j,t) \tag{3.4}$$

As next step, the Reference Area Method is applied. and the corrected signal is obtained:

$$\Delta T_C(t) = \Delta T_R(t) - \Delta T_N(t) \tag{3.5}$$

Same examples of $\Delta T_R\,(t)$, $\Delta T_N\,(t)$ and $\Delta T_C\,(t)$ signals acquired with the infrared cameras Flir SC6000, x6540sc, Sc6800 and T400 are reported in the following figures 3.11-3.14. Since the maximum frame rate allowable for the T440 is 30Hz, for the sake of a comparison, sequences of images are recorded at 30 Hz also for the cooled infrared cameras.

For each detector, ΔT_R is similar to ΔT_N even if they are evaluated in two different regions of space including different pixels. For a direct comparison ΔT_C plots of the four detectors are shown superimposed in Fig. 3.15; in particular a magnification within the 6-8 s range is also supplied (left side of Fig. 3.15).

To underline the effectiveness of the Reference Area Method, the signal mean value μ and its standard deviation σ before (μ_R, σ_R) and after correction (μ_C, σ_C) are evaluated and reported in Table 3.1.

In relation to the raw signals, the lowest noise level is achieved by the InSb detectors, while the highest one by the microbolometer. As can be seen, for all data reported in Table 3.1, the correction

with the Reference Area Method is effective to reduce the distance form $\Delta T = 0$ and the standard deviation [8].

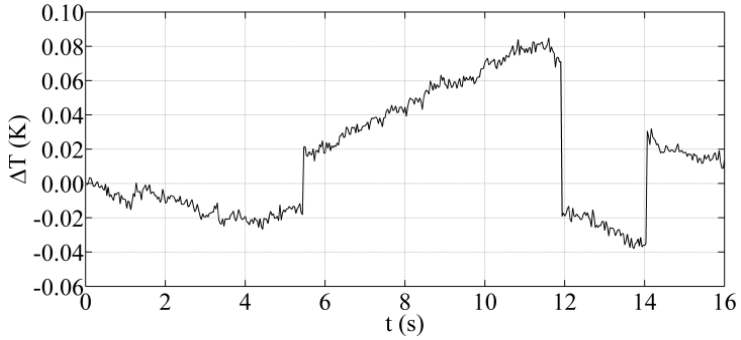

(a) ΔT_R.

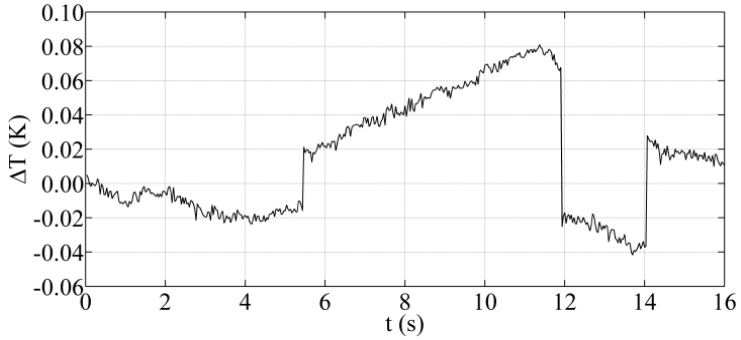

(b) ΔT_N.

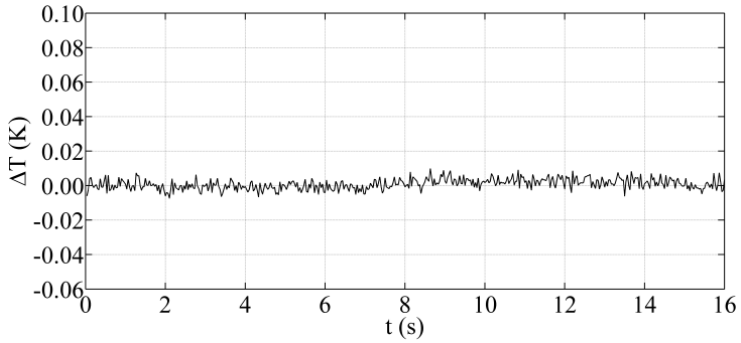

(c) ΔT_C.

Fig. 3.11. ΔT_R (a), ΔT_N (b) and ΔT_C (c) signals taken with SC6000 camera.

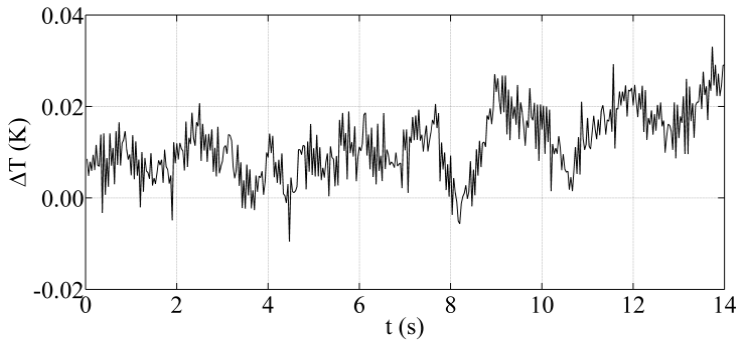

(a) ΔT_R.

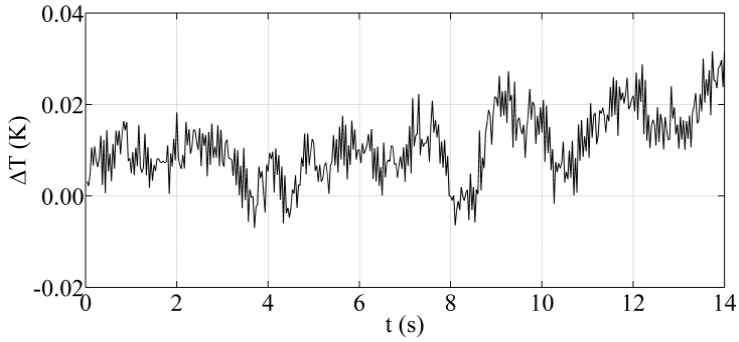

(b) ΔT_N.

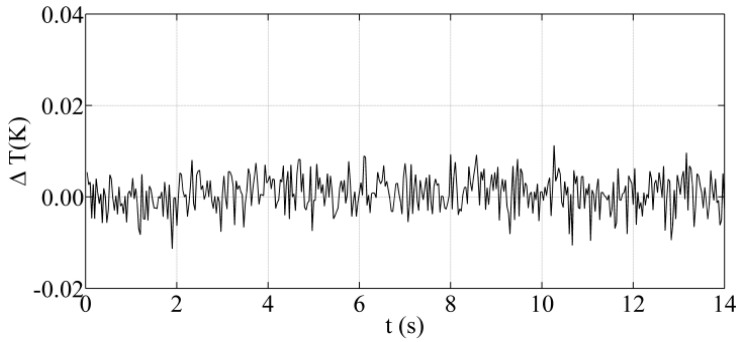

(c) ΔT_C.

Fig. 3.12. ΔT_R (a), ΔT_N (b) and ΔT_C (c) signals taken with x6540sc camera.

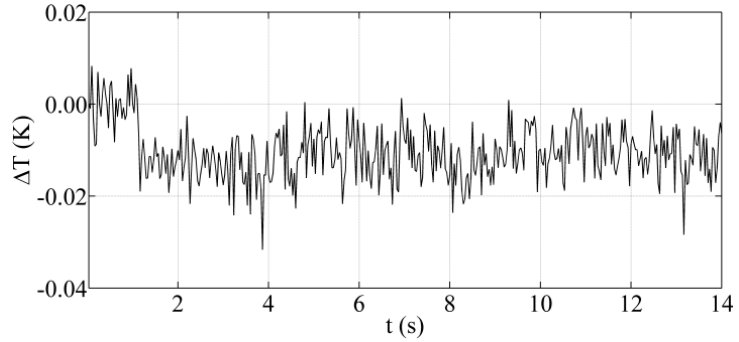

(a) ΔT_R.

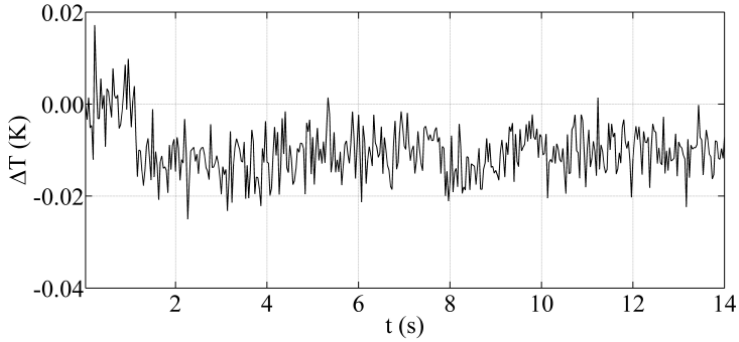

(b) ΔT_N.

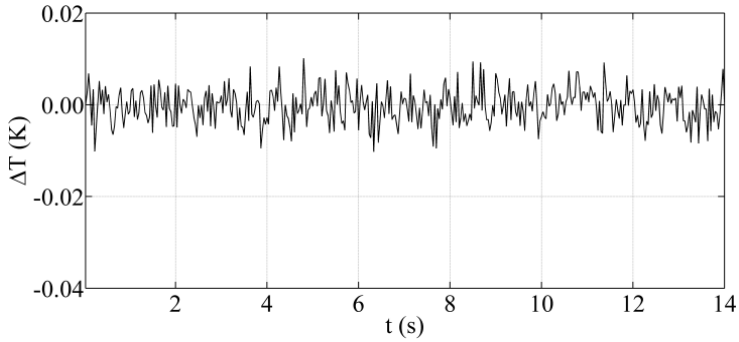

(c) ΔT_C.

Fig. 3.13. ΔT_R (a), ΔT_N (b) and ΔT_C (c) signals taken with SC6800 camera.

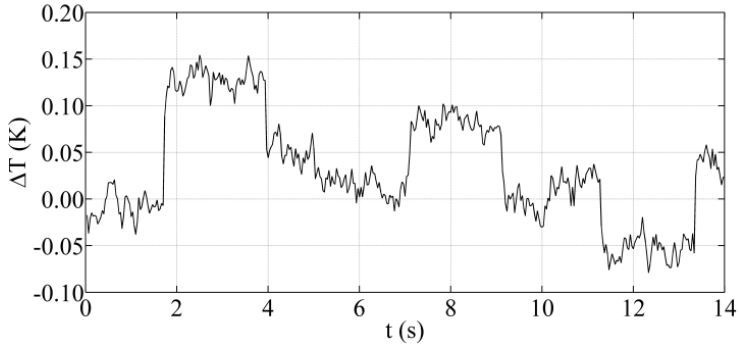

(a) ΔT_R.

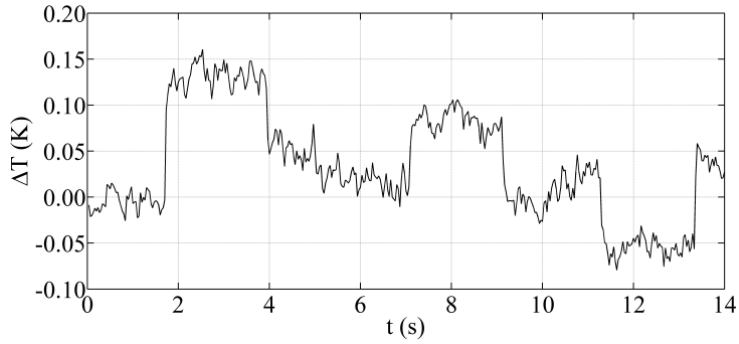

(b) ΔT_N.

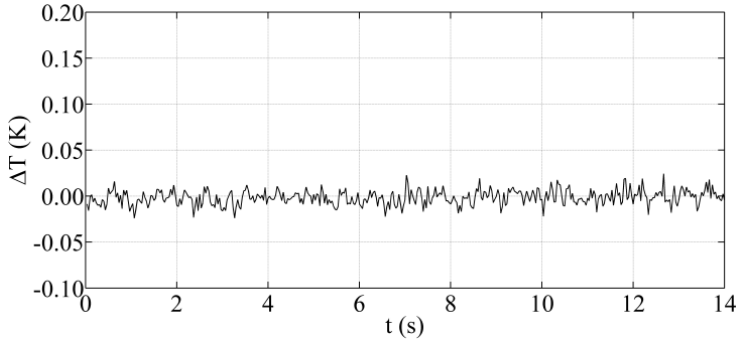

(c) ΔT_C.

Fig. 3.14. ΔT_R (a), ΔT_N(b) and ΔT_C (c) signals taken with T440 camera.

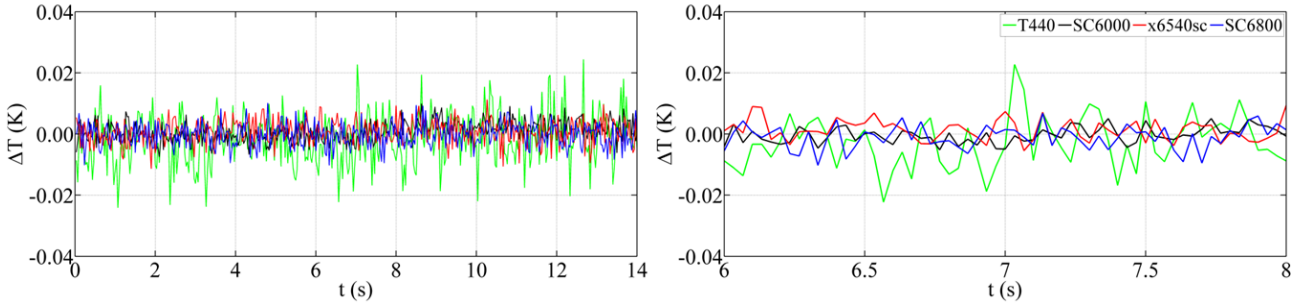

Fig. 3.15. A comparison of ΔT_C signals taken with the four cameras.

Camera	F_R(Hz)	$\mu_R\ \Delta T$(K)	$\sigma_R \Delta T$ (K)	$\mu_C\ \Delta T$(K)	$\sigma_C \Delta T$ (K)	σ_C/σ_R
T440	30	0.0282	0.0559	-0.0016	0.0083	0.1485
	15	0.0456	0.0519	0.0044	0.0097	0.1869
	7.5	0.0600	0.0408	0.0019	0.0098	0.2402
SC6000	30	0.0152	0.0347	0.0008	0.0032	0.0922
	45	-0.0161	0.0238	0.0011	0.0059	0.2479
	60	-0.0223	0.0184	0.0023	0.0022	0.1196
x6540sc	30	0.0135	0.0086	0.0008	0.0039	0.4535
	57	-0.0086	0.0064	-0.0060	0.0034	0.5313
	100	-0.0041	0.0056	0.0036	0.0031	0.5536
SC6800	30	-0.0105	0.0060	-0.0003	0.0037	0.6167
	69	-0.0124	0.0098	0.0026	0.0035	0.3571
	565.66	-0.0068	0.0053	-0.0006	0.0034	0.6415

Table 3.1. ΔT mean values and standard deviation for some raw and corrected signals.

3.5 Application of the Reference Area Method to a real surface.

The Reference Area Method is then applied by framing a real surface of a GLARE specimen ($\varepsilon \cong 0.9$) at ambient temperature; thermal images are recorded with the infrared camera SC6000 at sampling rate of 60 Hz.

A main problem when dealing with a real larger surface is the choice of the position of the reference area as well the size of such an area (number of pixels inside the reference area). To investigate the effects of the reference area position, 5 areas having the same dimension of 40 x 20 pixels are considered along the specimen length (Fig. 3.16). An average ΔT over time ($\Delta T_i\,(t)$) is evaluated inside each area frame by frame, obtaining 5 $\Delta T_i\,(t)$ signals.

Then, the unbiased standard deviation over time $\sigma(t)$ of the 5 $\Delta T_i\,(t)$ signals is evaluated frame by frame for each signal according to:

$$\sigma(t) = \sqrt{\frac{1}{K-1}\sum_{i=1}^{k}\left(\Delta T_i(t) - \mu(t)\right)^2} \tag{3.6}$$

The subscript i is the area number, $\Delta T_i\,(t)$ is the mean value of ΔT evaluated in the i-th area at time t, k is the total number of areas (5 in the present case) and $\mu(t)$ is the ΔT mean value evaluated amongst the 5 areas at time t by means of the following relationship:

$$\mu(t) = \frac{1}{K}\sum_{i=1}^{k} \Delta T_i\,(t) \tag{3.7}$$

The 5 $\Delta T_i\,(t)$ signals over time evaluated inside each area and the standard deviation are shown in Fig. 3.17.

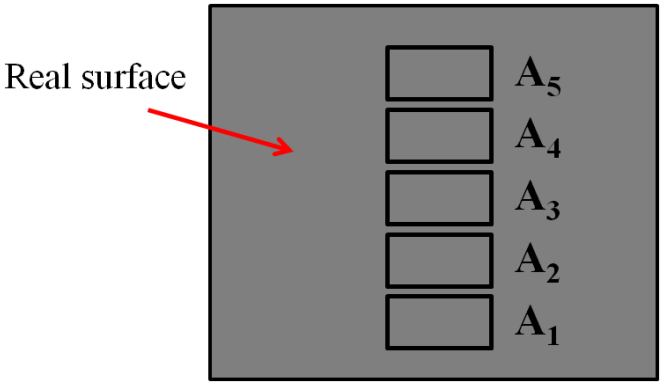

Fig. 3.16. Distribution of 5 reference areas over the real surface.

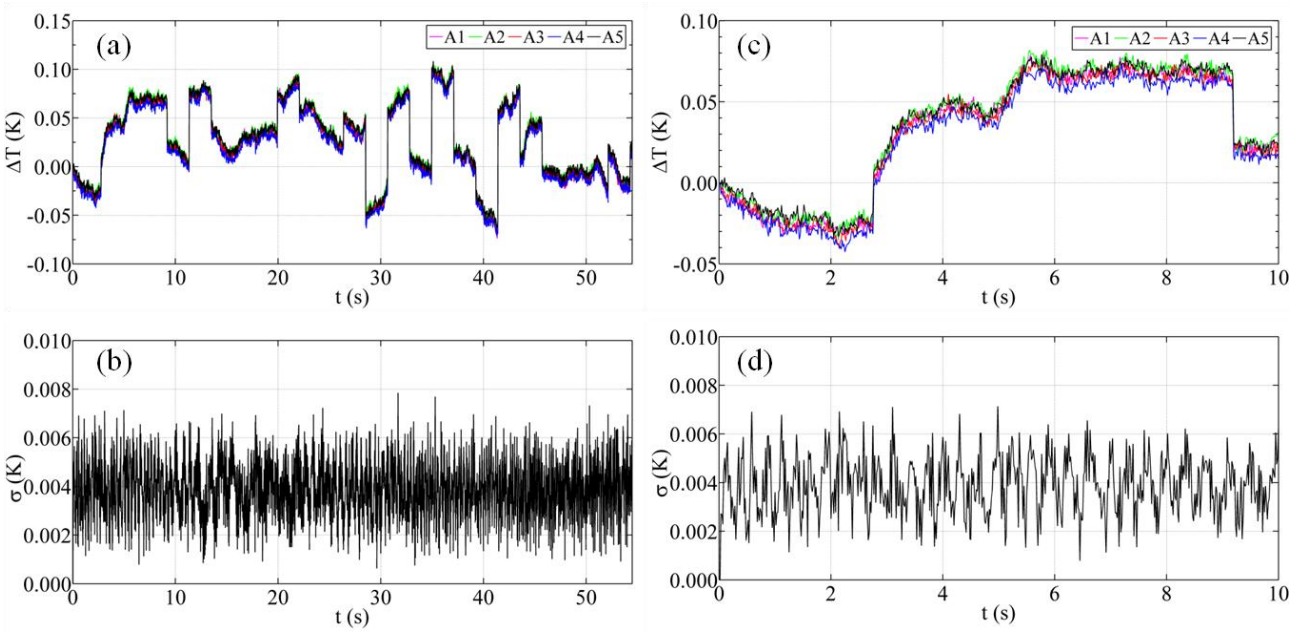

Fig. 3.17. Data acquired in the five areas and the standard deviation over time. Figures (a) and (b) are relative to a longer interval of time while in c and d only the first 10 seconds are considered.

As can be seen, the standard deviation value is low enough varying in the range from about 0.002 to 0.006K. Moreover, the mean value of the standard deviation (about 0.004 K) seems to be independent of time. The smallness of σ bears witness for absence of significant spatial noise. This reflexion allows to consider a generic $\Delta T(t)$ signal, measured in a generic area, as reference signal to be used to correct all the other signals. An example of correction is shown in Fig. 3.18 in which the area A1 is considered as reference area while the other four $\Delta T_i\,(t)$ in A2, A3, A4 and A5 are the

signals to be measured. More specifically, the signal A1 is subtracted from each the other signals according with Eq.(3.5).

As a result of good correction, all the corrected signals appear well overlapped; indeed, they differ only by the third decimal digit.

As a next step, the effects of the size of reference and measuring areas are investigated. To this end, 10 reference areas A_{Ri} and 8 measuring area A_i of increasing size are considered and schematically sketched in Fig. 3.19. Then, a mean $\Delta T(t)$ value is extracted inside each of them frame by frame. In particular, the side of the square reference area varies from 1 to 10 pixels so that the total number of pixels contained inside them varies from 1 up to 100. Also the measuring areas are concentric squares, but they are chosen far away enough to avoid any interference with the reference areas (no any pixel is shared between them). The side of the considered measuring areas includes the following number of pixels: 1, 2, 3, 5, 10, 20, 40 so that the number of pixels contained in it varies from 1 up to 1600. Besides, a rectangular measuring area of 20x40 pixels is considered too.

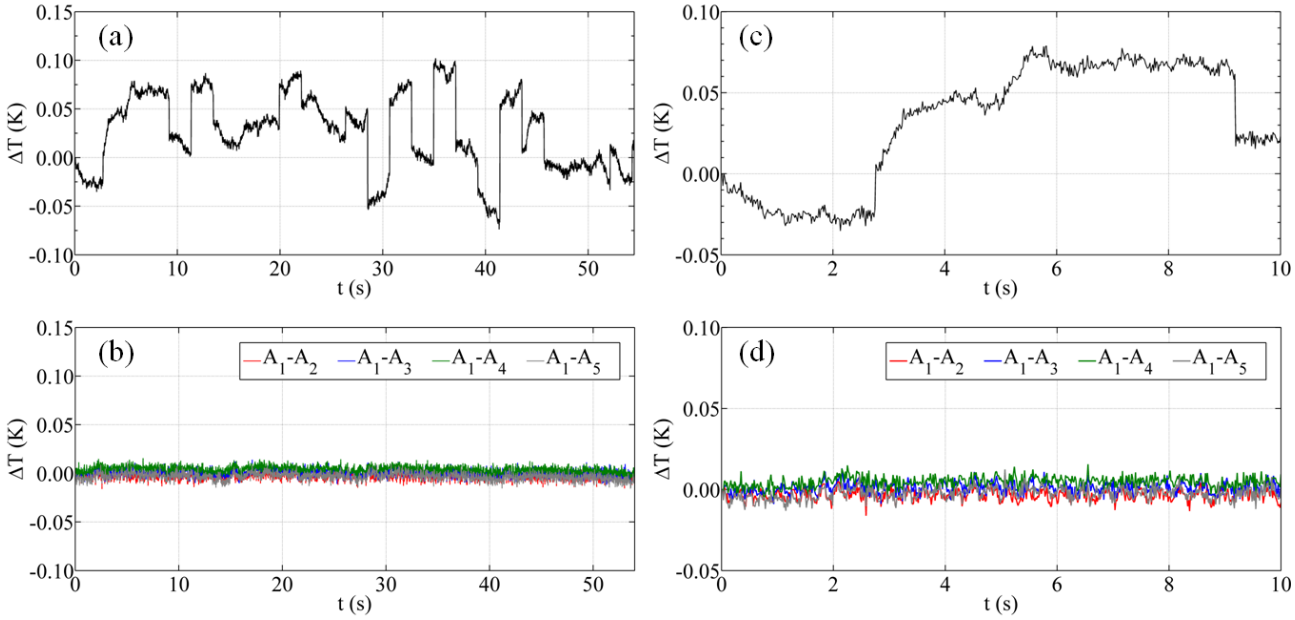

Fig.3.18. Example of correction; (a) and (c) show the original signal measured in A_1while (b) and (d) show the 5 corrected signals measured in A2, A3, A4, A5 (for all the mean values).

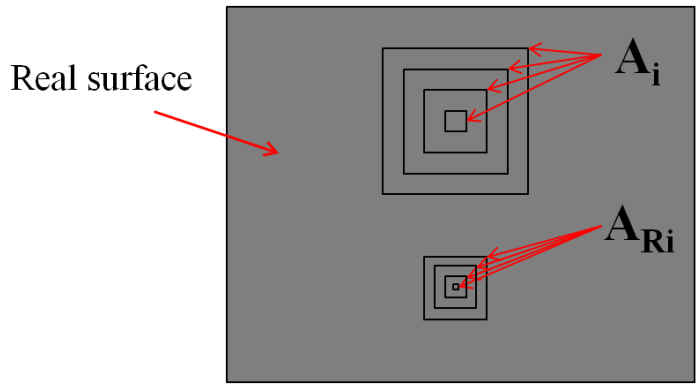

Fig. 3.19. Sketch of real surface with concentric A_i and A_{Ri} areas.

Some raw $\Delta T(t)$ signals evaluated inside the measuring areas are shown in Fig. 3.20 and 3.21, while the signals mean μ and standard deviation σ values are collected in Table 3.2. It can be observed that the abrupt jumps does not disappear with increasing the number of pixels inside the measuring area, but they remain in the same position and with the same amplitude. This, as shown in Table 3.2, does not allow for a significant decrease of the standard deviation with the increase of the number of pixels in the measuring area.

Some examples of corrected signals, which are obtained by using some measuring and reference areas containing an increasing number of pixels, are shown in Fig. 3.22. The ΔT mean values μ, standard deviation σ and the sum of mean value and standard deviation, in absolute value, for all the tested conditions are reported in the following Tables 3.3, 3.4 and 3.5; the first row for $A_R = 0$ indicates data relative to the uncorrected raw signal. The mean ΔT values μ evaluated inside the measuring area A and the standard deviations σ with respect to the number of pixels in the Reference Area A_R are plotted in the following Figs. 3.23 and 3.24.

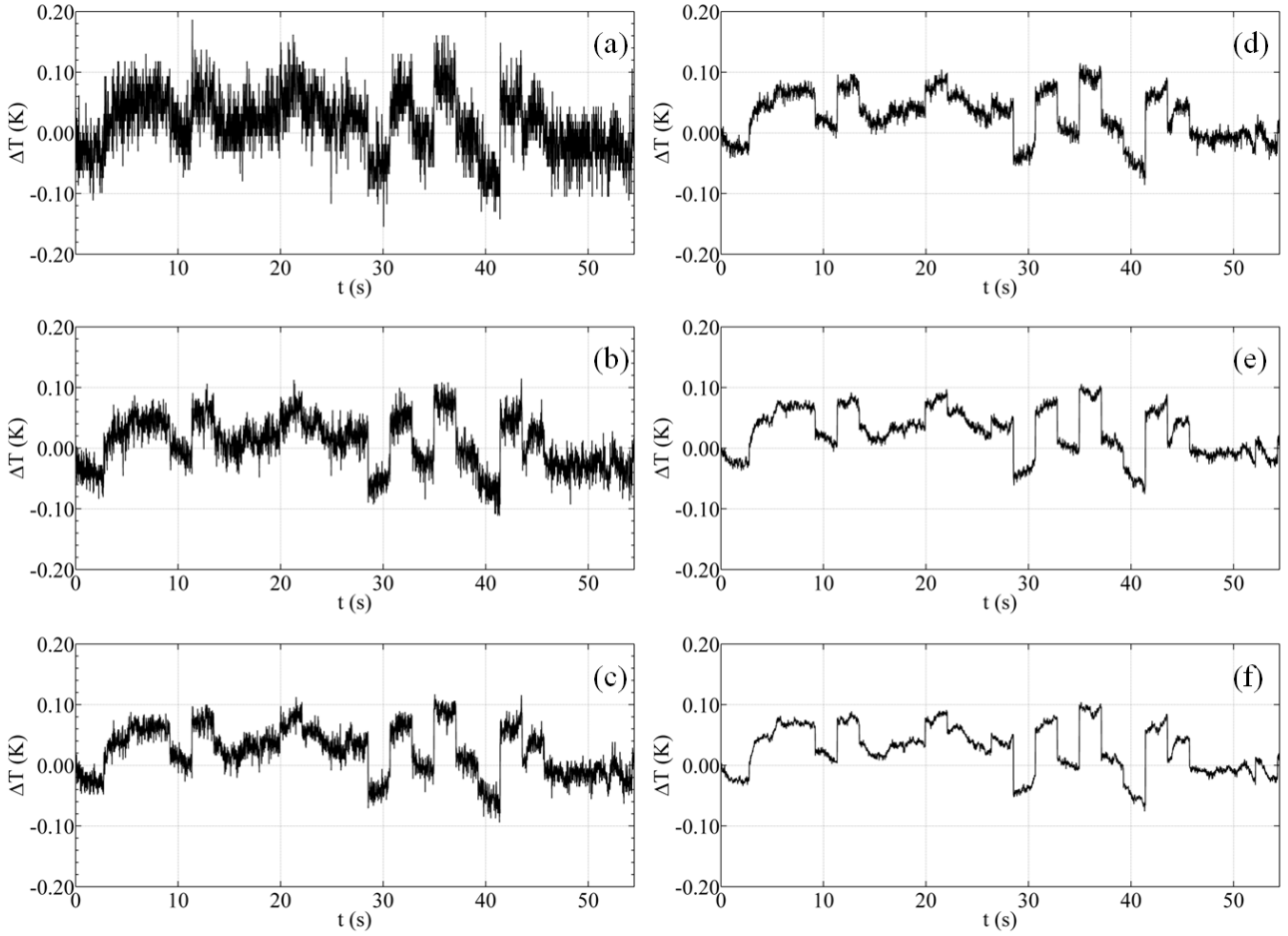

Fig. 3.20. Raw ΔT signals over time in measuring area *A* containing different pixels: (a)1 Pixel, (b) 4 Pixels (c) 9 pixels, (d) 25 Pixels, (e) 100 pixels; (f) 400 pixel.

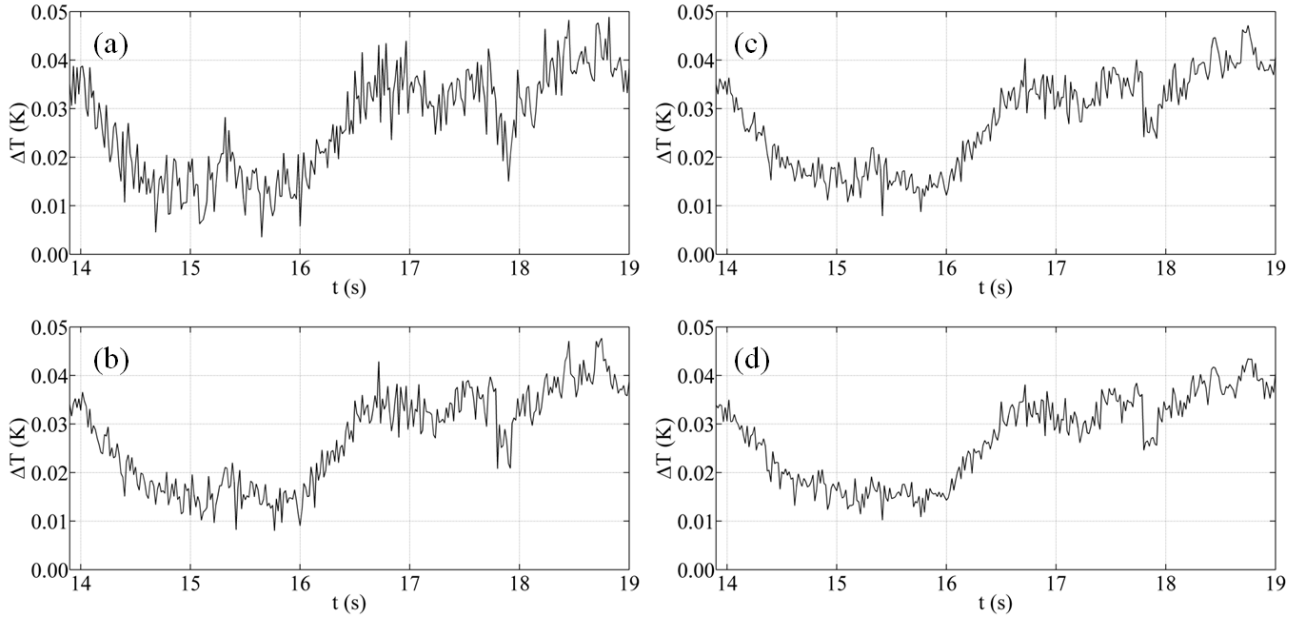

Fig. 3.21. Raw Δ*T* signals over time in measuring areas containing different pixels: (a)100 pixels, (b) 400 pixels, (c) 800 pixels, (d) 1600 pixels.

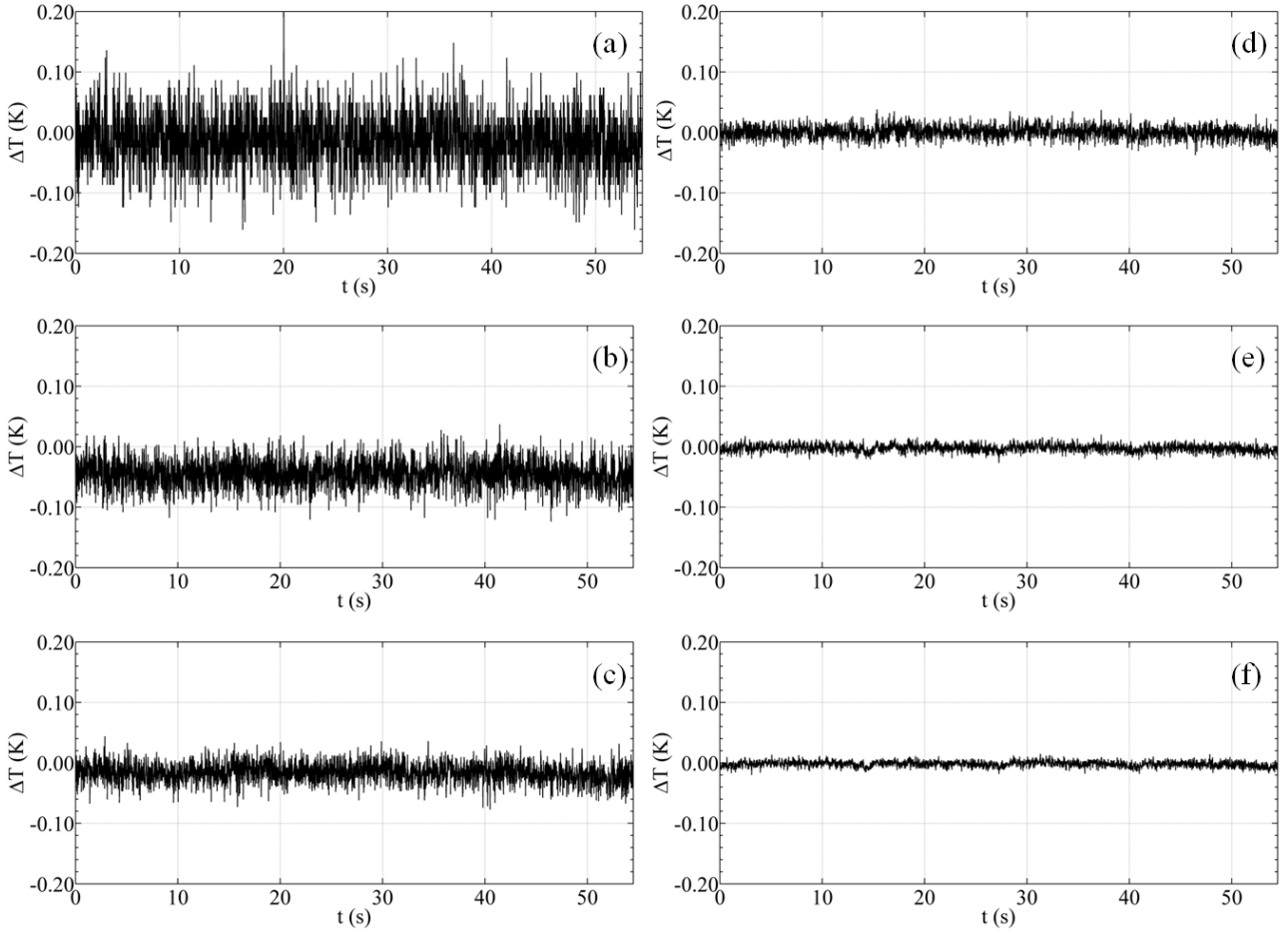

Fig. 3.22. Examples of corrected signals obtained by using measuring area and reference areas including a different number of pixels: (a) A=1, A_R=2, (b) A=4, A_R=4, (c) A=9, A_R=9, (d) A=25, A_R=25, (e) A=100, A_R=100, (f) A=1600, A_R=100.

Pixel	$\mu\Delta T$(K)	$\sigma\Delta T$(K)	dμ/Pixel	dσ/Pixel
1	0.0138	0.0512	-----	-----
4	0.0076	0.0417	0.002067	0.0031667
9	0.0228	0.0400	-0.003040	0.0003400
25	0.0276	0.0392	-0.000300	0.0000500
100	0.0265	0.0388	0.000015	0.0000053
400	0.0267	0.0387	-0.000001	0.0000003
800	0.0272	0.0385	-0.000001	0.0000005
1600	0.0270	0.0385	0.000000	0.0000000

Table 3.2. Mean value μ and standard deviation σ of raw signals in measuring areas containing a different number of pixels.

Looking at the corrected signals of figure 3.22, the following considerations can be done:

1. The abrupt jump disappears even if the Reference Area contains only one pixel.
2. The corrected signal mean value is about zero even when a small number of pixels is considered inside the measuring and reference areas
3. The data dispersion around the mean value of the corrected signal decreases as the number of pixels inside the reference and measuring areas increase.
4. The data dispersion around the mean decreases very quickly when only few pixels are considered inside the areas A and A_R and slows as the number of pixels increases.

A_R\A	1 Pixel	4	9	25	100	400	800	1600
0 Pixel	0.0138	0.0076	0.0228	0.0276	0.0265	0.0267	0.0272	0.0270
1	-0.0148	-0.0210	-0.0057	0.0010	-0.0020	-0.0018	-0.0013	-0.0016
4	-0.0388	-0.0450	-0.0298	-0.0250	-0.0260	-0.0259	-0.0254	-0.0256
9	-0.0256	-0.0318	-0.0165	-0.0118	-0.0128	-0.0126	-0.0122	-0.0124
16	-0.0135	-0.0197	-0.0044	0.0003	-0.0007	-0.0005	0.0001	-0.0003
25	-0.0137	-0.0199	-0.0046	0.0001	-0.0009	-0.0007	0.0003	-0.0005
36	-0.0153	-0.0216	-0.0063	-0.0015	-0.0026	-0.0024	-0.0019	-0.0022
49	-0.0186	-0.0248	-0.0095	-0.0048	-0.0058	-0.0056	-0.0052	-0.0054
64	-0.0180	-0.0242	-0.0089	-0.0042	-0.0052	-0.0050	-0.0046	-0.0048
81	-0.0150	-0.0212	-0.0060	-0.0012	-0.0022	-0.0021	-0.0016	-0.0018
100	-0.0153	-0.0215	-0.0062	-0.0015	-0.0025	-0.0023	-0.0018	-0.0021

Table 3.3. Average corrected signal evaluated in the measuring area A by using the reference signal measured in $A_{R.}$ The first raw shows original uncorrected values.

A_R\A	1 Pixel	4	9	25	100	400	800	1600
0 Pixel	0.0512	0.0417	0.0400	0.0392	0.0388	0.0387	0.0385	0.0385
1	0.0438	0.0336	0.0315	0.0301	0.0297	0.0294	0.0294	0.0293
4	0.0361	0.0232	0.0200	0.0174	0.0166	0.0162	0.0161	0.0160
9	0.0341	0.0203	0.0164	0.0136	0.0126	0.0120	0.0119	0.0118
16	0.0334	0.0190	0.0147	0.0116	0.0100	0.0093	0.0092	0.0091
25	0.0331	0.0184	0.0138	0.0105	0.0088	0.0079	0.0078	0.0076
36	0.0328	0.0180	0.0133	0.0100	0.0079	0.0071	0.0069	0.0068
49	0.0328	0.0179	0.0130	0.0095	0.0074	0.0065	0.0064	0.0061
64	0.0327	0.0177	0.0128	0.0092	0.0069	0.0061	0.0059	0.0057
81	0.0327	0.0177	0.0128	0.0091	0.0066	0.0058	0.0056	0.0053
100	0.0327	0.0177	0.0127	0.0088	0.0064	0.0055	0.0053	0.0050

Table 3.4. Signal Standard deviation evaluated in the measuring area A by using the reference signal measured in $A_{R..}$ The first raw shows original uncorrected values.

A_R\A	1 Pixel	4	9	25	100	400	800	1600
0 Pixel	0.0650	0.0493	0.0628	0.0668	0.0653	0.0654	0.0657	0.0655
1	0.0586	0.0546	0.0372	0.0311	0.0317	0.0312	0.0307	0.0309
4	0.0749	0.0682	0.0498	0.0424	0.0426	0.0421	0.0415	0.0416
9	0.0597	0.0521	0.0329	0.0254	0.0254	0.0246	0.0241	0.0242
16	0.0469	0.0387	0.0191	0.0119	0.0107	0.0098	0.0093	0.0094
25	0.0468	0.0383	0.0184	0.0106	0.0097	0.0086	0.0081	0.0081
36	0.0481	0.0396	0.0196	0.0115	0.0105	0.0095	0.0088	0.0090
49	0.0514	0.0427	0.0225	0.0143	0.0132	0.0121	0.0116	0.0115
64	0.0507	0.0419	0.0217	0.0134	0.0121	0.0111	0.0105	0.0105
81	0.0477	0.0389	0.0188	0.0103	0.0088	0.0079	0.0072	0.0071
100	0.0480	0.0392	0.0189	0.0103	0.0089	0.0078	0.0071	0.0071

Table 3.5. Sum of signal mean values and standard deviation absolute value evaluated in the measuring area A by using the reference signal measured in $A_{R.}$ The first raw shows original uncorrected values.

Looking at Tables 3.3-3.5 and at Figs. 3.23 and 3.24, the following considerations can be made:

- The mean ΔT value, relative to the original signal $A_R = 0$, attempts to stabilize around the value of 0.027 K as the number of pixels contained in the measuring area A increases. Besides the standard deviation is seen to stabilize around the value of 0.0385 after an initial fast decrease.
- The mean absolute ΔT value displays a decreasing trend as the number of pixels in the measuring area A increases for a given number of pixels inside the reference area A_R; this generally happens, except for some abnormal values within normal statistical fluctuations. It is also possible to see a less clear decreasing trend of the ΔT mean value with increasing the number of pixels inside the A_R.

- The standard deviation decreases as the number of pixels contained in A and in A_R increase. Moreover its value decreases quickly when the number of pixels contained in the measuring Area A and in the reference area A_R is small and tends to slow down when the number of pixels increases.

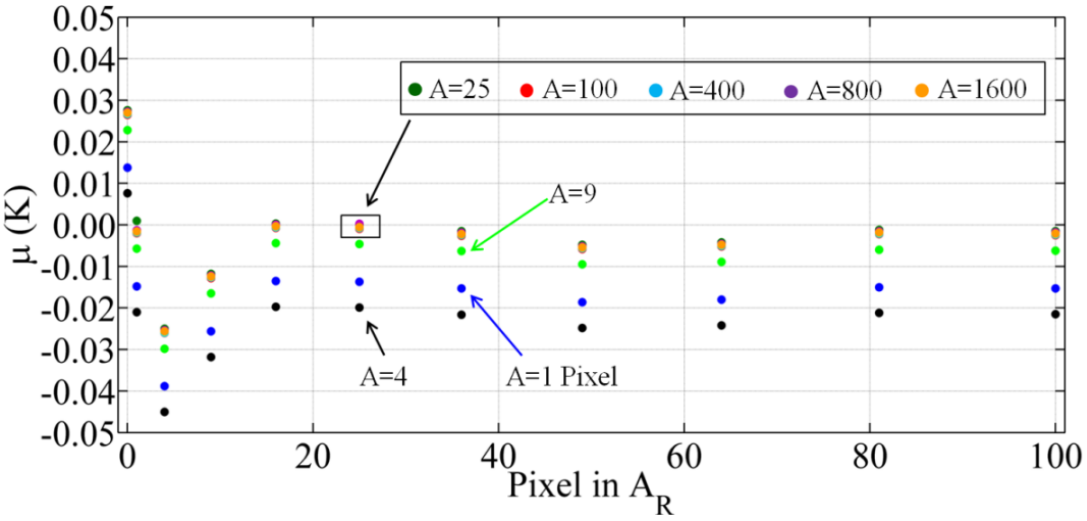

Fig. 3.23. Distribution of μ against the number of pixels in A_R.

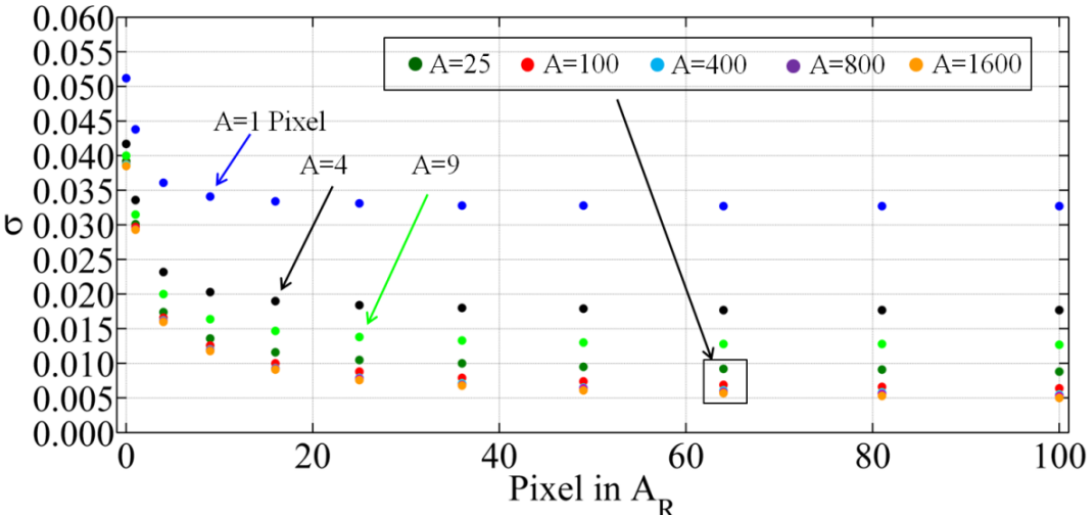

Fig. 3.24. Distribution of σ against the number of pixels in A_R.

3.6 Some effects of the reference area

This section is focused on the global effects of the Reference Area Method over the entire thermal image and its evolution in time (the whole viewed scene), which means the whole distribution of ΔT values in all the pixels contained in a set of consecutive images. To this end, a real surface at ambient temperature is viewed by means of the infrared camera SC6000 and 101 consecutive images are acquired at 83 Hz. According with equation 3.1. a sequences of 100 ΔT images (100 and not 101 because in the first image all the pixels assumes the 0 ΔT value due the subtraction) is created. Then, a reference area of 20x40 pixels is considered which is located on the top left corner

(Fig. 3.25) and the mean value of ΔT_N is evaluated inside it frame by frame. Then, a corrected sequence of ΔT_C images is created according with Eq.(3.2). By subtracting the temporal noise ΔT_N measured in A_R from all the pixels in the raw image ΔT_R at a given time *t*. The ΔT distribution for all the pixels contained in the 100 images considered before and after correction is shown in Fig. 3.26.

From the comparison between the two histograms before (Fig. 3.26a) and after correction (Fig. 3.26b), it is easy to understand the correction effectiveness. In fact, after correction the data distribution becomes a Gaussian distribution with a mean value close to 0 and with a significant reduction of the standard deviation. To better account for the correction effectiveness, only one pixel for image is considered and its data distribution before and after correction are plotted in Fig. 3.27. Again. it is possible to see as a recovered Gaussian distribution (Fig. 3.27b).

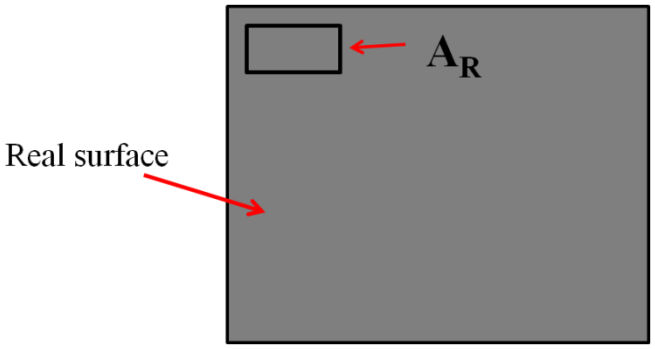

Fig. 3.25. Scheme for data analysis.

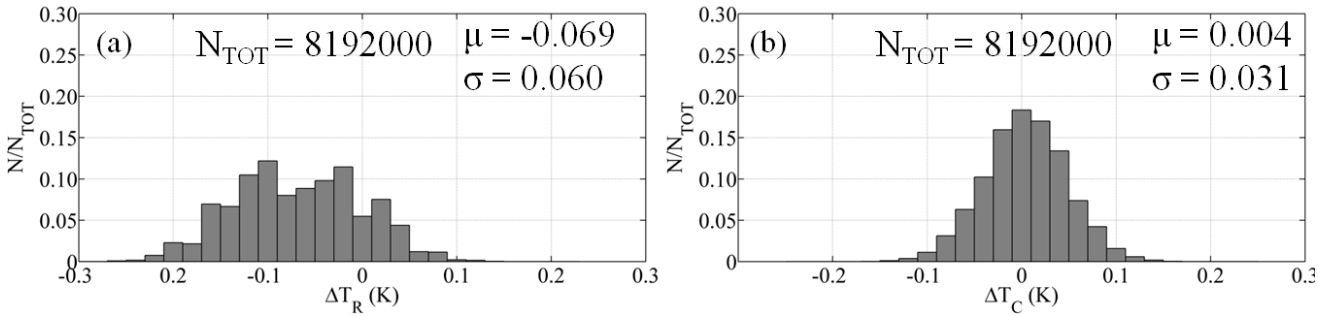

Fig. 3.26. Data distribution relative to the all pixel in the image before (a) and after correction (b).

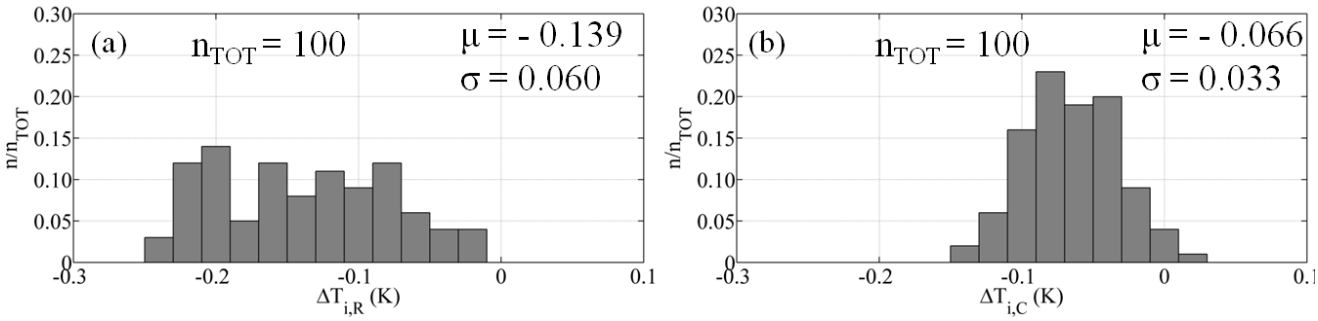

Fig. 3.27. Data distribution relative to only one pixel in each of the 100 image of Fig. 3.26, before correction (a) and after correction (b).

3.7 Practical applications

This chapter has been concerned with the temporal noise, which is mainly introduced by the instrument. A simple but effective correction method, which is based on a reference area, has been described first with the help of a blackbody and after validated with a real surface. This method will be used in the next chapters 4 and 5 to deal with measurements of thermo-elastic and thermoplastic phenomena coupled with either cyclic bending, or impact tests.

References to chapter 3

[1]. C. Meola, S. Boccardi, G.M. Carlomagno, Infrared Thermography in the Evaluation of Aerospace Composite Materials, Elsevie& Woodhead Publishing ISBN 978-1-78242-171-9, 2016.

[2]. C. Meola, S. Boccardi, G.M. Carlomagno, Measurements of very small temperature variations with LWIR QWIP infrared camera, Infrared Physics & Technol., 72, 195-203, 2015.

[3]. J. Pavelka, J. Šikula, M. Tacano, M. Toita, Activation energy of RTS noise, Radioengineering 20, 194–199, 2011.

[4]. A. Veprik, H. Vilenchik, S. Riabzev, N. Pundak, Microminiature linear split stirling cryogenic cooler for portable infrared applications, in: S.D. Miller, R.G.Ross Jr. (Eds.), Cryocoolers 14, International Cryocooler Conference Inc.,Boulder, CO, 2007

[5]. M. Singh, M. Sadana, S. Sachdev, G. Pratap, Development of miniature stirling cryocooler technology for infrared focal plane array, Defence Sci. J. 63, 571–580, 2013.

[6]. Flir Systems SC6000 Manual.

[7]. N.Y. Aziz, R.F. Cannata, G.T. Kincaid, R.J. Hansen, J.L. Heath, W.J. Parrish, S.M. Petronio, J.T. Woolaway, Standardized high performance 640 by 512 readout integrated circuit for infrared applications, in: Proc. SPIE 3698, Infrared Technology and Applications XXV, July 26, 1999, p. 766, http://dx.doi.org/10.1117/12.354577.

[8]. S. Boccardi, G.M. Carlomagno, C. Meola, The added value of infrared thermography in the measurement of temperature-stress coupled effects, Sensors & Transducers, 201, 43-51, 2016.

[9]. S. Boccardi, G.M. Carlomagno, C. Meola, Basic temperature correction of QWIP cameras in thermoelastic/plastic tests of composite materials, Applied Optics, 55, (34), D87-D94, 2016.

Chapter 4

Cyclic bending tests

Nomenclature

a,b	Coefficients of the exponential law (4.13).
c	Specific heat.
C%	Percentage of compatibilizing agent.
E	Flexural elastic modulus.
f	Maximum deflection.
f_b	Bending frequency.
F_r	Infrared camera frame rate.
h	Specimen thickness.
I	Momentum of inertia.
i	Row index.
j	Column index.
K	Material thermo-elastic constant.
k	Thermal conductivity.
L	Specimen length under deflection.
M	Bending moment.
P	Concentrated force.
R_f	F_r/f_b.
T	Temperature.
t	Image index in the sequence or time.
T_a	Absolute body temperature.
T_g	Glass transition temperature.
x	Spatial coordinate along the specimen length.
w	Specimen width.
wt%	Percentage by weigh.

Greek Symbols.

α	Thermal diffusivity.
ρ	Density.
$\Delta\sigma$	Mean stress amplitude variation.
ΔT	Temperature difference.
ΔT_A	Average maximum signal amplitude.
ΔT_{a1}	ΔT values measured in a single bending test.
ΔT_C	Corrected ΔT_R values.
ΔT_N	Temporal noise evaluated in the reference area.
ΔT_R	Raw Temperature difference ΔT.

Introduction

This chapter is concerned with on line monitoring of cyclic bending tests of different composite materials and represents an important part of this dissertation. These tests are involved with small temperature variations, which arise due to the thermo-elastic effect and are strongly affected by the instrument temporal noise and are well suited for the validation of the Reference Area Method described in Chapter 3.
Therefore, these cyclic bending tests are performed with two purposes. One is to validate the Reference Area Method for correction of the instrument temporal noise described in Chapter 3. The second one is to verify the possibility to get, in a simple and fast way, information, which may be useful for the characterization of new composite materials.
Infrared thermography is used to monitor temperature variations which are linked to thermo-elastic effects developing over the surface of a cantilever beam undergoing deflection under cyclic bending tests. The deflection is carried out by means of an electromechanical prototype machine, properly conceived and realized to perform the experimental tests. Indeed, this investigation builds on a previous feasibility study, which supplied information useful for test setup and choice of testing parameters.
As general information, one surface of the specimen is continuously viewed by the infrared imaging device during deflection and a sequence of images is acquired. The results obtained by post-processing of the acquired sequences and by exploiting the Reference Area Method already described in the previous chapter 3, demonstrate the suitability of infrared thermography to discriminate the small surface temperature variations, which are linked to the change of both matrix and reinforcement in composite materials.
The attention is devised towards different types of composite materials, involving either a thermoset, or a thermoplastic matrix, hybrid (Glare) ones and also towards the emergent natural composites made of a poly(lactic acid) (PLA) matrix reinforced with jute fibres.
On the whole, this chapter can be regarded as subdivided in three main sections. The first one is about some theoretical basis. The second section summarizes some previous attempts and feasibility studies which have demonstrated the suitability of infrared thermography to account for the thermal effects coupled with mechanical loading and have also supplied useful information about the related problems to be solved. The last section, which also represents the core of this chapter, includes several subsections and is concerned with description of test setup and specimens, post-processing of the recorded sequences of images and discussion of results.

4.1 Some theoretical considerations

The thermo-elastic effect was first conceived by Lord Kelvin (W. Thomson) in 1878 [1]. Many years later, in 1956 [2], Biot performed a thermodynamic analysis and formulated the classical thermo-elastic equation, which expresses the change in temperature (T) of a solid in terms of the change in the sum of the principal stresses ($\Delta\sigma$). The change in temperature is generally used to perform thermo-elastic stress analysis tests (TSA) [3–6]. Under reversible and adiabatic conditions (i.e., in the elastic regime and neglecting heat transfer within the body and to the environment), for isotropic materials, the temperature variation can be written as:

$$\Delta T = -KT_a\Delta\sigma \tag{4.1}$$

where T_a is the absolute body temperature, $\Delta\sigma$ is the mean stress amplitude variation, and K is the material thermo-elastic constant. Practically, Eq. (4.1) relates the temperature local variations to the volume variations. In particular, under adiabatic conditions, positive dilatation (tension) entails cooling of the material and vice versa. In metals, the thermo-elastic limit is generally assumed [7] as an indication for the yielding point. In orthotropic materials, as fibre-reinforced polymers (FRP), Eq. (4.1) modifies as [4]:

$$\Delta T = -\frac{T_a}{\rho c_p}\left(\alpha_1 \Delta\sigma_1 + \alpha_2 \Delta\sigma_2\right) \tag{4.2}$$

with α_1 and α_2 the mean thermal expansion coefficients along the principal material directions. Under certain conditions when the composite is made of plain weave fabric layers laid up to produce a symmetric laminate, the thermo-elastic response can be approximated as originating from the isotropic surface layer [6], making possible the use of the simpler Eq.(4.1).

In general, thermo-elastic effects are associated with the TSA technique, whose purpose being to monitor the progression of damage in specific conditions, such as in presence of notched specimens under cyclic tension compression tests. Owing to bending tests, Luong [8] reports on the use of infrared thermography for detecting the onset of intrinsic dissipation, or damage indicator, owing to the thermo-mechanical coupling. The adopted procedure was to acquiring a thermal image after a fixed number of cycles. In all these cases, the analysis was driven towards the thermoplastic phase in which the temperature variation is significant and then easy to be measured. A more difficult point is to deal with measurements of temperature variations experienced by the material during the elastic phase i.e., thermo-elastic effects. A way to exploit thermo-elastic effects is through monitoring of sound specimens during cyclic bending. Under cyclic bending, the material undertakes tension and/or compression with involved cooling/warming effects. For a cantilever beam (Fig 4.1a) the temperature variations (Fig 4.1b) typically follow the bending moment trend (Fig. 4.1c). Then, it is possible to acquire information on some material characteristics by simply monitoring the thermo-elastic effects.

A question which may arise is if, and how, material properties interfere with thermo-elastic effects and, in particular, if it is possible to discriminate any difference induced in the fibre and/or in the matrix by simply visualizing thermo-elastic effects. In light of these considerations, the attention of this chapter is focused on the use of an infrared imaging device for monitoring the thermal response, under cyclic bending tests, of different types of composites involving change of matrix and of fibres. To this end, a cantilever beam is considered and cyclic bending tests are performed on it.

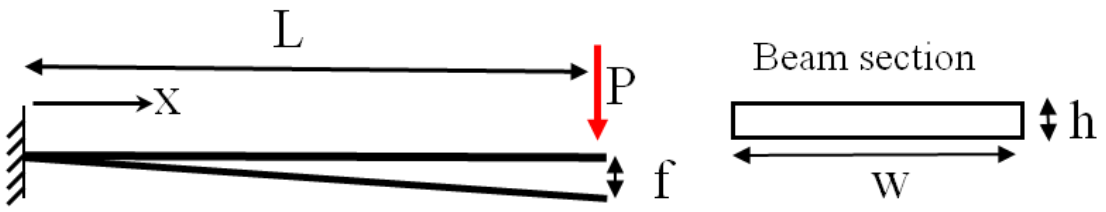

(a)

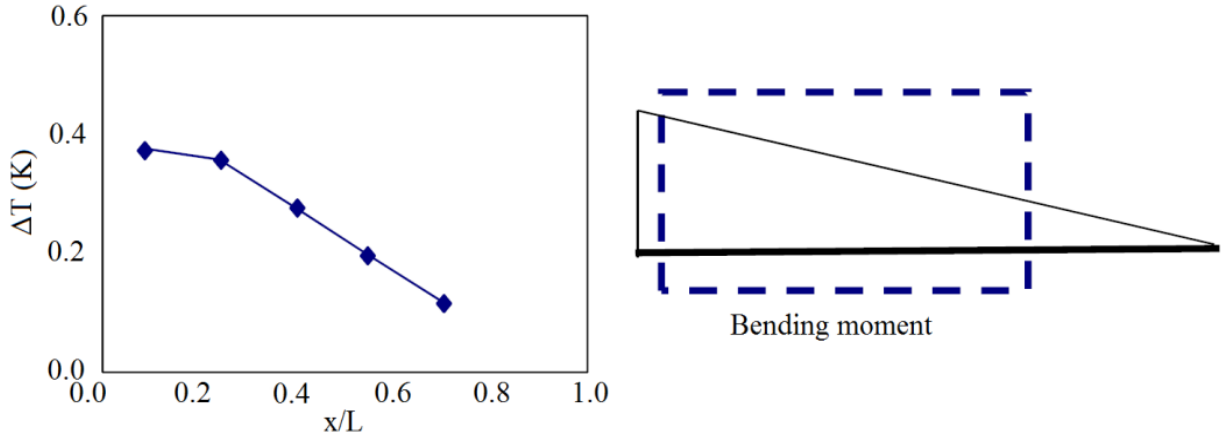

(b) (c)

Fig. 4.1. Sketch of a cantilever beam with concentrated force at its extreme (a) and a comparison of temperature variations (b) and bending moment (c).

It is well known that for a cantilever beam with a concentrated force P at its end (Fig. 4.1a) the following relationships apply:

$$P = \frac{3EIf}{L^3} \tag{4.3}$$

$$M(x) = P * (L - x) \tag{4.4}$$

where E is the material flexural elastic modulus and I is the momentum of inertia of the beam transversal section that for a rectangular section can be expressed as:

$$I = \frac{wh^3}{12} \tag{4.5}$$

It is possible to link the stress on the surface with the bending moment:

$$\sigma(x) = \frac{M(x)}{I} * \left(\frac{h}{2}\right) \tag{4.6}$$

and then substitute the momentum of inertia expression in equation (4.6) to obtain the following expression:

$$\sigma(x) = \frac{3Ef(L-x)}{L^3} * \left(\frac{h}{2}\right) \tag{4.7}$$

By substituting Eq.(4.7) in Eq.(4.1), the following relationship is found:

$$\Delta T = \frac{-KT_a\, 3Ef(L-x)}{L^3} * \frac{h}{2} \tag{4.8}$$

From Eq.(4.8), it is evident that ΔT depends on several quantities: the material elastic modulus E, the thermoelastic constant K and some geometrical parameters like the beam length (L), thickness (h) and the deflection under bending (f) as well.
Of course, what till now discussed refers to bending load without any secondary effect such as shear stresses near the fixture [9], and other effects induced by cyclic load conditions.

4.2 Some preliminary tests

This research started few years ago with the pioneering work by Meola, et al. [10]. Indeed, the obtained results have been promising and acted as breeding ground for the continuation of the research through this Ph.D thesis.
The preliminary tests are carried out as feasibility tests to ascertain the capability of an infrared imaging system to capture the weak signal associated with cyclic bending. Then, for quick testing a simple tool is considered, which allows for two cyclic bending test configurations (A and B) as sketched in Fig. 4.2. In the case of Configuration A (Fig. 4.2a), the specimen, a composite strip, is fixed at one end and is in contact with a punch in its central zone. Bending arises under the action of the force that is applied cyclically at the free end and is directed downside; the specimen displacement is applied manually. Two infrared cameras (Flir Systems) are used, which are the SC3000 and the SC6000, both equipped with a QWIP detector working in the 8-9 μm infrared band. The used infrared camera is positioned to see the top surface of the strip.

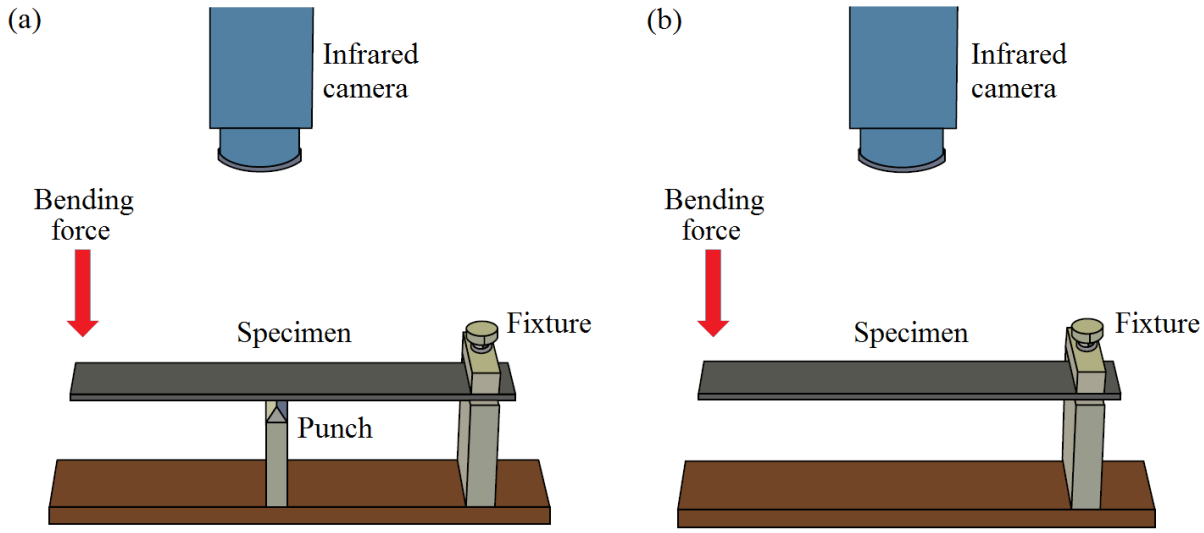

Fig. 4.2. Setup for bending tests with manual force application [10].
(a) Bending with central punch, (b) cantilever beam.

In the case of configuration B (Fig. 4.2b), the specimen is again fixed at one extreme but the punch is removed and then the configuration is that of a cantilever beam. Tests are performed with the force acting cyclically in the direction upside-rest, downside-rest and upside-downside (downside-upside). For each type of test the load is manually applied, while sequences of thermal images are recorded by the infrared camera. Both surfaces (top and bottom) are monitored with the infrared camera, the bottom surface being viewed with the aid of a mirror placed at 45 degrees underneath the specimen. The results, in terms of ΔT amplitude over time, obtained with configuration A are

shown in Fig 4.3a for several measuring positions. From the shown data it is also possible to recognize a good agreement between the bending moment and the ΔT over the span (Fig. 4.3b).
Several composite materials have been tested including glass fibres reinforced polymer (GFRP) carbon fibres reinforced polymer (CFRP), a type of hybrid composite made of aluminium and glass/epoxy (Glare).

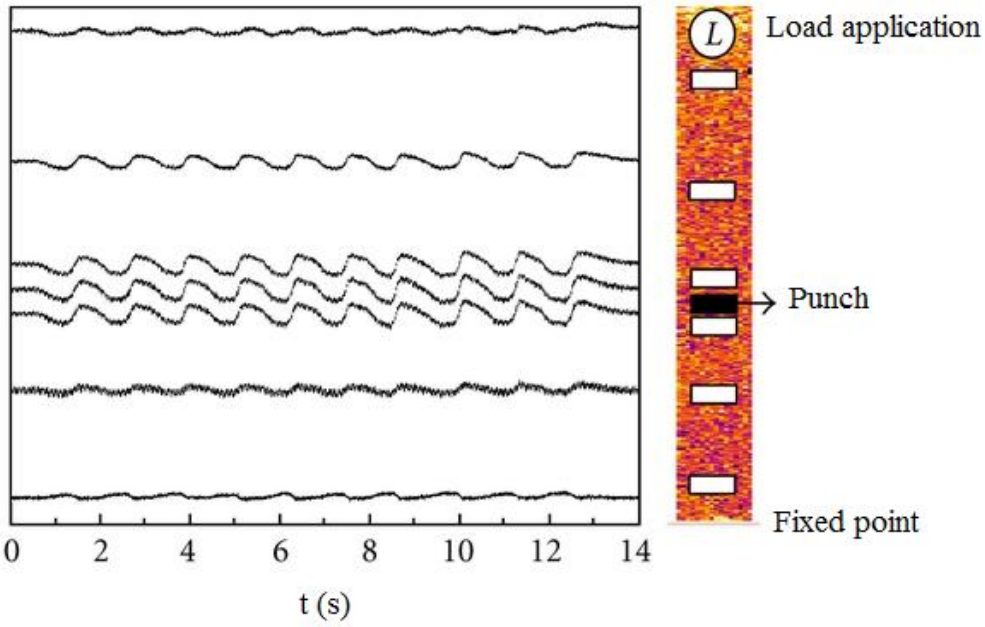

(a)

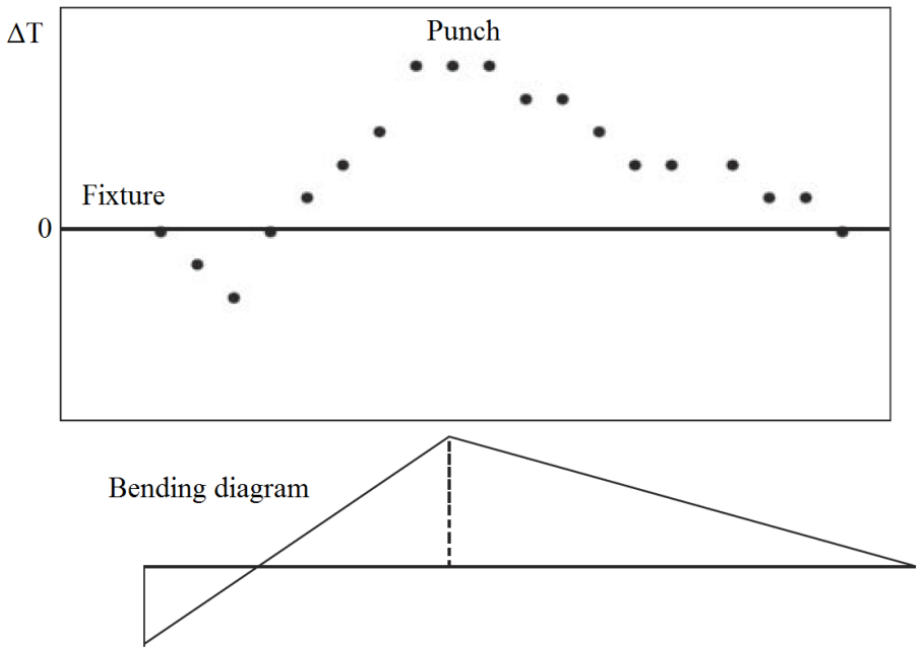

b)

Fig. 4.3. Results with configuration A; ΔT variation versus time in several areas located on the left and on the right of the punch (a), comparison between ΔT distribution and bending moment diagram (b).

The main findings are [10]:

- a quasi-sinusoidal trend that perfectly synchronizes with the cyclic displacement of the specimen free end, with decrease/increase of temperature over the surface being in tension/compression, respectively;
- a general agreement with the momentum diagram along the specimen length with deviations from the former being observed in presence of buried defects within the material.

The added value of Ref. [10] resides in the possibility to gain, in a fast and easy way through the use of a simple hand-held mechanism and an infrared-imaging device, some information, which can be usefully exploited for the material characterization. However, this study represents only a preliminary approach; in fact, the manual application of the cyclic load poses some problems such as the impracticality to change the load frequency as well as to assure overall test accuracy. This has led to the necessity of different tests with power-driven load application allowing change of parameters such as bending amplitude and frequency. Then, as a next step, a testing apparatus is realized to allow for a power-driven load application with changing of both bending frequency and amplitude. In addition, also the thermal image acquisition rate is varied in view of finding the optimal values to perform tests in a quick and reliable way [11,12]. It has been found that by introducing the parameter R_f as ratio between frame rate F_r and bending frequency f_b:

$$R_f = \frac{F_r}{f_b} \tag{4.9}$$

the condition:

$$R_f > 6 \tag{4.10}$$

must be satisfied to assure chasing of thermoelastic effects developing under bending tests. This condition corresponds to detecting not less than about seven frames, within a single loading cycle, so as to capture average ΔT values with a certain confidence. However, as a main novelty of Ref. [12], the noise correction method through the reference area is introduced for the first time.
The test setup of Ref. [12] as sketched in Fig. 4.4, consists of an apparatus, which includes positioning of the specimen and application of the cyclic bending force with an electric motor, via a piston rod and a loading arm (with a trench to insert the beam free end). More specifically, the cantilever beam specimen is clamped on one side, while it is free to bend under the cyclic force which is applied at the opposite end by the trench. The infrared camera SC6000 views the bottom specimen surface by means of the mirror. positioned underneath (Fig. 4.4). Tests have been performed on a Glare specimen by varying the bending frequency (f_b) between 2 and 14 Hz. As main finding, for all tests, a quasi-linear dependence of the temperature amplitude ΔT along the cantilever beam (x/L) has been found. However, the intercept of the line with the x axis does not exactly occur at $x/L = 1$ but at a value of about 0.9. This behaviour is most probably due to the small moment induced by the trench where the specimen free end is inserted.

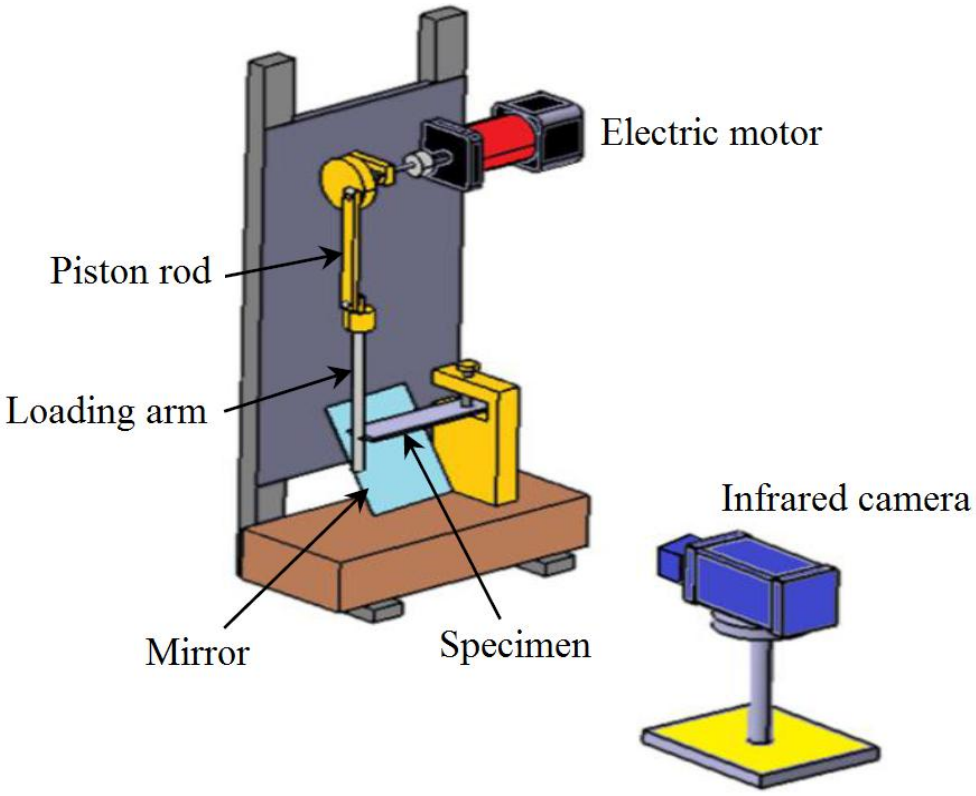

Fig. 4.4. Test setup of Ref [12].

4.3 New investigation

Drawing conclusions from preliminary tests has, from one side, encouraged the continuation of this kind of testing and, from the other, demanded for a new test setup. Then, a new test setup is arranged and different types of composites are considered for testing.

4.3.1 Test setup and procedure.

Cyclic bending tests are performed in cantilever beam configuration with the specimen clamped to a fixture at its bottom side and free to bend at the opposite (upper) end where the cyclic harmonic displacement is applied. Displacement is realized with a prototype bending machine properly conceived and realised to perform cyclic bending tests (Fig. 4.5). The bending machine is composed of an electro-mechanical actuator with a moving arm, two inextensible nylon wires, a small clip, a return spring and a fixture suitable to lodge up to two specimens. The infrared camera SC6000 is used to monitor the specimens surface during tests (see chapter 3 for camera specifications). The two specimens are clamped together from one end in the fixture, but only one is subject to cyclic deflection in response to the force applied to the other end; the other specimen remains unloaded being the beam used as reference for correction of the camera temporal noise. The upper end of the loaded specimen is inserted into the clip connected to the wire which forces the specimen to bend under the wire alternate displacement. The clip is only a guide for the loaded specimen free end it does not constraint it anyway; in fact, the clip can freely rotate around the wires and does not transmit bending moment to the sample free edge (Fig. 4.6).

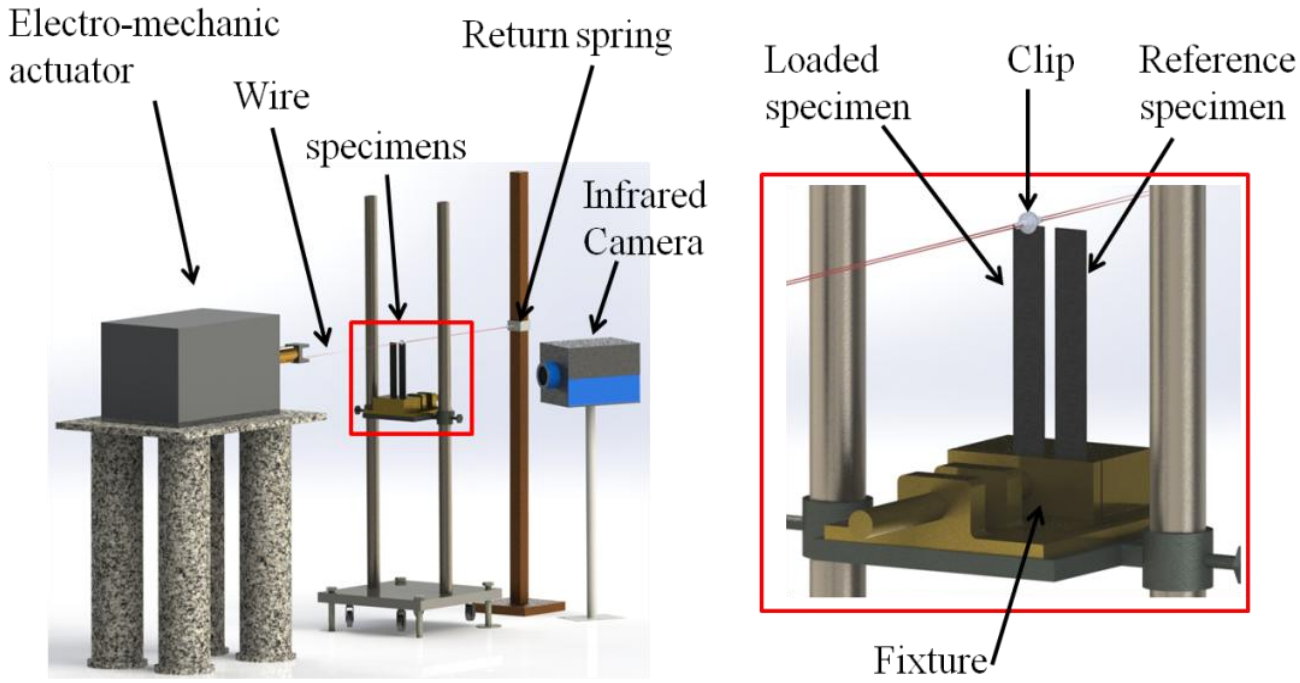

Fig. 4.5 Final test setup for cyclic bending tests.

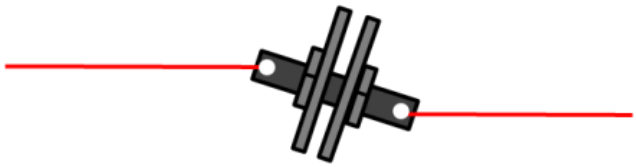

Fig. 4.6. Clip details.

The loaded specimen end, connected to the clip, follows the harmonic displacement of the moving arm; the bending frequency can be set through the electro-mechanical actuator control unit. The total displacement imposed to the loaded specimen coincides with the total displacement of the moving arm which is generally equal to 15 mm and cannot be changed. For each material under investigation, several experimental tests have been performed by considering two testing configurations (Fig. 4.7) and by changing the bending frequency. In configuration 1 (Fig. 4.7a) the surface viewed by the infrared camera is subjected alternatively to tension and compression conditions, with the imposed displacement being equal $f = \pm$ 7.5 mm (7.5 mm in tension and then 7.5 mm in compression and *viceversa*). Instead, in configuration 2 (Fig. 4.7b) the viewed surface is subjected only to tension with the total displacement being equal to -15 mm.

In particular, when the deflection is performed in configuration 2, the rear support of the clip is removed in order to avoid bumping of the specimen against it with its free edge when returning to its rest position after each load cycle.

The bending frequency f_b has been varied in the range from 0.05 Hz up to 4 Hz. In particular, f_b = 0.05 Hz is the minimum frequency value selectable, while at $f_b > 4$ Hz the vibrations induced by the electromechanical actuator becomes too much severe and hinders tests execution.

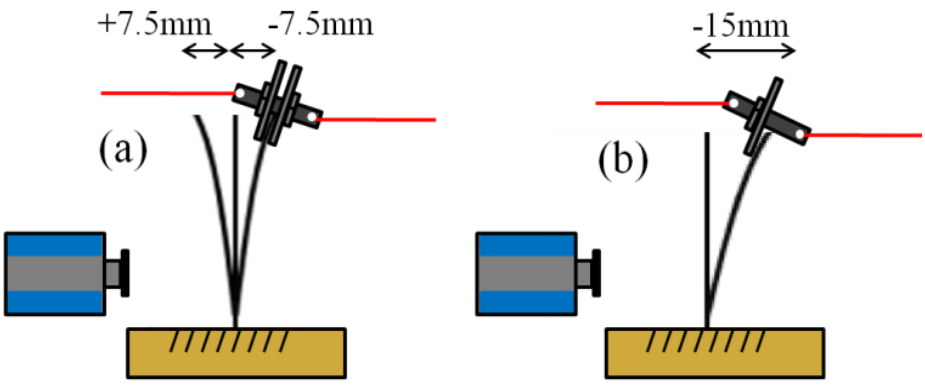

Fig. 4.7. Test configurations configuration 1 (a), configuration 2 (b).

In some tests a mirror (aluminium sheet) is introduced to visualize, in the same image and at the same time, both front and rear specimen surfaces (Fig. 4.8). In particular, the mirror is placed 10 centimetres behind the specimens; the infrared camera looks at the specimen rear surface reflected in the mirror. This allows to acquire information about the specimen rear surface. With this test setup the infrared camera is focused on the specimen front surface, while the image reflected by the mirror is not perfectly focused, but it appears a bit warped by the mirror effect. In reality, an aluminium sheet has been used as mirror and without any calibration, the purpose being, not to obtain quantitative data, but only to ascertain the correct functioning of the machine as well the coherent response of specimens.

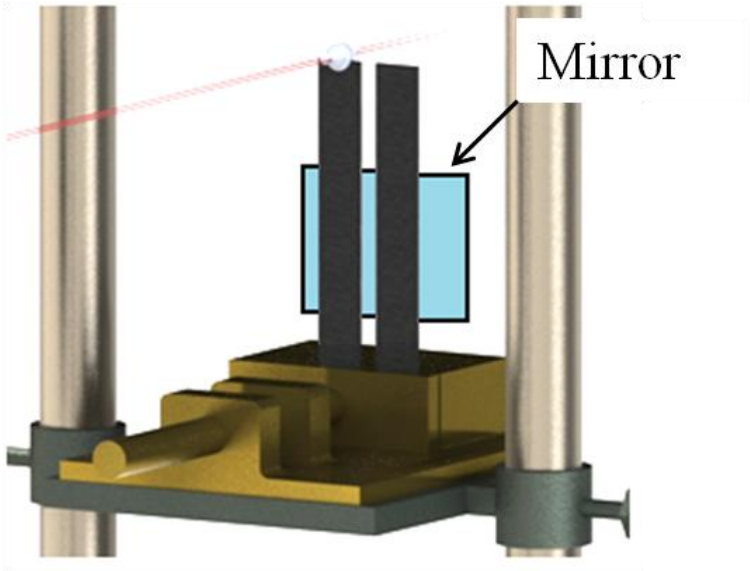

Fig. 4.8. Detail of mirror position behind the specimens (see also Fig. 4.5).

During each test, the infrared camera views the surface of both loaded and reference specimens and acquires a sequence of images beginning few seconds before starting of bending in order to record some images at ambient temperature. The sequences of thermal images are acquired at a frame rate Fr = 60, 30 or 18 Hz during bending. The recorded sequences undergo post processing by using the Researcher TM software (available from the Flir systems package) and specific routines developed in the Matlab environment.

4.3.2 Description of specimens

Several different specimens are fabricated involving change of matrix and/or fibres; they are summarized in Table 4.1 in terms of code, composition and thickness. Photos of some specimens are shown in Fig. 4.9. In particular, three specimens, which are named PP, PC2 and PC5, are only made of the basic matrix, which is polypropylene (PP grade MA712 from Unipetrol – Czech Republic with ρ = 0.9 g/cc, MFI at 230 °C/2.16 Kg = 12g/10 min), either neat, or modified with the addition of a given percentage (2%, or 5% by weight) of a common coupling agent, polypropylene grafted maleic anhydride (PP-g-MA) that is commercialized under the trade name of Polybond 3200 (MFI 115 g/10 min, 1 wt% maleic anhydride, from Chemtura). The specimens identified with codes: PPG, PGC2, PPJ, PJC2 and PJC5 include either a neat polypropylene matrix (PP), or a compatibilized one at 2% (C2), or at 5% (C5) of the coupling agent Polybond 3200, and reinforced with either glass (specimens with the letter G in their name), or jute fibres (specimens with the letter J in their name). More specifically, plain weave type woven glass fabric (E-type glass fibres having density of 2.54 g/cm^3) with a specific mass of 204 g/m^2 [13] or jute plain weave type fabric with a specific mass of 250 g/m^2 and furnished by Deyute (Alicante, Spain) [14]. It is worth noting that specimens reinforced with glass fibres include 20 balanced glass fibres layers, while the specimens with jute fibres include 8 woven jute fibres layers; all layers are symmetrically arranged with respect to the middle plane of the laminate. More specifically, PP layers were alternated with layers of jute glass fabric, using the film stacking and compression moulding techniques to prepare sample laminates.

Basically, the maleic anhydride coupling agent is used to improve adhesion between the polypropylene PP matrix and fibres [15-28] and, in turn, to improve the composite mechanical properties. In particular, glass fibres are usually pre-silanized and the added maleic anhydride grafted polypropylene reacts with the amine group of the fibre glass surface; instead, jute fibres are generally pre-dried before use and have a coarser texture warp which may entrap a larger amount of matrix.

Specimens PLAJ include a matrix made of poly(lactic acid) (PLA) resin supplied by Nature Works under the trade name Ingeo 7001D (ρ = 1.24 g/cc, MFI at 210 °C/2.16 Kg = 6g/10 min, T_g = 55-60 °C), reinforced with plain weave type jute fabric fibres by Deyute (also used to fabricate the specimens with the PP matrix). More specifically, films of neat PLA were alternated with layers of pre-dried jute fabric, using the film stacking and compression moulding techniques to prepare sample laminates consisting of 8 balanced fabric layers 0°/90°, symmetrically arranged with respect to the middle plane of the laminate $[(0/90)_4]$s. Each laminate has an average thickness of 3.8 mm.

Specimens indicated with the GLARE code belong to a type of fibre metal laminate (FRML) including 3 aluminium sheets with 2 glass/epoxy (GFRP) layers in between them. This type of material is brand named Glare®. These specimens are 1.5 mm thick and are cut from a large plate, which was fabricated following industrial standards with autoclave curing; their outside surface is covered with a green aeronautical coating having an emissivity coefficient of about 0.9.

GFRP specimens include E glass fibres embedded in a low viscosity epoxy matrix. More specifically, this type of specimen is obtained by hand layup of eight epoxy adhesive preimpregnated unidirectional glass fibres and allowed to cure at ambient temperature. The stacking sequence is $[0_2/90_4]_s$ with an overall specimen thickness h = 2.9 mm.

All the specimens used for cyclic bending tests have been cut from larger plates and have width of 25 mm (specimen involving PP and PLA as matrix), or of 30 mm (GFRP and GLARE), and total length of 125 mm.

It is worth to underline that the specimen width of at least 25 mm, or 30 mm in some cases, has been chosen in order to frame a wide enough portion of material under deflection. Besides, the specimen length of 125 mm has been imposed by the maximum dimension of the plate from which specimens were cut. Each specimen is inserted inside the fixture by 20 mm in order to assure a perfect clamping, while 105 mm are free to bend under the harmonic solicitation. For almost all the specimens under investigation, the width is lower than 25.4 mm, while the span-to-thickness ratio is greater than 15 as prescribed by ASTM D747 − 10 [29].

Specimen Code	Composition (Matrix – Reinforcement)	Thickness (mm)
PP	Neat PP - only matrix	**4.0**
PC2	Modified PP (2 wt% PP-g-MA)	**4.0**
PC5	Modified PP (5 wt% PP-g-MA)	**4.0**
PPG	Neat PP - Woven glass fibres	**3.0**
PGC2	Modified PP (2 wt% PP-g-MA) Woven glass fibres	**3.0**
PPJ	Neat PP - Woven jute fibres	**3.8**
PJC2	Modified PP (2 wt% PP-g-MA) Woven jute fibres	**3.8**
PJC5	Modified PP (5 wt% PP-g-MA) Woven jute fibres	**3.8**
PLAJ	Neat PLA-Woven glass fibres	**3.8**
GFRP	Epoxy adhesive preimpregnated unidirectional glass fibres $[0_2/90_4]_s$	**3.1**
GLARE	3 aluminium sheets with 2 glass/epoxy (GFRP) layers in between	**1.5**

Table 4.1. Some details of investigated specimens.

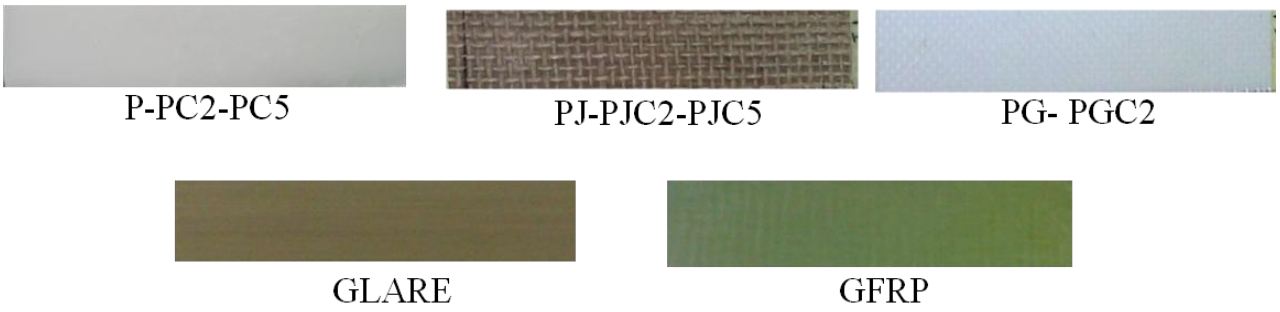

Fig. 4.9. Photos of some specimens.

4.4 Data post-processing

As already described in chapter 3, the acquired sequences of thermal images are post processed to extract ΔT images according to:

$$\Delta T(i,j,t) = T(i,j,t) - T(i,j,0) \tag{4.11}$$

i and *j* representing lines and columns of the surface temperature array and *t* the time instant at which each image is recorded; more specifically, $t = 0$ indicates the first image of the sequence, before loading, for which the specimen surface is at ambient temperature. Then, the so obtained sequences of ΔT images are further processed to extract more useful information. In particular, two methods, which are named: Area Method (AM) and Whole Width Method (WWM) are used. As a general comment, whatever the type of analysis is going to be performed, a drawback is represented by the instrument noise, which may affect small ΔT values as already evidenced in chapter 3. In this context, the main difference amongst the two methods lies in the noise correction which in one case is limited to the pixels contained inside a given area, while in the other case is expanded to practically all the pixels in the whole visualized surface of interest.

4.4.1 Description of the Area Method

The AM is the first method developed and used to analyze the data acquired during cyclic bending tests. Considering that for cyclic bending the interest is toward the variation of ΔT by moving away from the fixture in comparison with the bending moment distribution over the beam, several points are selected along the beam length [9].

The reference signal that is going to be used to reduce the temporal noise $\Delta T_N(t)$ is extracted from a reference area, which is constituted of a rectangular 20 x 40 pixels region, over the unloaded specimen, as it appears at the bottom right side of Fig. 4.10 (red rectangle). Instead, four measurement positions (PMs) are chosen over the loaded specimen, evenly distributed along the beam length *L*, starting about 10 mm far from the fixture ($x = 0$) and moving towards the forced end (black rectangles of Fig. 4.10).

For each PM position over the specimen, an average ΔT value is computed, frame by frame, in an area 20 x 40 pixels (about 5 mm along the width and 10 mm along the span) and plotted against time in Fig. 4.11. Practically, such an average value corresponds to the ΔT value at the central black dot of every rectangular black area. As can be seen, the raw signal $\Delta T_R(t)$ is affected by random abrupt jumps like those already displayed in Chapter 3.

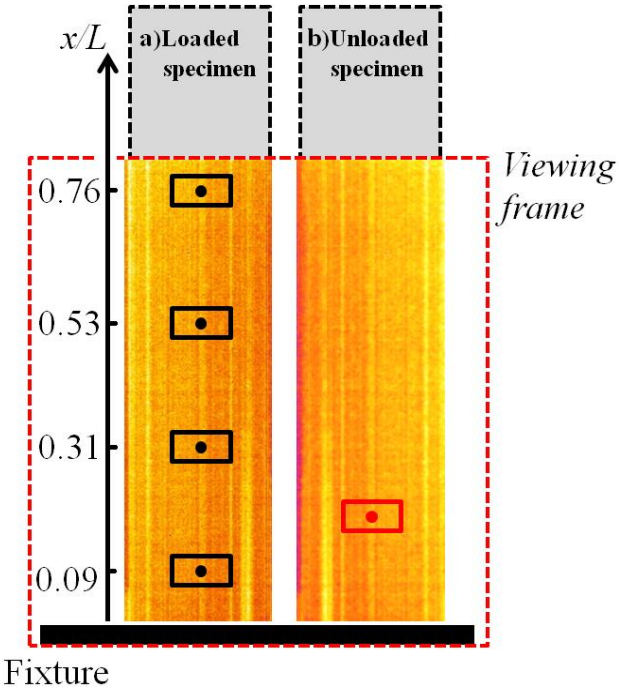

Fig. 4.10. Reference Area A_R (red) and measuring areas PM (black).

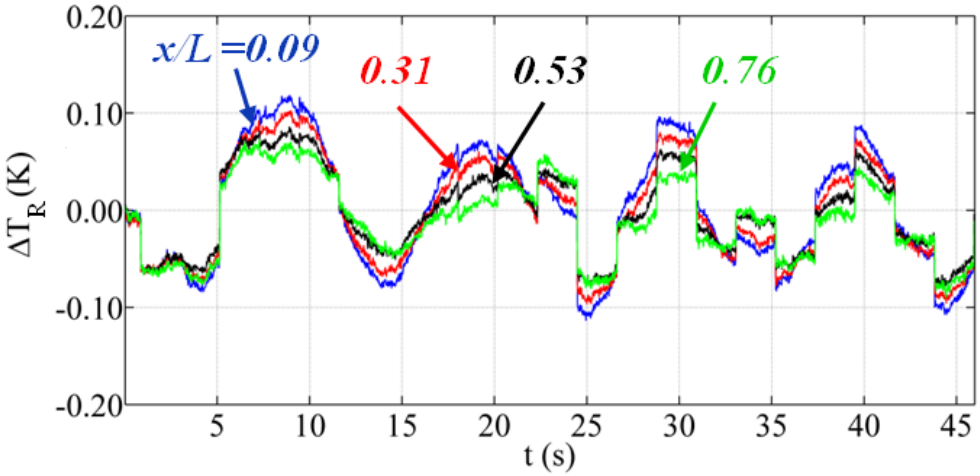

Fig. 4.11. Example of raw ΔT signals.

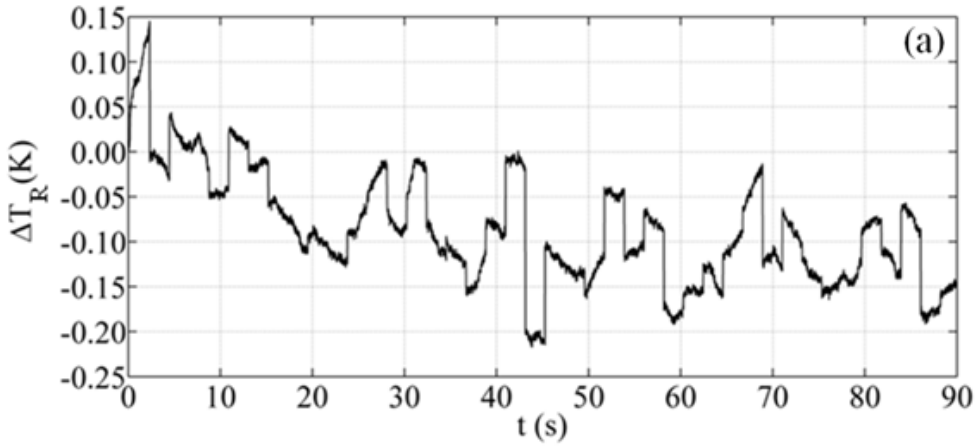

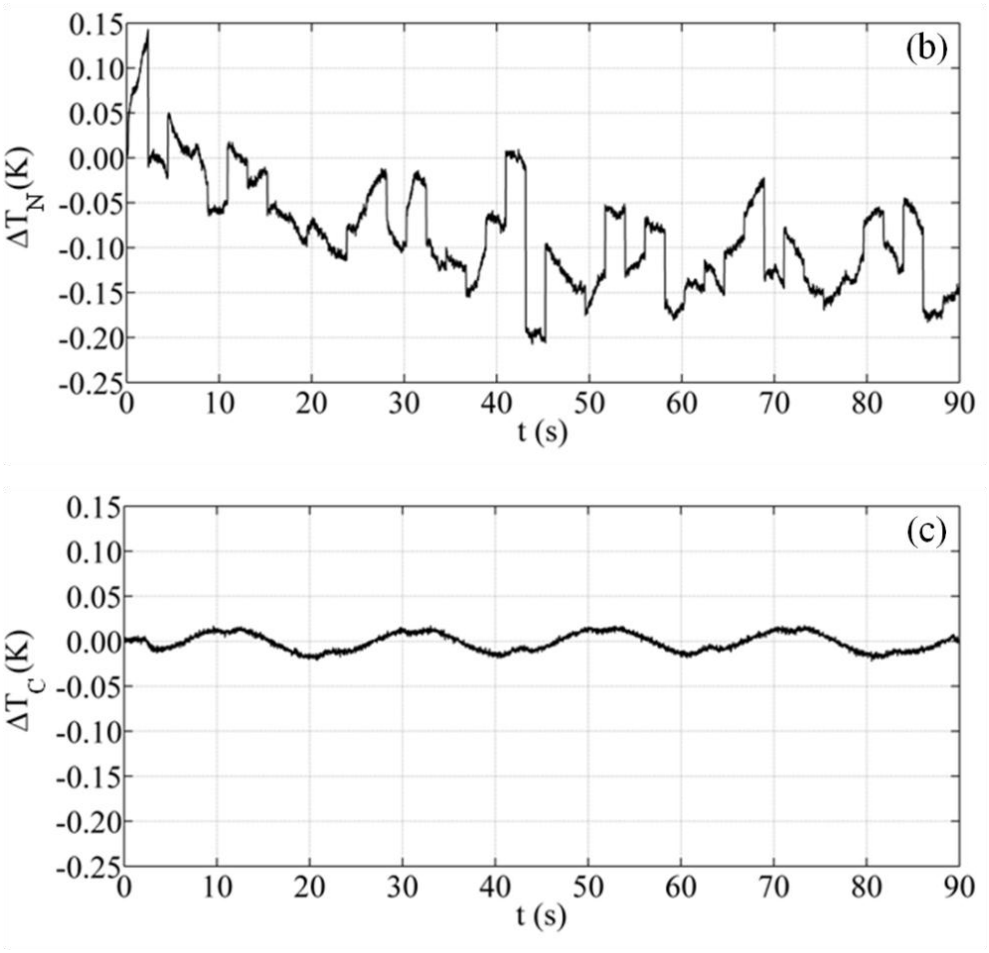

Fig. 4.12. Comparison of ΔT_R (a), ΔT_N (b) and ΔT_C (c) signals at x/L = 0.09 of a Glare specimen tested at f_b = 0.05 Hz.

By applying the Reference Area Method, the corrected $\Delta T_C(t)$ signal is obtained. More specifically, ΔT_C is obtained by means of the relationship, which was already described in Chapter 3 and herein reported again for easy reading:

$$\Delta T_C(t) = \Delta T_R(t) - \Delta T_N(t) \tag{4.12}$$

Plots of ΔT_R, ΔT_N and of ΔT_C, relative to a specimen of Glare and a bending frequency of 0.05 Hz and relative to the PM point at x/L = 0.09, are shown in Fig. 4.12 a, b and c, respectively. Instead, Fig. 4.13 (a, b and c) shows ΔT_R, ΔT_N and ΔT_C signals relative to four PMs positions of a PPG specimen at bending frequency of 0.1 Hz.

From figures 4.11-4.13 it is possible to notice that the main disruption of ΔT_R, signals, which should be harmonic, corresponding to the cyclic traction/compression, is caused by the random jumps that characterize the ΔT_N signal. Instead, the corrected ΔT_C plots bear witness for the effectiveness of the Reference Area Method applied to restore the measured signal in the real experimental situation. In fact, jumps completely disappear and the expected harmonic trend is recovered. This trend is perfectly coupled with the alternate cooling/heating, which corresponds to the specimen surface traction/compression, respectively. Moreover, all the corrected signals have a frequency equal to the f_b value imposed by the electro-mechanical actuator.

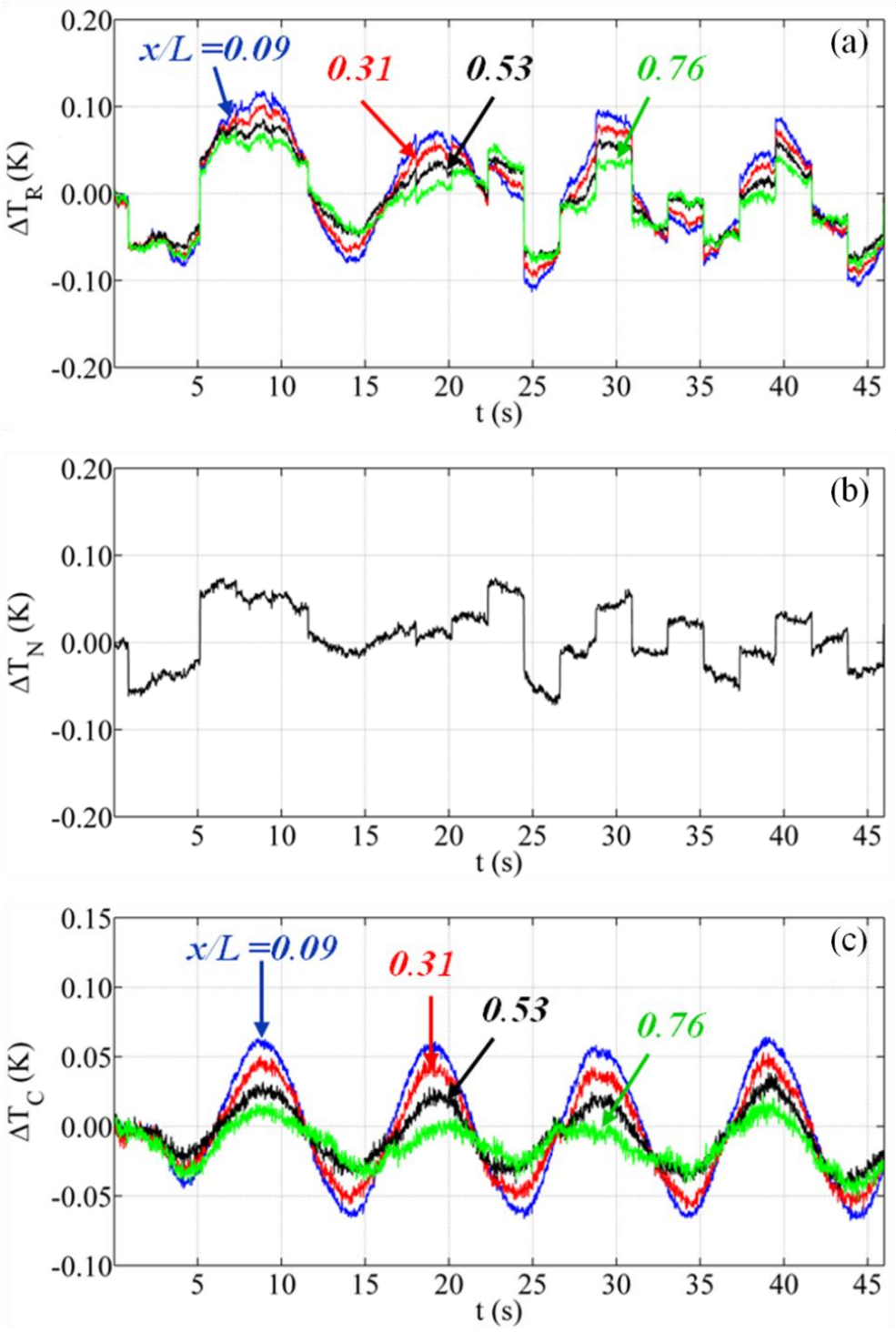

Fig. 4.13. Comparison of $\Delta T_{R,}$(a), ΔT_N (b) and ΔT_C (c) signals of a PPG specimen for f_b = 0.1 Hz.

Then, from ΔT_C plots, the average maximum signal amplitude, named ΔT_A, can be extracted amongst a fixed number of cycles (Fig. 4.14 a). ΔT_A values are evaluated as difference between two consecutive peaks and valleys, on the corrected ΔT_C signals, slightly after the bending machine start up phase. These ΔT_A values are plotted against x/L in Fig. 4.14b and show a quasi-linear dependence.

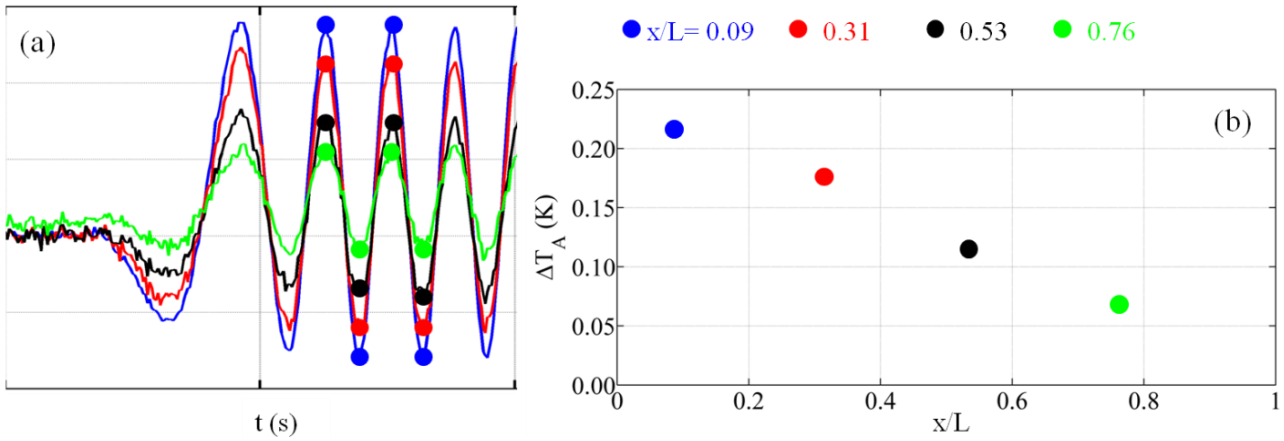

Fig. 4.14. Example of evaluation of ΔT_A values starting from ΔT_C (t) plots. Dots indicate the peaks and valleys (a) on the ΔT_C signal used to evaluate average ΔT_A values along the span reported in figure (b).

4.4.2 Description of the Whole Width Method

The Whole Width Method is an evolution of the Area Method properly conceived and used in order to investigate with higher spatial detail the ΔT along the entire span and not only in specific positions. As for the Area Method, starting from the acquired ΔT sequence, the reference signal is evaluated frame by frame inside the reference area of 20x40 pixels over the unloaded specimen. Differently from the AM, in the WWM, the ΔT_R amplitude is extracted no longer in certain positions only, but in every pixels along the specimen length [30]. More specifically, as explicable looking at Fig. 4.15, each PM point (yellow points in figure 4.15 right side) represents the average value amongst 50 pixels along the specimen width. Of course, this is done by suppressing border appraisals, as well unstable effects due to start-up and shutdown of the electro-mechanical actuator.

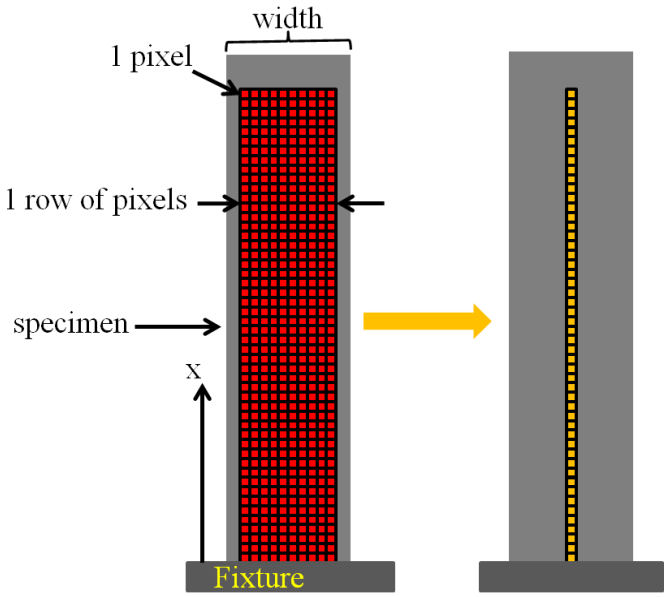

Fig. 4.15. Details of the Whole Width Method.

As a result, a distribution of ΔT_R values over the specimen surface is reduced to a line of PM points along the specimen length. Then, the Reference Area Method is applied to correct such ΔT_R values and to create a time sequence of ΔT_C values in each PM point. Then, in each PM point an average value is extracted amongst a certain number of load cycles, which ranges from 3 up to 8 depending on the bending frequency (Fig. 4.16a). Finally, ΔT_A values are evaluated from the average load cycle as difference between peak and valley, as already described. The distribution of ΔT_A along the specimen length, as shown in Fig. 4.16b, is again quasi-linear and tending to zero for $x/L \rightarrow 1$.

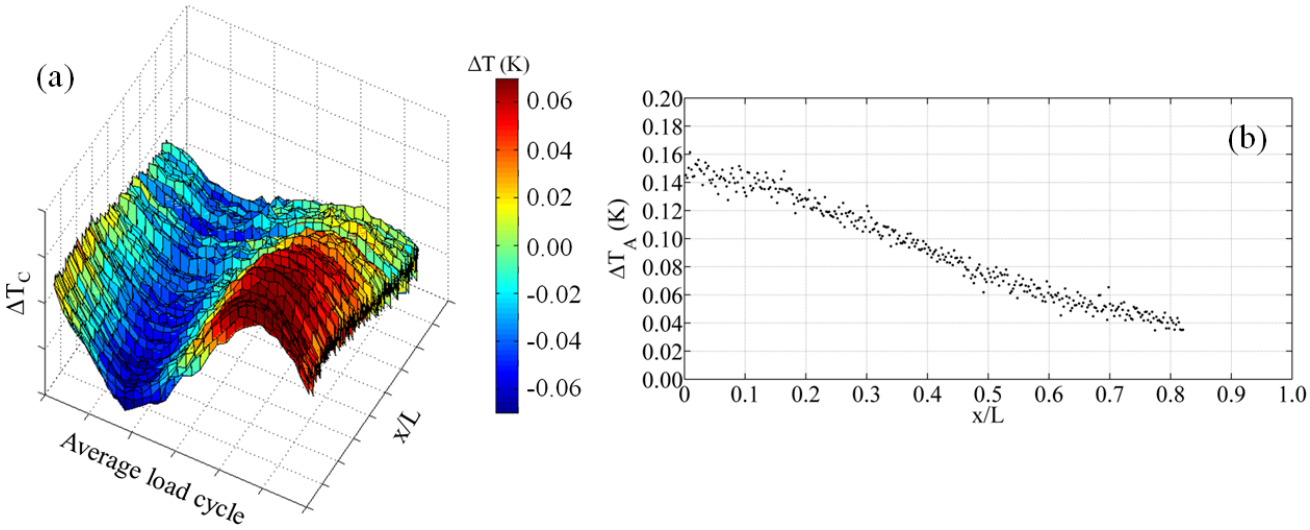

Fig. 4.16. Representation of ΔT_C values; average load cycle (a); ΔT_A values against x/L obtained with WWM (configuration 1) (b).

4.5 Qualitative evaluation of ΔT on the rear specimen surface

As already said in section 4.3.1, some tests have been performed by using a mirror (aluminium sheet) to visualize also the rear specimen surface in order to gain information about the ΔT evolution over this surface in comparison to what happens on the front surface. The acquired data are post processed by means of the Area Method, previously described (Section 4.4.1), with the only difference that also a PM point on the rear surface near to the fixture is considered (Fig 4.17).

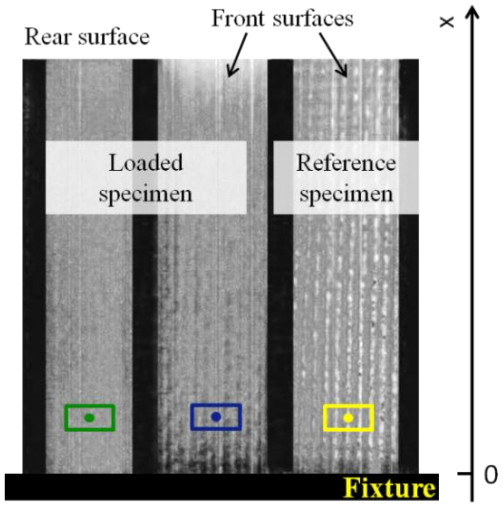

Fig. 4.17. Details of specimens surface viewed with the aid of a mirror.

Some results obtained for specimens PPG and PJC2 solicited at a bending frequency of 0.5 Hz with the test configuration 1 are shown in Fig. 4.18. In both plots, the red curve is relative to the PM point over the front surface directly viewed by the infrared camera, while the black curve indicates the ΔT evolution over the rear surface. It is worth noting that, due to the distortion effects introduced by the mirror, the position of the PM point on the rear surface is about 0.1 mm far from the fixture and not perfectly coincident with the position on the rear surface. Moreover, since care was posed to focus the detector on the specimen front surface, the portion of image relative to the back surface reflected by the mirror appears a bit blurred.

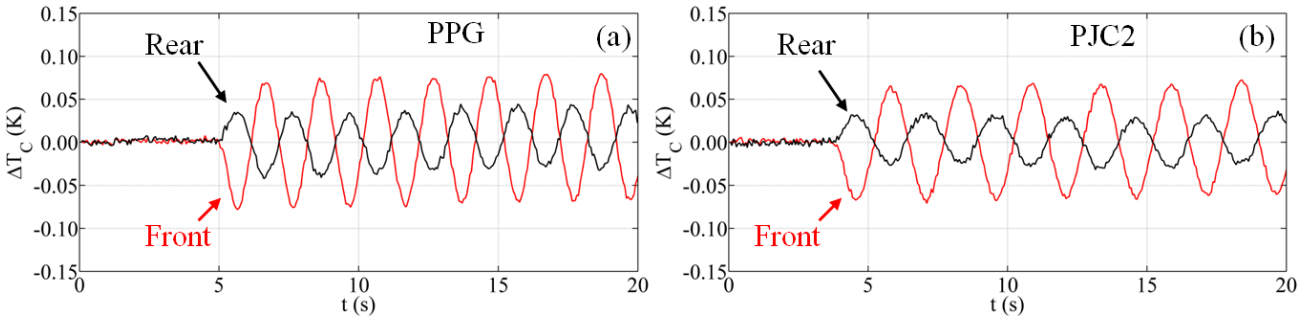

Fig. 4.18. A comparison of ΔT_C plots at x/L = 0.1 and f_b = 0.5 Hz on PPG (a) and f_b = 0.4 Hz on PJC2 (b) specimens.

It has to be noted that, for all the investigated specimens, the signal measured over the rear surface (reflected by the mirror) is out of phase by 180° with respect to the signal measured over the front surface. This is in agreement with the thermoelastic effect linked to the specimen oscillation; in fact, when the front surface is in tension (cooling down), the rear one is in compression (heating up) and *viceversa*, with an alternate cooling/heating effect. In addition, the signal reflected by the mirror has a lower amplitude because of the absorption of the mirror and to defocusing effect; this effect can be corrected through adequate calibration.

4.6 Influence of the bending frequency.

The frequency is a critical parameter in cyclic bending. Herein, the effects of bending frequency on tests performed with configuration 1 are considered with the attention focused on plots of ΔT_C signals (Fig. 4.19) and mainly on the distribution of ΔT_A against x/L (Fig. 4.20). In particular, Fig.4.19 refers to ΔT_C signals over time for the PLAJ specimen at different PM positions and different bending frequencies from 0.1 Hz up to 2 Hz. Instead, Fig.4.20 shows examples of the bending frequency effect on the distribution of ΔT_A against x/L for some of the investigated specimens.

Looking at Fig 4.19, some comments can be made. On the whole, ΔT displays harmonic variations, which are perfectly coupled with the cyclic load. The ΔT amplitude increases with increasing the bending frequency. The harmonic trend is more regular for the lowest x/L value, or better closest to the specimen fixture (x/L = 0), where the bending moment reaches the highest value. As x/L increases, i.e. moving towards the forced extremity, ΔT decreases mingling with the background noise of the instrument. Moreover, from figure.4.20, it is possible to see that all ΔT_A data lie over a

straight line with the maximum value achieved close to the fixture in agreement with the bending moment.

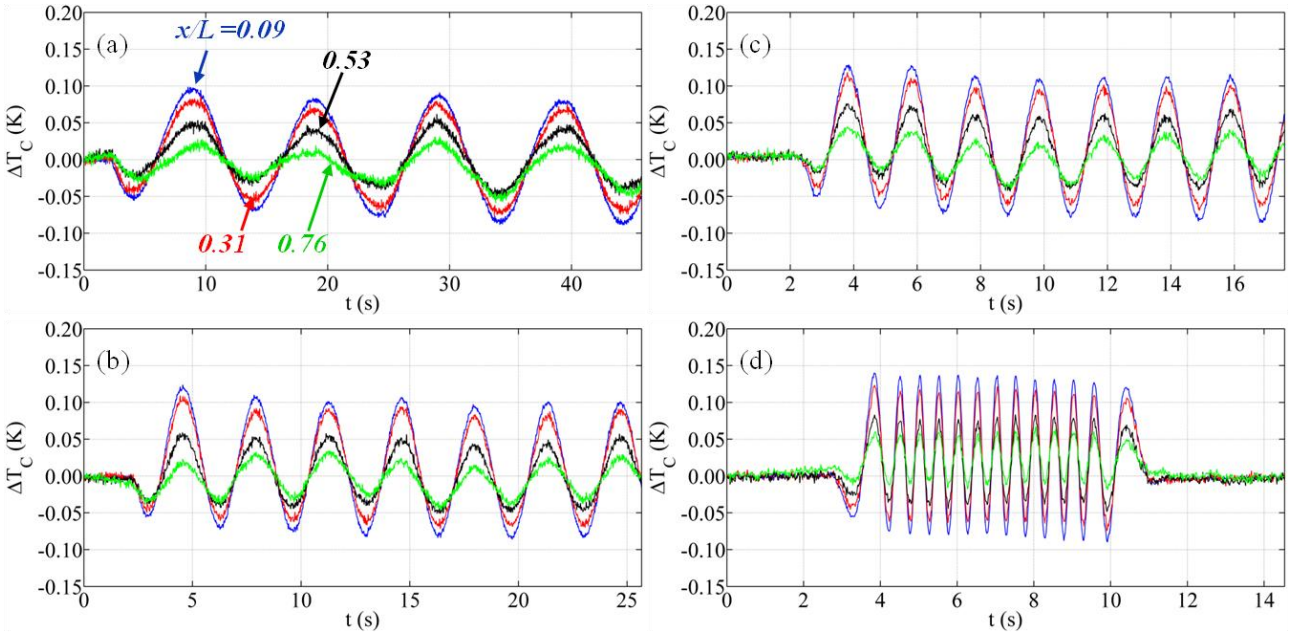

Fig. 4.19. ΔT_C over time for different f_b values: (a) 0.1 Hz, (b) 0.3 Hz, (c) 0.5 Hz, (d) 2.0 Hz. Test with configuration 1 on specimen PLAJ.

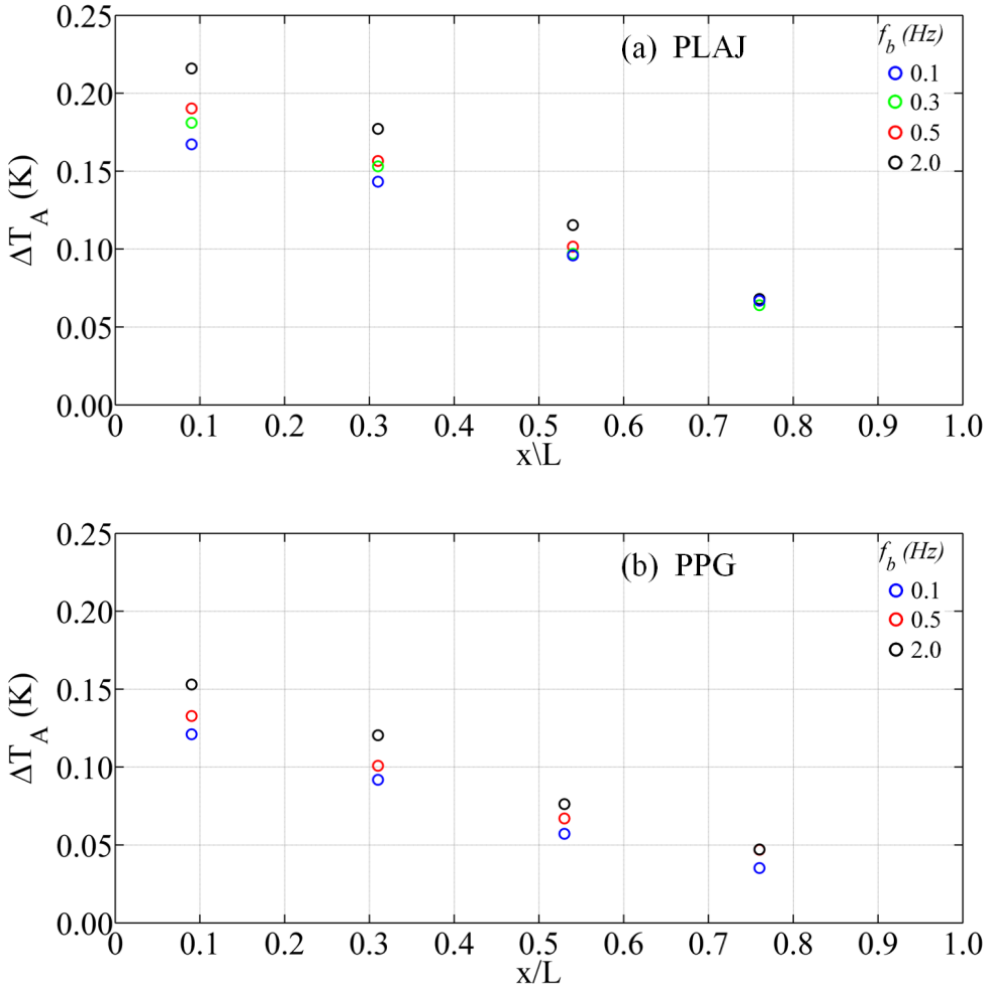

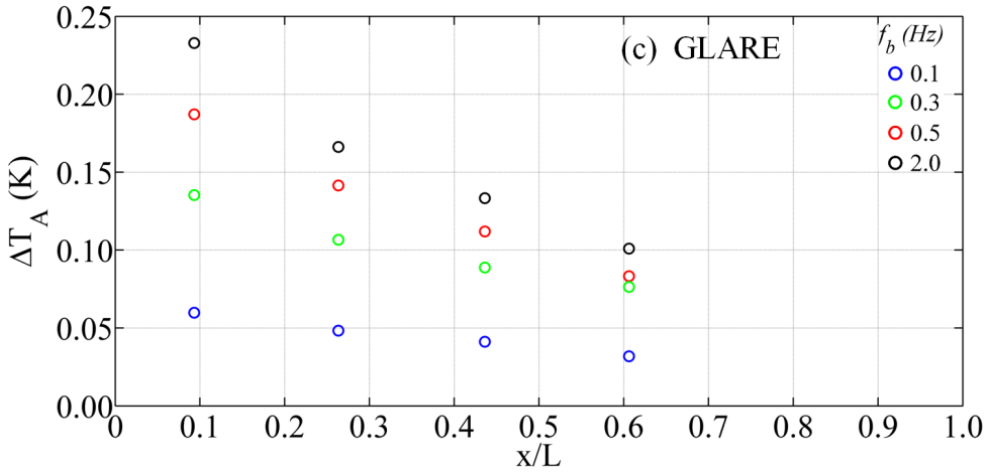

Fig. 4.20. Effect of bending frequency on ΔT_A values for all the investigated specimens (Test configuration 1).

To better investigate the role of the bending frequency in figure 4.21 are reported ΔT_A values versus f_b for x/L=0.09 with the relative interpolation curves; these data are relative to Glare, GFRP and PPG specimens.

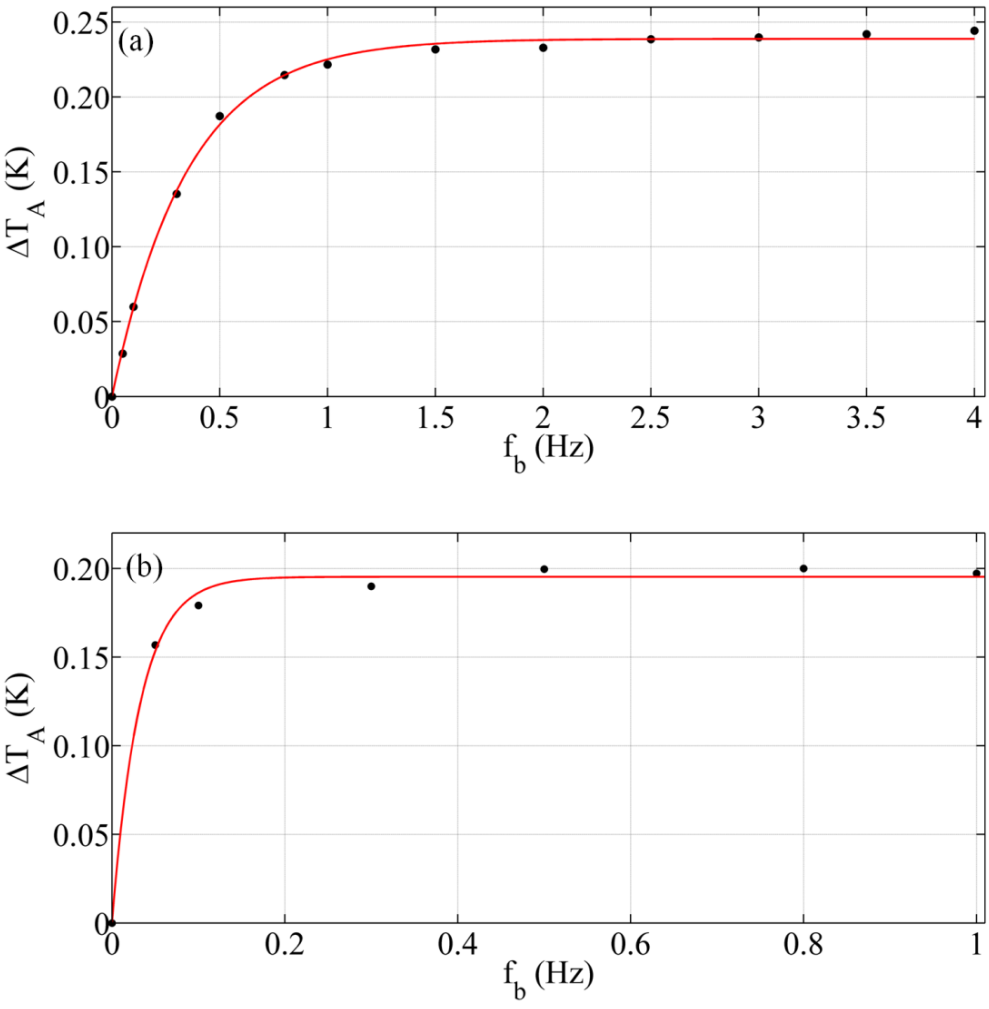

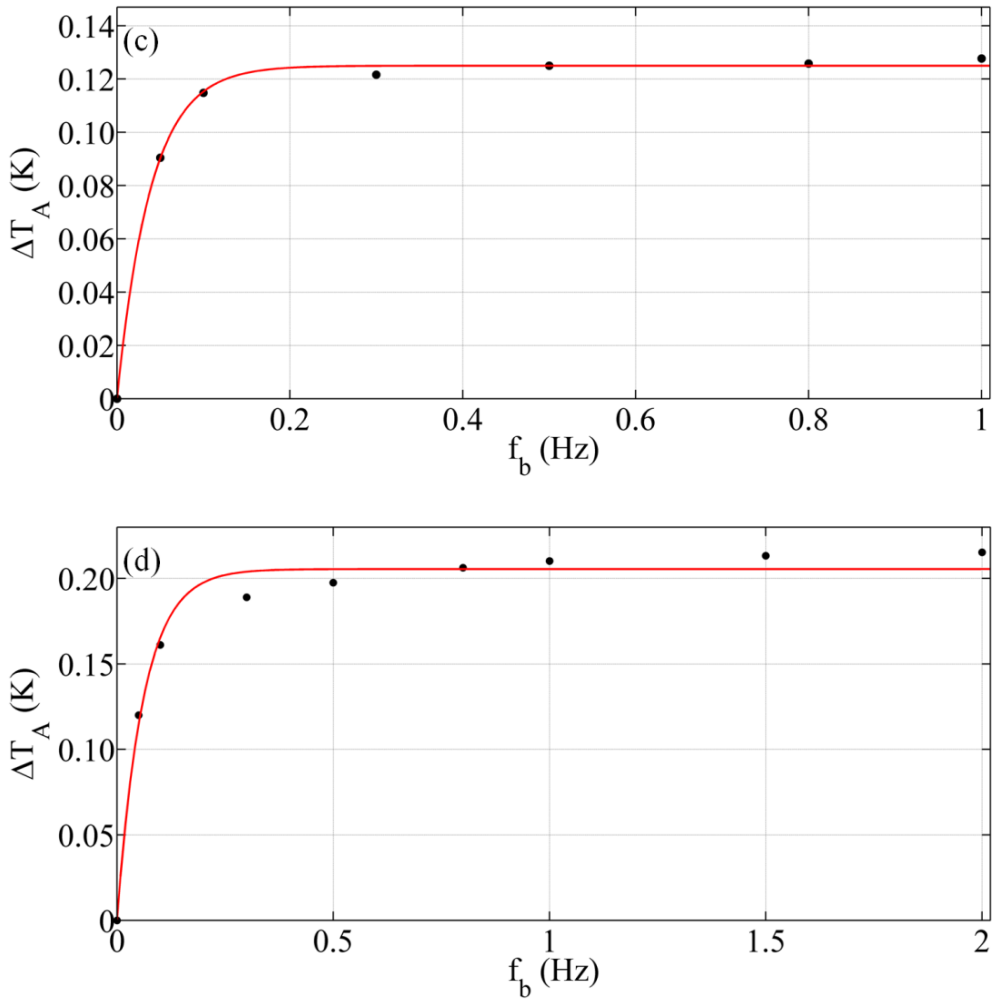

Fig .4.21. ΔT_A against f_b at x/L = 0.09 for GLARE (a), GFRP (b), PPG (c) and PLAJ (d) specimens. (Test configuration 1).

From Fig. 4.21 and by considering also values for others investigated specimens (not shown herein), it seems that the ΔT_A distribution is described by an exponential law:

$$\Delta T_A = a\left(1 - e^{bf_b}\right) \tag{4.13}$$

with a and b, collected in Table 4.2, which seems to depend on the material characteristics. Of course, more tests with a wider number of specimens is necessary to establish a correlation.

Specimen Code	***a*** (K)	***b*** (s)
GLARE	0.2388	-2.857
GFRP	0.1953	-30.740
PPG	0.1250	-25.56
PLAJ	0.2054	-16.33

Table 4.2. Values *a* and *b* relative to Eq. (4.13).

It has been observed that, in all the investigated cases, the bending frequency f_b = 2 Hz guarantees that the horizontal asymptotic value is reached. For this reason, the values of f_b = 2.0 Hz is

considered as the best choice to compare the ΔT_A values of different specimens. For lower values of the bending frequency (f_b = 0.05 Hz ÷ 0.1 Hz) the required adiabatic condition is not guaranteed because there is enough time for the material under investigation to exchange heat with the environment and through its thickness; this may cause a significant reduction of the measured ΔT values. Of course, the minimum value of the bending frequency that allows to perform the cyclic bending tests under adiabatic condition is not the same for all the investigated materials but depends on their thermal diffusivity α, which is defined as:

$$\alpha = \frac{k}{\rho c} \tag{4.14}$$

where k, c and ρ are thermal conductivity, specific heat and density, respectively of the considered material. In general, an average α value has to be considered for composite materials being them composed of fibres and matrix that are characterized by different values of k, c and ρ.

4.7 The effects of the matrix on ΔT values in thermoplastic specimens

In this section, the effects of the matrix on ΔT_A values are analyzed. This is done by considering specimens that include a different matrix reinforced with the same type of fibres. In particular, Fig. 4.22a displays ΔT_A values for four different specimens, which include the same jute fibres, but embedded in a different type of matrix, which is:

- neat polypropylene (PP)
- polypropylene grafted with 2% of maleic anhydride (PC2)
- polypropylene compatibilized with 5% of maleic anhydride (PC5)
- poly lactic acid (PLA)

Instead, Fig. 4.22b displays ΔT_A values for two specimens, which include glass fibres embedded in either a neat polypropylene, or a 2% grafted one. The ΔT_A values, reported in Fig. 4.22 (a) and (b) are obtained with the test configuration 1 and f_b =2 Hz.

From figure 4.22a it is evident that the specimens involving jute fibres embedded in a PLA matrix exhibits higher values of ΔT_A with respect to all the other specimens involving a PP matrix. As second observation by comparing ΔT_A values displayed by a specimen of pure polypropylene (e.g., PPJ) to those involving percentages of 2% (PJC2) and of 5% (PJC5) it is possible to see a systematic increase of ΔT_A with increasing the percentage of compatibilizing agent. For a direct understanding of the influence of the compatibilizing agent, data taken with PP jute reinforced specimens at f_b = 2 Hz are plotted against the percentage of compatibilizing agent C% in Fig.4.23. As can be seen, ΔT_A displays an almost linear increase with C%.

Looking at figure.4.22b, which is relative to PP glass reinforced specimens, it appears that ΔT_A values decrease by increasing the percentage of the coupling agent. This is in contrast with what showed by jute reinforced specimens. The coupling agent seems to have a different effect on ΔT_A values depending on the type of matrix-fibre combination. To better investigate the role played by the coupling agent in specimens involving a PP matrix and to avoid any time-dependent effect, ΔT_A values are extracted from simple bending tests, which practically involve only the ΔT_C values

relative to the first valley as indicated in Fig. 4.24. More specifically, these bending tests are performed by applying to each specimen a simple bending of -7.5 mm, or -15 mm, starting from the unloaded condition. These values, named ΔT_{a1}, are plotted for x/L = 0.09 in Fig. 4.25.

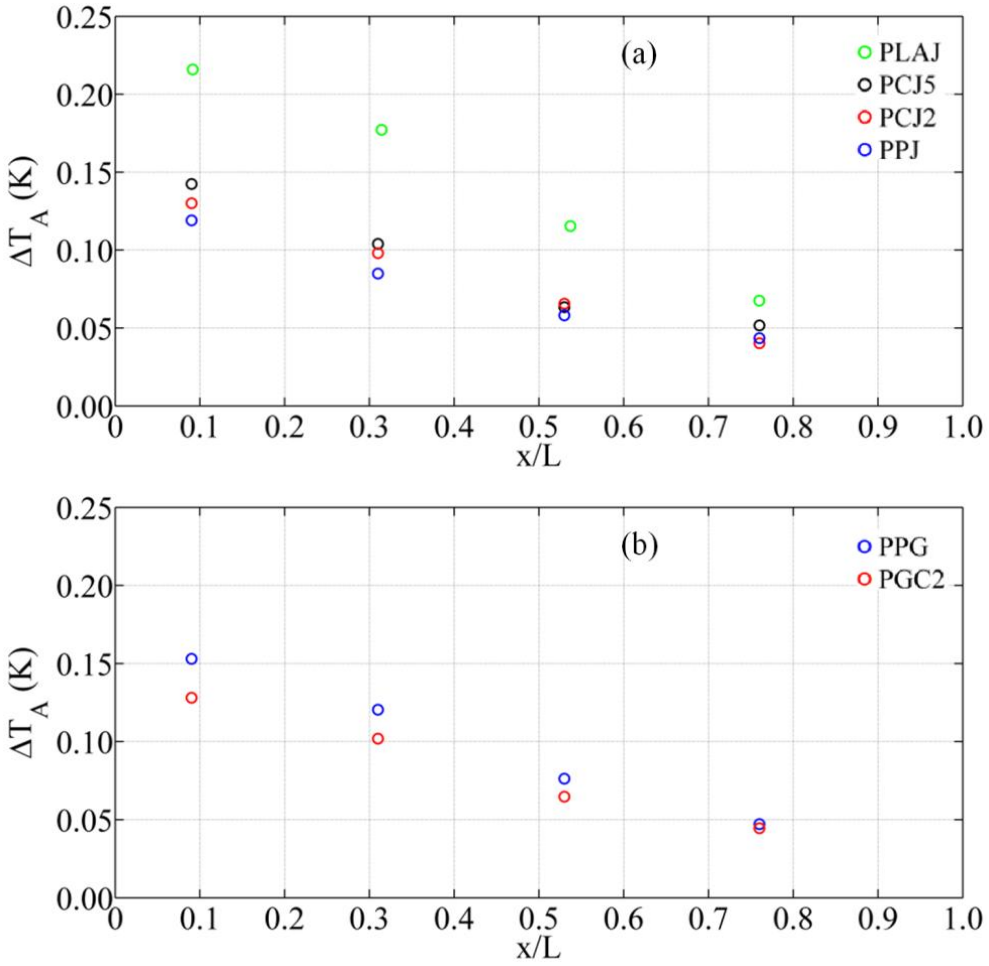

Fig. .4.22. ΔT_A against x/L for different thermoplastic composites; jute fibres reinforced (a) and glass fibres reinforced (b). Results are relative to test configuration 1 and f_b = 2 Hz.

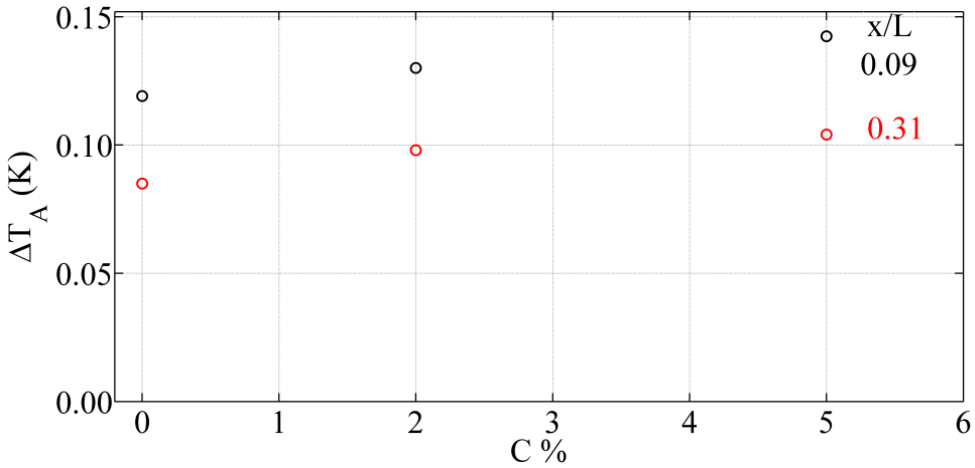

Fig. 4.23. ΔT_A against C% for f_b = 2 Hz for specimens involving PP matrix and reinforced with jute fibres. (Test configuration 1).

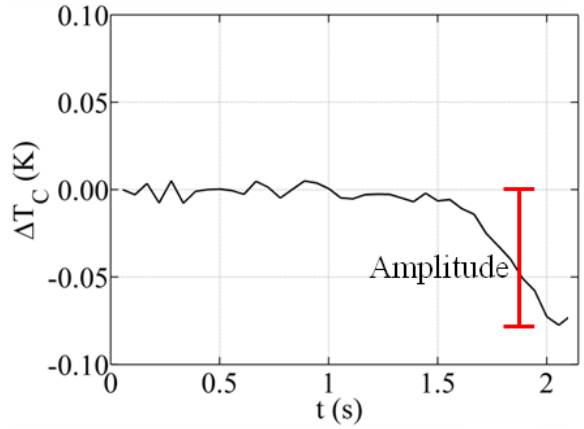

Fig. 4.24. A sketch of calculation of ΔT_{a1}.

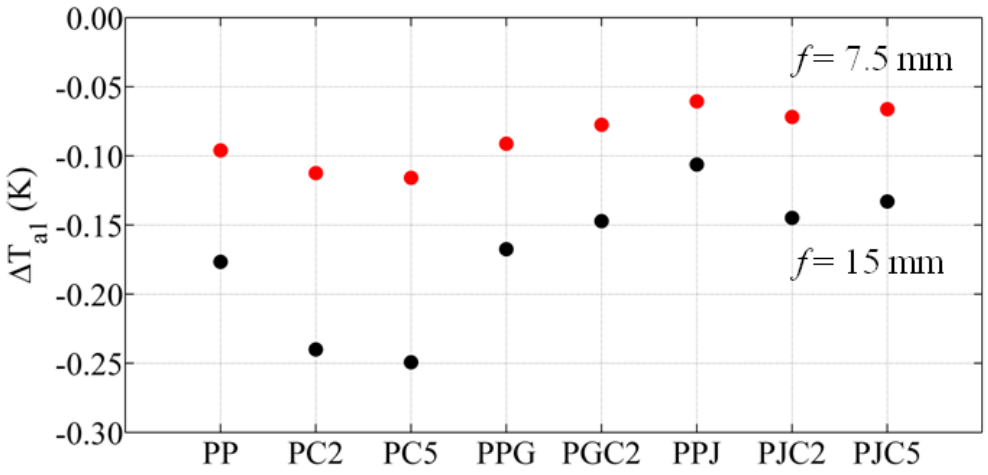

Fig. 4.25. ΔT_{a1} at x/L= 0.09 for the different specimens.

Looking at figure 4.25, it is possible to see that the amplitude (absolute value) attains a maximum for specimens made of sole matrix and a minimum for specimens including jute fibres; for all specimens the ΔT_{a1} amplitude is practically proportional to the imposed deflection. It is also possible to see that the grafted matrix entails increase of ΔT_{a1} only for specimens made of either sole matrix, or, to a certain extent, reinforced with jute fibres. On the contrary, ΔT_{a1} seems to decrease when a grafted matrix is reinforced with glass fibres. In particular, the increase of ΔT_{a1} is more significant in response to the addition of a percentage of 2% rather than to the 5% percentage. In fact, the specimen PC5 displays a smaller ΔT_{a1} increase with respect to the PC2 one, while a small decrease is observed by comparing ΔT_{a1} values of the PJC5 specimen to those of the PJC2 one.

To gain more insights about the role played by matrix and fibres, a comparison between the three types of specimens: sole matrix, reinforced with glass fibres and reinforced with jute fibres is analyzed and results are compared in Fig. 4.26. It is possible to see that the highest values of ΔT_A are achieved by the specimen PP (sole matrix) and the lowest ones by the PPJ (jute fibres); for each specimen, all the points lie over an almost straight band in agreement with the bending moment trend which attains a maximum near the fixture and decreases moving to the free edge. In particular, the distribution of the PPJ specimen appears to display an up and down trend (Fig. 4.27a). These peaks seem to be driven by the fibres texture (Fig. 4.27b.) on the external layer

(viewed by the infrared camera). In fact, the down peaks appear located in correspondence of the vertical jute bundles with amplitude variations linked to the step weaving.

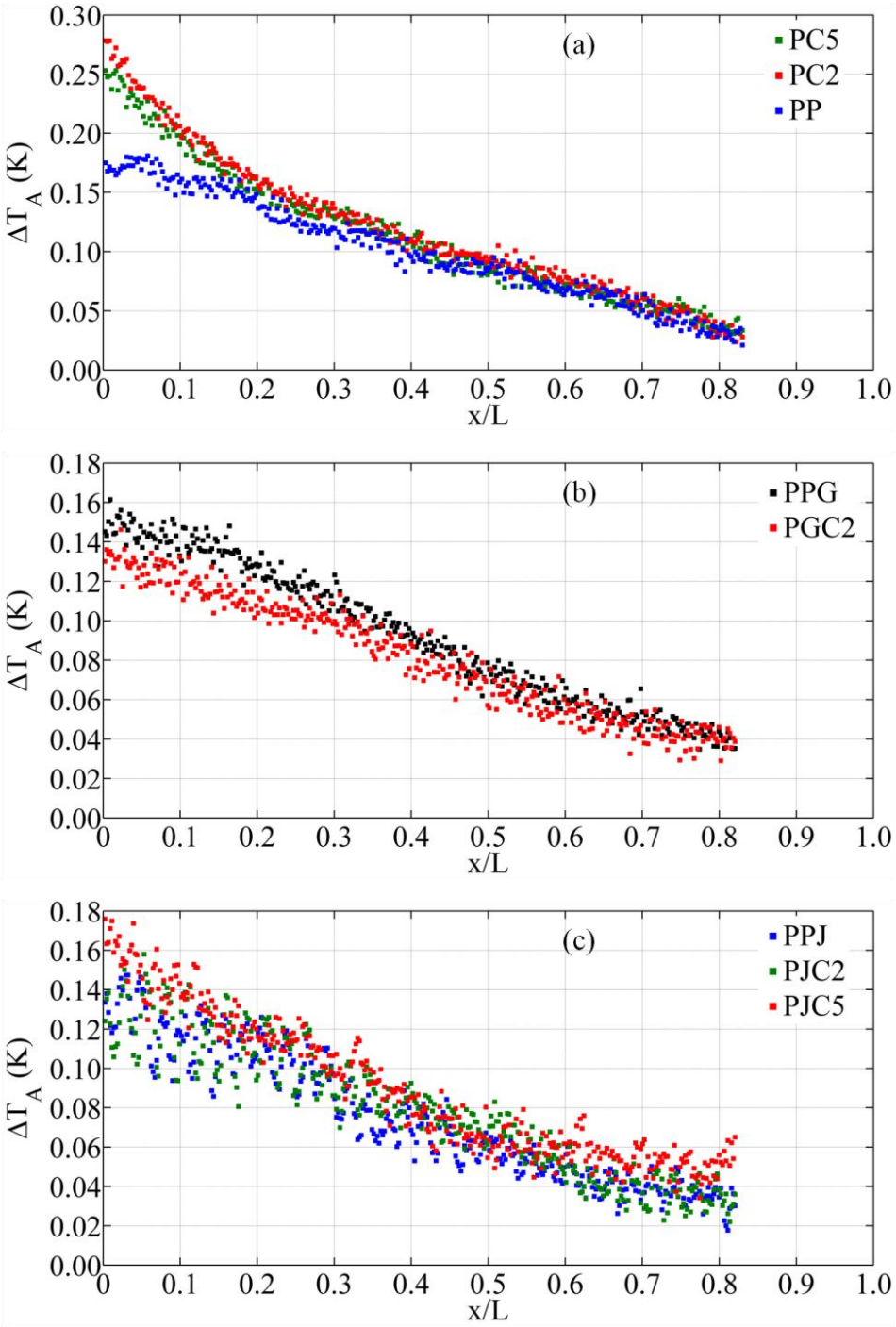

Fig. 4.26. The compatibilizing agent effect on ΔT_A from bending at f_b = 2Hz (Test configuration 1) of different types of specimens and obtained with the WWM method; specimens made of only PP matrix (a); specimens made of PP reinforced with glass fibres (b) and jute fibres (c).

To be more accurate, we have to consider the effect of the jute fibres orientation with respect to the direction of the applied load. In other words, the main difference between ΔT_A ups and down peaks seems to reside in the fact that the down peaks include the average value amongst pixels mostly located all over jute fibres; conversely, the ups peaks include the average value amongst pixels

partly located over jute fibres (horizontal tracts) and partly over the matrix (i.e., the space between two horizontal tracts). Thus, taking into account that, for a given load, it is expected that reinforcing fibres are less deformed than the matrix, the expected reduction of the thermo-elastic effect in correspondence of jute fibres and the increase of the same when the hosting matrix is partially considered can easily explain the detected ups and down trend for ΔT_A values.

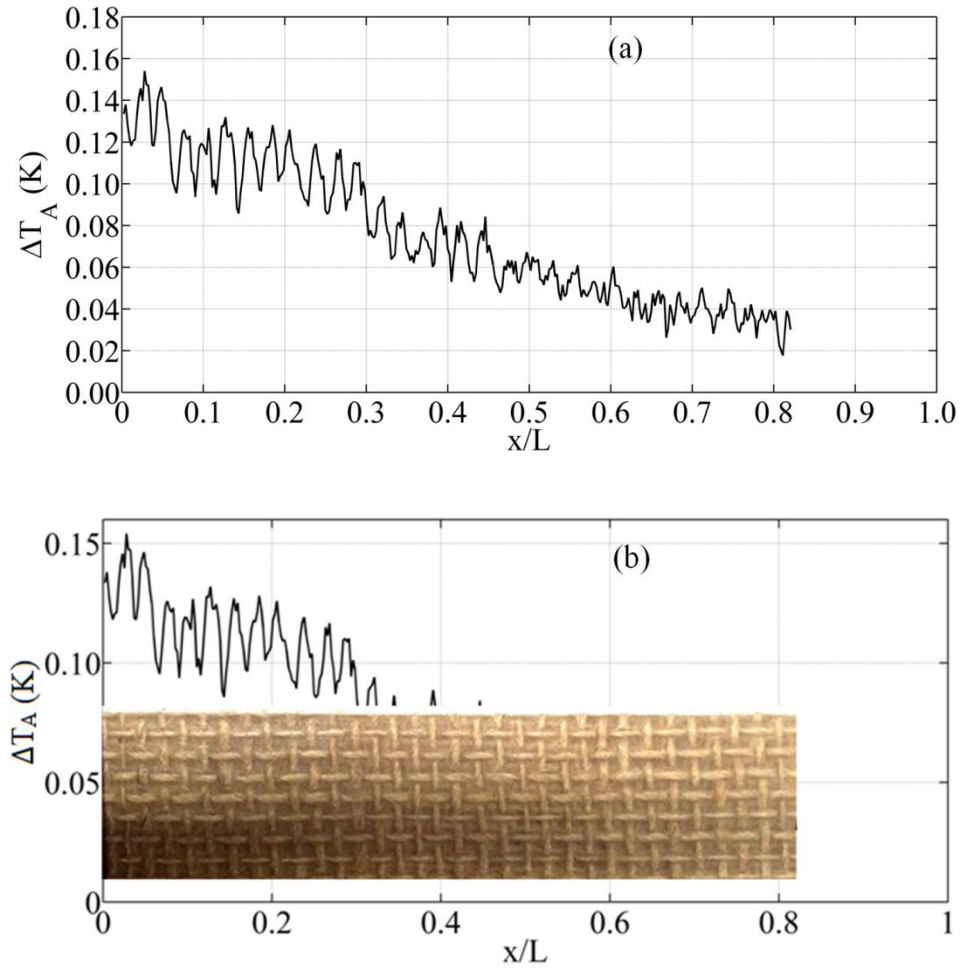

Fig. 4.27. ΔT_A against x/L for PPJ specimen at f_b = 2 Hz: position of ups and down peaks (a) with respect to fibres bundles (b).

The presence of 2% PP-g-MA (Fig. 4.26 a) affects significantly ΔT_A values. In fact, the ΔT_A values of the PC2 specimen (sole matrix) displays a strong rise especially for small x/L values. Instead, to an increase of the PP-g-MA content from 2% to 5% by weight corresponds a decrease of ΔT_A. By comparing Fig. 4.23b to Fig. 4.23c it is possible to see that, as an action of the grafted matrix, the PGC2 ΔT_A distribution has slipped down, while the PJC2 ΔT_A distribution has moved up, displaying an opposite thermal effect.

To deepen such a controversial behaviour we have to focus on two main aspects. One is the action of the coupling agent within the specific matrix/fibre system, which is to improve adhesion between fibres and matrix. The other one is the link between an improved interface (as consequence of matrix grafting) and thermo-elastic effects. However, for a more comprehensive understanding, the thermo-elastic effect, or better the Gough-Joule effect resulting from coupling of thermal and mechanical fields [31,32] should be regarded from the atomic perspective [33]. In other words, it

should be considered the effects that the variations induced by the change of ingredients (addition of PP-g-MA) in a pure matrix material, or at the interface of a composite material, may have on the oscillation of individual particles.

4.8 A comparison between epoxy/resin and PP matrices in glass reinforced specimens.

In this section the results obtained with GFRP, PPG and PGC2 specimens are compared to underline the matrix effect on ΔT values. The specimens under investigation have almost the same thickness and volumetric percentage of glass fibres. As difference between specimens, in PPG and PGC2 the reinforcement consists in plain woven whilst in GFRP unidirectional layers at 0° and 90° are arranged to obtain symmetrical and balanced laminates. This difference in fibres disposition is not so important because a laminate having unidirectional fibres at 0 and 90 degrees can be regarded as a composite material composed of plain woven having the same volumetric percentage of fibres. The main difference consists in the used matrix and then in the interaction between fibre and matrix at the interface. In Fig. 4.28 are reported the ΔT_A values of these specimens obtained with both methods AM (Fig. 4.28a) and WWM (Fig. 4.28b).

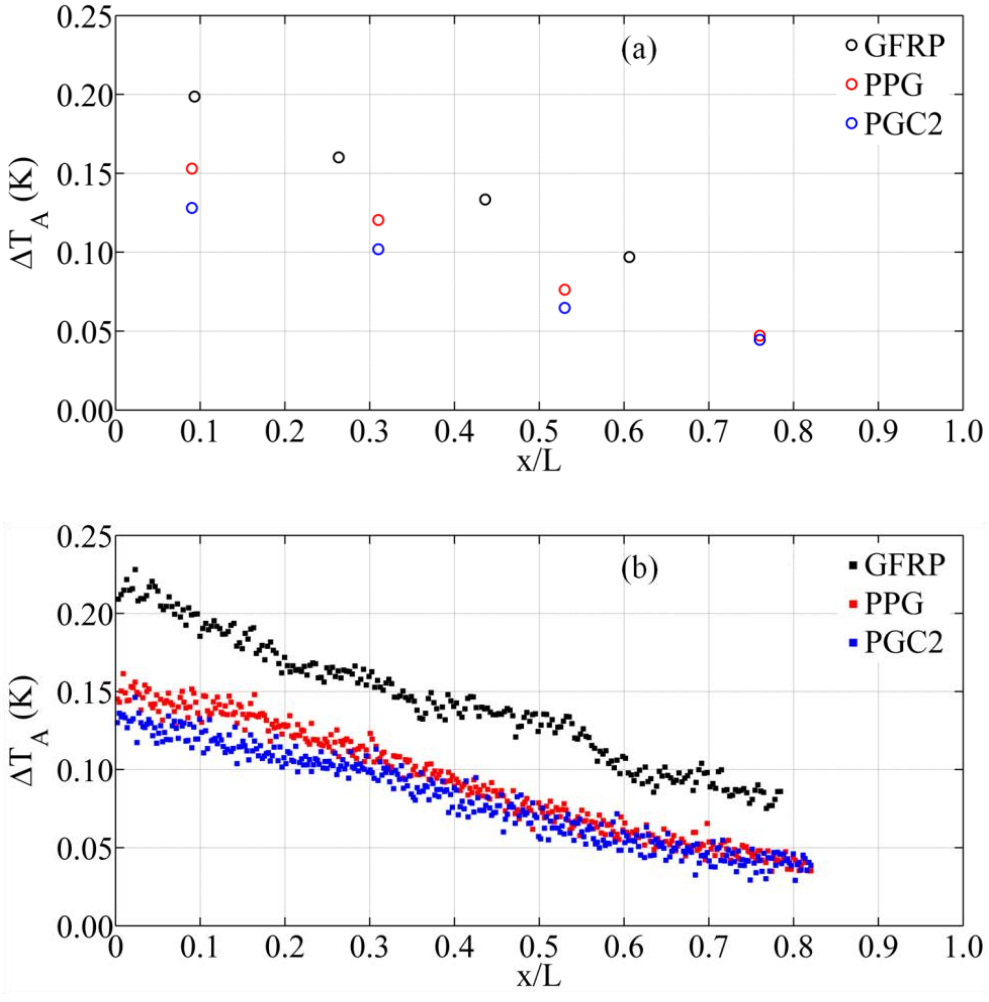

Fig. 4.28. Comparison between ΔT_A values of specimens involving PP and epoxy/resin as matrix for test configuration 1 at f_b = 2 Hz; AM (a) and WWM (b).

From a comparison of ΔT_A values, it is evident the different response of epoxy matrix based specimens, which supply higher values. This is evident especially for data close to the fixture where the ΔT_A values of specimens involving the epoxy matrix are higher of about 0.05 K with respect to the specimens having PP as matrix. This difference, looking at equation 4.8, may be ascribed to a difference of the elastic modulus E that is higher for specimens involving the epoxy matrix.

4.9 The influence of fibres in thermoplastic matrix based specimens

In this section, to gain information about the role played by the fibres on ΔT_A values, the results obtained with specimens involving a neat PP as matrix reinforced with either glass, or jute are compared. Notwithstanding the different thickness of the involved specimens, the obtained results are compared in Fig. 4.29 because some interesting considerations can be made.

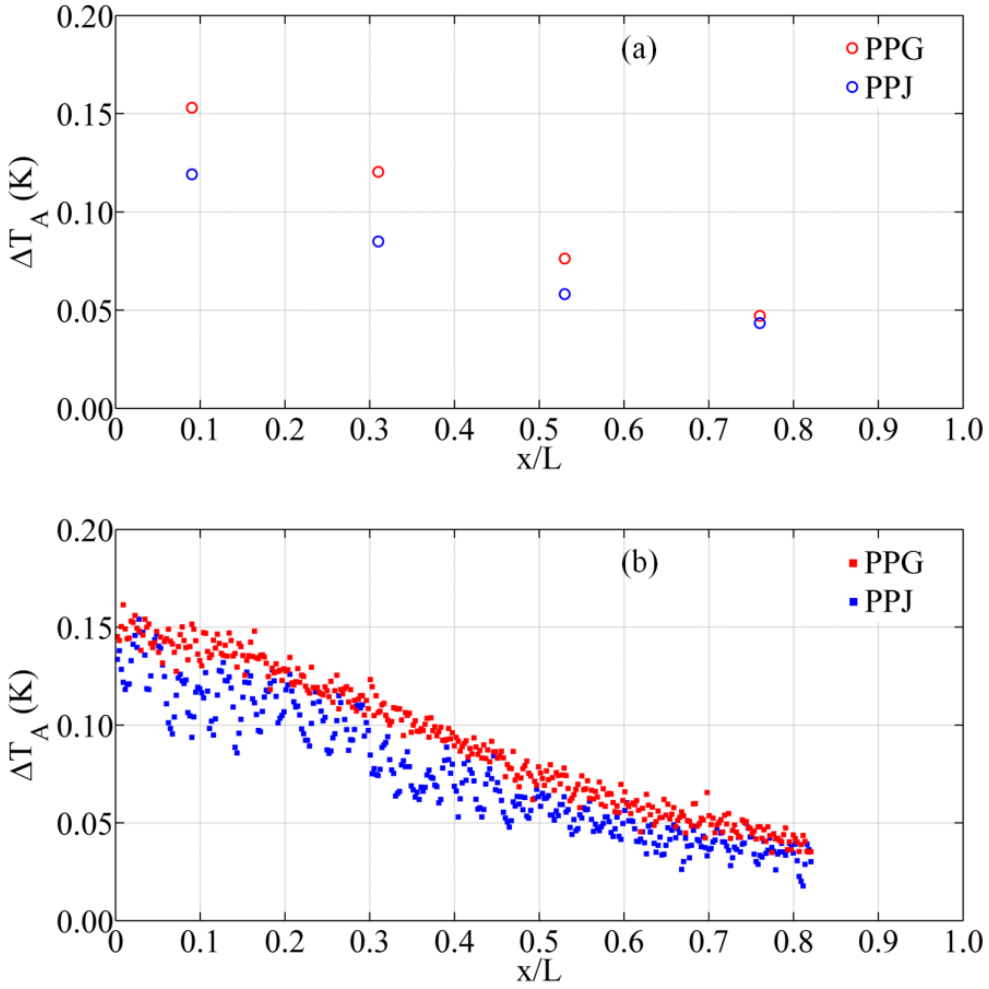

Fig. 4.29. A comparison of results for PPG and PP specimens. (Test configuration 1).

The ΔT_A values for the PPG specimen are higher than those relative to the PPJ specimen; this is probably due to the higher elastic modulus of the glass fibres with respect to that of the jute ones (see Table 1.1 chapter 1). Quantitatively, the difference in terms of ΔT_A is lower (about 0.02 K) with respect to the difference in terms of elastic modulus. This can be explained by considering that the PPG specimen is about 21% thinner than the PPJ one; in fact, from Eq.(4.8) it is possible to see

that ΔT varies linearly with the thickness h. Moreover, the differences in the fibres (glass and jute) affects the thermo-elastic constant K.

4.10 Some bending coupled effects.

All the results till now showed are mostly relative to the test configuration 1 in which the specimen is subjected to alternate tension/compression with a maximum deformation f of ± 7.5 mm. In this section, the results obtained with the two different test configurations (1 and 2) are compared in order to investigate the influence of the test configuration on ΔT values. To this end, the cyclic bending tests performed with $f = \pm 7.5$ mm (configuration 1) are compared with tests performed with f = - 15 mm (configuration 2).
Looking at Eq.(4.3), it is clear that, for a given sample of given E and I values, if the deflection f doubles also the applied concentrate force P doubles.
The results obtained with the different specimens PP, PC2, PPJ, PJC2, PPG, PGC2, at x/L = 0.1 for the bending frequency of 2 Hz are shown in the following figures 4.30 - 4.32.

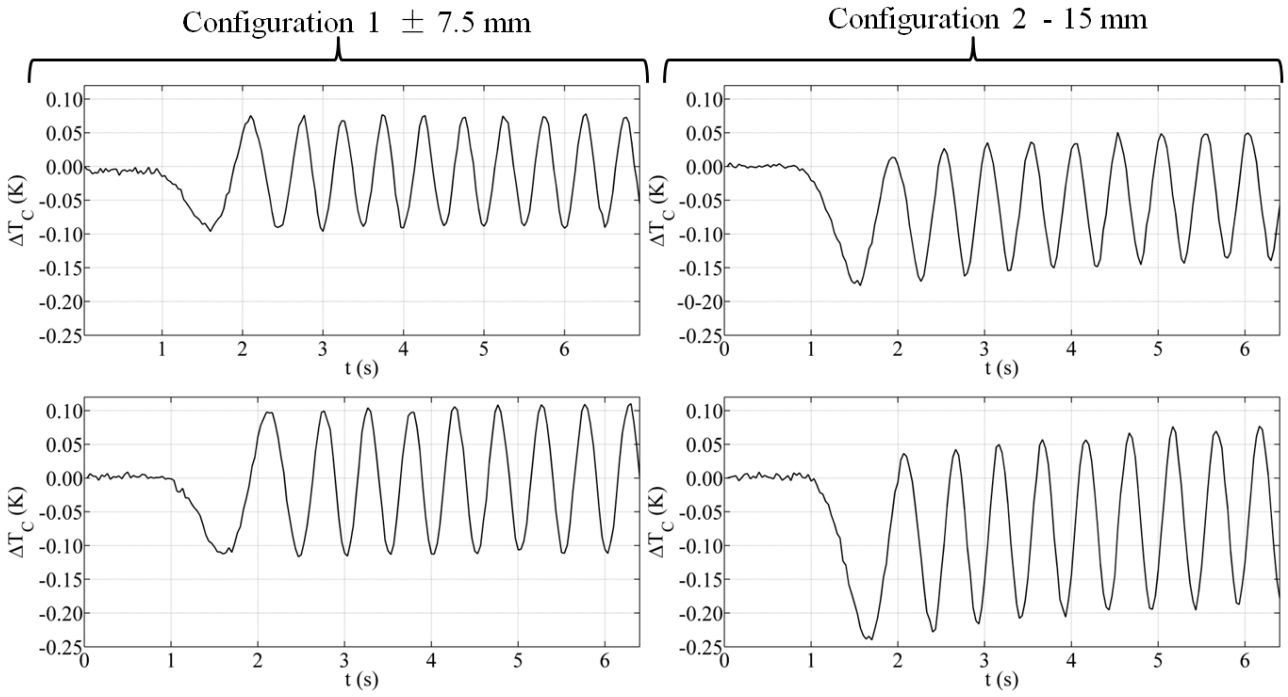

Fig. 4.30. ΔT_C plots at x/L = 0.1 for bending tests performed at f_b = 2 Hz on PP and PC2 specimens; comparison between tests configurations 1 and 2.

First of all, looking at the plots (Figs. 4.30-4.32), it is possible to see that what already observed and discussed in the previous sections for the test configuration 1 generally applies also for the test configuration 2. In particular, also for configuration 2, it is possible to recognize a harmonic trend over time whose frequency is equal to the applied bending frequency f_b. The compatibilizing agent has almost the same influence on the ΔT amplitude already described for each material tested with configuration 1. However, some differences can be observed. First of all, for each specimen under investigation the ΔT signal amplitude is higher for all the tests performed with configuration 2. Moreover, for tests performed with configuration 2, a clear heating up effect can be noticed.

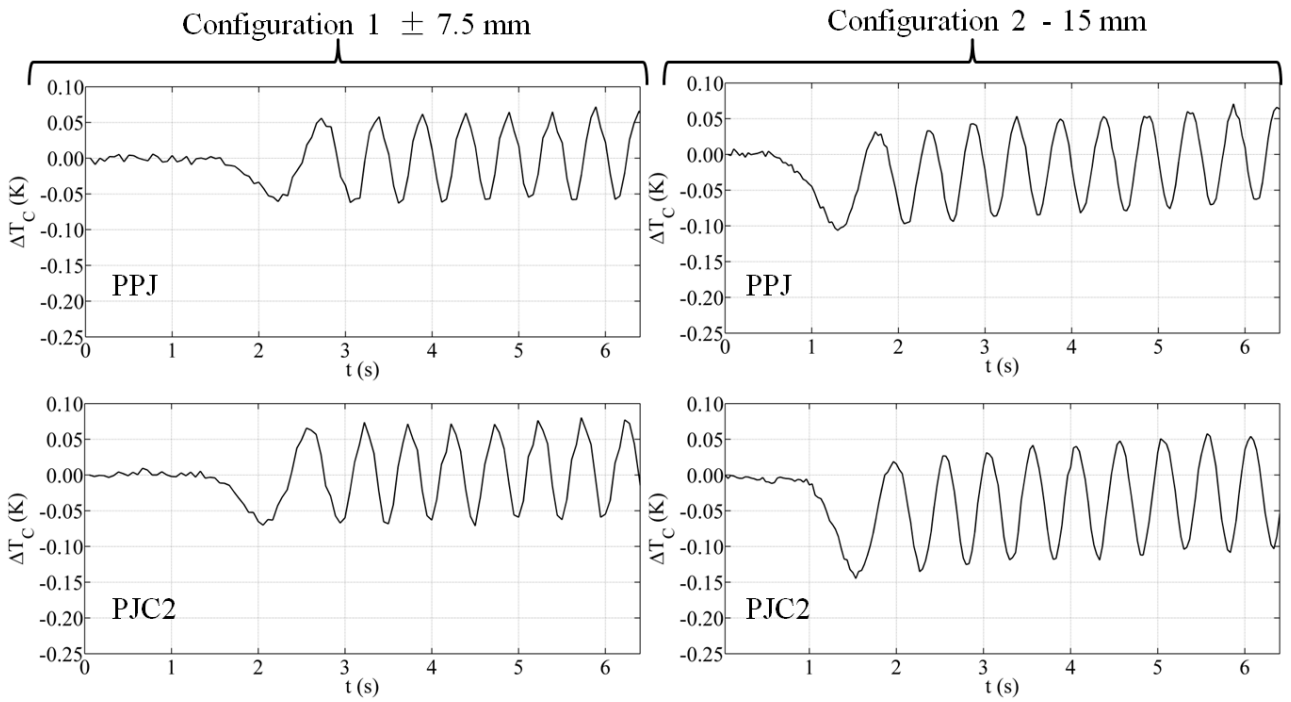

Fig. 4.31. ΔT_C plots at x/L = 0.1 for bending tests performed at f_b = 2 Hz on PPJ and PJC2 specimens; comparison between tests configurations 1 and 2.

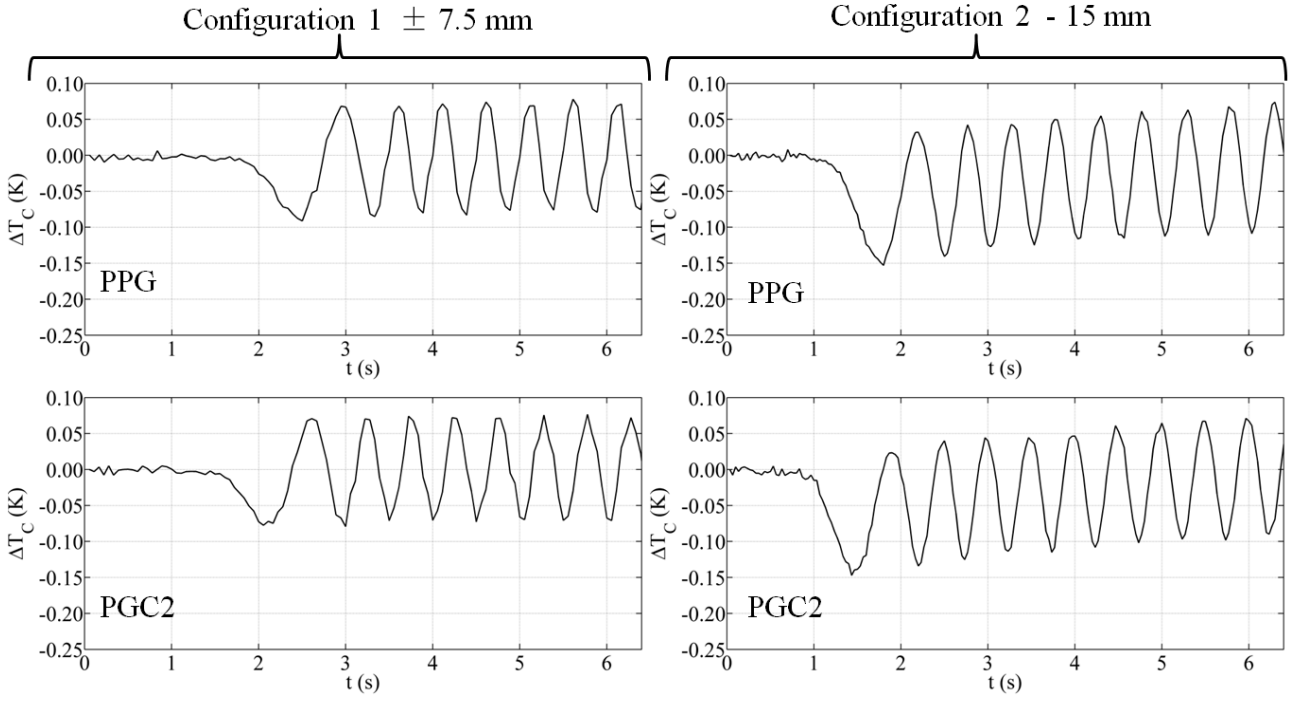

Fig. 4.32. ΔT_C plots at x/L = 0.1 for bending tests performed at f_b = 2 Hz on PPG and PGC2 specimens; comparison between tests configurations 1 and 2.

In particular, for all the tests performed by means of configuration 2, ΔT_A increases with the number of cycles enclosed. This difference may be due to the different test dynamic. In fact, in configuration 2 the specimen is subjected to a one side deflection of 15 mm which is higher with respect to the 7.5 mm undergone on the same side under test configuration 1; this of course entails also higher internal stresses. Moreover, in configuration 1 the observed surface is subjected to

alternate tension and compression conditions that causes ΔT variations from negative to positive values, which may reduce the total ΔT amplitude. It is also worth noting that, in configuration 2, the observed surface is subjected only to tension conditions that should cause only cooling linked to the thermo-elastic effect. Instead, as already mentioned, even if the applied deflection remains constant, ΔT tends to increase; this effect appears sudden after the first cycle, when the ΔT value does not return to 0 as it should be, but becomes positive, with the specimen surface recovering its undeformed condition. In addition, there is a positive increment of the ΔT amplitude after any cycle of load as can be seen in Fig. 4.30-4.32 for test configuration 2. Besides, after a certain number of cycles, only positive ΔT values are displayed as Fig. 4.33 shows.
It is clear that, as the distance from the fixture increases, the bending moment and the internal stresses remain not constant along the beam but they decrease with the distance. Also, the afore mentioned heating up effect decreases along the beam as shown in Fig. 4.33 in which ΔT signals measured at three PM points along a PPG specimen for f_b = 2 Hz (x/L = 0.1, 0.3, 0.5) are reported. This may be explained by considering that the dissipated energy depends on internal stresses as will be later explained.

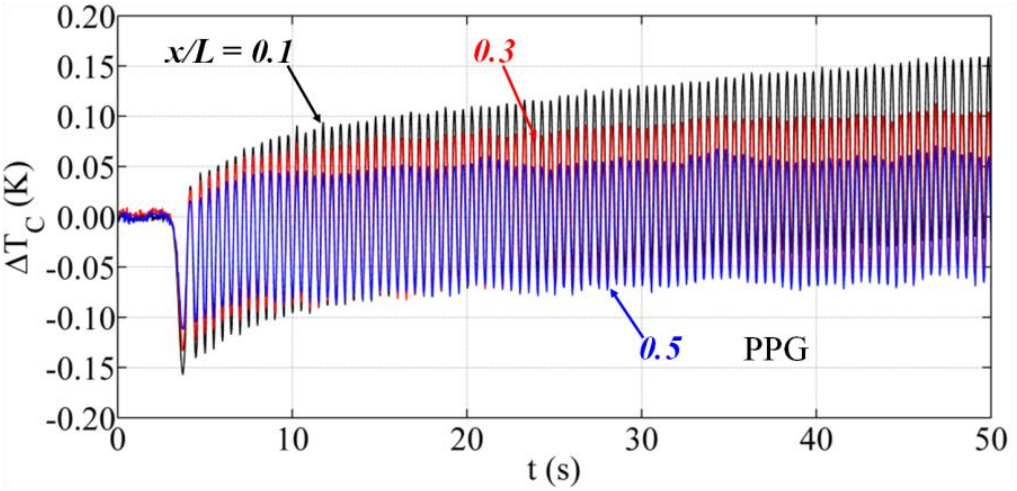

Fig. 4.33. Heating up effect for varying the distance from the fixture
for specimen PPG under bending configuration 2

4.10.1 Some considerations about the heating up effects

The polymeric materials, especially the thermoplastic ones at temperature over the glass transition one T_g, show a visco-elastic behaviour [34,35] rather than a pure elastic one like metals. The polymeric materials, even if solicited in elastic conditions, dissipate a little amount of energy, which is due to the internal friction between the polymeric macromolecules chains that, under deformation, tend to move respectively. In composite materials, the internal energy dissipation is not only due to the macromolecules interactions, but also to the friction at the interface between the fibres and matrix. Of course, the higher is the total displacement f imposed to the specimen, higher is the internal friction and much more important are the dissipative effects and in turn the dissipated energy with temperature rise.
In particular, close to the clamp, where the stresses are the highest, the macromolecules, constituting the matrix, are subjected to higher viscous interactions. Here, the relative displacement attains a maximum, which promotes the dissipative phenomena and in turn temperature rise. Going

far from the fixture there is a gradual reduction of internal stresses with in turn a reduction of displacement and dissipative phenomena and in turn lower temperature rise.
Of course, after each cycle of load, a small amount of energy is released by the dissipative phenomena with an addition effect; this may justify the observed drift warming up effect in configuration 2. In truth, this heating up effect is present also for bending tests in configuration 1, but of reduced slope; indeed, this heating up effect becomes distinguishable only after a consistent number of consecutive cycles of load (Fig. 4.34).

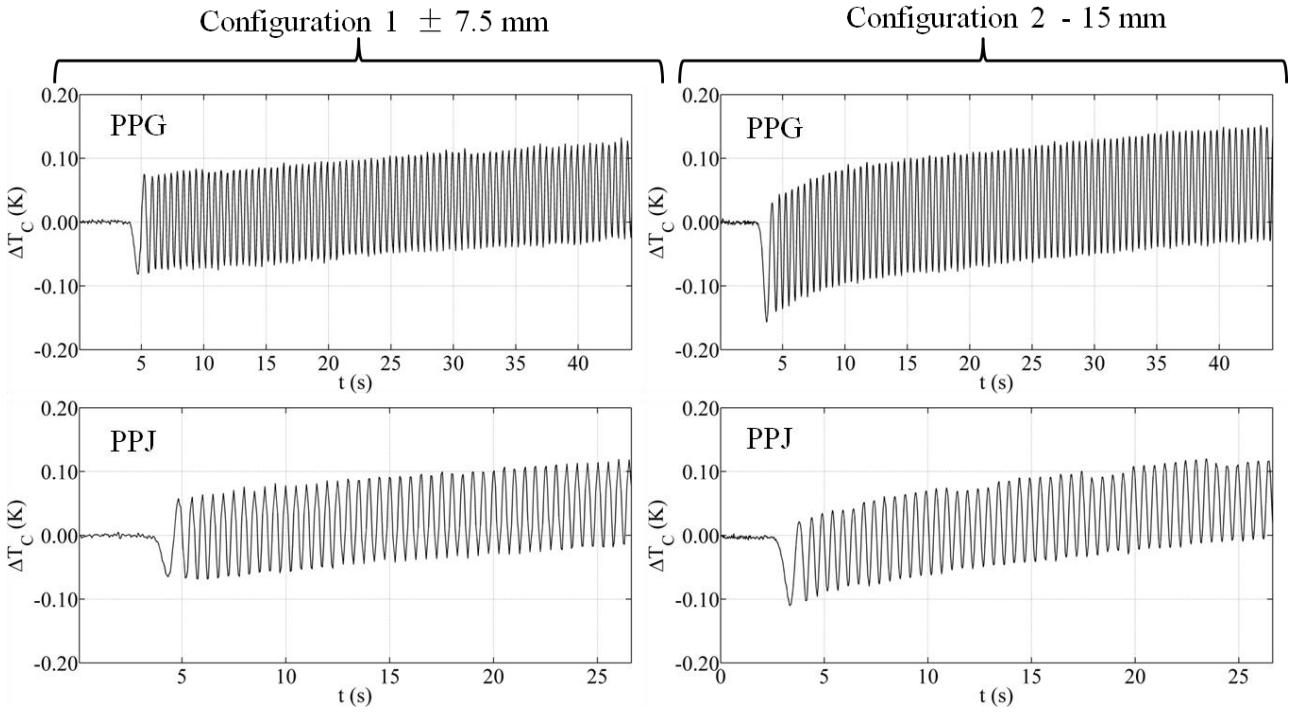

Fig. 4.34. ΔT_C plots at x/L = 0.1 for bending tests performed at f_b = 2 Hz with configurations 1 and 2 on PPG and PPJ specimens.

Comparing the results obtained with the two test configurations 1 and 2 (Fig. 4.34), it is evident that the slope of the heating up effect is higher for tests performed with configuration 2. Besides, for all the tests performed by means of configuration 1, the heating up effect manifests itself like a ramp having a small slope just starting from the first cycle. Whilst, in configuration 2, the heating up effect starts with an abrupt increase which is later, after about 5s, followed by a gradual ramp. These differences in the heating up effect observed for bending configurations 1 and 2 may mean that something different is occurring inside the material when it is subjected to the different load conditions.
In particular, focusing the attention on the bending configuration 2, the change in slope would mean that initially, within the first few cycles, the amount of dissipated energy coupled with viscous phenomena attains its maximum and then it decreases towards an almost constant value.

4.10.2 The influence of bending frequency on the heating up effect

It is well known that the visco-elastic behaviour of a material depends on the solicitation frequency [34,35]. In this section, the dependence of the heating up effect from the bending frequency is investigated for specimens involving the PP matrix. In particular, some ΔT plots at x/L = 0.1,

obtained with bending configuration 2 on specimens PPG and PPJ are shown in Fig. 4.35. To allow for a comparison, only five consecutive cycles of load are considered for each material; this because at low f_b values, data for only few cycles of load have been acquired, to avoid computer memory overhead.

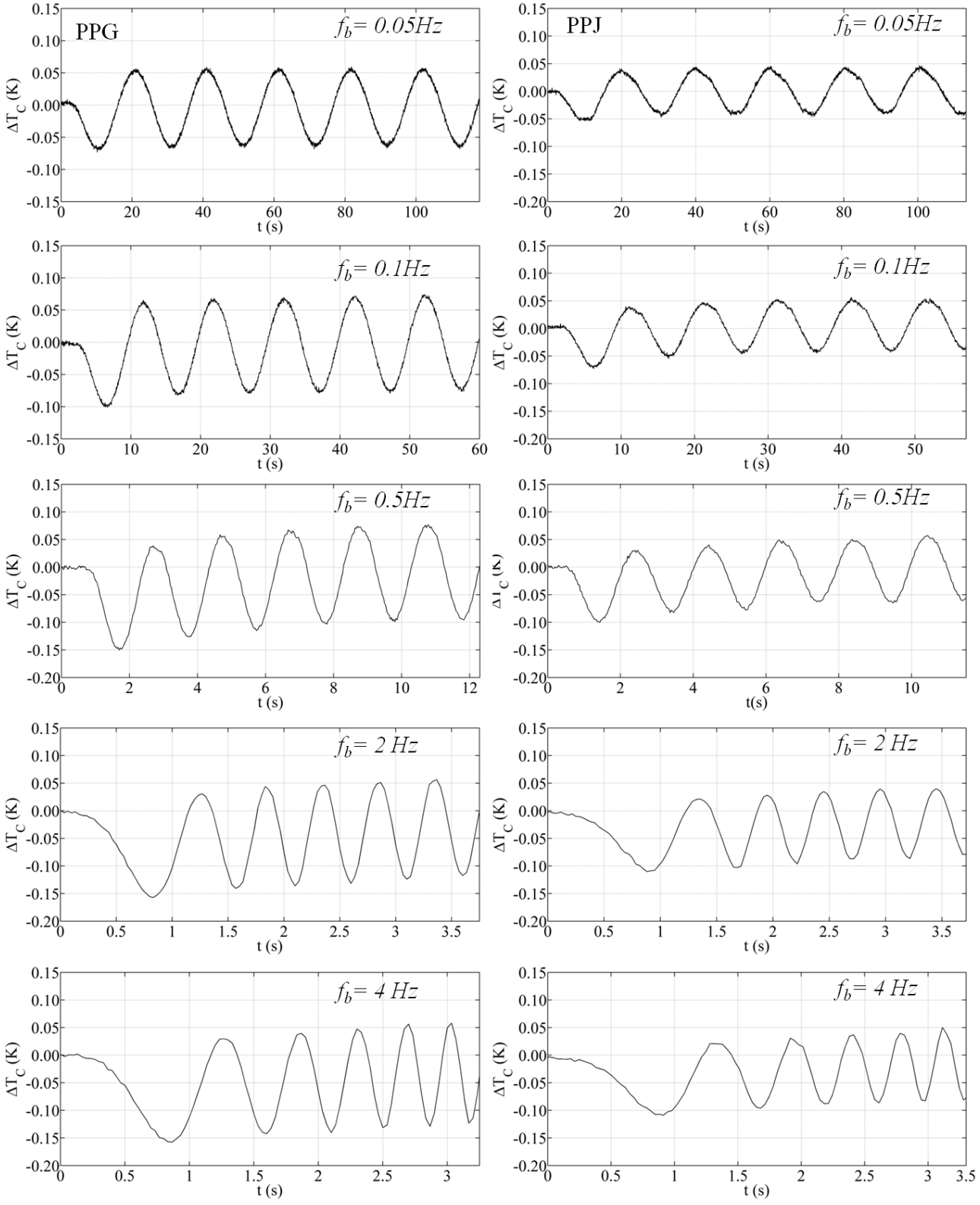

Fig. 4.35. The effect of the bending frequency f_b on the heating up effect for test performed on PPG (left) and PPJ (right) in configuration 2.

Looking at the plots of Fig. 4.35 it is possible to underline some differences relative to the heating up effect with the bending frequency. In both of the cases for low values of the bending frequency (f_b = 0.05 and f_b = 0.1 Hz) the ΔT signals are almost symmetric with respect to the 0 value; this happens also when the bending is performed by means of configuration 2. This experimental evidence might seem strange because in bending configuration 2 the observed surface undergoes only tension and then, the cooling effect should prevail. Instead, for these values of f_b the ΔT signal appears almost symmetric with respect to 0 with its average value remaining almost equal to about 0 over time. This behaviour may be explained by considering that for low values of the bending frequency the adiabatic condition is not fulfilled and the material under investigation has enough time to exchange heat through its thickness and with the environment. Of course, it is worth underlining that as f_b increases the required adiabatic condition becomes ever more verified.

4.11 Some remarks to Chapter 4

As a main comment, the Reference Area Method has proved to be very effective in restoring all the measured ΔT signals even when they were completely destroyed by the temporal noise.
For all the investigated materials ΔT attains its maximum value near the fixture and decreases linearly to 0 at the free tip in agreement with the bending moment. In particular, the ΔT amplitude depends on the bending frequency f_b and it tends to assume a constant value for bending frequencies equal to 2 Hz, or higher. This because the hypothesis of cyclic adiabatic condition for low f_b values is not fulfilled.
Besides, it has been noticed that the ΔT amplitude depends on the type of material employed, meaning the type of matrix and/or reinforcement and on the likely presence of coupling agent, which drives the internal stresses.
An heating up "ramp" effect has been observed mainly in thermoplastic matrix based materials and especially for bending tests performed in configuration 2. This is due to materials internal dissipations linked to viscoelastic effects and friction at the interface between the fibres and matrix. Furthermore, the slope of the ramp seems to be dependent on the distance from the fixture, the bending frequency and the material under investigation.

References to chapter 4

[1]. W. Thomson, On the thermoelastic, thermomagnetic and pyroelectric properties of matters. Phil Mag 5, 4–27, 1978.
[2]. M.A. Biot, Thermoelasticity and irreversible thermodynamics. J Appl Phys,27, 240–53, 1956.
[3]. J.M. Dulieu-Barton, P. Stanley, Development and applications of thermoelastic stress analysis. J Strain Anal, 33, 93–104, 1998.
[4]. P. Stanley, W.K. Chan, The application of thermoelastic stress analysis to composite materials. J Strain Anal, 23, 137–42, 1988.
[5]. U. Galietti, D. Modugno, L. Spagnolo, A novel signal processing method for TSA applications. Meas Sci Technol, 16, 2251–60, 2005.
[6]. T.R. Emery, J.M. Dulieu-Barton, J.S. Earl, P.R. Cunningham, A generalised approach to the calibration of orthotropic materials for thermoelastic stress analysis. Compos Sci Technol, 68, 743–522, 2008.
[7]. M.G. Beghi, C.E. Bottani, G. Caglioti, Irreversible thermodynamics of metals understress. Res Mech, 19, 365–79, 1986.
[8]. M.P. Luong Fatigue limit evaluation of metals using an infrared thermographic technique. Mech Mater, 28, 155–63, 1998.

[9]. S. Boccardi, G.M. Carlomagno, C. Meola, G. Simeoli, P. Russo, Infrared thermography to evaluate thermoplastic composites under bending load, Composite Structures, 134, 900-904, 2015.
[10]. C. Meola, G.M. Carlomagno, C. Bonavolontà, M. Valentino, Monitoring composites under bending tests with infrared thermography, Adv. Opt. Technol. 2012, 7 p. 2012.
[11]. S. Boccardi Master Thesis,Termografia all'infrarosso nel monitoraggio di materiali compositi sotto carico di flessione, 2013.
[12]. S. Boccardi, G.M. Carlomagno, C. Bonavolontà, M. Valentino, C. Meola, Infrared thermography to monitor Glare® under cyclic bending tests with correction of camera noise, in: Proc. QIRT 2014, Bordeaux, France, July 2014, pp. 7-11 paper 215.
[13]. L. Sorrentino, G. Simeoli, S. Iannace, P. Russo, Mechanical performance optimization through interface strength gradation in PP/glass fibre reinforced composites, Composites Part B, 76, 201-208, 2015.
[14]. P. Russo, G. Simeoli, D. Acierno, V. Lopresto, Mechanical properties of virgin and recycled polyolefin-based composite laminates reinforced with jute fabric, Polymer Composites 36, 2022-2029, 2015.
[15]. H.A. Rijsdijk, M. Contant, A.A.J.M. Peijs, Continuous-glass-fibre-reinforced polypropylene composites: I. Influence of maleic-anhydride-modified polypropylene on mechanical properties, Compos. Sci. Technol., 48, 161–172, 1993.
[16]. E. Mäder, H.J. Jacobasch, K. Grundke, T. Gietzelt, Influence of an optimized interphase on the properties of polypropylene/glass fibre composites, Compos. Part A 27, 907–912, 1996.
[17]. K.L. Pickering, M.G. Aruan Efendy, T.M. Le, A review of recent developments in natural fibre composites and their mechanical performance, Compos. Part A 83, 98-112, 2016.
[18]. S.M.B. Nachtigall, G.S. Cerveira, and S.M.L. Rosa, New polymeric-coupling agent for polypropylene/wood-flour composites, Polym.Test., 26, 619-628, 2007.
[19]. M. Sain, P. Suhara, S. Law, and A. Bouilloux, Interface modification and mechanical properties of natural fiber-polyolefin composite products, J. Reinf. Plast. Compos., 24, 121-130, 2005.
[20]. M. Van den Oever, T. Peijs, Continuous-glass-fibre-reinforced polypropylene composites II. Influence of maleic anhydride modified polypropylene on fatigue behavior. Compos Part A, 29, 227-239, 1998.
[21]. D. Bikiaris, P. Matzinos, A. Larena, V. Flaris, C. Panayiotou, Use of silane agents and poly(propylene-g-maleic anhydride) copolymer as adhesion promoters in glass fibre/polypropylene composites. J Appl Polym Sci, 81, 701-709, 2001.
[22]. L. Sorrentino, G. Simeoli, S. Iannace, P. Russo; Mechanical performance optimization through interface strength gradation in PP/glass fibre reinforced composites, Composites part B, 76, 201-208, 2015.
[23]. P. Russo, G. Simeoli, D. Acierno, V. Lopresto, Mechanical Properties of Virgin and RecycledPolyolefin-Based Composite Laminates Reinforced With Jute Fabric, Polymer Composites, 36, 2022-2029, 2015.
[24]. M.A. Kha, G. Hinrichsen, L.T. Drzal, Influence of novel coupling agents on mechanical properties of jute reinforced J. Mater. Sci. Lett., 20, 1711-1713, 2001.
[25]. A.H. Haydaruzzaman, M.A. Khan, A. Hossain Mubarak, A. Khan Ruhul, M.A. Khnn Hakim, Fabrication and Characterization of Jute Reinforced Polypropylene Composite: Effectiveness of Coupling Agents, J. Comp. Mater., 44, 1945-1963, 2010.
[26]. S. Boccardi, C. Meola, G.M. Carlomagno, L. Sorrentino, G. Simeoli, P. Russo, Effects of Interface Strength Gradation on Impact Damage Mechanisms in Polypropylene/Woven Glass Fabric Composites, Composites Part B: Engineering, 90, 179-187, 2016.
[27]. S. Boccardi, G.M. Carlomagno, C. Meola, G. Simeoli, D. Acierno, S. Iannace, L. Sorrentino, P. Russo, Lock-In Thermography (LT) for Investigation of Impact Damage Hibrid Polypropylene/Glass composite, IEEE A&E System Magazine, 2016.
[28]. G. Simeoli, D. Acierno , C. Meola , L. Sorrentino, S. Iannace, P. Russo, The role of interface strength on the low velocity impact behaviour of PP/glass fibre laminates, Composites: Part B, 62,88-94, 2014.
[29]. ASTM D747 − 10, Standard Test Method for Apparent Bending Modulus of Plastics by Means of a Cantilever Beam.
[30]. S. Boccardi, G.M. Carlomagno, C. Meola, G. Simeoli, P. Russo, Visualization of Thermal Effects in Polypropylene-Based Composites under Cyclic Bending Tests, International Symposium on

Dynamic Response and Failure of Composite Materials, DRAF 2016, Procedia Engineering, 167, 71-79,2016.
[31]. J. Gough, Memoirs of the Literary and Philosophical Society of Manchester, Second series 1, 288 1805.
[32]. J.P. Joule, On Some Thermo-Dynamic Properties of Solids, Phil. Trans. Roy. Soc. London 149, 91-131, 1859.
[33]. B. Schweizer, J. Wauer, Atomistic explanation of the Gough-Joule-effect, The European Physical Journal B, 23, 383-390, 2001.
[34]. J.D. Ferry, Viscoelastic Properties of Polymers, 1980, 3° edition, Wiley ISBN 978-0-471-04894-7.
[35]. H.F. Brinson, L.C. Brinson, Polymer Engineering Science and Viscoelasticity Springer, New York, 2015, ISBN: 978-1-4899-7484-3.

Chapter 5
Impact tests

Nomenclature

A_h	Warm area.
D_A	Impact damage measured along the +45° direction.
D_{av}	Impact damage average diameter.
D_B	Impact damage measured along the -45° direction.
D_H	Impact damage measured along the horizontal direction.
D_V	Impact damage measured along the vertical direction.
E	Impact Energy.
E_a	Total impact energy absorbed by the specimen.
E_b	Amount of the impact energy absorbed as bending energy by the specimen.
E_d	Amount of the impact energy absorbed as damage energy by the specimen.
E_{db}	Amount of E_d used for fibre breakage.
E_{dd}	Amount of E_d used for delamination.
E_m	Amount of the impact energy absorbed as membrane energy by the specimen.
f	Lock-in heating frequency.
F_R	Infrared camera frame rate.
i	Row index.
j	Column index.
K	Frame number denoting the generic ΔT image in the sequence immediately after the end of the cooling down effect
N	Number of pixels having a given value of ΔT.
p	Dept starting from the material surface.
P_h	Number of pixels affected by the heating-up effect due to the impact.
s_r	Spatial resolution.
t	Image index in the sequence or time.
t_p	Time to reach the ΔT_{Min}.
T	Temperature.
x	Spatial coordinate along the horizontal direction.
y	Spatial coordinate along the vertical direction.

Greek Symbols.

α	Thermal diffusivity.
ΔT	Temperature difference.
Δt	Impact duration in time of the cooling effect.
ΔT_b	ΔT threshold value.
Δt_D	Time to the heating onset.
ΔT_C	Corrected ΔT values.
ΔT_{CRef}	Corrected ΔT_{Ref} image.

ΔT_{Cw} Corrected ΔT_w image
ΔT_{Max} Maximum absolute value of ΔT.
ΔT_{Min} Minimum absolute value of ΔT.
ΔT_{RN} Temporal noise evaluated in the reference area.
ΔT_{Ref} Reference average Image immediately before the impact.
ΔT_w Warm image; reference average Image after the impact the impact.
μ Thermal diffusion length.
σ Standard deviation.
ϕ Image phase angle.

Introduction

The weakness of composites, at least those based on a thermoset matrix, to impact load is a well known problem [1-4]. Mostly dangerous is the impact at low energy, which does not produce damage visible on the external surface but rather buried delamination between the layers. In general, composites are able to absorb the impact energy within their polymeric matrix that distributes the energy in the material; in this way, a low-energy (low-velocity) impact does not produce perforation but delamination between the layers, with no visible surface manifestation, whereas the structural integrity may be severely affected [5].
Indeed, the impact damage of composites happens through complex mechanisms and is still not completely understood. This is mainly due to the multitude of materials that can be created by changing any of their constituents: matrix, reinforcement, stacking sequence, curing process etc. In fact, it is sufficient to add a new ingredient in the matrix, or change the orientation of a fibres layer to develop a new material.
Since the introduction of composites in the construction of aircraft, a primary task was to establish the delamination threshold load (DTL) [6-8]. However, notwithstanding the huge amount of available data coming from both numerical simulation and experimental testing (see also references to chapter 1), a methodology to unambiguously establish the DTL still has not been completely achieved. This is because the DTL depends on many factors, first of all the material mechanical characteristics but also the geometry of the target [8,9] and of the impactor [10].
Another problem within composites is linked to defects that can be accidentally induced during their manufacturing processes. Indeed, these processes are probably primarily responsible for the occurrence of defects, particularly for porosity formation. In fact, porosity typically forms during an incorrect curing procedure due to uncontrolled or unexpected variations of the involved parameters, such as temperature, pressure, duration etc. A certain percentage of gas may remain entrapped within the material (essentially the matrix) and may give rise to formation of voids, which may modify the material in service performance. In fact, the detrimental effects of voids on composites' mechanical properties [11,12] are well recognized. Of course, the presence of porosity may also affect the behaviour of the material under impact load, with amplification of the bulk material weakness. Porosity is linked to manufacturing processes and can be reduced but not completely eliminated [13]. Perhaps this is one of the reasons why composite materials display a large variety of damaging behaviours under impact [14]. The negative effects of voids and other manufacturing defects on the impact damage of glass/epoxy specimens were also observed by Meola and Carlomagno [15] while using infrared thermography to investigate the response of composites to impact events.
Thus, once a new material is created, it is mandatory to assess its impact damage resistance especially if such material is predestined to an application sector which is highly exposed to impact load.

5.1.Description of specimens

Several different specimens are considered, which involve different types of matrix and fibres. In particular, owing to the type of matrix, the specimens are grouped into two families:

- thermoplastic matrix based specimens
- thermoset matrix based specimens.

This distinction is performed because of the dominant role played by the matrix in the material damaging modality. It is worth noting that also an aluminium foam sandwich panel has been investigated, which does not belong neither to the thermoplastic, nor to the thermoset, classification made before. Each specimen is identified with a code involving the used matrix, fibres and other most important characteristics. The specimens code with the most important details are collected in Table 5.1.

Specimen Code	Composition (Matrix – Reinforcement)	Thickness (mm)
PPG	Neat PP - Woven glass fibres	**3.0**
PGC2	Modified PP (2 wt% PP-g-MA) Woven Glass fibres	**3.0**
PPJ	Neat PP - Woven jute fibres	**3.8**
PJC2	Modified PP (2 wt% PP-g-MA) Woven jute fibres	**3.8**
PLAJ	Neat PLA-Woven glass fibres	**3.8**
PEF	Neat PE-Unidirectional flax fibres at 0°	**3.6**
GFRP	Epoxy adhesive preimpregnated unidirectional glass fibres $[0_2, 90_4]s$	**3.1**
$CFRP_U$	Unidirectional carbon fibres [0/90°/+45/-45°]s preimpregnated with epoxy resin	**2.3**
$CFRP_F$	Fabric carbon fibres [0/90°/+45/-45°]s preimpregnated with epoxy resin	**3.2**
$CFRP_{FU}$	Fabric and unidirectional carbon fibres [0/90°/+45/-45°]s preimpregnated with epoxy resin	**5.0**
$CFRP_{NC}$	Non-Crimp Fabrics (NCF), Multiaxial Reinforcements (MR) and 5 Harness Satin Weave (HSW)	**7.8**
AFS	Aluminium foam sandwich panel	**10.0**

Table 5.1. Some specimens details.

Some specimens, such as those identified with the codes:

- PPJ
- PJC2
- PPG
- PGC2
- PLAJ
- GFRP

were already described in chapter 4 and then, the reader is sent back there for more details. Instead, more details for new specimens are listed below:

- **$CFRP_U$** includes a thermoset (epoxy resin) matrix reinforced with unidirectional carbon fibres following the stacking sequence [0/45/90/-45]s. More specifically, 12 pre-

impregnated plies are overlaid by the hand lay-up technology and cured in autoclave. Specimens are 150x100 mm^2 and are 2.3 mm thick.

- **$CFRP_F$** is a panel of square side 500 mm. It is made of carbon fibres woven fabric layers embedded in epoxy resin. The total numbers of overlapped plies allows to obtain a total thickness of 3.2 mm.
- **$CFRP_{FU}$** is a panel of square side 500 mm and nominal thickness 5 mm. It is a multilayer laminate reinforced with carbon and involving epoxy resin matrix. The fibres are oriented following the stacking sequence [0/90/+45/-45]s; fibres are of both fabric and unidirectional types.
- **$CFRP_{NC}$** has a complex architecture including Non-Crimp Fabrics (NCF), Multiaxial Reinforcements (MR) and 5 Harness Satin Weave (HSW) and has a thickness of 7.8 mm and square shape of side 485 mm. It is fabricated by the hand lay-up technology and appropriate curing cycle in autoclave.
- **PEF** is a square panel of 600x600 mm^2 made of flax unidirectional fibres at 0 degrees embedded in a Polyethylene (PE) matrix with a total thickness of 3.6 mm.
- **AFS** is an aluminium foam sandwich panel consisting in a three-layer composite comprising a foamable (containing TiH2 as a blowing agent) aluminium alloy sheet as a core layer and two face sheets still in aluminium alloy on both sides. The AFS panel is 92 x 48 mm^2 and has a total thickness equal to 10 mm, with foam thickness of 8 mm and average cell size of the foam bubbles of 2 mm. The surface viewed by the infrared camera was painted with opaque paint in order to increase its emissivity.

It is worth noting that aluminium foam sandwiches (AFS) [16-18], obtained by combining metal face sheets with a lightweight metal foam core, have peculiar properties (low specific weight, efficient capacity of energy dissipation, high impact strength, acoustic and thermal insulation, high damping), that make them interesting for a number of practical applications, such as the realization of lightweight structures with high mechanical strength and good capacity of energy dissipation under impacts. Core deformation and failure are decisive factors for the energy absorption capability of sandwich structures. After fracture of the skin, the impacting object may damage and penetrate into the core. With aluminium honeycomb cores, damage consists of crushing or "buckling" of cell walls in a region surrounding the impact point, while, in foam cores, damage looks more like a crack for low-energy impacts [19].

5.2. Conventional procedure for assessing impact resistance of new composite materials.

The performance to impact of new composite materials is generally assessed through specific impact tests [20]. Amongst other tests, it is generally required to draw damage maps, or plots of damage area vs. impact energy. This also means to search for the impact energy that has caused a damage of given size; this size is generally intended to include the whole extension of delamination and is established through specific testing procedures. First of all, several specimens must be fabricated of specific dimensions, according to the testing machine to be used. Specimens may be

relatively small to allow for one impact only, or quite large allowing for more than one impact, each in a different place. Then, an initial value of the impact energy is chosen, according to current knowledge and relaying to the behaviour of similar materials previously tested. The procedure consists in a sequence of operation: A) put the panel in the impact machine, B) perform the impact, C) remove the panel, D) perform non-destructive tests and evaluate the resulting extension of delamination.
At this point, three cases may arise:

1. the requested size is found at the first attempt and tests stop;
2. the measured delamination is smaller than the prefixed value requiring more tests at increasing energy;
3. the measured delamination is larger than the prefixed value requiring more tests at decreasing energy.

However, it is generally unlikely to hit the imposed damage extension at the first attempt (point 1); usually (points 2 and 3), many attempts are necessary with repetition of the operations at point A. This involves removing and putting again the same, or another, specimen, in the impact machine for another impact of different energy and so on. This also requires successive non-destructive testing (NDT) and damage area measurement. Naturally, this procedure is time consuming and, sometimes, not very accurate. In fact, the most commonly in use NDT techniques may fail to detect the actual delamination extent essentially because of two main problems:

- Two delaminated surfaces tend to tightly adhere once the impactor moves away.
- Delamination propagates through tortuous pathways.

These problems may led to undetected delamination, or to underestimation of its real size with obvious negative consequences on the component life.
Conversely, using infrared thermography, it is possible to recognize the type of arisen damage, from the temperature rise and from the extension of the warm area, directly during online monitoring with time saving. This is because the thermal signatures can be related to what occurred to the material under load and help to understand the impact damage mechanisms, as well to estimate the overall affected impact zone.
In the next section an example of inspection of impacted laminates is given by using two NDT techniques: Lock-in thermography (LT) and Phased Array Ultrasonic (PAUT)

5.2.1 Lock in thermography: test setup and procedure

As shown in Fig. 5.1, the present test setup for LT includes the specimen, the infrared camera and one or two halogen lamp (1 kW each) for thermal stimulation of the specimen; in particular, one lamp is enough for small specimens, while two are used for larger ones. The heating source and the infrared camera are positioned on the same side with respect to the observed surface (reflection mode). The used infrared camera is the SC6000 (Flir systems). The distance of both camera and lamp (lamps) to the specimen surface is varied between 0.5 and 1 m with care put to their mutual orientation to avoid reflections. The camera is equipped with the Lock-in module that drives the

halogen lamp to generate a sinusoidal thermal wave of selectable frequency f and the IRLock-In© software (supplied with the IR Lock-in package) for performing lock-in thermography analysis. Lock-in thermography is well described in literature [21-30]. The thermal wave, delivered to the specimen surface, propagates inside the material and gets reflected when it reaches zones where the heat propagation parameters change. The reflected wave interacts with the surface wave producing an oscillating interference pattern, which can be measured in terms of either temperature amplitude or phase angle ϕ, and represented as amplitude, or phase, images, respectively. The basic link of the thermal diffusion length μ to the heating frequency f and to the mean material thermal diffusivity coefficient α is via the relationship:

$$\mu = \sqrt{\frac{\alpha}{\pi f}} \tag{5.1}$$

The depth range for the amplitude image is given by μ, while the maximum depth p, which can be reached for the phase image, corresponds to 1.8 μ [22-24]. In general, it is preferable to reduce data in terms of phase image because of its insensitivity to both non uniform heating and local variations of emissivity coefficient, over the monitored surface. Hence, the material thickness, which can be inspected, depends on the wave period (the longer the period, the deeper the penetration) and on the material thermal diffusivity. According to Eq.(5.1), the knowledge of the mean thermal diffusivity is fundamental to evaluate the depth at which any detected anomaly is located, or to chose the frequency value to check the material conditions at a given depth. To this end, the overall thermal diffusivity α can be evaluated with the lock-in technique itself [31,32], or with flash thermography [33,34].

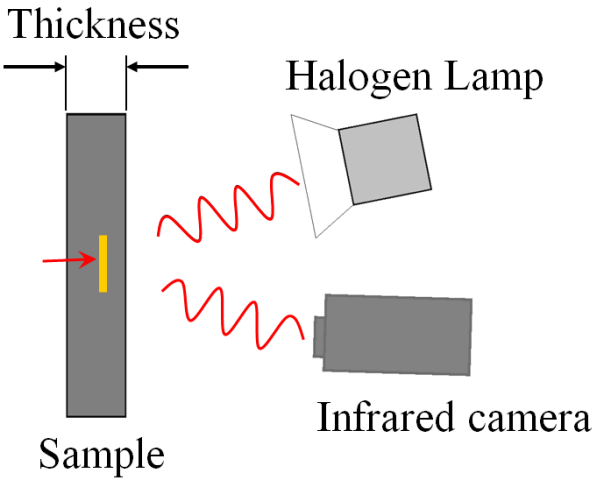

Fig.5.1. Lock-in test setup.

5.2.2 PAUT test setup

PAUT tests are performed with an Olympus OmniScan SX flaw detector with a 16:64PR phased array unit equipped also with a conventional UT channel for pulse-echo, pitch-catch, or TOFD inspection [35,36]. Phased array elements are pulsed in such a way as to cause multiple beam components to combine with each other and form a single wave front travelling in the desired direction. Similarly, the receiver function combines the input from multiple elements into a single presentation. Because phasing technology permits electronic beam shaping and steering, it is

possible to generate a vast number of different ultrasonic beam profiles from a single probe assembly, and this beam steering can be dynamically programmed to create electronic scans. Phased array ultrasonic instruments utilize high frequency sound waves to check for the internal structure of a test piece, or measure its thickness, and rely on the same basic laws of physics that govern sound wave propagation. The ability to generate multiple transducer paths within one probe adds a powerful advantage in the detection, and naturally increases the ability to ‘‘visualize” an inspection by creating an image of the inspected zone. Phased array imaging provides the user with the ability to see relative point to point changes and multi-angular defect responses, which can assist in flaw discrimination and sizing [37]. An encoded 5 MHz, 64 element linear array probe with a straight wedge and by employing a specific gel as coupling medium has been used. Besides, no calibration blocks are used, the measurement of the specimen thickness being taken as reference; it is worth noting that it is generally difficult to fabricate reference blocks.

5.2.3 Some results of LT inspection

Some phase images of specimens, all impacted at 10 J, are shown in the following figures 5.2-5.4. Fig.5.2 and Fig. 5.3 show phase images taken at different frequencies on the impacted surface of PPG and PGC2 specimens, respectively.

From phase images and by knowing the spatial resolution of the used instrument (infrared detector and lens), it is possible to measure the size of the damaged area; for present tests, the spatial resolution is in the range 3–3.7 pixels/mm. Quantitative measurements are expressed in terms of the two diameters D_H and D_V (along horizontal and vertical directions), which are reported on phase images taken at f = 0.15 Hz (Figs. 5.1c and 5.2c) [38]; a threshold value according to Ref [28] has been considered. D_H and D_V values are reported on Table 5.2.

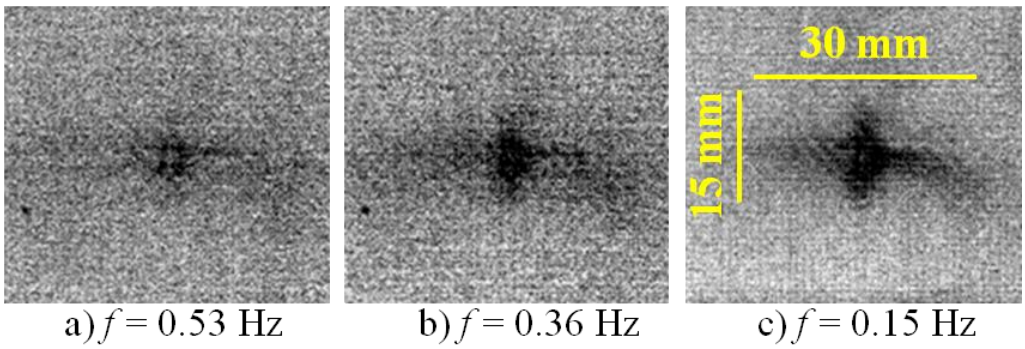

Fig. 5.2. Phase images of specimen PPG impacted at E =10 J; (a) f =0.53 Hz; (b) f =0.36 Hz; (c) f =0.15 Hz.

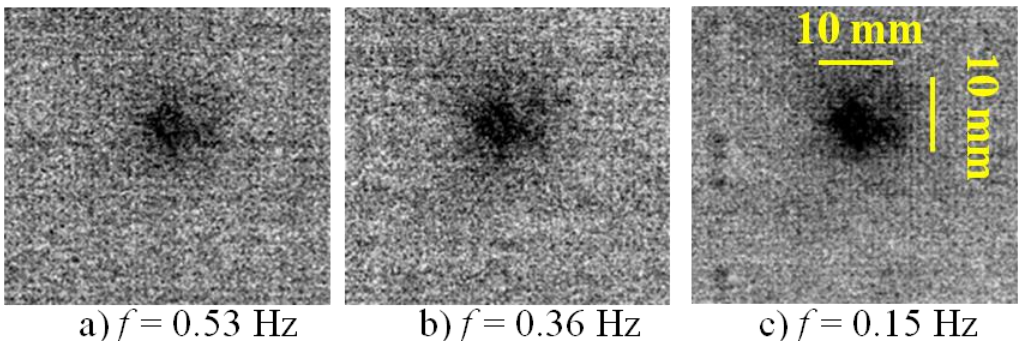

Fig. 5.3. Phase images of specimen PGC2 impacted at E = 10 J;(a) f =0.53 Hz; (b) f =0.36 Hz; (c) f =0.15 Hz.

As can be seen, for the specimen PGC2 at f = 0.53 Hz (Fig. 5.3a), an almost circular dark zone, which enlarges by decreasing the heating frequency to 0.15 Hz, is present. Such a variation of area accounts for the damage progression through the specimen thickness. The damaged area assumes a different shape for the specimen PPG (Fig. 5.2), showing a long branch along the horizontal direction and a shorter one in the vertical direction. The presence of the two branches accounts for a larger damaged zone; in particular, the different length of the two branches indicates a different extension of the damage along the two directions [39].

The phase images taken from the rear surface (opposite to the impacted one) of the two specimens $CFRP_U$ and GFRP, showing the largest detectable damage, are compared in Fig. 5.4 with their characteristic dimensions D_H and D_V. As can be seen, the damage develops mostly along the fibres direction [40]. In fact, a long horizontal stripe with smears along the fibres at 45° is visible for the CFRP specimen (Fig. 5.4a); instead, an oblong structure with its longer side along the vertical direction is visualized for the GFRP specimen (Fig. 5.4b). For both specimens it is also possible to see the presence of other signs, like fibres orientation, presence of porosity and further details.

Particular consideration deserves the GFRP specimen being the material translucent in the visible wavelength. In fact, after impact, a local permanent faded area is visible to the naked eye in transparency, which corresponds to the damaged area and can be assumed as a reference. Such visible area (Fig. 5.4c) well matches the damaged area detected by LT (Fig. 5.4a).

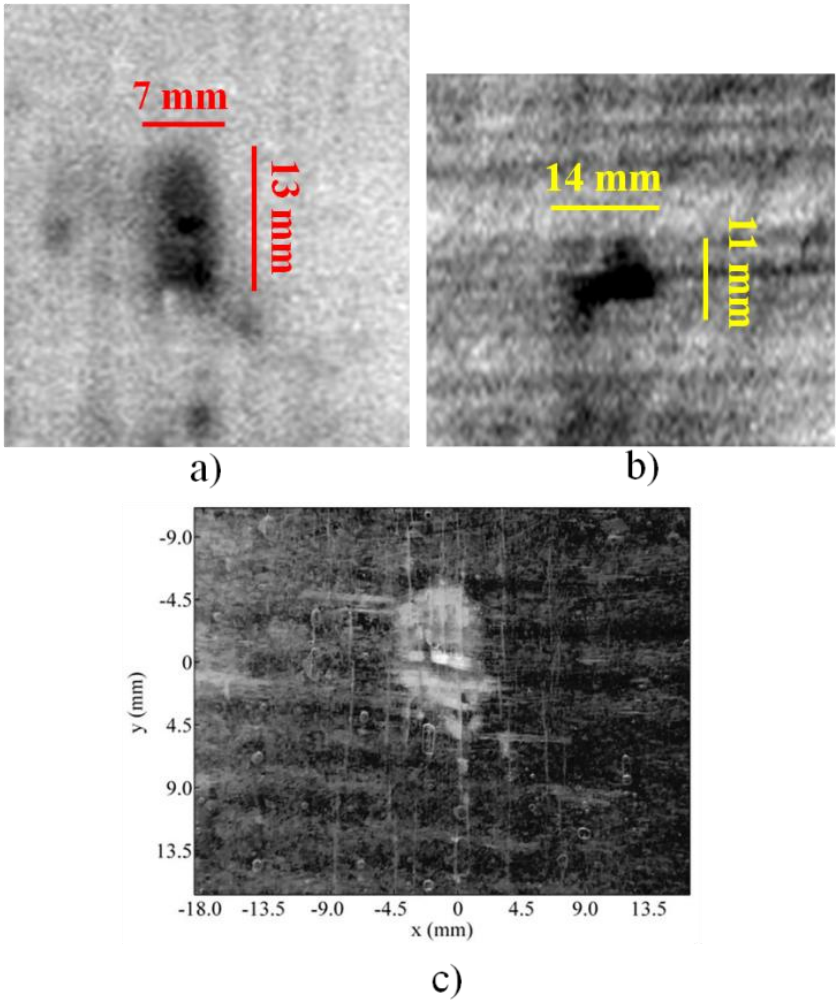

Fig. 5.4. Phase images showing the largest detectable damage for thermoset matrix specimens, taken from the rear side at f=0.05 Hz; (a) GFRP; (b) $CFRP_U$. (c) Visible image taken from the rear side GFRP.

Specimen	D_H (mm) (LT)	D_V (mm) (LT)
$CFRP_U$	14	11
GFRP	7	13
PPG	30	15
PGC2	10	10

Table. 5.2. Comparison of D_H and D_V performed obtained with LT; impact at E = 10 J.

5.2.4 Comparison of LT and PAUT results

A comparison is made between results obtained with the specimen $CFRP_{FU}$ (see Table 5.3) that has been impacted in three different places with three values of impact energy 18, 29 and 39 J, respectively. The inspection with LT is performed by viewing the side opposite to impact (the same viewed during impact monitoring) and by varying the heating frequency. A thermal diffusivity equal to 0.0085 cm^2/s was evaluated with lock-in thermography itself owing to a sound material zone; of course, thermal diffusivity varies with the material being damaged. The three impacts are distinguishable already at f = 0.88 Hz (depth of about 1 mm, evaluated from Eq.(5.1)), but the best contrast is attained for f = 0.36 Hz. A phase image of the entire specimen is shown in Fig. 5.5 with superimposed, for more details, also single images for each impacted zone.
The single images were taken with enhanced resolution (shorter distance) and refer to the same frequency of 0.36 Hz of the whole image (depth p = 1.7 mm). From the phase images, it comes out that the most important damage develops along the direction D_B (along -45°). In particular, D_B = 24, 32 and 34 mm for E = 18, 29 and 39 J, respectively. Some damage occurs along D_A (i.e., +45°) but it is milder and tends to get confused with the differences in the phase angle induced by the material architecture.

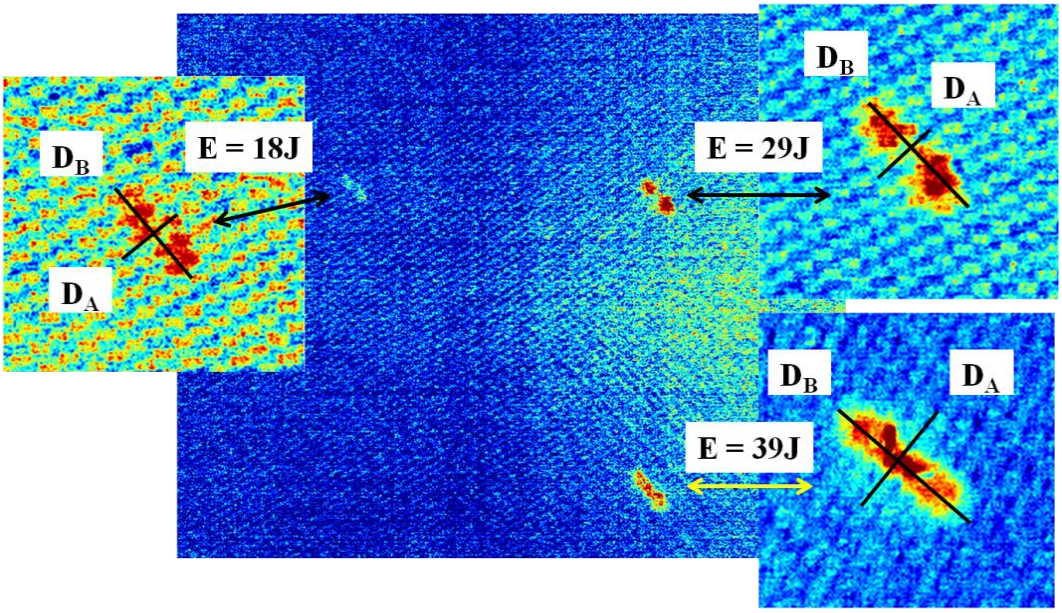

Fig. 5.5. Phase image taken at f = 0.36 Hz, p = 1.7 mm.

C_scans and S_scans obtained with PAUT are reported in the following Figs. 5.6–5.8.The C-scan images (Figs. 5.6a, 5.7a and 5.8a) show presence of surface damage. In particular, the central red areolas, which increase in number with increasing of the impact energy, indicate indentation

damage, impact surface penetration and surface cracks. The surrounding yellow/blue areas, with a lower signal amplitude, immediately suggest the presence of wider delaminations of different orientations and at different depths through the thickness. From the circular C_scan view, it is possible to measure an average diameter D_{av} that gives values equal to 24 mm (Fig. 5.6a), 32 mm (Fig. 5.7a) and 34 mm (Fig. 5.8a) which practically coincide with D_B values obtained from phase images. However, the C_scan supplies a total view of the damage and does not allow for a direct comparison with the phase image that is more selective in depth. Instead, a comparison with the S_scan is feasible for locating the damage in depth. In fact, from the S_scans, it seems that, apart from surface indentation, the most important damage is located between 1 and 1.6 mm from the bottom. This is in general agreement with LT observations. Damage diameters obtained from LT and PAUT images are reported in Table 5.3.

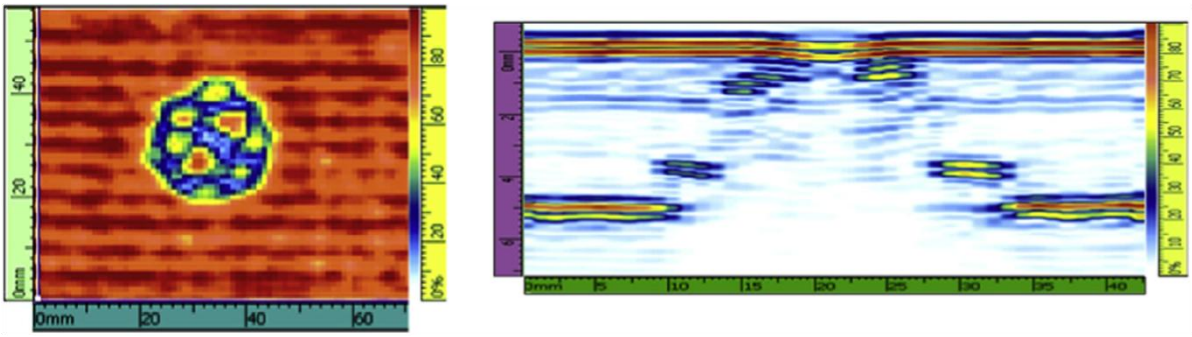

(a) (b)

Fig. 5.6. PAUT results *E* = 18 J. C_scan (a), S-scan (b).

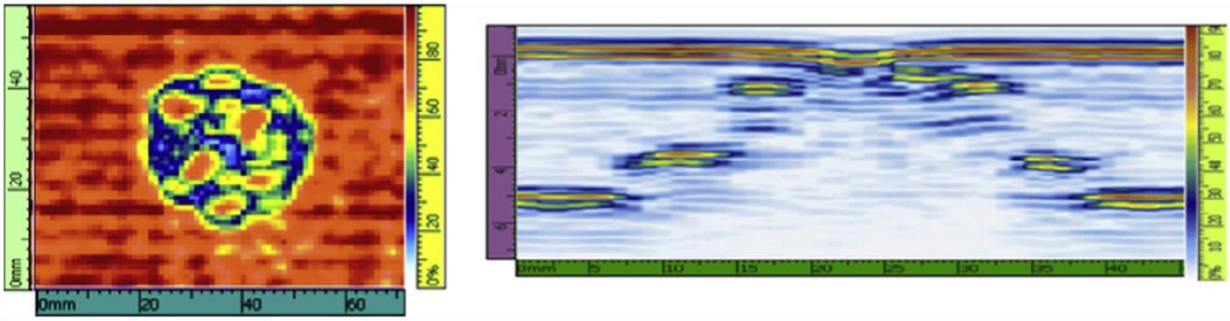

(a) (b)

Fig. 5.7. PAUT results *E* = 29 J. C_scan (a), S-scan (b).

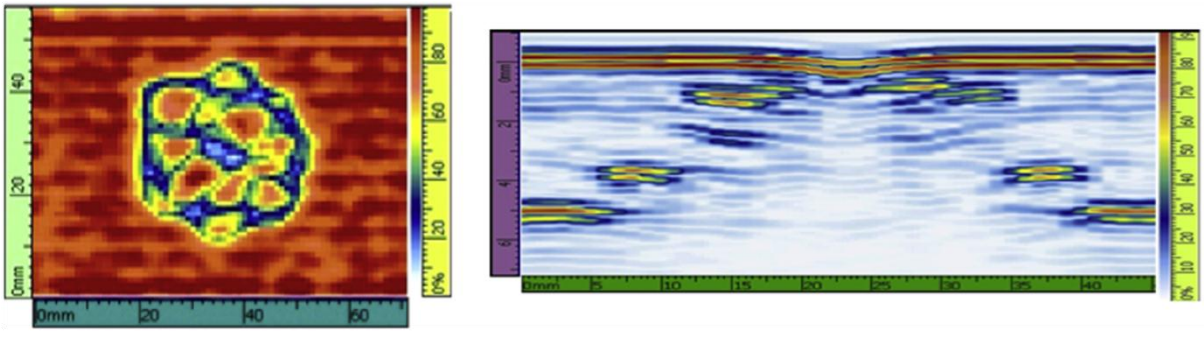

(a) (b)

Fig. 5.8. PAUT results specimen *E* = 29 J. C_scan (a), S-scan (b).

E (J)	D_B (LT)	D_{av} (PAUT)
18	24	24
29	32	34
39	34	34

Table 5.3 Quantitative data for damage extension.

Non-destructive testing with lock-in thermography and PAUT show a satisfactory agreement and allow identification of impact damage [41-44]. Both LT and PAUT have their own advantages and limitations. LT is fast to detect impact damage over large panels in non contact mode, but is affected by loss of contrast in presence of deep defects. PAUT is more effective in the estimation of the thickness and in the inspection of thick parts, but can be applied only over smooth surfaces and requires a coupling medium. However, from an integrated analysis of C_scan, S_scan and phase images it is possible to get useful information for a better evaluation of the material and for the comprehension of some aspects, which may appear not understandable owing to the output of one technique alone. In fact, the C_scan supplies a total view of the occurred damage, the S_scan helps to locate the damage through the specimen thickness, while the phase images allow understanding the evolution of the damage with respect to the fibre direction.

5.3. The added value of online monitoring

The scope of this section is to describe data obtained with online monitoring and to show as the use of infrared thermography may be advantageous to get information, which are useful to estimate the performance under impact of new composite materials. In particular, the main aim is to gain new information about the damage mechanisms of several kinds of composites starting from the sequences of thermal images acquired during the impact event. This is possible since the percentage of impact energy, which produces the damage, is dissipated as heat with a local increase of temperature. Then, the material damage can be associated with the surface temperature variation visualized by the infrared camera.

It is worth noting that, during the impact event, the impact energy is in part elastically stored by the material and returned back to the impactor, while the remaining part is mostly dissipated to produce the damage. In particular, the specimen initially bends under the impactor pushing force and so, the material surface opposite to the impacted one is subjected to a positive volume variation and experiences a fast cooling down. This is due to the thermoelastic effect that vanishes once the impactor pushing force is removed and the surface recovers its straight appearance. As will be shown later, the cooling down effect, visualized by the infrared camera, can be used to obtain useful information about the elastic energy stored by the material, the impact duration as well as the overall extension of the impact affected area. Conversely, the material heating up can be exploited to know more on its damaging under impact.

Different types of composites are considered, which involve change of either the matrix, or the reinforcement.

The experimental investigation is conducted with two main purposes:

1. Analysis of impact dynamics - by visualizing the evolution in time and in space of thermo-elastic/plastic phenomena arising during an impact event in order to get information useful for a deeper understanding of the impact damaging mechanisms.

2. Evaluation of the impact damage - by developing a procedure to define the limit between sound and damaged materials in order to outline and quantitatively measure the overall extension of the impact affected area by using the acquired thermal images.

More specifically, the discussion will start with some qualitative considerations on the acquired images and proceeds towards more quantitative outcomes with the two points 1 and 2, first, separately addressed and, then, mutually considered since the outcomes of one point may help dealing with the second one.

5.4 Preliminary tests of impact monitoring

The intention of this section is a brief excursus through the pioneering work performed by Meola, Carlomagno and others that have inspired part of my research activity in focusing the attention on monitoring of the impact tests with infrared thermography.
Throughout the past few years, the application of infrared thermography for monitoring of impact tests was investigated at the University of Naples by varying the type of material, the impact energy, the hammer nose diameter, the infrared camera and the acquisition frame rate as well [45-51, 15]. The first impact tests have been carried out with the intention to ascertain the capability of an infrared imaging system to follow the very fast impact dynamic and capture the thermal phenomena associated to the impact [45]. To this end, some impact tests have been performed on a glass/epoxy material transparent in the visible band to allow detection of impact damage with the naked eye and comparison with thermographic images. It was sudden realized that impact tests should be performed with a modified Charpy pendulum which involves enough room for positioning of the infrared camera (Fig. 5.9). More specifically, in Fig. 5.9 the infrared camera is positioned to view the surface opposite to that struck by the impactor, as better shown in Fig. 5.10. Initially, the QWIP SC3000 LW infrared camera was used to acquire sequences of images at frame rate F_R = 900 Hz and 300 Hz. Afterwards, these sequences were post-processed by subtracting the first image (t = 0 s) of the sequence, i.e. the specimen surface temperature (ambient) before impact, to each subsequent image so as to generate a map of temperature difference ΔT:

$$\Delta T(i,j,t) = T(i,j,t) - T(i,j,0) \tag{5.2}$$

i and j representing lines and columns of the surface temperature map.
Some examples of thermal images acquired during impact at 10 J on GFRP specimens are shown in Fig. 5.11. It is worth noting that the field of view includes either 48, or 16, horizontal lines for 300 or 900 Hz, allowing visualization of only the thermal signatures evolving in the horizontal direction. However, as can be seen from the plots of Fig. 5.12, the thermoelastic effect is very fast and can be visualized only at high frame rate. In particular, Fig. 5.12 displays plots of ΔT values in three points over images taken during impact at 9.7 J on a GFRP specimen. It is possible to see that ΔT starts from zero, before the impact, decreases to negative values, as the specimen bends under the

impactor pushing force, and increases as the material undergoes some damage with the appearance of hot spots. Apart from assessing feasibility of online impact monitoring, the preliminary tests with the SC3000 camera, showed that important information can be derived which can help understand more about the complex impact damaging of composites. However, it also soon appeared the need of a wider field of view. This was in part fulfilled by viewing the specimen contemporaneously also with another infrared camera (Cedip Jade III), which allowed, through its windowing option, to view a larger enough surface to account for heating delamination coupled effects. A comparison between online monitoring, non-destructive evaluation and visible inspection of a GFRP specimen impacted at 9.7 J is reported in Fig. 5.13. In particular, the thermal image (Fig. 5.13b) was taken during impact with the Jade III camera, the phase image (Fig. 5.13a) was taken with the SC3000 coupled with the lock-in option and the last (Fig. 5.13c) is a photo taken on the specimen surface after impact. Being the surface translucent in the visible, it is possible to clearly see the damage stain and compare it with infrared thermography thermal and phase images.

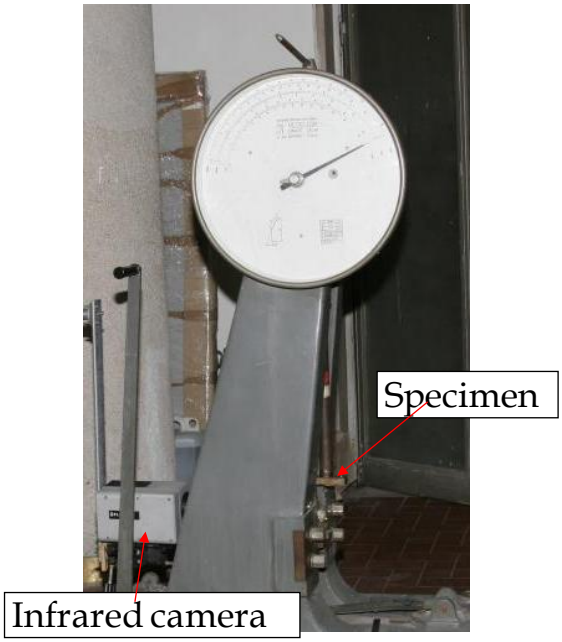

Fig. 5.9 Test setup for impact tests with a modified Charpy pendulum

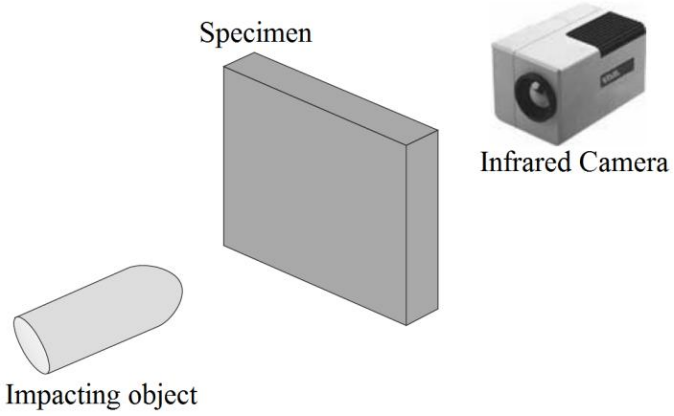

Fig. 5.10. Sketch of impactor and infrared camera mutual position with respect to the impacted specimen.

Looking at figure 5.13, it is possible to see good agreement amongst results coming from the different types of examination: visualization during impact, non-destructive inspection and visual inspection. It is possible to see that three dots appearing in the phase image (b) correspond to the three hot spots, which were observed during impact monitoring (a). Such spots may be assumed to represent breakage loci. The delamination contour visualized by the phase image (b) practically coincides with the largest hot zone, which develops during impact (a), and with the stain which remains permanently on the specimen (c) after impact [48].
Later, the investigation was focused more on the evolution of the warming, or thermoplastic, phase especially in presence of manufacturing defects with images taken at lower frequency (96 Hz) with the QWIP SC6000 camera [15].

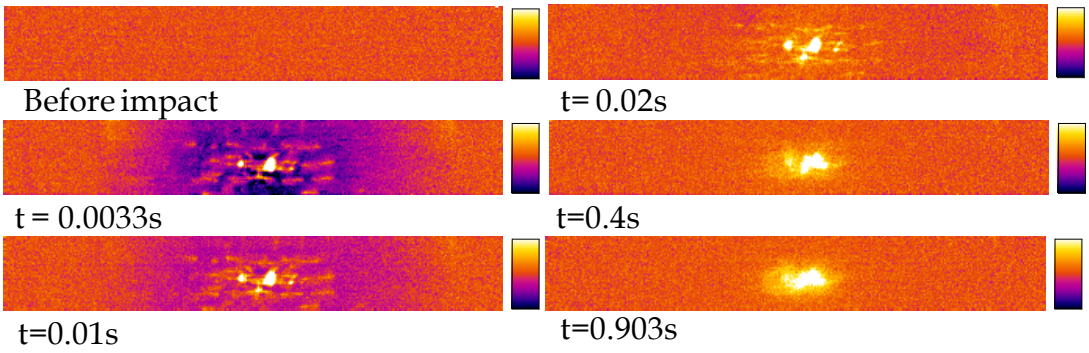

a) F_R = 300 Hz

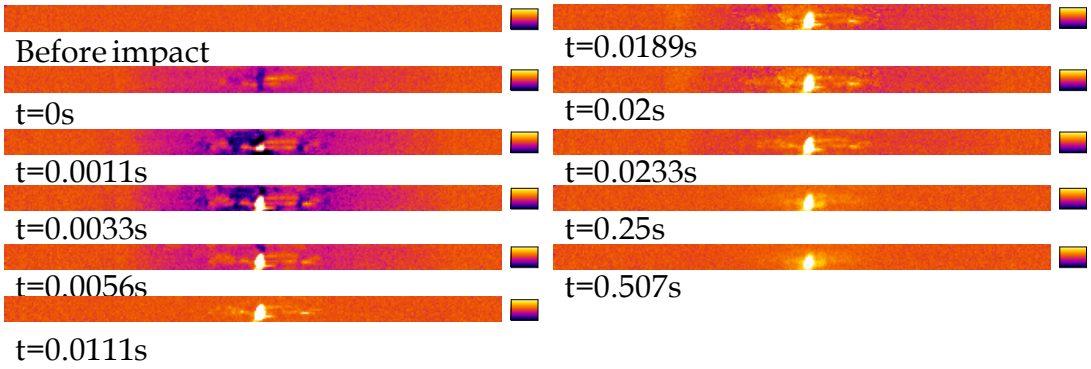

b) F_R = 900 Hz

Fig. 5.11. Examples of thermal images acquired, during impact at *E* = 9.7 J on GFRP samples, with the QWIP SC3000 camera at two frame rates. 300 Hz (a) and 900 Hz (b).

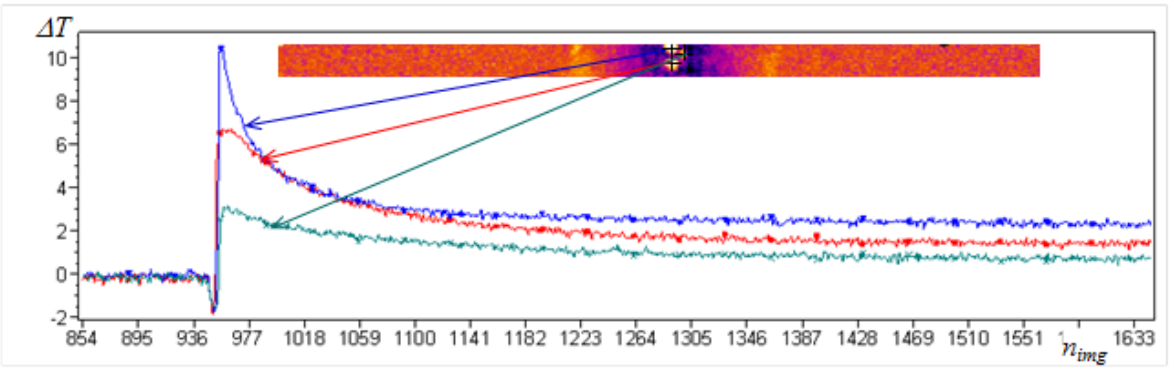

Fig. 5.12. Plots of ΔT values in three points over the zone impacted at *E* = 9.7 J.

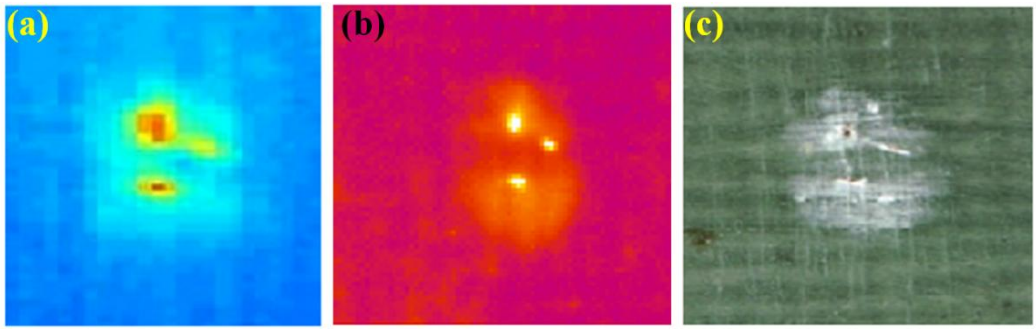

Fig. 5.13. Comparison of images of a GFRP specimen impacted at 9.7 J; thermal image with the Jade III camera (a), phase image at f = 0.14 Hz (b), visible image (c).

The most important results obtained within the first few years of investigation [15, 45-50] can be summarized as:

- Online monitoring of the thermal signatures helps gaining information on the impact dynamics since hot spots coincide with the damage loci and the hot area with the overall delaminated area. In particular, large ΔT values indicate occurrence of important delamination and fibre breakage, while small ΔT values account for formation of microcracks in the matrix and/or light delamination.
- By comparing thermal images to the phase ones, it is possible to observe that the warm area is similar to the damaged area detected through non-destructive evaluation. In addition, the warm area seems to coincide with the stain, which is visible to the naked eye on a translucent impacted material.
- During impact, the monitored surface is seen to first cooling down due to thermo-elastic effects and then heating up because of dissipation of the impact energy. In particular, within the elastic phase, temperature variations occur during a very short time (fractions of a second), and thus, their visualization is possible only with a high-frequency imaging device.
- From temperature–time maps it is possible to perceive initiation of the damage phase.
- It is possible to individuate initiation and propagation of the damage through measurements of both temperature rising and warm area extension.
- It seems there exists a correlation between the impact energy and the maximum positive ΔT.
- The impactor geometry plays a key role and the effective contact area between the impactor nose and the specimen surface must be considered for the evaluation of the impact damage and, in turn, material impact resistance.

The obtained results demonstrate the suitability of infrared thermography to be used coupled with impact tests for a faster evaluation of impact damage. However, the achieved results represent only the first step in the investigation, which needs further tests with a wider assortment of specimens.
Besides, it is worth remembering that despite the huge amount of literature on the impact problem (see also references to Chapter 1), no work seems to have been specifically concerned with heat generation at damage onset. Moreover, the available quantitative data about initiation and propagation of delamination with impact energy are mainly for some specific materials and for specific test configurations which make difficult any comparison.

5.5. New investigation

From this point on, only the new impact tests carried out and the results achieved during the PhD course are described.

5.5.1 Test setup and experimental procedure

Impact tests are carried out with a modified Charpy pendulum, which, as already said, allows enough room for positioning of the infrared camera to view the rear specimen surface (i.e., opposite to that struck by the hammer). Fig. 5.14 shows a sketch of the last setup which was modified to include the reference specimen. Specimens are placed inside a special lodge which includes two rigid plates, working as fixture and each having a window 12.5 cm x 7.5 cm to allow for the contact with the hammer from one side and optical view (by the infrared camera) from the other one. The hammer has a hemispherical nose 12.7 mm in diameter. The impact energy E is chosen between 2 and 60 J, depending on the specimen under test and is set by suitably adjusting the falling height of the Charpy arm; the latter is set by means of an external control unit that allows to link the angle between the pendulum oscillating arm and the vertical direction with the impact energy. In particular, the values of the impact energy have been selected so as to have either barely visible damage, or material breakage, but never a complete penetration of the sample. A reference specimen is used for correction of the detector noise. More specifically, as shown in Fig. 5.14b, a small sample (reference specimen) of the same material is attached over the specimen lodge so as to be included in the camera field of view without undergoing percussion. This reference specimen is mechanically separated from the impacted specimen and is not affected by the impact.

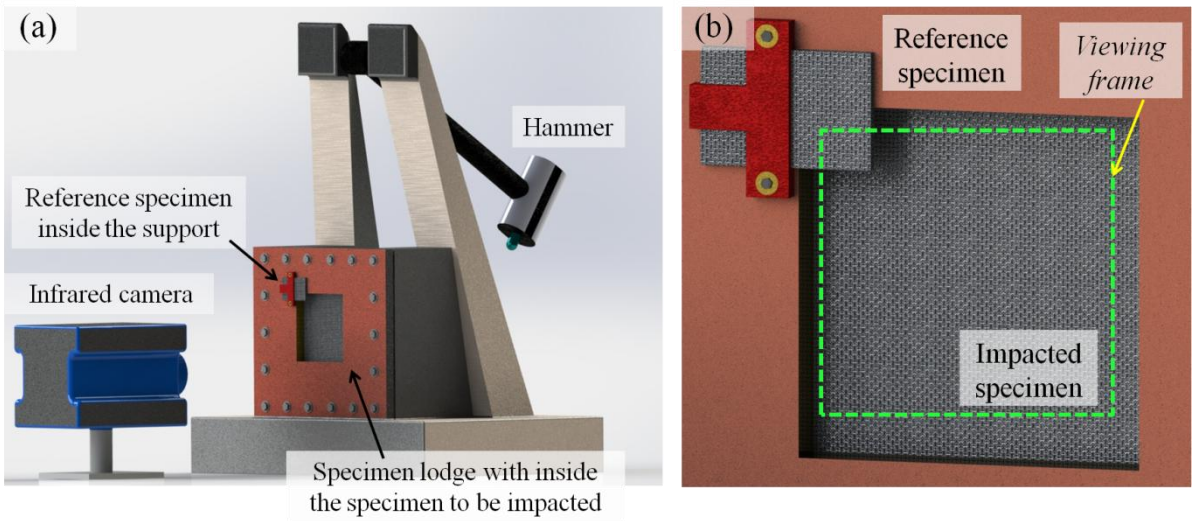

Fig. 5.14. Sketch of setup for impact tests (a) and details of the viewing frame (b).

During each test, the infrared camera visualizes both the impacted specimen and the reference specimen and acquires a sequence of images starting few seconds before the impact and lasts some time after in order to follow the evolution of surface thermal signatures.
The infrared camera mostly used is the Flir QWIP SC6000 LW, which was already described in Chapter 3. In some tests, two infrared cameras of different characteristics are used to acquire sequences at two different values of frame rate and to try to make the best amongst higher thermal

sensibility and higher frame rate. The second camera is the SC6800 MW already described in Chapter 3. The integrated use of the two cameras, both managed with the ResearcherIR software (supplied with the Flir package) at two different frame rate values F_R = 83 Hz for the SC6000 and F_R = 960 Hz for the SC6800 and two different recording times, allows to contemporaneously visualize thermoelastic and thermoplastic phenomena without either overloading the computer's memory, or complicating post-processing.
Several impact tests have been performed, all at environmental temperature (15< T <25 °C), but at several values of the impact energy. Depending on the specimen size, the several impacts have been performed either on the same specimen, at different places, or on different specimens made of the same material.
The acquired sequences of thermal images undergo post processing by using the Researcher TM software (available from the Flir systems package) and specific routines developed in the Matlab environment.

5.5.2 Interpretation of infrared images recorded during impact tests

Some ΔT images (Eq.5.2) recorded with the SC6800 camera are reported in the following figures 5.15- 5.20. In each figure, the first image (t = 0 s) refers to the surface ΔT distribution before the impact event, while the other images show variations at different instants during the impact.
From all of the showed figures, two main phenomena: cooling down (dark zones) and heating up (light ones) with respect to the initial ambient temperature, can be observed. The analysis of these two effects allows getting information about the impact damaging of the different tested specimens.
On the whole, the cooling down indicates that the viewed surface is under tension due to the impact pushing force (thermoelastic effect), while the heating up is due to dissipation of the energy absorbed by the specimen (thermoplastic effect).
In particular, the temperature increase is produced by the fraction of energy absorbed by the material. The mechanism of energy absorption by the composite during impact depends on many factors such as: impact velocity, geometrical parameters and material inherent characteristics (i.e., brittle, or ductile) [52,53]. For low-velocity impacts, the energy E_a absorbed by the specimen is generally regarded as the sum of: membrane energy E_m, bending energy E_b and damage energy E_d.

$$E_a = E_m + E_b + E_d \tag{5.3}$$

The importance of each component depends on the material properties. In particular, for a brittle material, E_d includes two terms, one accounting for fibre breakage E_{db} and the other one for delamination E_{dd}. Instead, for a ductile material, the energy is predominantly spent in deformation and delamination perpendicular to the impactor axis. Considering that most of the absorbed energy is dissipated as heat, it is apparent that the sequence of thermal images, taken (at the rear side) with the infrared camera during the impact event, can be usefully exploited for either a better understanding, or validation, of previous hypothesis about the mechanisms of energy absorption. To this end, it is important to take into account the material thermal properties and the involved heat transfer mechanisms. As a general rule, the formation of micro-cracks is accompanied by small energy dissipation, which in turn gives rise to small temperature increase. Conversely, a fibre

breakage involves large amount of energy dissipation with an abrupt local increase of temperature [38,48,54,55].

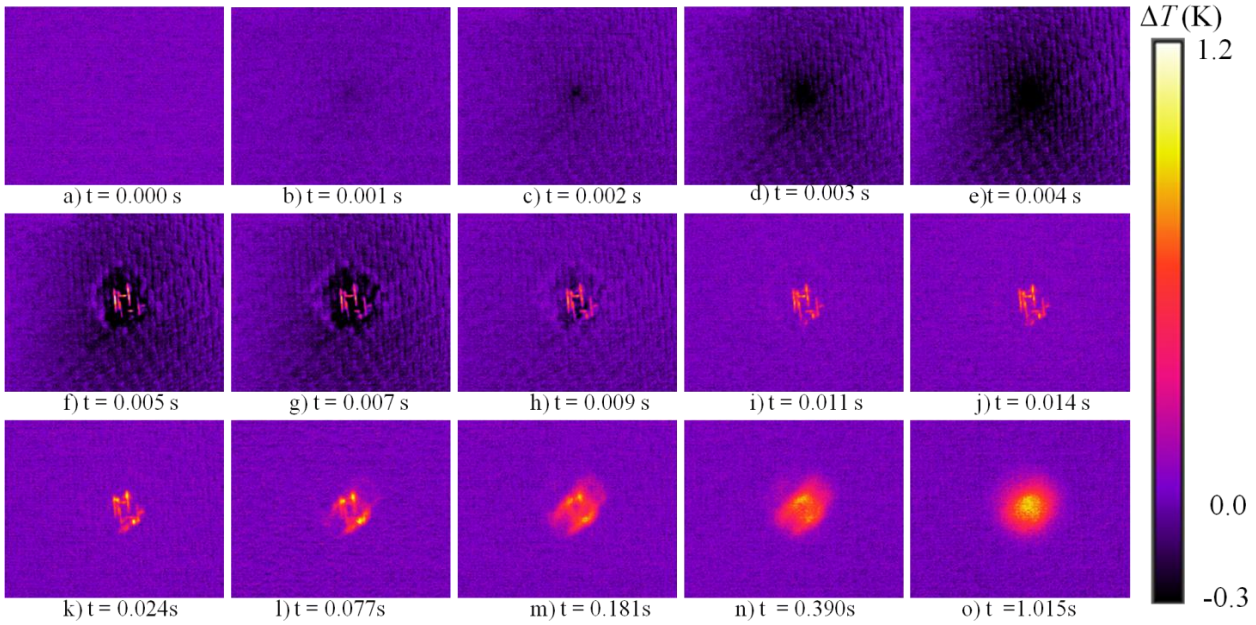

Fig. 5.15. Some ΔT images of $CFRP_{FU}$ specimen impacted at E = 10 J.

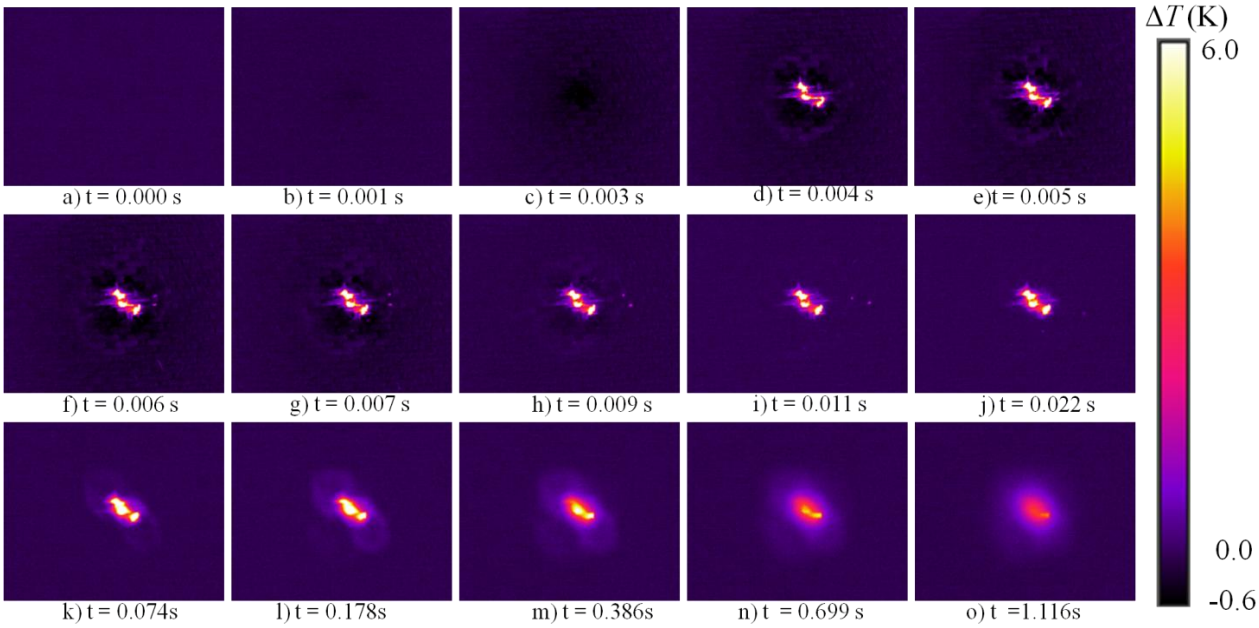

Fig. 5.16. Some ΔT images of $CFRP_{FU}$ specimen impacted at E = 18 J.

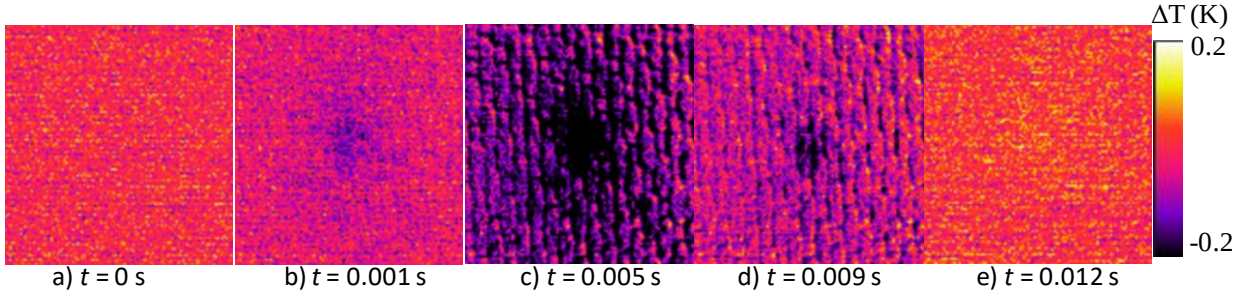

Fig. 5.17. Some ΔT images for $CFRP_{NC}$ impacted at E = 39 J.

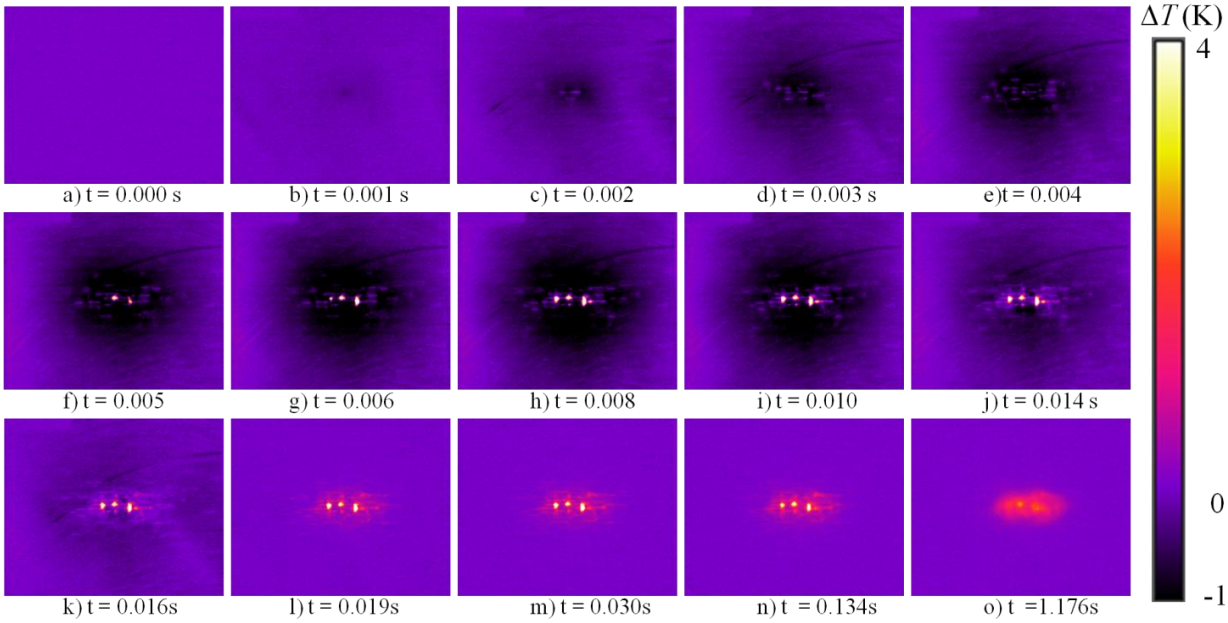

Fig. 5.18. Some ΔT images of GFRP specimen impacted at E = 8.3 J.

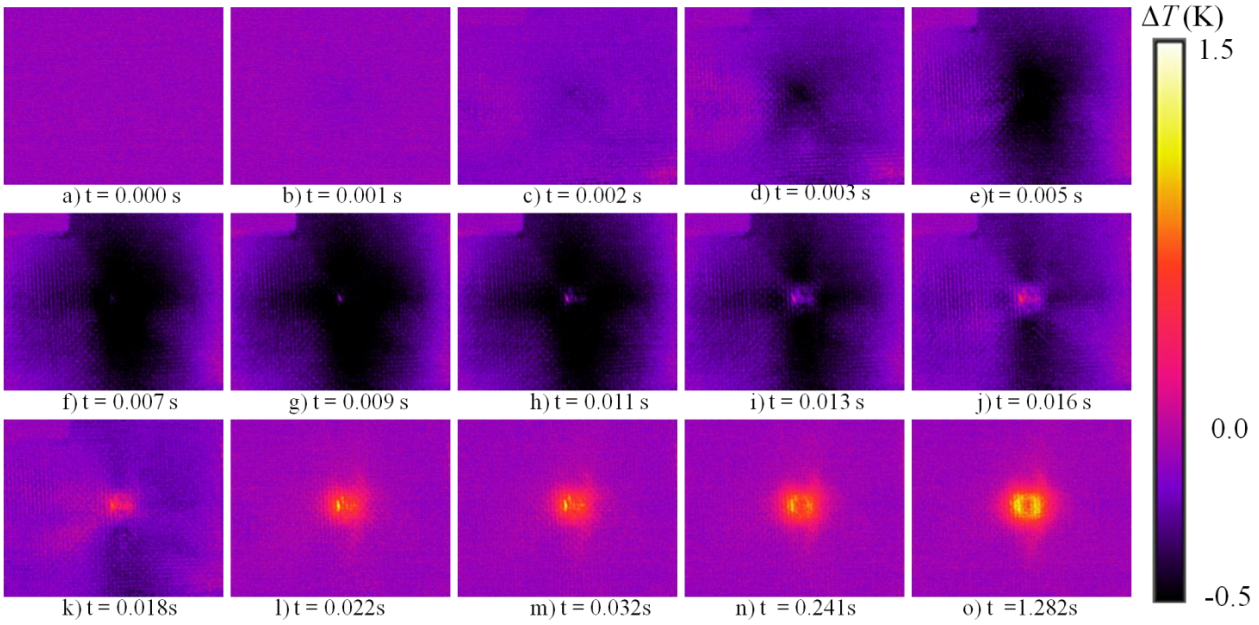

Fig. 5.19. Some ΔT images of PPG specimen impacted at E = 12 J.

As already said, for all the showed figures, the first image (a) (t = 0) represents the specimen surface just before the impact. Then the ΔT variations in the successive images have to be considered as induced by the impact. It is worth noting that the same scale was chosen for all the reported ΔT images to give information about the ΔT variations with time; while maxima and minima values of ΔT are reported in Table 5.4. Starting from the $CFRP_F$ specimen impacted at 10 J (Fig. 5.15), it is possible to see a darker spot firstly appearing at t = 0.001 s (Fig. 5.15b) (not existing in the initial image shown in Fig. 5.15a); such a darker spot lets to suppose that the impactor nose just touched the specimen surface. Later, (Fig. 5.15c,d,e), this dark spot reinforces and enlarges, meaning that the specimen is bending under the impactor pushing force (i.e., the

viewed surface is in tension) while hot stripes appear inside the darker zone (Fig. 5.15f), highlighting the fibres texture of the $CFRP_{FU}$ specimen.
Going on in time, the dark zone becomes smaller until it disappears (Fig. 5.15i); this means that the specimen has recovered its undeformed configuration (the material is no more under tension). The lighter (hot) structures appear at t = 0.005 s (Fig. 5.15f) and evolve into a well consolidated almost circular area (Fig. 5.15k–o). As the impact energy increases to 18 J (impact performed on another place of the same specimen), the most important feature to evidence is the material break up displayed through a hot zigzag structure surrounded by a darker zone. This darker zone disappears at about 0.01 s, meaning that the surface is no more under tension. Later, the hot area enlarges along the - 45° direction (Fig. 5.16k and l). More later, the warm area appears to enlarge also along fibres at +45° (Fig. 5.16 m-n) and further on tend to assume a circular shape (Fig. 5.16o). The thicker $CFRP_{NC}$ specimen impacted at 39 J (Fig. 5.17) displays only thermoelastic effects; in fact, a dark central zone is present on images taken at t in the range 0.001s - 0.009 s while for t = 0.012 s the specimen surface recovers its undeformed condition and practically the initial temperature distribution.
From Fig. 5.18, it is possible to get information on the response of the GFRP specimen to an impact of 8.3 J. Signs of cooling down can be firstly recognized at t = 0.001 s (Fig. 5.18b), which accounts for starting of the surface bending under the impactor pushing force and which would also mean that the surface is in contact with the impactor nose. Such a cooling down later strengthens (Fig. 5.18c-j) as the surface further bends under the pushing impact force. For t = 0.002-0.003 s (Fig. 5.18c-d), a fibres bundle inside the cool stain displays slight temperature increase ($\Delta T \cong 0$) bearing witness for the formation of micro-cracks there. For t = 0.004 s (Fig. 5.18e) one small hot spot appears and is later followed by other hot spots. More later, any dark zone completely disappears (Fig. 5.18l) and the hot spots enlarge and tend to coalesce (Fig. 5.18o) while a unique slight warm area forms around them; indeed, at last, a unique warm area forms accounting for the whole damaged area. The duration of the cooling down may be assumed to coincide with the whole time the surface is affected by bending, triggered by the impact pushing force. Instead, the size of the cool (dark) stain supplies information on the extension of the surface affected by deformation induced by the impact and so on the extension of the whole impact-affected area.
A different shape is attained by the dark (cold) stain for the specimens having a thermoplastic matrix. In fact, for the PPG specimen (Fig. 5.19) impacted at the energy of 12 J, the cooling down starts with oblique rays which evolve first into an oblong structure and later reduces into fans mostly along the vertical direction. At t = 0.009 s (Fig. 5.19g), a hot spot appears at the centre, which grows in time to form a rectangular shaped structure for t = 0.016 s (Fig. 5.19j). In the meantime, the dark zones first become clearer fanning out and after disappear. By following the evolution of the dark zone it may be possible to get information about the surface deformation under impact.
Some ΔT images, of the specimen PLAJ (involving natural fibres of jute embedded in a matrix of PLA) impacted at 3 J, are shown in Fig. 5.20. Also in this case, the first ΔT image (Fig. 5.20a) displays an almost uniform colour (ΔT = 0) when the specimen surface is at ambient temperature immediately before the impact. Sudden at the impact, a central dark zone (Fig. 5.20b) indicates local cooling down in correspondence of the surface bending under the impactor pushing force. Later, a small light (hot) dot appears (Fig. 5.20d); this is located almost at the tip of the impactor and may indicate that the maximum curvature for the material elastic phase has been reached and cracks start to form. Afterward, other hot spots appear drawing a bright path along fibres bundles,

which also indicate the fibres breakage and pullout direction. More specifically, the hot spots are distributed aligned over two lines horizontal and vertical to form a cross (Figs. 5.20f-o).

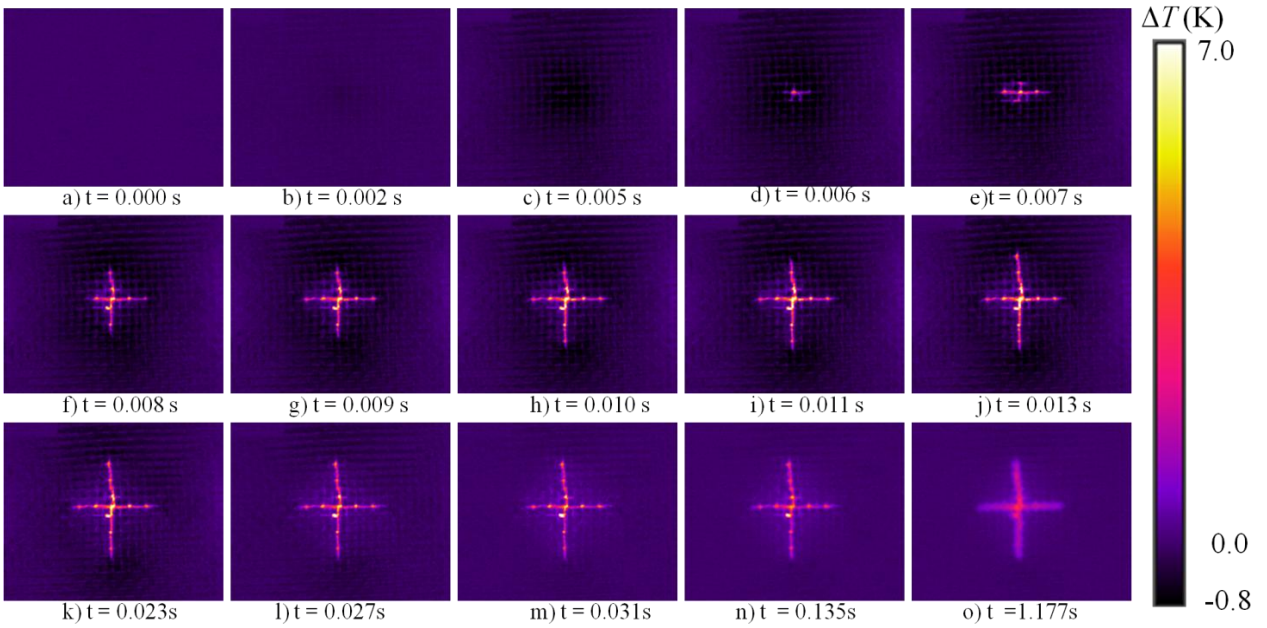

Fig. 5.20. Some ΔT images of the PLAJ specimen impacted at E = 3 J.

From an analysis of all thermal images, the following information can be obtained:

A. Locate the initial formation of hot spots which correspond to the initiation of the impact damage.

B. Follow the evolution of such hot spots to get information on the damage progression.

C. Check the maximum temperature rise since high ΔT values are caused by fibres breakage.

D. Assess the extension of the warm area to find the extension of delamination; in other words, finding the border of the heat affected zone would mean locate the extension of delamination.

These pieces of information can be exploited to advance knowledge about the behaviour of composites under impact.

5.6. Analysis of impact dynamics

To investigate the impact dynamics, the sequences of images acquired with the SC6800 camera are analyzed. As a first step, each sequence of thermal images is post-processed in order to extract the corresponding ΔT images according to Eq.(5.1)

5.6.1 ΔT evolution under impact

In general, it is possible to follow any temperature variation in time pixel by pixel over the whole specimen surface. As an example, the ΔT distribution in a small central area (4x4 pixels) over the

surface of the specimen GFRP impacted at E = 2.8 J is displayed in Fig. 5.21. As can be seen, at the impact, ΔT starts from a zero value (before the impact), suddenly decreases below zero (to about 1 K), abruptly goes up to a value of about 4 K and then progressively tends to decrease towards zero.

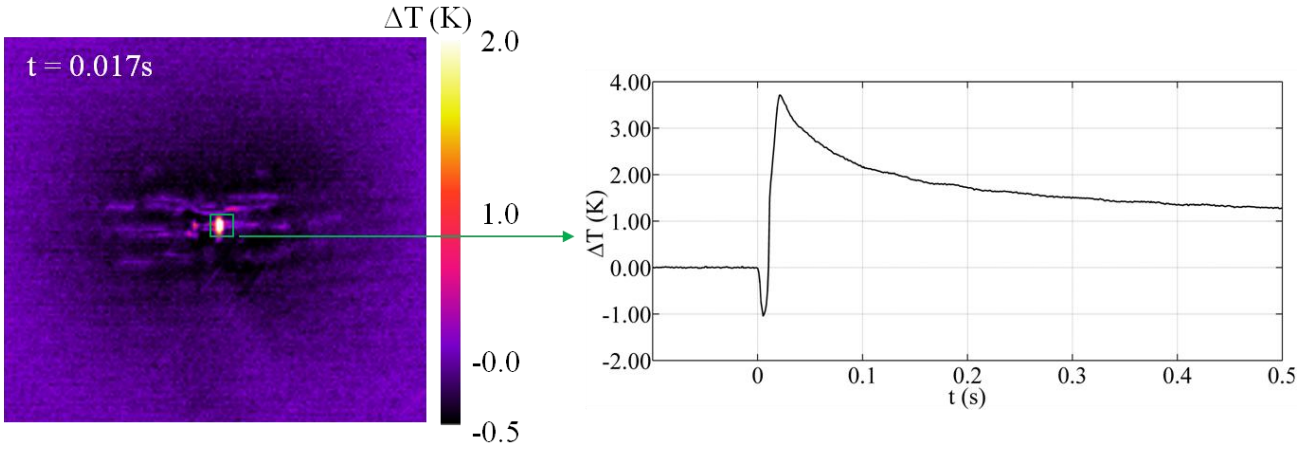

Fig. 5.21. Distribution of the average ΔT value inside the green area of the specimen GFRP impacted at 2.8 J.

As already affirmed, the cooling down is associated with the material elastic expansion in which the impact energy is absorbed without retaining any permanent volume and shape variations. Instead, the heating up is associated with the plastic deformation in which a part of the impact energy is dissipated and absorbed by the material as internal energy with permanent material modifications.
As the impactor touches the specimen surface, a sudden cooling down ($\Delta T < 0$) is visualized on the opposite (to the impacted one) surface, which undergoes convex curvature. The temperature decrease is proportional to the surface curvature, the material characteristics and the impact energy; in particular, ΔT may generally range from a value close to zero down to about -2, or -3 K. As already shown, the material behaves in a different manner under impact, owing to the type of matrix being: thermoset, or thermoplastic. In particular, for thermoset matrix based composites, two phases: thermo-elastic and thermo-plastic ones can be recognized through the manifestation of cooling/heating thermal effects. So, a thermoset matrix composite, at very low impact energy, may display only thermo-elastic effects. Conversely, a thermoplastic matrix based composite behaves in a different manner, generally undergoing plastic modifications also at very low impact energy. To avoid confusion, in this chapter the term thermoplastic (one word) is used when referring to the type of matrix, while the term thermo-plastic is used when referring to thermal effects.

5.6.2 Quantitative analysis of results

To better investigate impact dynamic effects, minima and maxima ΔT values are extracted, from each image of the sequence, in a region sufficiently wide (142x166 pixels) to include the overall impact affected area, and plotted against time in the following Figs. 5.22 and 5.23. In particular, Fig. 5.22 displays the distribution of ΔT values for each specimen with the scale optimized to visualize minima (minima and maxima values are collected in Table 5.4 together with time parameters defined in Fig. 5.24).

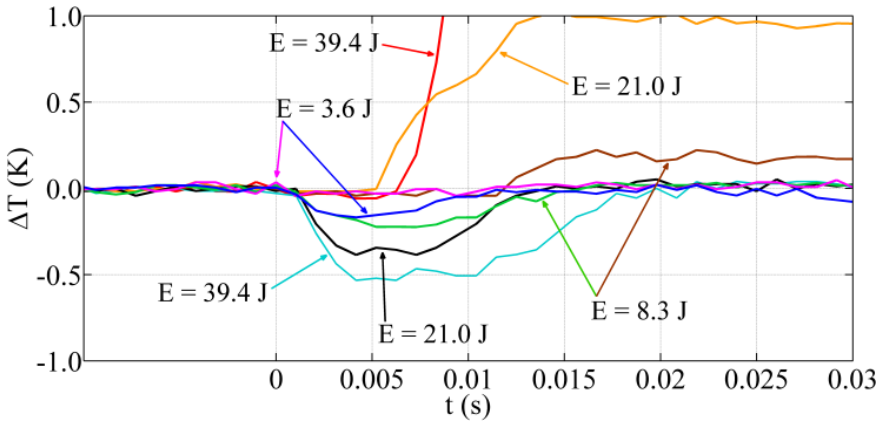

a) AFS specimen.

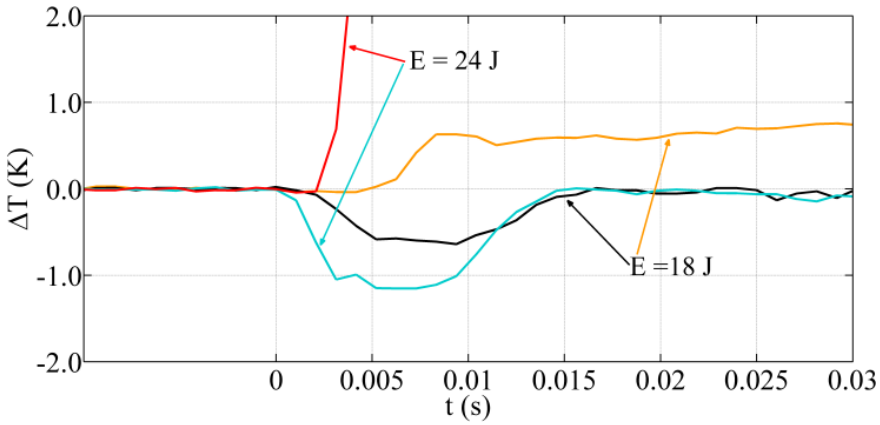

b) $CFRP_F$ specimen.

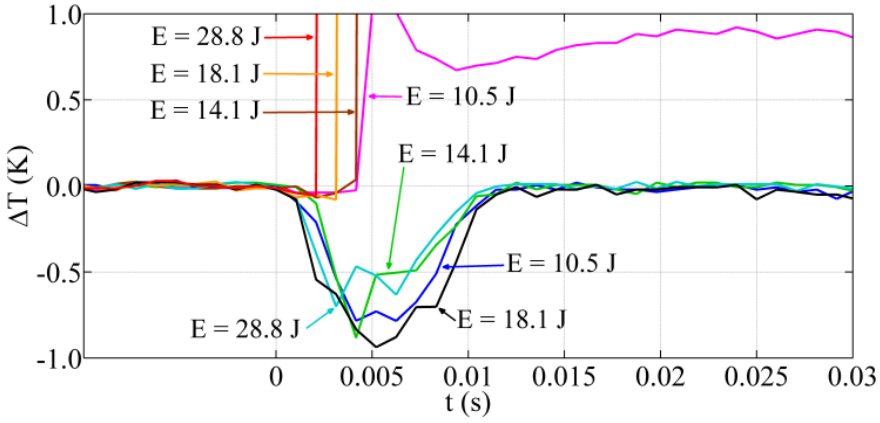

c) $CFRP_{FU}$ specimen.

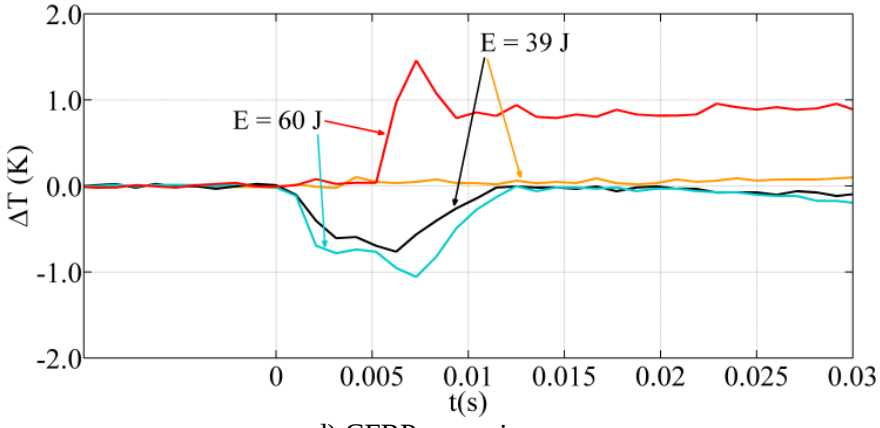

d) $CFRP_{NC}$ specimen.

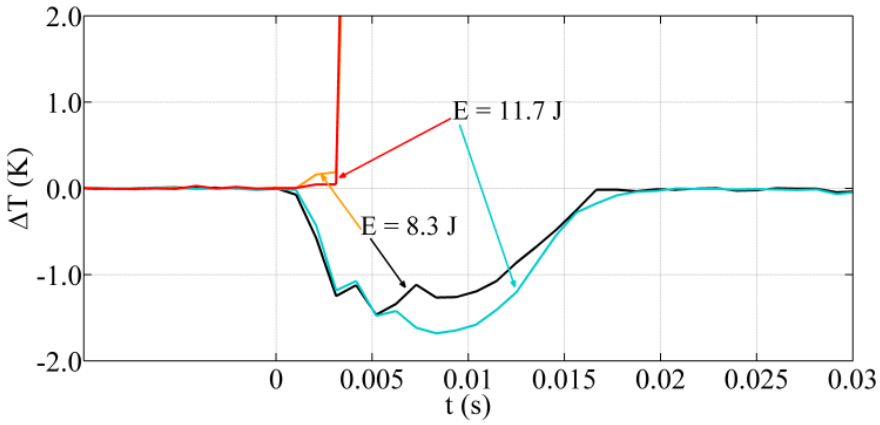

e) $CFRP_U$ specimen.

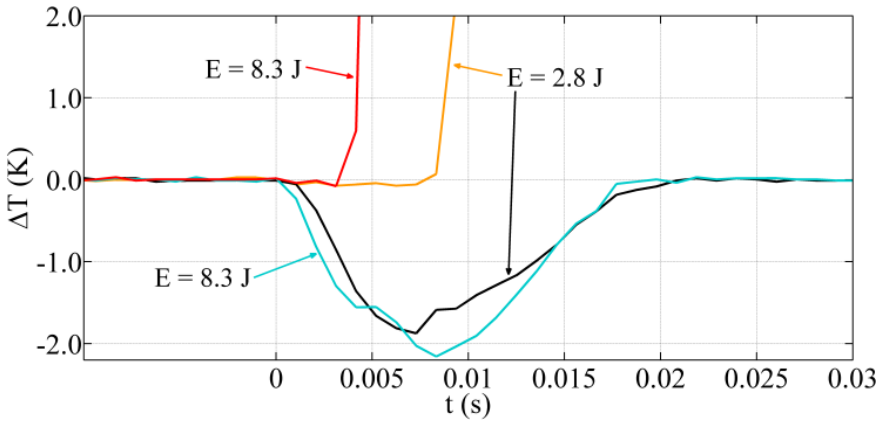

f) GFRP specimen.

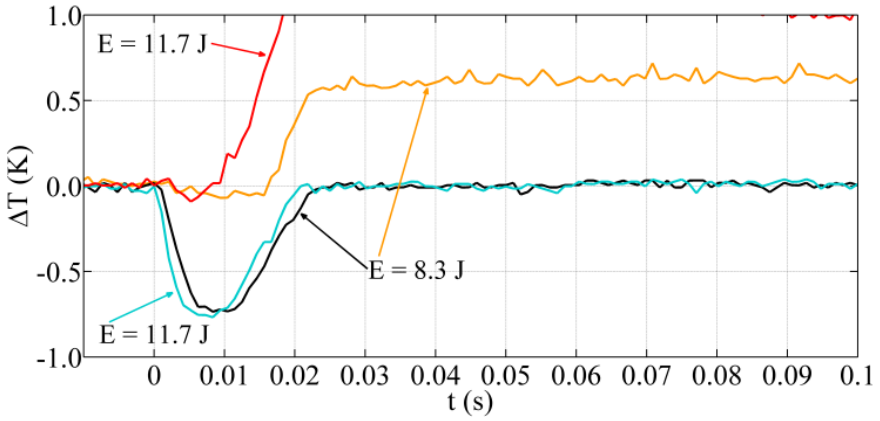

g) PPG specimen.

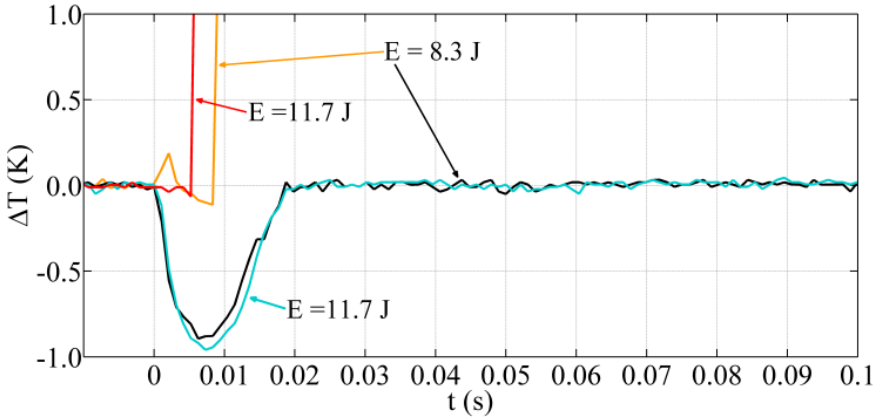

h) PGC2 specimen.

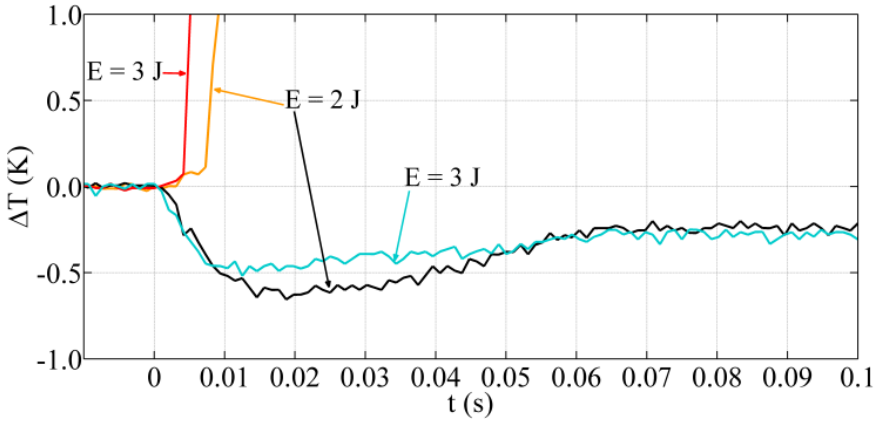

i) PPJ specimen.

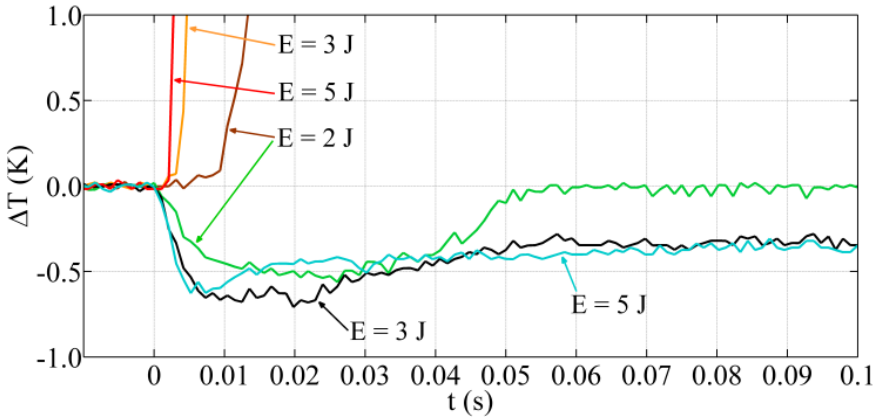

j) PJC2 specimen.

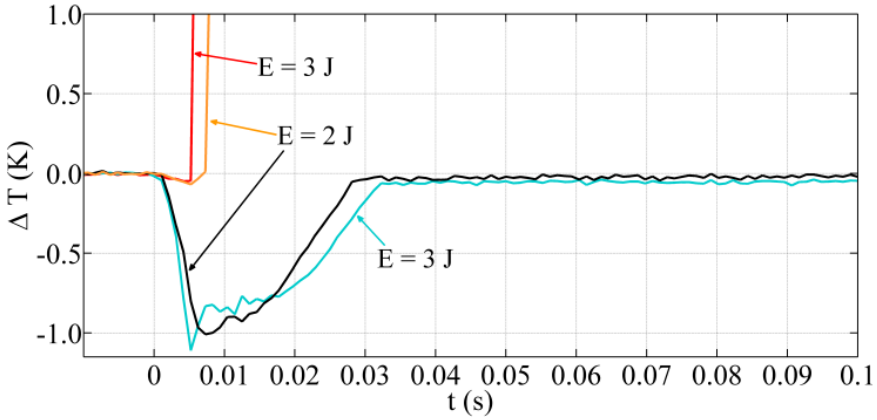

k) PLAJ specimen.

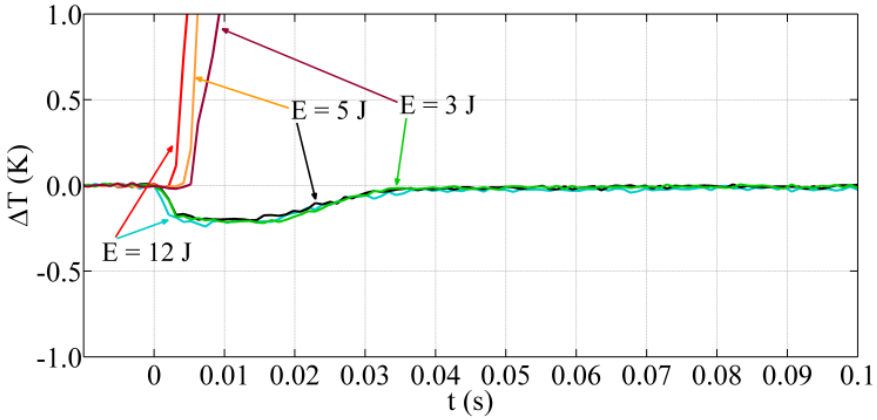

l) PEF specimen.

Fig. 5.22 Δ*T* evolution with time.

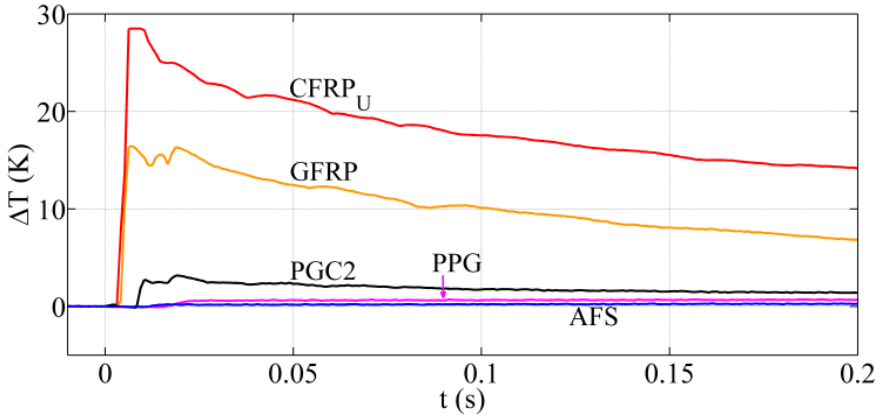

a) ΔT_{Max} for E = 8.3 J.

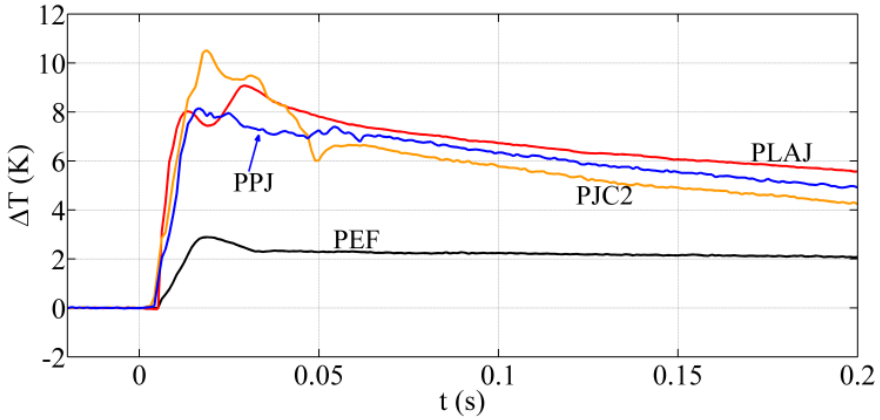

b) ΔT_{Max} for E = 3 J.

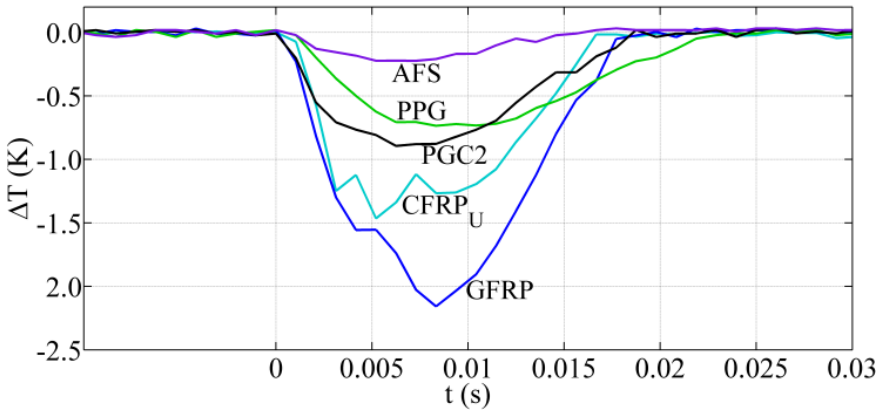

c) ΔT_{Min} for E = 8.3 J.

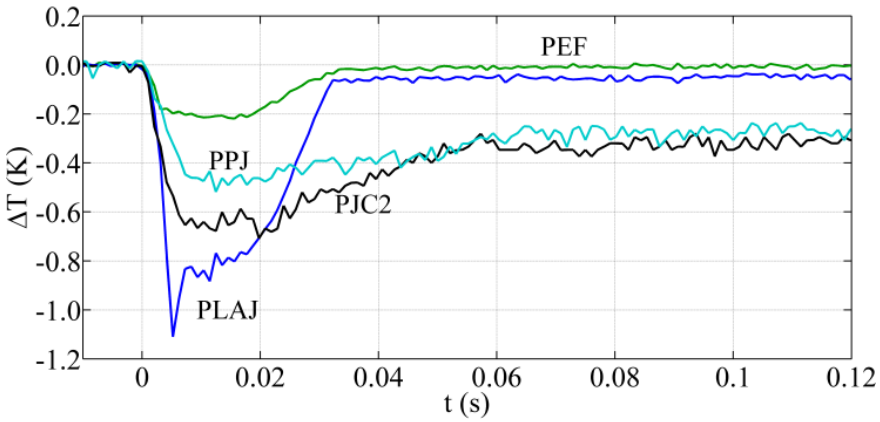

d) ΔT_{Min} for E = 3 J.

Fig. 5.23 Distribution of ΔT_{Max} and ΔT_{min} values.

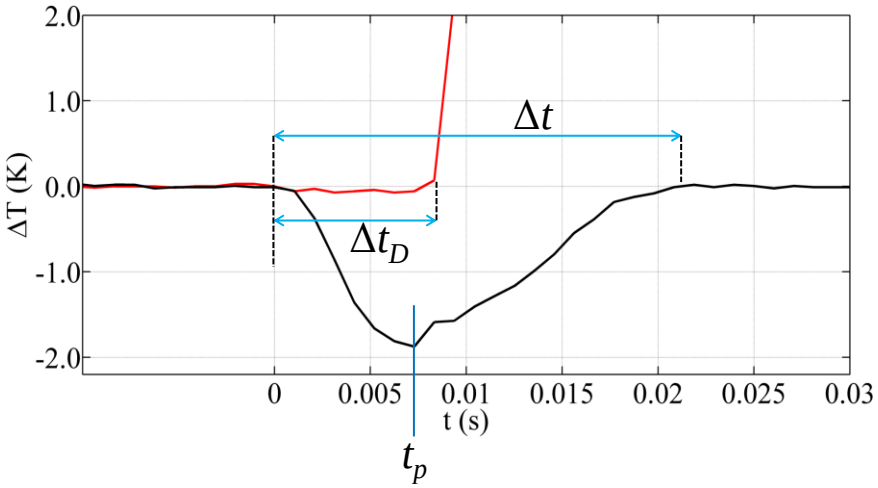

Fig. 5.24 A scheme with time parameters.

A comparison between maxima and minima of several different specimens impacted at the same energy is supplied in Fig. 5.23. As it can be seen, for each impact energy, the relative graph displays a concavity in the ΔT_{Min} values and a hill with a first abrupt rise in the ΔT_{Max} values.

Starting from ΔT_{Min} values, the concavity can be analyzed in terms of width and height (i.e., its extension along the coordinate axes), which also means the minimum value reached (ΔT_{Min}) and the duration in time (Δt), respectively. On the whole, for specimens of the same material and thickness, ΔT_{Min} generally decreases with increasing the impact energy. However, as can be seen from Figs. 5.22b–f, the latter effect is more accentuated for specimens involving a thermoset matrix. Instead, ΔT_{Min} seems to be almost independent of the impact energy for specimens based on a thermoplastic matrix, which display a much smoother concavity (see Figs. 5.22g-l). From the comparison of ΔT_{Min} for thermoset and thermoplastic matrix based materials in Fig. 5.23c for E = 8.3 J, it is possible to seen as the three specimens GFRP, PG and PGC2 are characterized by different curves, notwithstanding they only differ for the matrix composition.

From all the shown graphs, it can be inferred that the lowest ΔT_{Min} value, which is reached at the tip of the concavity at time t_p, corresponds to the impactor strongest pushing force, or better to the peak contact force [20,56,57]. In addition, as the impactor moves back, ΔT_{Min} tends to recover its initial zero value, but at different times Δt depending on the type of material. At this point, to try to understand more on the reaction of composites to impact, in particular, the time interval the impactor nose remains in contact with the surface of the specimen and what happens to the surface once this contact dies away.

Then, the two parameters ΔT_{Min} and Δt are separately analyzed.

As regards ΔT_{Min}, t_p broadly lies within the interval 0.003 s $\leq t_p \leq$ 0.012 s for most specimens and impact energies. In particular, t_p generally attains lower values for CFRP specimens and higher ones for thermoplastic specimens. Except for the AFS specimen in which Δt seems to be more influenced by the impact energy, the value of Δt depends strongly on the type of material (e.g. Figs. 5.22a and l) and slightly on the impact energy (e.g., Fig. 5.22c). Within the investigated specimens, the minimum $\Delta t \cong 0.013$ s is reached by the thicker specimens $CFRP_{NC}$ (Fig. 5.22d) and $CFRP_{FU}$ (Fig. 5.22c), while the maximum $\Delta t \cong 0.065$ s is attained by the PPJ specimen (Fig. 5.22i), meaning that Δt strongly depends on the material stiffness. The inversion of the slope may be assumed as indicative of the time instant in which the impactor ceases to push. Once the pushing force ceases, two different behaviours can be observed depending on the type of material.

- Thermoset matrix – the surface tends to straighten and, as it recovers its undisturbed unbent configuration, any cooling effect disappears. The two sides of the concavity ascent and descent are almost equal. It is worth noting that the jagged contour prevents from a definite location in time of the ΔT_{Min} minimum (t_p value).
- Thermoplastic matrix and AFS – the surface undergoes plastic deformation while bending under the impactor pushing force and so, it remains curved also after removal of the pushing force. Then, it continues to appear cold for a longer time till a thermal equilibrium is reached due to conduction heat transfer; this may take some time and then the ascent side is longer than the descent one. Besides, for specimens PPJ, PJC2 and PLAJ impacted at 3 and 5 J the ΔT values, after the descent tracts, does not return to 0 but remains constantly negative for a long time (Figs. 5.22i, j). This occurs because of material breakage with total penetration as can be seen from photos of the PPJ specimen (Fig 5.25).

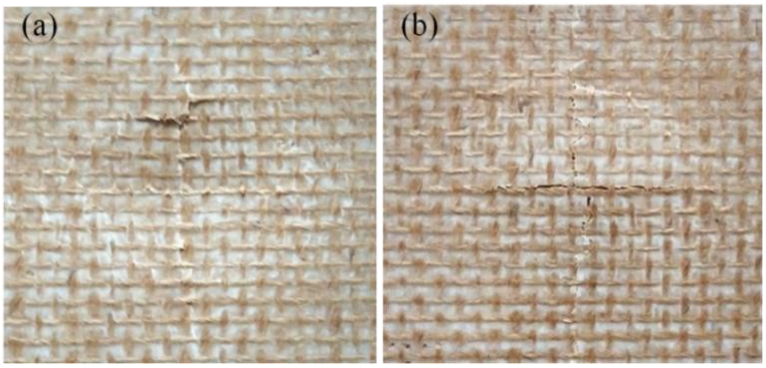

Fig. 5.25. Photos of PPJ specimen impacted at 5 J. (a) Front surface, (b) Rear surface.

In any case, the duration of the descent side may be assumed as indicative of the time interval to reach the peak contact force, while the successive evolution (ascent side) may help to evaluate the overall impact affected-area. Turning back to the analysis of ΔT_{Max} values, it is possible to see again different behaviours of the different specimens.

The heating phase is completely absent - This means that the impact energy entails only reversible thermo-elastic phenomena and it is released without permanent material deformation as for the $CFRP_{NC}$ specimen impacted at E = 39 J (Fig. 5.17).

The heating phase is present but lags behind the cooling one - This means that a part of the impact energy is absorbed with permanent material deformation; many examples are evident from Figs. 5.22a–l. The evaluation of the time delay (Δt_D) coupled with the ΔT_{Max} value (Table 5.4) may help understand more about the occurred damage. On the whole, it is possible to see that ΔT_{Max} increases with increasing the impact energy and Δt_D decreases. However, some exceptions can be found such as a higher ΔT_{Max} value at a lower impact energy (see ΔT_{Max} values for the $CFRP_{FU}$ specimen); this may be most probably due to the presence of local inhomogeneities.

The heating phase starts simultaneously with the cooling one - This means that the impact energy is high and causes important damage, sudden at the impact. Of course, this is true to the accuracy of the used frame rate of 960 Hz. An example is provided by the $CFRP_{FU}$ specimen impacted with E = 28.8 J (Fig. 5.22c) where a sudden breakage of fibres occurs accompanied by an abrupt temperature rise (ΔT_{Max} = 33 K, Table 5.4).

Code	Thickness (mm)	Energy (J)	ΔT_{Min} (K)	ΔT_{Max} (K)	Δt (s)	Δt_D (s)
$CFRP_U$	2.3	8.3	-1.47	28	0.017	0.001
$CFRP_U$	2.3	11.7	-1.68	29	0.021	0.003
$CFRP_F$	3.2	18	-0.64	0.6	0.017	0.005
$CFRP_F$	3.2	24	-1.15	25	0.016	0.002
$CFRP_{FU}$	5.0	10.5	-0.78	1.3	0.013	0.004
$CFRP_{FU}$	5.0	14.1	-0.88	31	0.013	0.004
$CFRP_{FU}$	5.0	18.1	-0.70	27	0.013	0.003
$CFRP_{FU}$	5.0	28.8	-0.94	33	0.013	0.002
$CFRP_{NC}$	7.8	39	-0.77	<0.1	0.013	----------
$CFRP_{NC}$	7.8	60	-1.10	1.5	0.013	0.005
GFRP	2.9	2.8	-1.87	9	0.021	0.007
GFRP	2.9	8.3	-2.16	16	0.019	0.003
PPG	3.0	8.3	-0.74	0.6	0.024	0.016
PPG	3.0	11.7	-0.77	1.2	0.021	0.009
PGC2	3.0	8.3	-0.89	3.1	0.019	0.008
PGC2	3.0	11.7	-0.96	32	0.019	0.005
PPJ	3.8	2	-0.65	7.0	0.066	0.006
PPJ	3.8	3	-0.52	8.2	0.066	0.004
PJC2	3.8	2	-0.56	3.3	0.056	0.009
PJC2	3.8	3	-0.71	10.5	0.057	0.003
PJC2	3.8	5	-0.63	9.7	≅0.067	0.002
PLAJ	3.8	2	-1.01	5.09	0.028	0.007
PLAJ	3.8	3	-1.11	9.08	0.032	0.005
PEF	3.6	3	-0.21	2.89	0.042	0.005
PEF	3.6	5	-0.20	5.94	0.050	0.004
PEF	3.6	12	-0.24	10.59	0.048	0.002
AFS	10.0	3.6	-0.17	<0.10	0.021	-------
AFS	10.0	8.3	-0.22	0.30	0.019	0.011
AFS	10.0	21	-0.39	1.20	0.016	0.005
AFS	10.0	39.4	-0.53	4.88	0.022	0.006

Table 5.4. ΔT and Δt values of the different specimens.

As can be seen from Figs. 5.22a–k and Table 5.4, the material characteristics, mainly the type of matrix, play a key role in the development of ΔT_{Max} values. This is better shown in Fig. 5.23 where ΔT_{Max} plots of different materials impacted at the same energy are compared. In particular, the comparison is made between three matrices: epoxy resin (CFR_{PU}, GFRP), neat polypropylene (PG) compatibilized polypropylene (PGC2), reinforced with carbon fibres (CFR_{PU}) and glass fibres (GFRP, PG, PGC2). It seems that the time of the heating onset Δt_D depends on the matrix, while ΔT_{Max} is influenced by the fibres types. In fact, within the same epoxy resin matrix, the specimen $CFRP_U$ involving carbon fibres is more vulnerable to fibres breakage, which is accompanied by a larger quantity of energy dissipation and rise of ΔT_{Max} (Fig. 5.23a), while the GFRP specimen including glass fibres appears more bendable showing the lowest ΔT_{Min} value (Fig. 5.23c). While

keeping constant the reinforcement (glass fibres), the type of matrix affects both ΔT_{Max} and Δt_D (Fig. 5.23a). In particular, the addition of a small percentage (2%) of compatibilizing agent to the pure polypropylene modifies the behaviour of the material; in fact, with respect to the PG specimen, the PGC2 one shows higher ΔT_{Max} and lower Δt_D one. As a general observation, it seems the trend of ΔT_{Min} values be disrupted by the appearance of hot spots/areas, mainly apparent for CFRP specimens. In fact, it is possible to see a sudden slope inversion in correspondence of the vertical tracts (see Figs. 5.22c-e). In addition, as already evidenced, for specimens PPJ and PJC2, impacted at 3 J the ΔT_{Min} values, after the descent tracts, does not return to 0 but remains constantly negative for a long time (Fig. 5.23d).

5.6.3. ΔT and Δt as clues of the impact damage

The attention now is devised to see whether the five parameters: ΔT_{Min}, ΔT_{Max}, t_p, Δt and Δt_D in Table 5.4 can be exploited to quickly evaluate onset and importance of impact damage.
Starting with ΔT_{Max}, it was already observed for glass/epoxy specimens a link between onset of material breakage and abrupt temperature rise [48]. Such a link, owing to Table 5.4, seems practically confirmed, for almost all the investigated materials. In particular, the $CFRP_F$ specimen displays a ΔT_{Max} value of only 0.6 K when impacted at 18 J, while a value of 25 K when impacted at 24 J. Such a stronger heating, which, at first sight, may appear exaggerated as compared to the variation of impact energy, is fully understandable considering the way a thermoset matrix based composite reacts to the impact [58-61]. In fact, micro-cracks in the matrix and light delaminations are accompanied by small temperature variations while breakage of fibres entails a strong rise of temperature [48]; these observations well comply with the existence of the two regions of damage initiation and propagation [62,63]. More specifically, for low impact energy the damage is mostly characterized by matrix cracks and small delamination ($E_d = E_{dd}$ in Eq.5.3); as the impact energy reaches a critical value, the damage becomes more important with fibres breakage and large delaminations ($E_d = E_{db} + E_{db}$ in Eq.5.3). This critical impact energy, as well as the associated ΔT_{Max} value, strongly depends on the type of material and the eventual presence of defects. In fact, the local volumes of matrix and fibres, the likely present manufacturing defects and other factors may affect the subdivision of E_d between E_{db} and E_{dd}, which in turn affects the temperature rise. Of course, the energy spent to produce one point break in a fibre may be the same of that spent to produce a large disband of two surfaces. The two energies may be equal but the local temperature rise is certainly greater in the first case and then the variations of ΔT_{Max} with impact energy and materials are justified.
As a main finding, what we have to learn is that an infrared imaging device is able to tell exactly what is happening during an impact event.
With regard to t_p, as already mentioned, it can be assumed to coincide with the time necessary to reach peak contact force since ΔT_{Min} should be associated with the maximum surface displacement. Unfortunately, the Charpy pendulum was not instrumented to allow recording of time history (deceleration/acceleration, contact force, etc.) to have a direct validation. From a comparison with data available in literature [56,57], a general agreement is found in regard to the orders of magnitude. Indeed, some discrepancies are found in literature since it seems the time to reach peak force is double in Ref. [56] with respect to that of Ref. [57]; this may be justified by the different materials and thicknesses involved. However, a comparison may be critical because the impact

event is strongly influenced by many factors such as the type of composite material and its thickness, impactor geometry, boundary conditions and test fixture as well. Nevertheless, it seems some important impact features can be derived directly from thermographic images.
The value of ΔT_{Max} coupled with Δt_D may help the comprehension of damage importance and dynamics. In fact, as already discussed, ΔT_{Max} supplies indications about the importance of the damage occurred since a low ΔT_{Max} value is a symptom of light delamination, or small material permanent deformations, while a high ΔT_{Max} value surely indicates severe damage with fibres breakage. In the meantime, the value attained by Δt_D bears evidence of the occurred damage and also serves as validation for the information supplied by ΔT_{Max}. As a first observation, there is a link between Δt_D and ΔT_{Max} since ΔT_{Max} increases as Δt_D decreases and viceversa. In particular, a very small Δt_D value means that the plastic phase starts contemporaneously with the thermo-elastic one meaning that the material suddenly breaks at the impact. In this case, the absorbed energy (Eq. 5.3) is mostly spent in fracturing the material and very little to delaminate it; the overall delamination is slightly extended. Conversely, a large Δt_D value is generally coupled with a small ΔT_{Max} value, meaning that the damage is slight and the overall impact affected area is driven by ΔT_{Min}, and Δt values.
As an important finding, for each of the investigated test conditions (types of material and impact energies, see Figs.5.22a–l), it seems that the maximum Δt_D value is achieved in correspondence of the ΔT_{Min} peak (i.e., peak contact force). It is worth noting that the orange line in Fig. 5.22g, which is relative to the PG specimen impacted at E = 8.3 J, does not indicate a longer Δt_D value, but rather absence of the heating phase since the ΔT_{Max} value is very small. Practically, owing to a thin thermoset matrix panel, the longer Δt_D value represents the time instant at which cracks begin to form on the rear (opposite to impact) surface when it has reached its critical curvature under the impactor pushing force. This may also be assumed to correspond to the critical impact energy for which a percentage of impact energy is absorbed and the material behaviour is no more in its reversible elastic phase. This is in general agreement with the general belief that the damage process is initiated by matrix cracks [59,60].

5.7 Measurement of impact damaged area.

Assessing the importance of the damage for a given energy represents perhaps the most important aspect of impact tests. To this end, the first step is to define the meaning of the impact-damaged zone. In this regard, it is possible to distinguish almost two zones of different importance: one of severe damage including fibre breakage and the other one of slight delamination. The first one may be small, sometimes including only some hot spots, or wider including large breakage and important delamination. The second one is quite large, enclosing the entire impact-affected area with of course light delamination over the contour. The extension of the overall impact-damaged area can be approximately sketched (Fig. 5.26) in analogy with the propagation of seismic waves. More specifically, the central red zone is that impacted by strong damage and is surrounded by circles of increasing diameter that represent regions of decreasing damage levels . It is worth to underline that the red circle does not coincide necessarily with the impact point but it indicates the most severe damage with the highest value of ΔT.

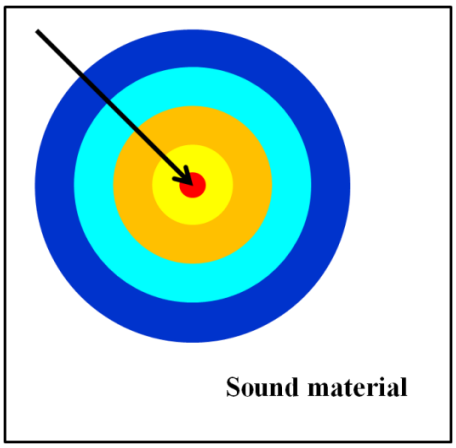

Fig.5.26. Schematic representation of impact damage levels. The arrow indicates the increasing level of damage and of ΔT.

However, this is only a schematic representation, while, for a full description, the material characteristics must also be considered. Basically, the matrix drives the damaging modes meaning that composites should be grouped owing to the type of matrix: thermoset, or thermoplastic. Starting with thermoset composites, two basic behaviours under impact can be recognized, depending on the thickness of the laminate [64]. Thin laminates can absorb the impact energy as bending deformation with the highest stresses developing at the laminate rear surface; the damage is described with the reversed pine tree pattern (Fig. 5.27). In the case of thick laminates, the matrix cracks form at the impact surface due to the high contact stresses arising under the contact with the impactor; the damage spreads out from the impact to the rear surface through the typical pine tree configuration. However, since there is not a defined thickness value separating the above described behaviours, when analyzing specimens with a wide range of thicknesses a more complex behaviour might be observed.

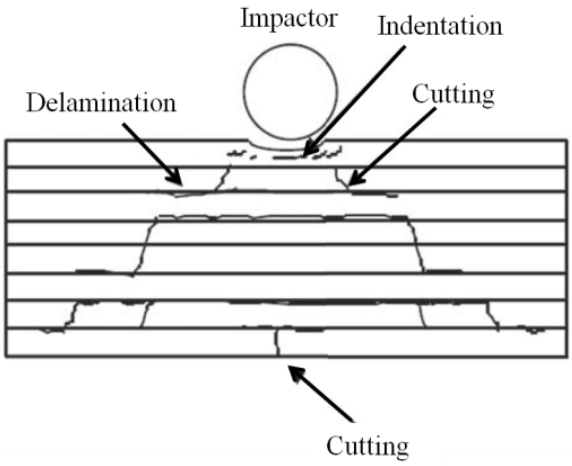

Fig.5.27. A scheme of impact damage evolution in thin thermoset matrix based composites.

Composites including a thermoplastic matrix behave in a different manner under impact. In fact, they undergo visible deformation displaying an indentation (a small concavity) on the impacted side and a protrusion on the rear one. Of course, these modifications are very small for very low impact energy, while they become ever more evident with increasing the impact energy. However, thermoplastic composites, while resembling ductile metals for the superficial appearance, are

characterized by more complex impact damage mechanisms, which strongly depend on the type of matrix and on the impact energy.
Whatever the type of composite, it is important to know:

1. if a hot zone (with material breakage) is present and how wide it is;
2. what happens to the material in the absence of breakage;
3. how wide the impact-affected zone is.

Finding an answer to these questions may help understanding more on the impact damaging mechanisms in the light of the failure prediction and design of composite materials. Infrared thermography can be exploited to get such answers.
To get information about the overall extension of the impact damage, sequences of ΔT images are subjected to successive post-processing with routines specifically developed in the Matlab environment.

5.7.1 Estimation of the impact damage along horizontal and vertical directions

The first step in evaluating the impact damage extension starting from IR images, is to measure two diameters along horizontal and vertical directions of the heated area. To this end, the sequences of ΔT images are post processed by using the Matlab software in order to extract ΔT profiles along x and y directions for several values of t (time after impact). Some examples are reported in the following Figs. 5.28-5.35.

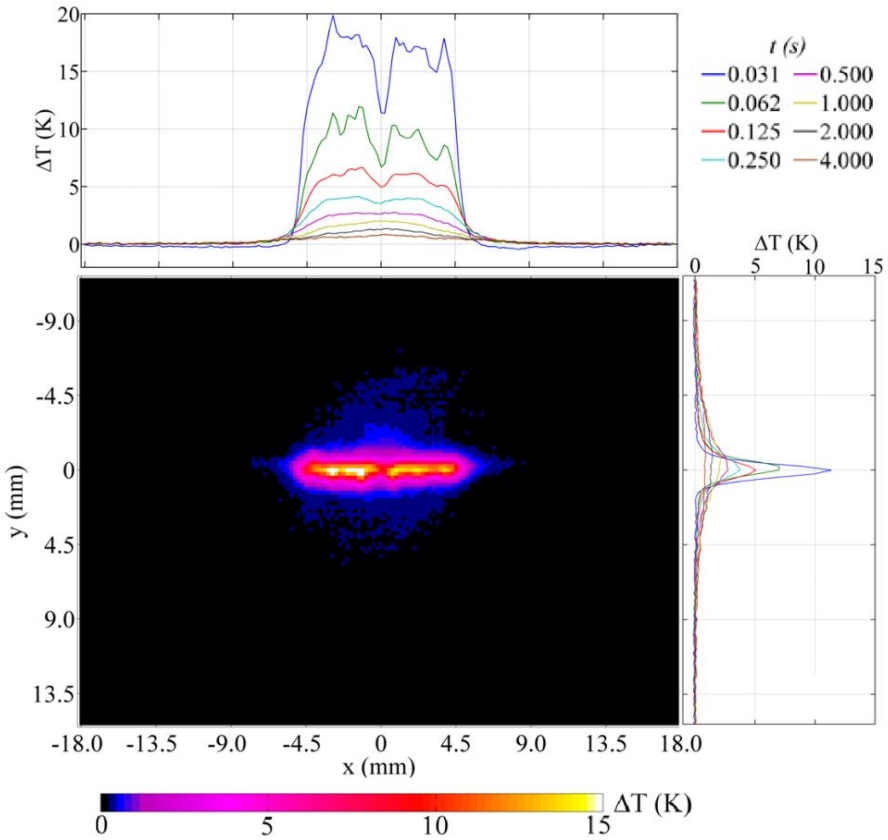

Fig. 5.28. ΔT image taken at t = 0.031 s and profiles along x and y directions of the specimen $CFRP_U$.

A ΔT image, taken with the SC6000 camera 0.031 s after impact at 10 J of a $CFRP_u$ specimen, is reported in Fig. 5.28 together with ΔT profiles along the vertical and horizontal directions. More specifically, $\Delta T(x)$ passes through $y = 0$, while $\Delta T(y)$ passes through $x = 0$. In particular, a hot (white) oblong structure is present over the CFRP specimen accounting for fibres breakage along their horizontal (longer side) direction. Such a structure is surrounded by a lighter area on top and bottom and spiky ends on left and right sides; the lighter colour (i.e. slight temperature rise) indicates the overall delamination. From the ΔT profiles, it is possible to measure the two diameters D_H and D_V along horizontal and vertical directions, respectively. Basically, since the hot zone lasts for some time (see the different curves), one could perform measurements of D_H and D_V within a certain time interval. However, some problems may arise because of the lateral thermal diffusion, for which, as the maximum ΔT decreases, the warm area tends to enlarge, especially along y this may lead to an overestimation of the D_V value.

Since it appears clear that all curves overlap towards $\Delta T = 0$, the two graphs of Fig. 5.28 are shown again in Fig. 5.29a and b with magnification (smaller ΔT scale) to facilitate discrimination between the different curves and to better appreciate the small differences from the 0 value of ΔT. It has to be noticed that the blue curve attains the highest ΔT value but presents also negative values being affected by the thermo-elastic effects, still present for $t = 0.031$s. Then it seems more appropriate to refer to the second curve, which seems no more affected by thermo-elastic effects and not yet by the diffusive ones.

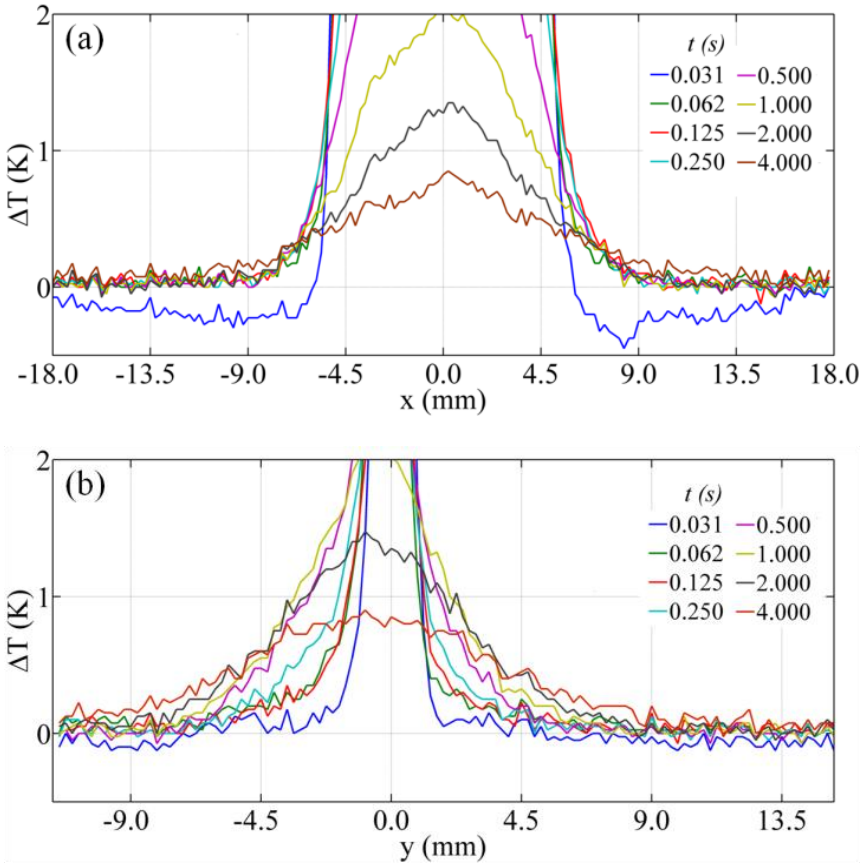

Fig. 5.29. Magnification of ΔT profiles of Fig. 5.27.

Attempting to measure D_H along the x direction (Fig. 5.29a), it seems that, by excluding the first blue and the last red, all curves appear well overlapped not only in the horizontal tracts but also at

the beginning of the lift at about ±10 mm from the centre (x = 0). Owing to the change of slope of the curves and assuming a ΔT_b value close to zero, the distance of about 20 mm can be assumed as the overall D_H value, or better, as the overall extension of delamination along x. More complex appears the evaluation of D_V along the y direction because of the large data fluctuations (Fig. 5.29b). However, by discarding the first blue curve the successive three ones (taken till 0.250 s) remain overlapped until the beginning of the lift at about ± 7 mm from the centre (x = 0). Analogously, the distance of about 14 mm can be assumed as the overall D_V value, or better as the overall extension of delamination along y. Of course, by varying the ΔT_b value, it is possible to discriminate between more important damage and slight delaminations. In particular, if ΔT_b = 1 K it comes up D_H = 11 mm and D_V = 3 mm which correspond to the dimensions of the cut (i.e. the oblong structure).

A ΔT image acquired with the SC6000 camera at t = 0.04 s after impact at 10 J of a GFRP specimen is shown in Fig. 5.30. This specimen shows a hot (white) spot surrounded by lighter vertical tracts interspersed by darker zones. The hot spot indicates a local breakage, while the lighter tracts help to identify fibres bundles; more specifically, fibres appear vertically as they are on the external layer. It is possible to distinguish either fibres misalignment, or nonuniform distribution of resin epoxy. In particular, it has to be observed that the hot spot engages breakage of fibres over two tracts one of which (left side in Fig. 5.30) appears interrupted because of a zone rich of resin. It has been already demonstrated [15] that the presence of manufacturing defects amplifies the weakness of the material to impact. The ΔT profiles at different time instants along x and y directions, are reported in Fig. 5.31a and b, respectively. The specimen GFRP displays sudden at the impact a hot spot of high temperature increase ($\Delta T \cong$ 25 K) surrounded by intermittent distribution of warmer tracts over the entire viewed surface; this accounts for local breakage and wide impact-affected zone.

Both graphs are presented in a magnification fashion to allow discrimination of the different curves plotted for the different time instants. By setting ΔT_b = 1 K, it results that $D_H \cong$ 4 mm and $D_V \cong$ 3 mm which correspond to the dimensions of the hot spot (i.e. fibre breakage). Again, from Fig.5.31a, by discarding the first blue curve, which is still affected by thermo-elastic effects, and searching for any change of curve slope (low ΔT_b), it can be assumed $D_H \cong$ 21.5 mm with a distance from the hot spot centre of about 12.5 mm on the left and of about 9 mm on the right. Going to the next graph in Fig. 5.31b, the different curves do not have any straight tract but depart sudden with a slope; this because, due to the presence of fabrication defects, almost the entire viewed surface shows some impact effects.

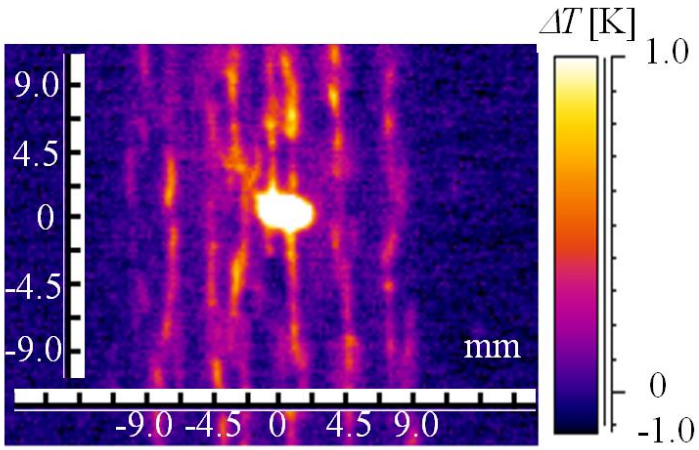

Fig. 5.30. ΔT image of GFRP t = 0.04 s after impact at 10 J.

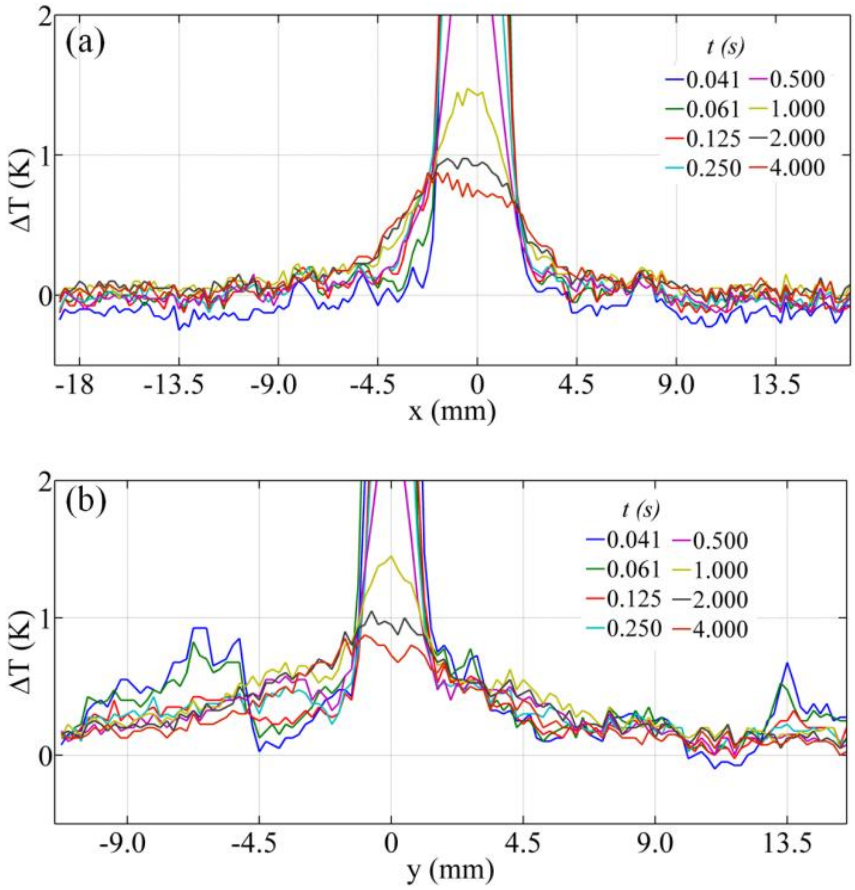

Fig. 5.31. Δ*T* profiles for GFRP specimen impacted at 10 J along *x* (a) and *y* (b) directions (Fig. 5.30).

Δ*T* images acquired with SC6000 of PPG and PGC2 specimens both impacted at 10 J are shown in Fig. 5.32a and b; Δ*T* profiles are shown in Fig. 5.33.

As already said, the two specimens differ for only the presence of the compatibilizing agent in the matrix of the PGC2 specimen. It is simple to notice that the warm area has a quasi circular shape so it can be assumed $D_H = D_V$ and then only one diameter has be evaluated from profiles along the single direction *x*. Besides, the warmer zone is smaller for the PGC2 specimen (Fig. 5.32b) with respect to that of the PPG one (Fig. 5.32a). This is due to the presence of the compatibilizing agent which prevents large deformations. In fact, as already said in chapter 4, the compatibilizing agent is used to improve the interface adhesion between fibres and matrix and this causes a more brittle behaviour of the material (specimen PGC2). In Fig. 5.33, Δ*T* profiles along *x* for PPG (Fig. 5.33a) and PGC2 (Fig. 5.33b) specimens are, respectively, compared. For $\Delta T_b = 1$ K, D_H is about 12 mm for the PPG specimen and about 8 mm for the PCG one; instead, for the same reasoning as for the specimen CFRP, the overall deformation extends for a diameter of about 20 mm for PGC2 specimen and greater than 28 mm for the PPG specimen (measurements not reliable on the right side of Fig. 5.33a).

In Fig 5.34 are reported the Δ*T* profiles along *x* and *y* directions of the PLAJ specimen impacted at 2 (Fig. 5.34a) and 3 J (Fig. 5.34b) from images acquired with the SC6800 camera. The Δ*T* profiles of Fig. 5.34 are obtained by searching for maxima values along *x* and *y* directions (*y*=0 and *x*=0) over Δ*T* images taken at three time intervals: 0.010, 0.015 and 0.020 s; the shown Δ*T* images refer to *t* = 0.015 s. The directions *x* and *y* coincide with the fibres orientations (0° and 90°) along which the most important damages with fibres pullout and breakage occur. For both impacts, the line of

material failure (hot stripe in the central image) is still in progress at t = 0.010 s (blue curve). It is worth noting that the light blue lines over the ΔT image indicate the maximum extension of D_H and D_v evaluated for $\Delta T \rightarrow 0$ while in Table 5.5 are reported also the D_H and D_v for$\Delta T \rightarrow .1$ At the impact of E = 2 J, D_V is much longer than D_H; instead, at the impact energy of 3 J, the two diameters become almost equal, with D_V slightly longer than D_H. In addition, the ΔT profiles display waviness with peaks highlighting the intersections of the fabric weft and warp.

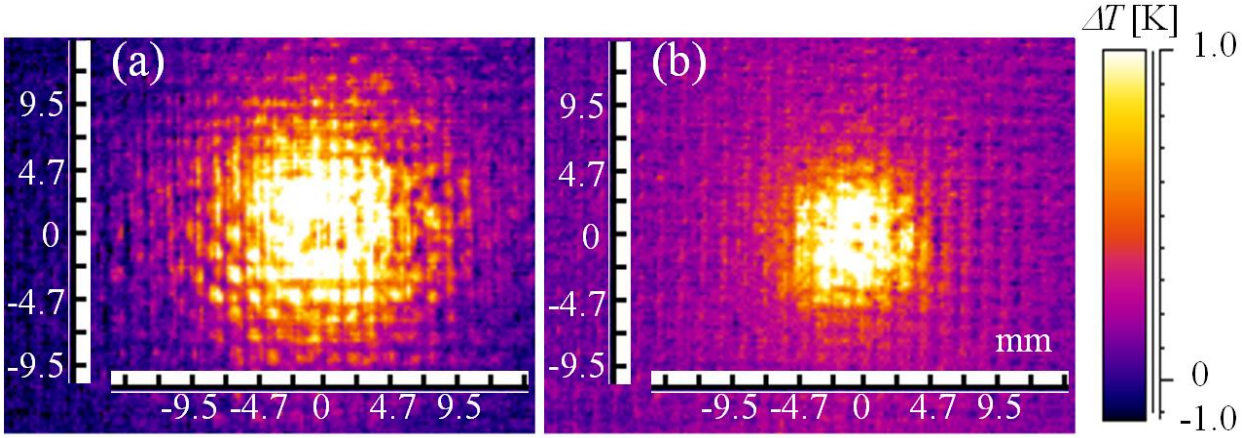

Fig. 5.32. ΔT images taken 0.04 s after impact of PPG (a) and PGC2 (b) specimens impacted at 10 J.

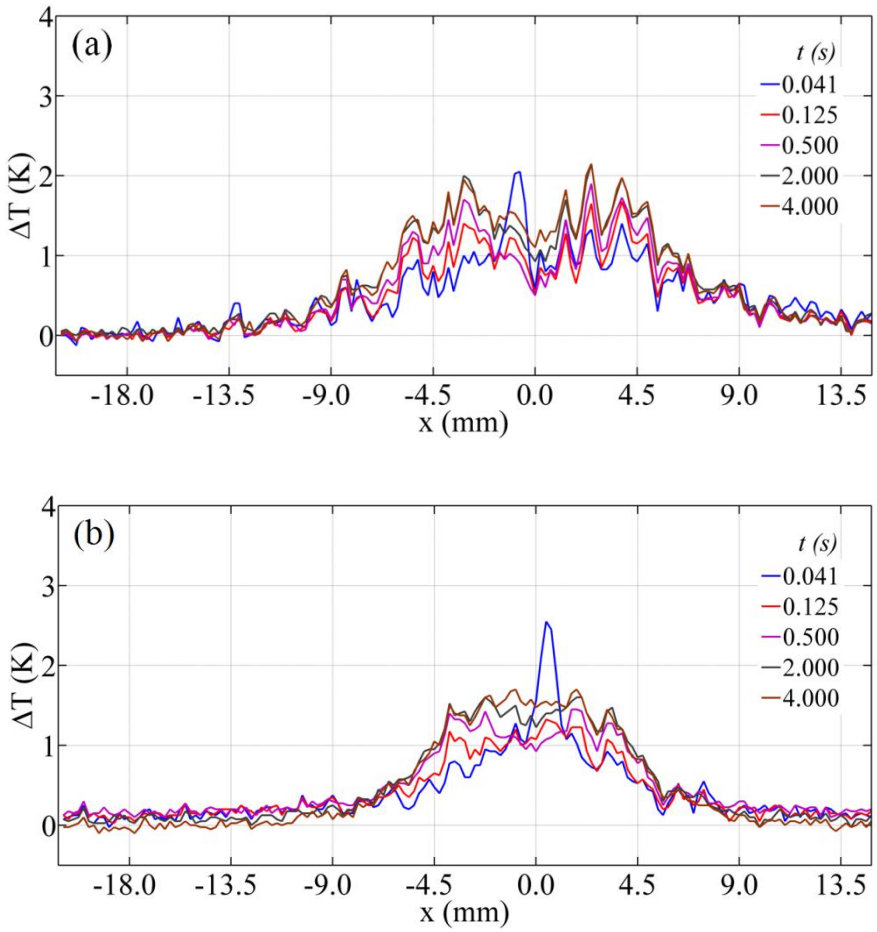

Fig. 5.33. ΔT profiles for PPG (a) and PGC2 (b) specimens impacted at 10 J (Fig.5.31).

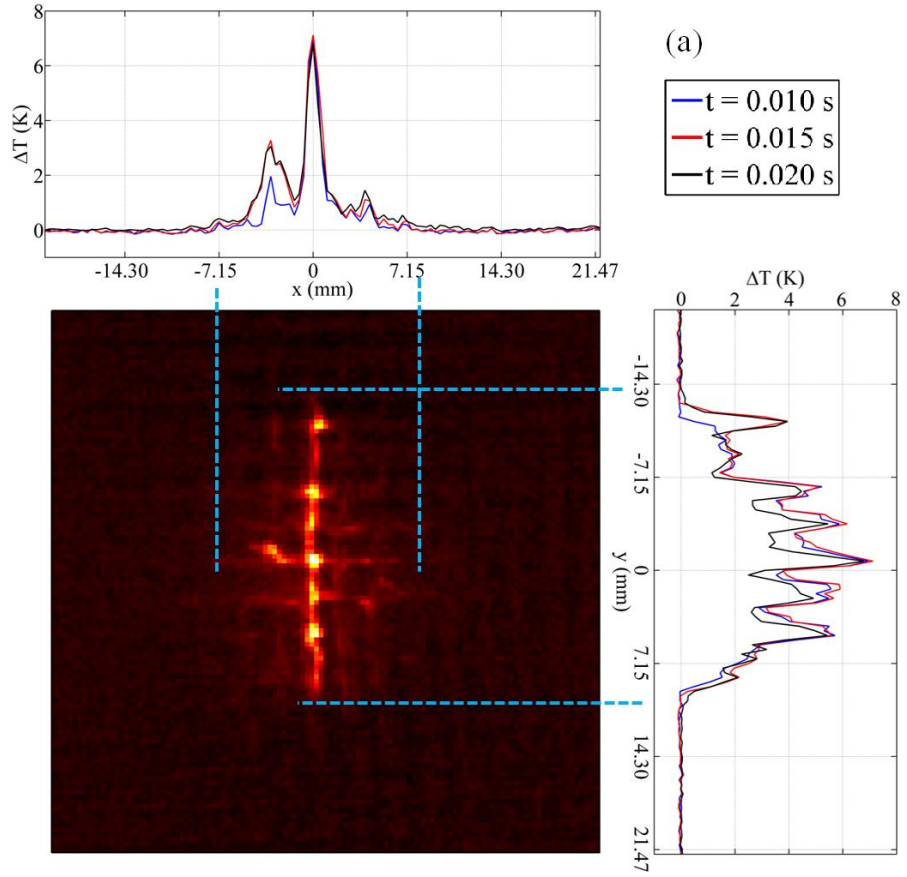

a) E = 2J.

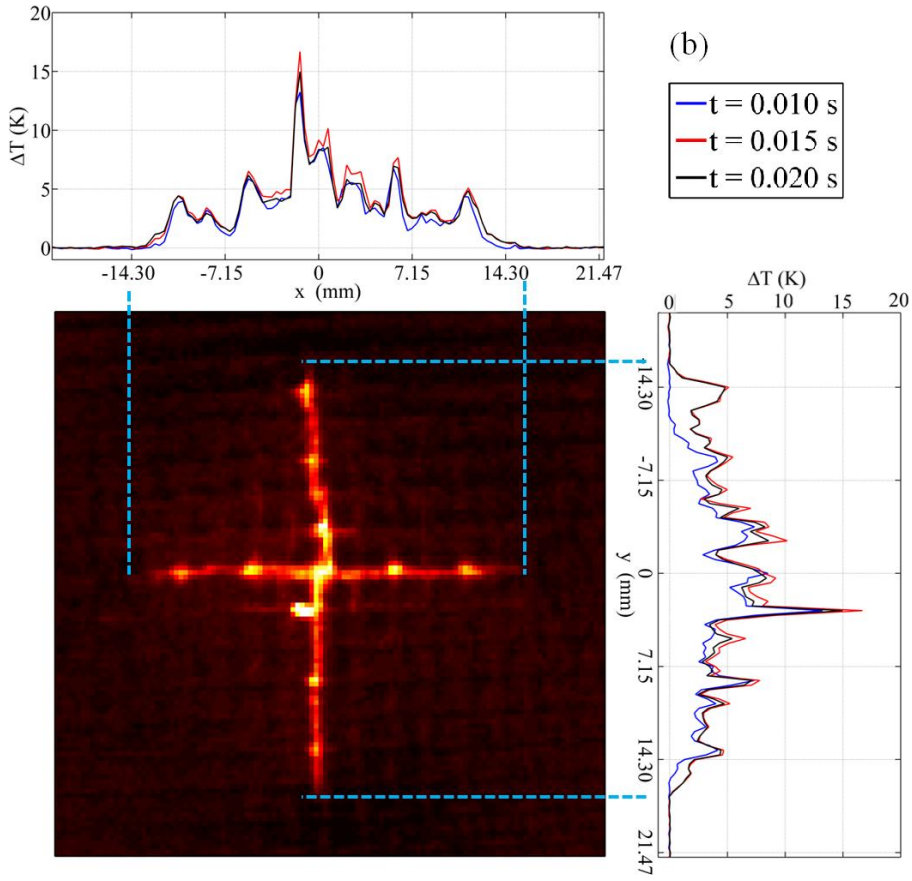

b) E = 3J.

Fig. 5.34. ΔT images of PLAJ taken 0.15s after impact and time profiles along x and y.

Figure 5.35 shows a ΔT image together with profiles along x and y of the AFS specimen impacted at 39 J. As already specified, the AFS specimen is completely different from all the other materials considered until now because it is not a fibre reinforced composite material but an aluminium foam. In this case the impact energy is mainly dissipated to produce wide plastic deformations on the external surfaces and ruptures of the aluminium bubbles which form the internal core of the foam [65]. Notwithstanding this, it is very interesting to underline how useful information about the impact affected zone can be derived also for this material by considering profiles along x and y directions. The warm area assumes a quasi circular shape with the D_H diameter slightly greater than the D_v one; in fact, for $\Delta T_b = 1$ K, D_H is about 16 mm while D_v is about 15 mm.

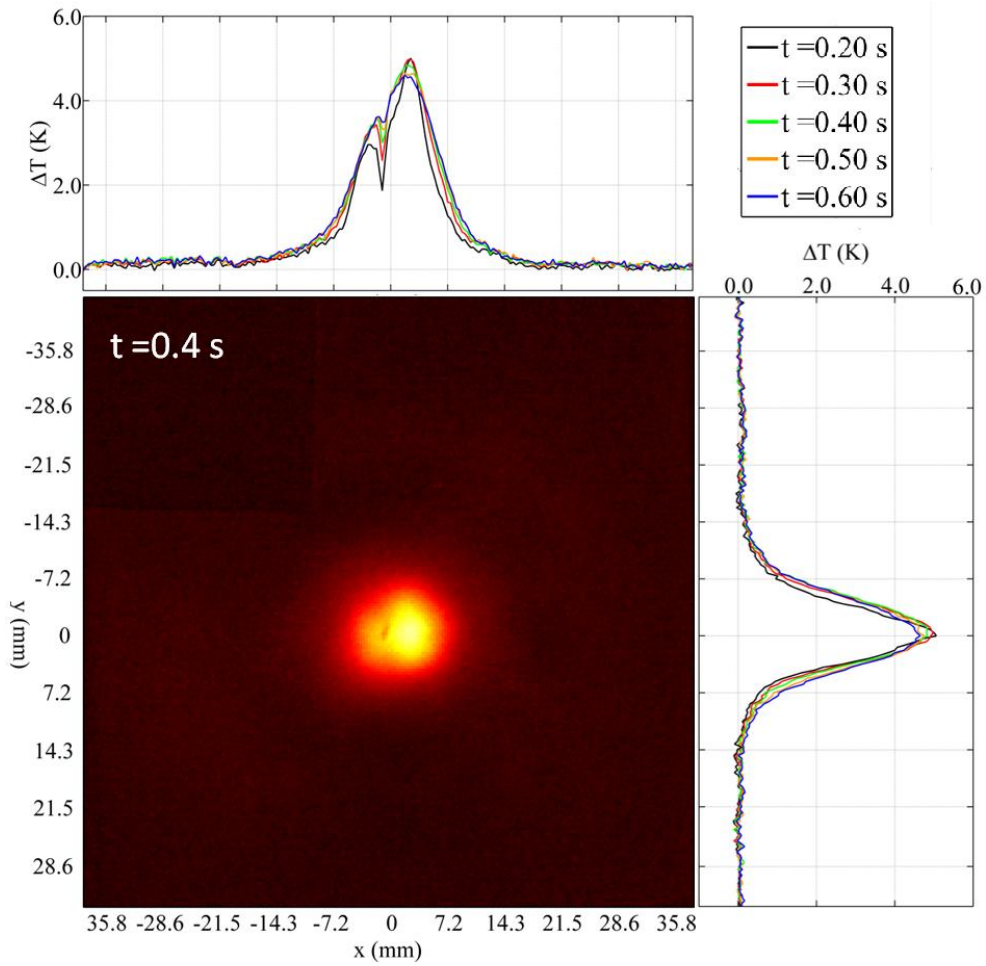

Fig. 5.35. ΔT image taken 0.4 s after the impact at 39 J of the specimen AFS and profiles along x and y directions for several time instants after impact.

The values of D_H and D_V evaluated for two different values of $\Delta T_b = 1$ and $\Delta T_b \rightarrow 0$ are reported in Table 5.5.

By comparing data of Table 5.5 with those of Table 5.2, for PPG, PGC2 and GFRP specimens, it is possible to notice that for $\Delta T_b \rightarrow 0$ at least one value of D_H, or D_V evaluated on ΔT images (online monitoring) is considerably higher than the correspondent value evaluated on the phase image obtained with LT (NDE). This because very light delaminations may get confused with the background scene also because similar small variations of the phase angle may be induced by local material non-uniformities.

The measurement of D_H and D_V strongly depends on the chosen value of ΔT_b and less on the time instant within fractions of one second. However, by changing ΔT_b and t the obtained D_H and D_V values display more or less fluctuations depending on the type of material. In particular, the very thin delaminations at the edge of the damaged area are linked to very small variations of ΔT with respect to 0 and then, it is very difficult to discriminate such small ΔT variations from the background. Besides, the instrument thermal sensitivity is of great concern [66-68].

Specimen code	D_H (mm) $\Delta T_b \rightarrow 0$	D_H (mm) $\Delta T_b \rightarrow 1$	D_V (mm) $\Delta T_b \rightarrow 0$	D_v (mm) $\Delta T_b \rightarrow 1$
$CFRP_U$	20	11	14	3
GFRP	21.5	4	////	3
PPG	>28	12	>28	12
PGC2	20	8	20	8
PLAJ, E = 2J	16	8.8	25	21
PLAJ,E =3 J	29	25	33	30.5
AFS	40	16	32.3	15

Table 5.5. D_H and D_V values evaluated on the infrared images for two value of ΔT_b.

5.8 Methods of warm area measurement

To locate the damage, it is important to discriminate between sound and damaged areas. Bearing in mind that we are analysing thermal images, what we can measure is the extension of the warmed-up area, which also means delineating the zone interested by the temperature increase induced by the dissipated impact energy. At first sight, this may seem rather simple to do. Conversely, two main questions may arise during evaluation of the extension of the warmed-up zone.

The first one regards the choice of the ΔT image in the sequence to be considered. In fact, while it is easy to understand that the images taken immediately after the impact, which are affected only by cooling down thermoelastic phenomena must be discarded (are linked with the elastic energy), it is not so easy to discriminate between the images in which thermoplastic phenomena occur with temperature rise over $\Delta T = 0$. This choice may involve considerations about impact-damaging mechanisms, energy-absorption mechanisms and heat-diffusion rates.

The second question regards the temperature difference threshold ΔT_b which must be introduced to be considered as a limit in the ΔT maps to clearly identify the damaged zone; therefore, a criterion is necessary to avoid under/overestimation issues.

At this point, the question arises on how to proceed. The literature is apparently full of methods with powerful ability to discover hidden details within a rather confused scene, but, unfortunately, most of these methods were developed within the visible framework.

So a new method, which is based on a reference area, is proposed and described. More specifically, two variants will be considered:

- Reference-based method (R method) - a simple and fast method, which involves only the impacted specimen.

- Noise correction reference method (NCR method) - a method similar to the first, but with the introduction of a reference specimen to account for the instrument noise.

5.8.1 Description of the R method.

The R method basically consists of a comparison between a ΔT image taken after impact ΔT_w and one taken before ΔT_{Ref}. To this end, the sequences of ΔT images created with Eq.(5.2) are subjected to successive post-processing with routines specifically developed in the MATLAB environment.
Considering that a generic ΔT image, before the impact, is obtained as the difference between two images both at ambient temperature, this difference should be zero for each pixel. Instead, a certain pixel temperature deviation is observed due to the instrument noise. This problem may be accounted for by acquiring a relatively large number of images q (e.g., 100) before the impact and generating an average reference ΔT_{Ref} image (reference image):

$$\Delta T_{Ref}(i,j) = \frac{1}{q} \sum_{t=1}^{q} \Delta T(i,j,t) \tag{5.4}$$

where i and j are the row and column numbers, respectively, and t the frame number in the ΔT sequence. So, for each pixel the temperature standard deviation $\sigma(i,j)$ can be computed.

$$\sigma(i,j) = \sqrt{\frac{1}{q-1} \sum_{t=1}^{q} \left[\Delta T(i,j,t) - \Delta T_{Ref}(i,j)\right]^2} \tag{5.5}$$

Then, $\Delta T_b(i,j) = 3\sigma(i,j)$ is assumed as threshold value. The value 3σ is generally used as a standard for control limits [69].
The ΔT image after impact is called warm image ΔT_W and is obtained as the average amongst p (e.g. 50) ΔT images, their number depending also on the camera frame rate:

$$\Delta T_W(i,j) = \frac{1}{p} \sum_{t=k}^{k+p} \Delta T(i,j,t) \tag{5.6}$$

with k denoting the generic ΔT image in the sequence immediately after the end of the cooling down effect. A scheme is depicted in figures 5.36 and 5.37 to clear the choice of ΔT_{Ref} and ΔT_W for $q = 100$ and $p = 50$.
Then, it is possible to transform a ΔT_W image into a binary image in which any pixel can assume a value equal to either 0, or 1, i.e. whether it is cold (black pixel), or warm (white pixel), respectively, according to:

$$\begin{cases} \Delta T_w(i,j) > \Delta T_{Ref}(i,j) + 3\sigma(i,j) \rightarrow \text{pixel} = 1 \\ \Delta T_w(i,j) \leq \Delta T_{Ref}(i,j) + 3\sigma(i,j) \rightarrow \text{pixel} = 0 \end{cases} \tag{5.7}$$

An example of transformation in the binary image is given in figure 5.38b for the PGC2 specimen impacted at $E = 5$ J with the black/white colour indicating the presence of cold/warm pixels,

respectively. In other words, a cold pixel represents the pixel not affected by heating effects caused by the impact for which $\Delta T_w = \Delta T_{Ref}$. Instead, the warm pixel is characterized by a ΔT_w value significantly higher with respect to the ΔT_{Ref} one being affected by the heating up effect caused by the impact.

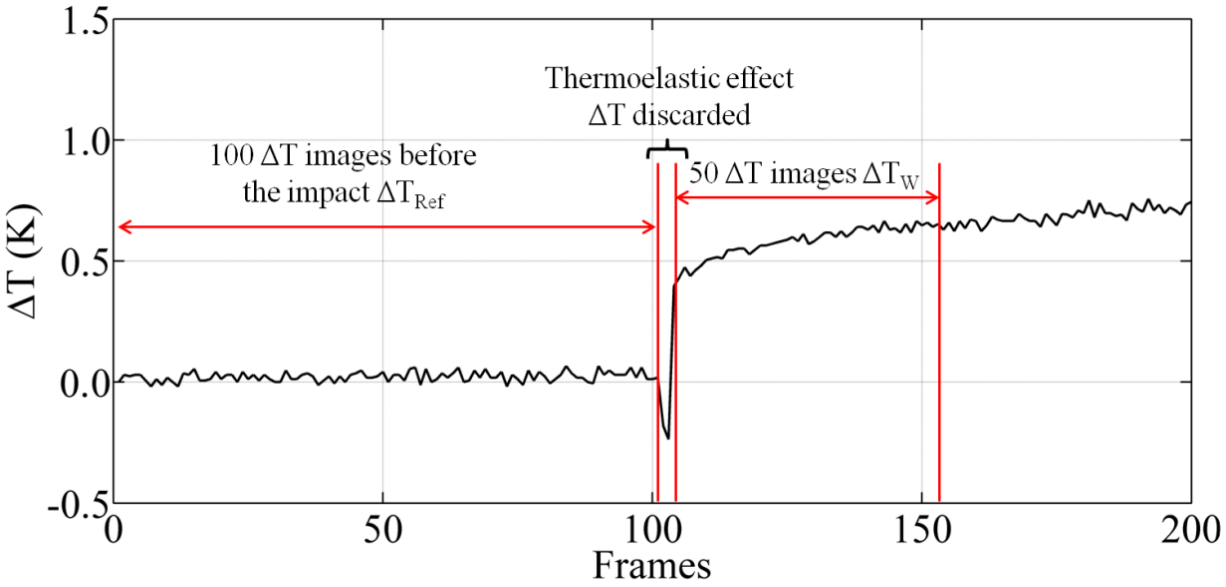

Fig. 5.36. Schematic representation of the creation of ΔT_{Ref} and ΔT_W images.

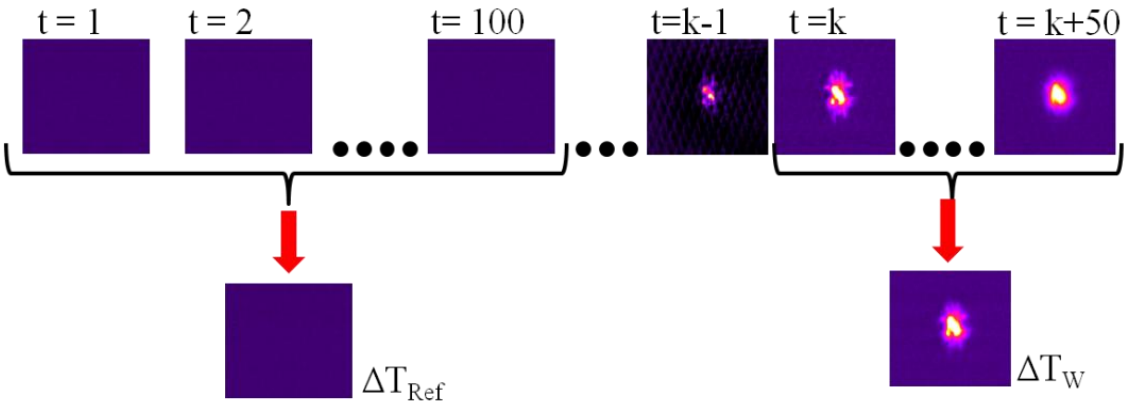

Fig. 5.37 Sketch of average ΔT_{Ref} and ΔT_W images construction.

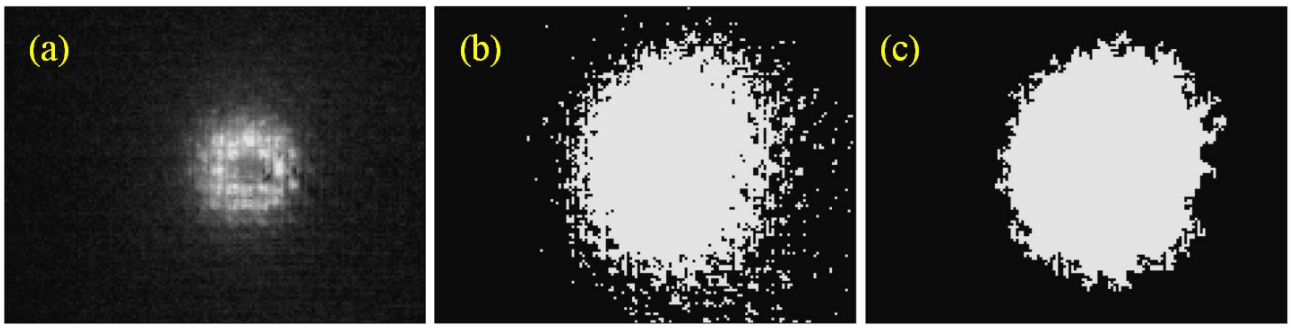

Fig.5.38. An example of raw and binary images of PGC2 specimen impacted at E = 5 J.
(a) Raw ΔT image, (b) binary image, (c) corrected binary image.

More specifically, Fig 5.38a shows the raw ΔT_W, while Fig 5.38c is practically a duplicate of Fig 5.38b but corrected for isolated cold/warm pixels with the MATLAB functions imfill and bwareaopen. The MATLAB function imfill includes, in the warm area, all the cold pixels (black pixels of Fig. 5.38b) that are completely surrounded by the warm pixels (white ones). Moreover, the bwareaopen function removes, from the image, all the isolated warm pixels/regions (white areas) that contain a too low number of connected pixels. In particular, the parameters of the function bwareaopen have been selected in order to remove, from the image, all the warm regions containing less than 1% of the total number of pixels contained in the whole ΔT_W image. Fig 5.39 shows two raw ΔT_W images with the warm area perimeter (boundary) superimposed. The boundary of the warm area is obtained using the MATLAB function bwperim. Of course, we are considering the entire warm area, which is composed of a central hottest zone surrounded by a lighter corona.

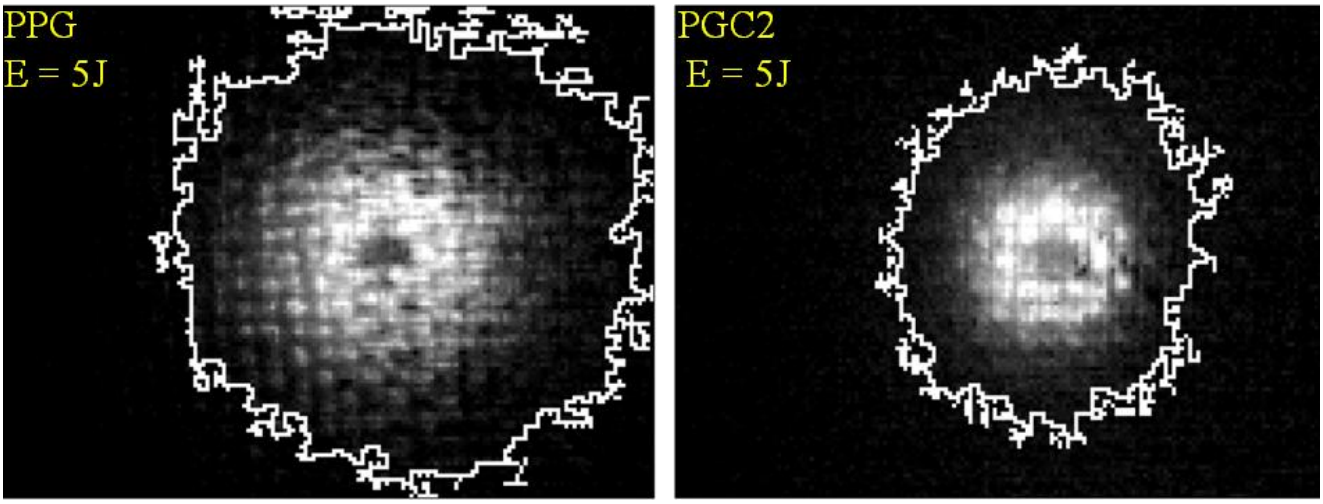

Fig. 5.39. Examples of raw ΔT images contoured by the warm area perimeter for PPG and PGC2 specimens.

Finally, the evaluation of the warm area A_h is obtained by counting the number of hot pixels P_h in the white stain and considering the camera spatial resolution s_r, which means applying the relationship:

$$A_h = P_h * s_r^2 \tag{5.8}$$

From Fig. 5.39 it is simple to notice that the A_h values displayed by the PGC2 specimen at the impact energy of 5 J are systematically smaller than those displayed by the PPG specimen. This because, as already mentioned the presence of the compatibilizing agent in the matrix (PGC2 specimen) improves the adhesion between the fibres and the matrix and prevents large deformations of the impacted zone [70,71].

5.8.2 Comparison of the R method with the Otsu's method.

The Otsu's method [72] is generally considered as the optimum [73] for image thresholding purposes because it chooses the threshold value that maximizes the between-class variance (or

conversely minimizes the within-class variance). Within this method, the total image intensity is separated into two intensity classes (e.g. objects and background) with the optimal threshold selected as a global property from the integration of the grey levels histogram. This method works well under the assumption of bimodal images with implicit uniform illumination. Conversely, it may be limited by the small object size, the small mean difference, the large variances of the object and the background intensities, as well as the presence of a large amount of noise [74]. Regarding the ΔT images under examination in the present work, it is worth noting that they do not show a bimodal appearance as can be seen from the histogram shown in Fig. 5.40, where N indicates the number of pixels having a given value of ΔT.

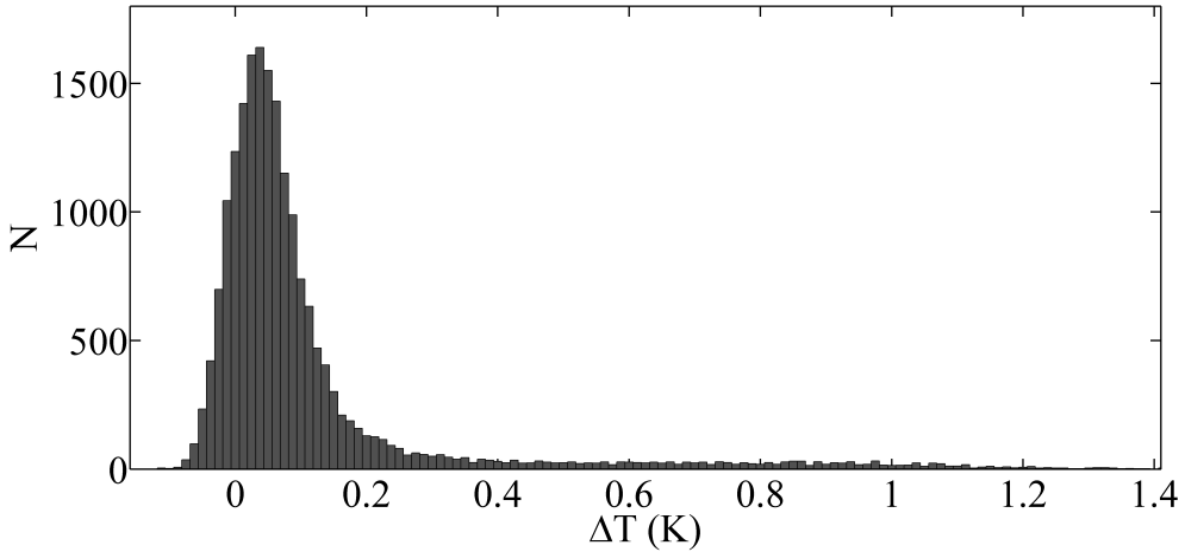

Fig. 5.40. A characteristic ΔT distribution for ΔT images.

In particular, the histogram refers to the ΔT_W image (averaged over 50 images) of the PGC2 specimen impacted at 5 J. From such premises it seems obvious that this method is not suitable to circumscribe the whole extension of the warm area (impact damage extension). In addition, a major problem is that only the pixels' intensity is considered in Otsu's method and not any relationship between them. Conversely, assessing the damage extension from thermographic images implies a comparison between temporal variations undertaken by the same pixel, which means a comparison between images. However, for the sake of a comparison, the Otsu's method is also applied to the present ΔT_W images by means of the Matlab function graythresh implement with the Otsu's method. An example of comparison is given in Fig 5.41 for the PGC2 specimen impacted at 5 J; more specifically, the smaller internal circumference is computed according to Otsu's method, while the outer one is the same as that illustrated in Fig. 5.39b.

To better evidence differences, two ΔT profiles along x and y directions are also added. As can be seen, the area outlined by Otsu's method is much smaller than the area outlined by the reference-based method. In particular, it is easy to see that the vertical and horizontal red bars (Otsu's method) intercept the profiles at an average value of $\Delta T \cong 0.5$ K against the $\cong 0.1$ K intercept by the blue bars (reference-based method). This means a general underestimation of the impact damaged area.

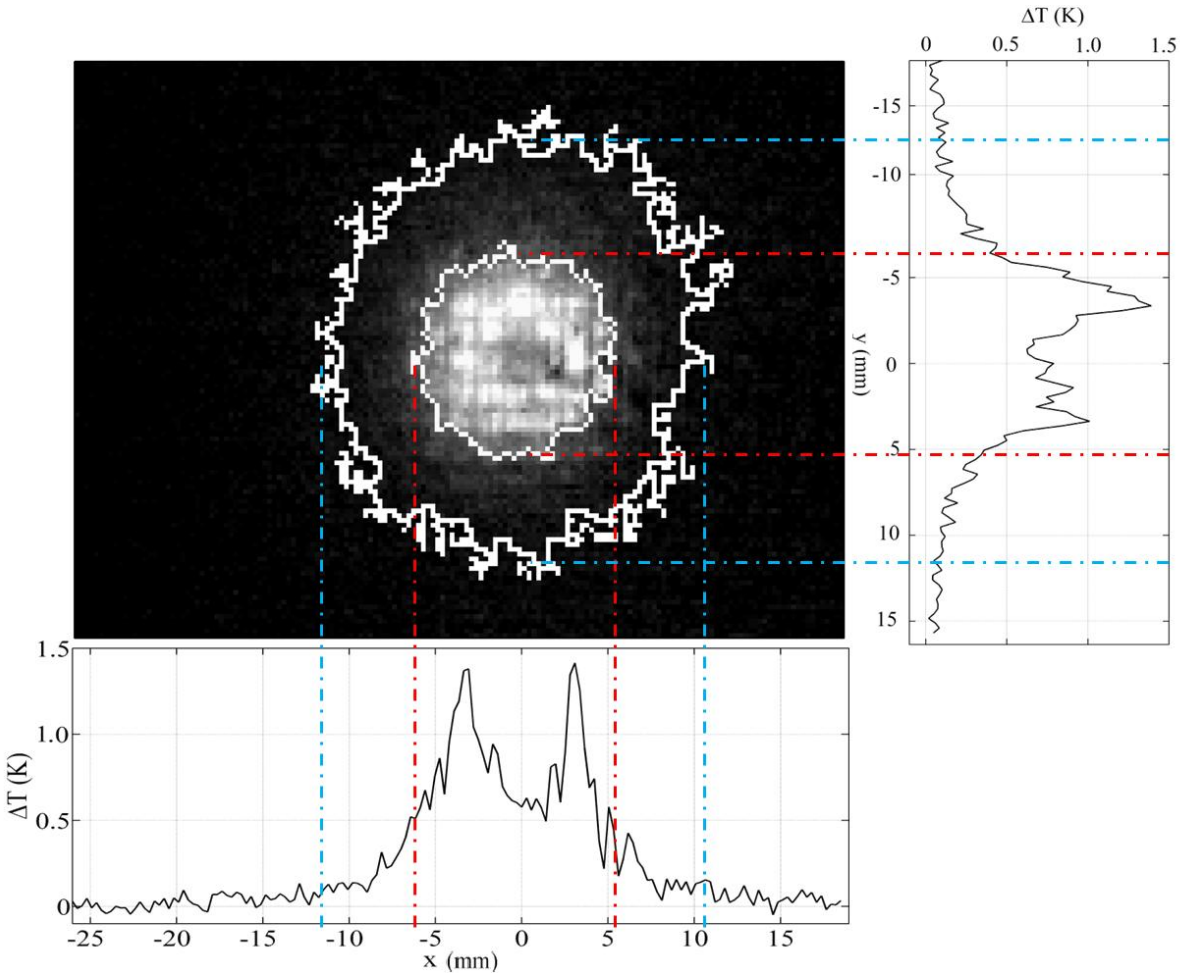

Fig. 5.41. A comparison between the reference-based method and Otsu's method.

5.8.3 Limitations of the R method and introduction of noise correction.

One main limitation of the previously described reference-based method is that it is referred to two average ΔT images (above a set of ΔT images) taken before and after impact, which cannot account for the random noise instrument. As a main weakness, the presence of unpredictable random temporal noise (See chapter 3), which manifests as jumps, may entail dummy shift of either the ΔT_W image, or the ΔT_R one making the two images no longer comparable. As already seen in chapters 3 and 4, the temporal noise can be removed only by referring to an unloaded specimen enclosed in the camera field of view. The noise instrument affects any small ΔT value and therefore all those at the boundary between delamination and sound material. Indeed, the signal recorded at such a boundary region being very small may benefit more than others from correction with the signal recorded in a sound zone [68]. The results obtained with the R method could be affected by the effects of the temporal noise and this could lead to underestimate, or overestimate, the extension of the damaged area. To eliminate a-priori the temporal noise effect, the R method is modified with the introduction of the Reference Area Method to obtain the Noise Correction Reference Based method, abbreviated as NCR method. Within the NCR method, the ΔT images coming from Eq. (5.2) are restored by subtracting the ΔT_{RN} signal, recorded at the same time over the reference specimen (Fig. 5.14b), to each pixel in the image [75]. As a result, a ΔT_C sequence of corrected images is created and used for implementation of the previously described R method.

$$\Delta T_C(i,j,t) = \Delta T(i,j,t) - \Delta T_{RN}(t) \tag{5.9}$$

$\Delta T_{RN}(t)$ in Eq.5.9 is the average value of ΔT evaluated frame by frame in a Reference area of 40x20 pixels over the reference specimen. After correction, the relationship 5.7 can be rewritten as:

$$\begin{cases} \Delta T_{Cw}(i,j) > \Delta T_{CRef}(i,j) + 3\sigma_c(\mathrm{i,j}) \rightarrow \mathrm{pixel} = 1 \\ \Delta T_{Cw}(i,j) \leq \Delta T_{CRef}(i,j) + 3\sigma_c(\mathrm{i,j}) \rightarrow \mathrm{pixel} = 0 \end{cases} \tag{5.10}$$

where the subscript C means that the corrected ΔT_C sequence is used. To underline the effectiveness of the Reference Area correction, in Fig. 5.42 are shown the raw and corrected signal acquired with SC600 and relative to the specimen $CFRP_{FU}$. In particular, the average raw signals measured in A_1, A_2 and A_3 of 3x3 pixels are reported in Fig. 5.42b; while the raw and corrected ΔT plots taken in the area (A3), over thermal images, far from the impact (Fig. 5.42a), where ΔT attains very low values are reported in Fig. 5.42c and e. The noise evaluated in the reference area is reported in Fig. 5.42d.
From a comparison between raw ΔT (Fig. 5.42c) and ΔT_{RN} (Fig. 5.42d), it is possible to see as the random jumps (encircled in Figs. 5.42c and d) are intercepted through the use of the reference area (placed over the portion of the image of the unloaded reference specimen (Fig. 5.42a)) and removed through Eq.(5.9). Moreover, looking at Figs. 5.42a and e, it is possible to notice in the corrected signal also a reduction of others irregularities, which are present in the raw signal. The two plots, raw ΔT and ΔT_C, are reported again superimposed in Fig. 5.43 to better show the effect of the correction.
It can be noticed that the raw signal (black line) presents a jump which affects the evaluation of the ΔT_W image in the R method. This has surely a negative effect on the evaluation of the overall extension of the warm area. In fact, looking at the raw signal (black line) the abrupt jump involves about 50 images, before impact, which represent half of the 100 images that are used to extract the ΔT_{Ref} to be compared with the ΔT_W, which is, in turn, extracted from the successive 50 images. It is easy to understand that, without correction, a significant error is introduced in Eq.(5.7). In the corrected signal the abrupt jump disappears making the 2 images ΔT_{CRef} and ΔT_{CW} comparable with a reduced error through Eq.(5.10).
A comparison between the results obtained with the two methods (R-Method and NCR-Method) on the $CFRP_{FU}$ specimen is reported in Fig. 5.44. The ΔT_W images obtained with the two method are shown and the boundary of the warm area is encircled by means of a white line. The values of ΔT in the colour bar have been chosen to highlight the small values of ΔT_W to better appreciate the contour of the warm area.
By comparing Fig. 5.44a and b, it is possible to see that a consistent portion of the warm area remains un-contoured (Fig. 5.44b) when applying the R method, which leads to an underestimation of about 40% of the warm area. This error is not negligible considering that it may lead to overestimate the resistance to impact of the composite material, which may be a critical parameter especially for composites employed in the construction of aircraft. In particular, the R method fails to recognize a warm region characterized by values of ΔT very small and close to 0. It is worth noting that the two images have a different background colour even if the scale is the same; this difference is caused by the temporal noise, which entails shift of ΔT values.

Of course, the importance of the errors depends on the temporal noise which affects the infrared images. As already said, the NCR method is able to remove, or reduce, also other very small and unpredictable disturbances coming from the environment which may affect measurements; this because, any temporal disturbance affects the entire viewed scene and can be accounted for by the reference specimen; this assures ΔT_{CRef} and ΔT_{CW} images to remain comparable even if in presence of unpredicted external disturbances. For this reason, independently of the used infrared camera, the use of a reference specimen coupled with the NCR method can be strongly recommended.

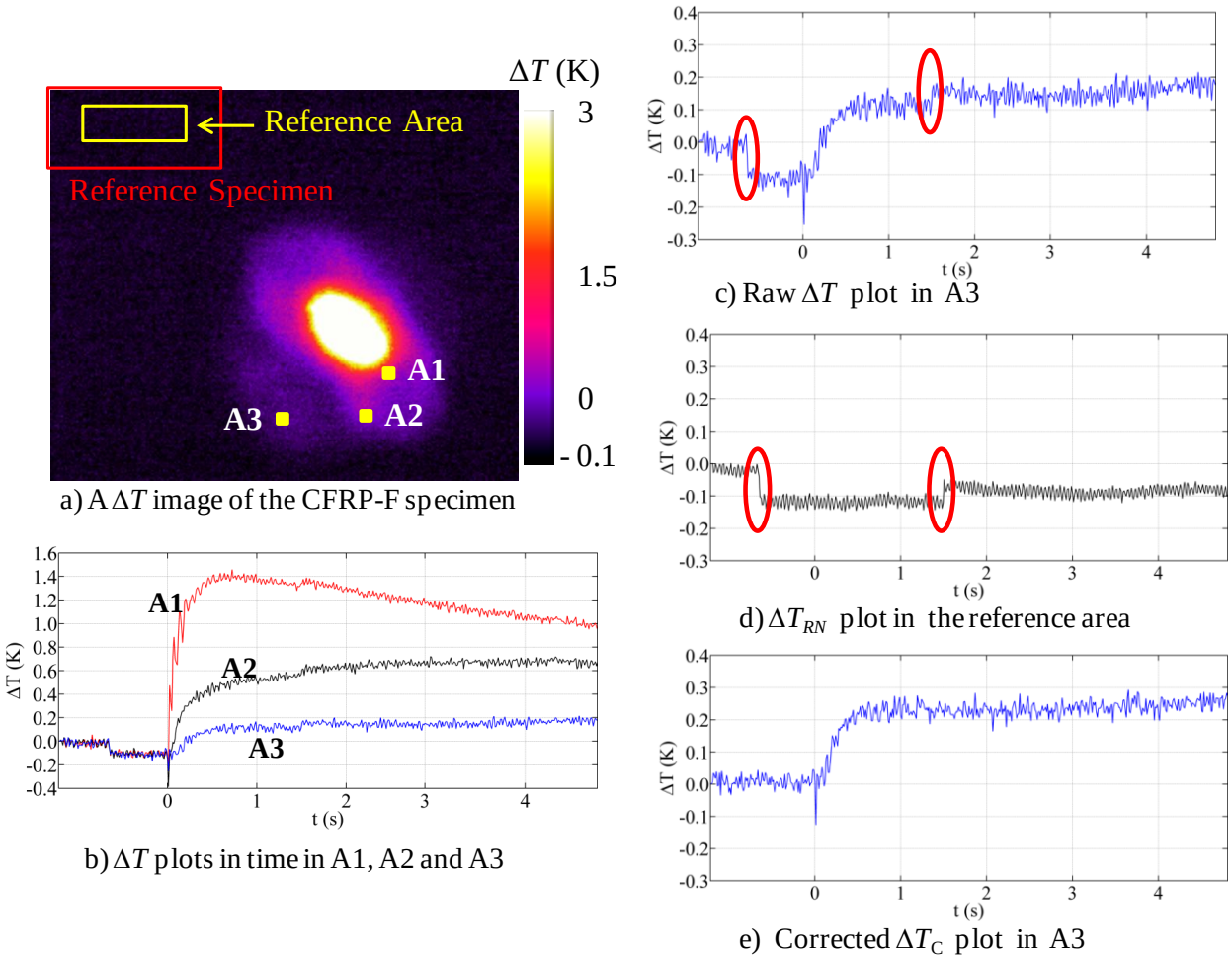

a) A ΔT image of the CFRP-F specimen

c) Raw ΔT plot in A3

d) ΔT_{RN} plot in the reference area

b) ΔT plots in time in A1, A2 and A3

e) Corrected ΔT_C plot in A3

Fig. 5.42. Example of correction of ΔT profiles from the random detector jumps.

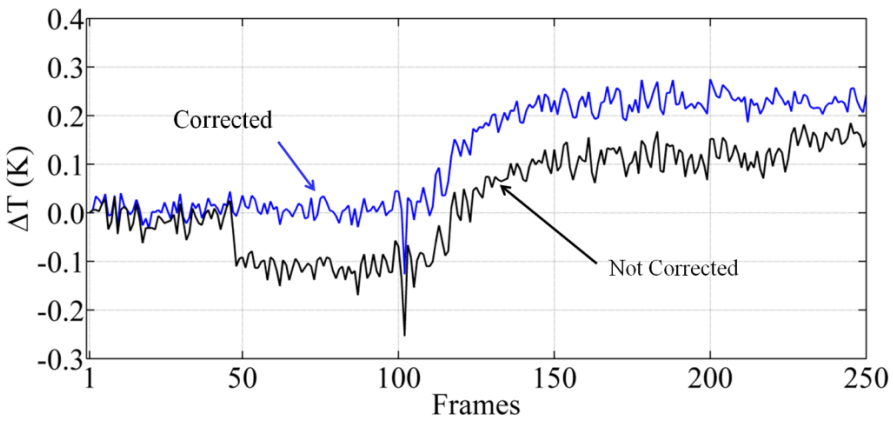

Fig. 5.43. Comparison of raw and corrected ΔT distributions.

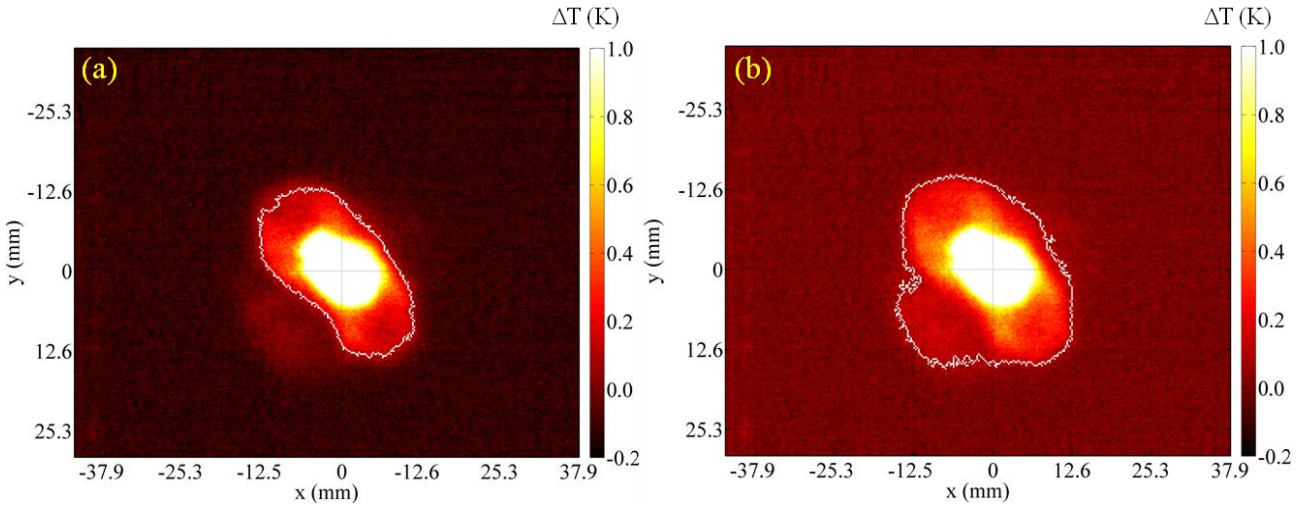

Fig. 5.44. Results comparison for specimen $CFRP_{FU}$ impacted at 18 J obtained with R method (a) and NCR method (b).

5.8.4. Some results obtained with the NCR method

Some results obtained by applying the NCR Method are shown in the following figures 5.45-5.55, while quantitative data are collected in Table 5.6.

In almost all the shown images, the warm area encircled by the NCR method is composed by a warmer (sometimes white) area surrounded by lighter (yellow, or light red) regions. In particular, in the warmest region the ΔT values overcomes 1 K and this region generally corresponds to the region with the most severe damage (see Table 5.4).The encircled warm areas of the AFS specimen, impacted at several energy values, are reported in Fig 5.45.

First of all, it is necessary to give some preliminary advices about the shown images. The dull darker region on top left, or top right (Fig. 5.46), which in some cases, as in Fig. 5.45c, hides a portion of the warm area, represents the reference specimen; sometimes, others artefacts may appear such as the piezoelectric patch on the bottom left side of the $CFRP_F$ specimen (Fig. 5.46).

As a general observation, by comparing all the contoured images (Figs. 5.45-5.55) it appears that the boundary of the warm area enlarges as the impact energy increases and the NCR method is able to follow such enlargement; this is evident by comparing Fig. 5.45a to Fig. 5.45b and c. In addition, the NCR method is also effective to discriminate the very small increases of ΔT within an almost uniform background as in the case of Fig. 5.45a. Independently of the impact energy, the warm area encircled by the NCR method is mostly driven by the type of material. And then, the warm area assumes a circular shape over AFS (Fig. 5.45) and PGC2 (Fig. 5.55), or an oval shape over $CFRP_F$ (Fig.5.46), $CFRP_U$ (Fig. 5.48), GFRP (Fig. 5.49) and PPG (Fig. 5.54), or a jagged outline in the case of more complex impact damage, such as that displayed by $CFRP_{FU}$ (Fig. 5.47), or PLAJ (Fig. 5.51), PPJ (Fig. 5.52), PJC2 (Fig. 5.53).

Looking at the specific specimens, more information can be derived. In particular, in Fig 5.46b the material texture is clearly visible, while it remains hidden in the background noise for the lowest impact energy of 18J (Fig. 5.46a). The NCR method seems effective to encircling the warm area and making possible to appraise the development of the warm area, which happens mostly along the fibres direction at -45°.

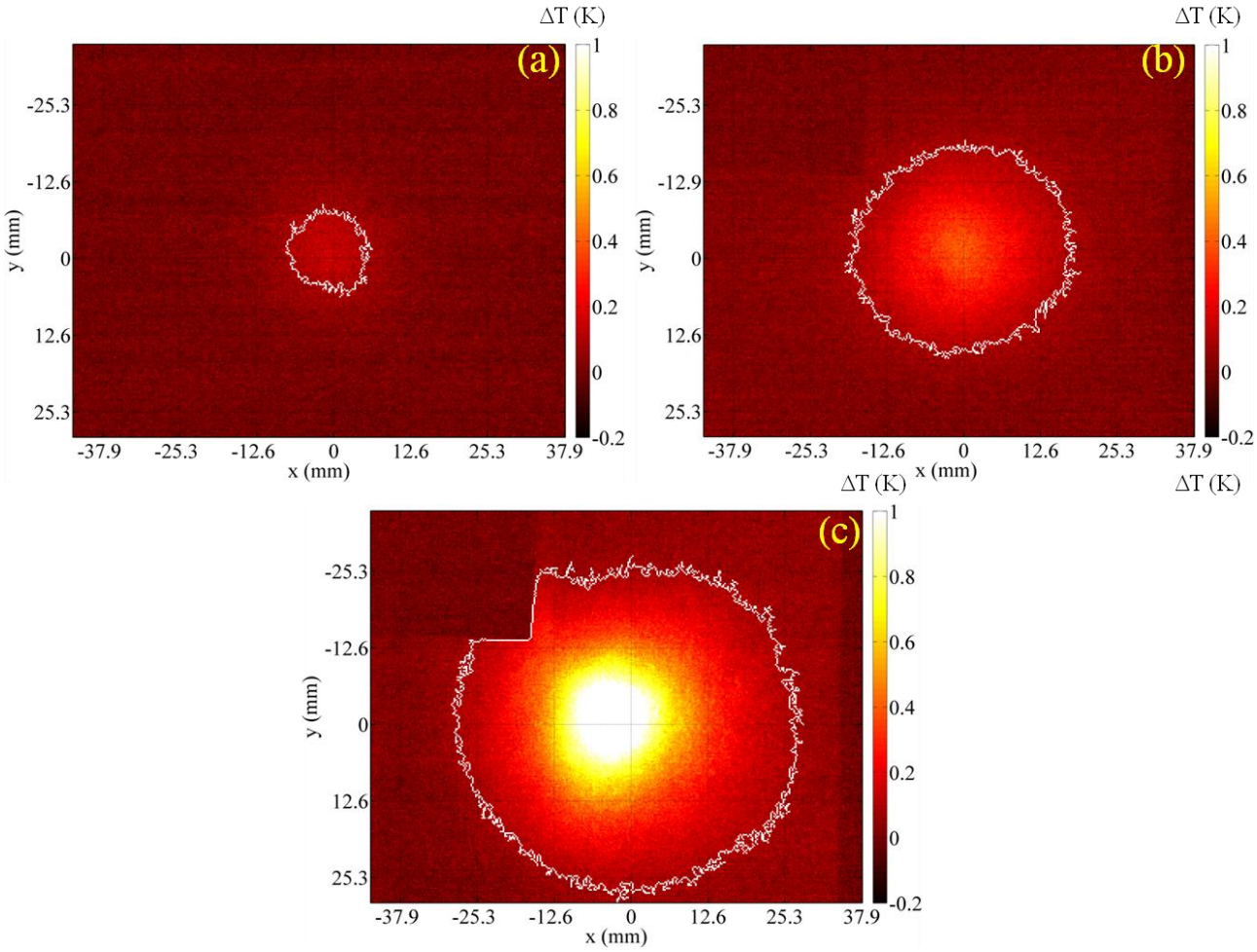

Fig. 5.45. Contoured warm area for AFS specimen impacted at E = 3 J (a), E = 8,3 J (b) and E = 21J (c).

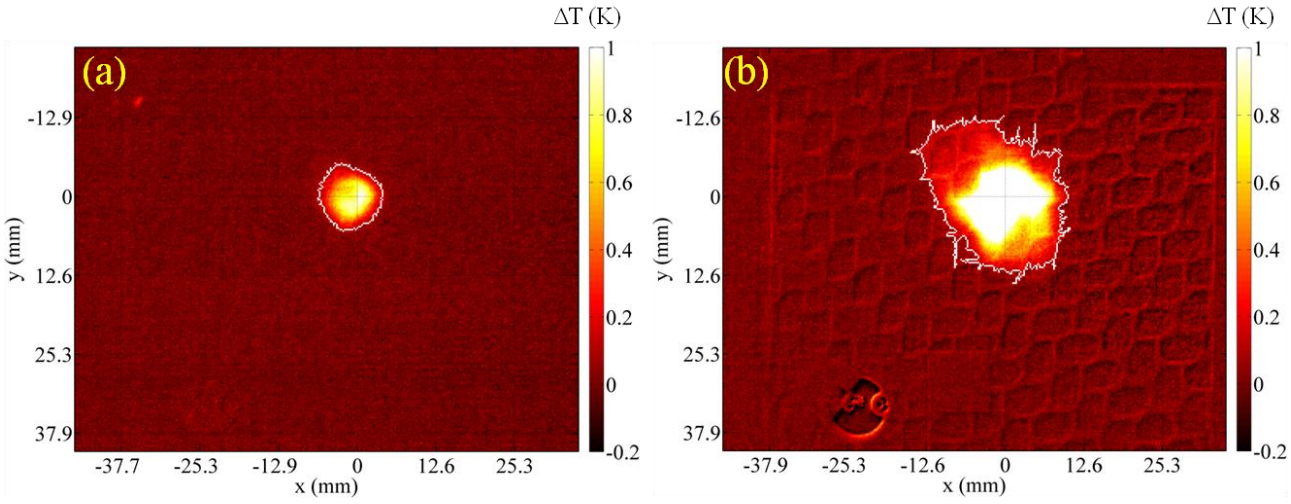

Fig. 5.46. Contoured warm area for $CFRP_F$ specimen impacted at E = 18J (a) and E = 24 J (b).

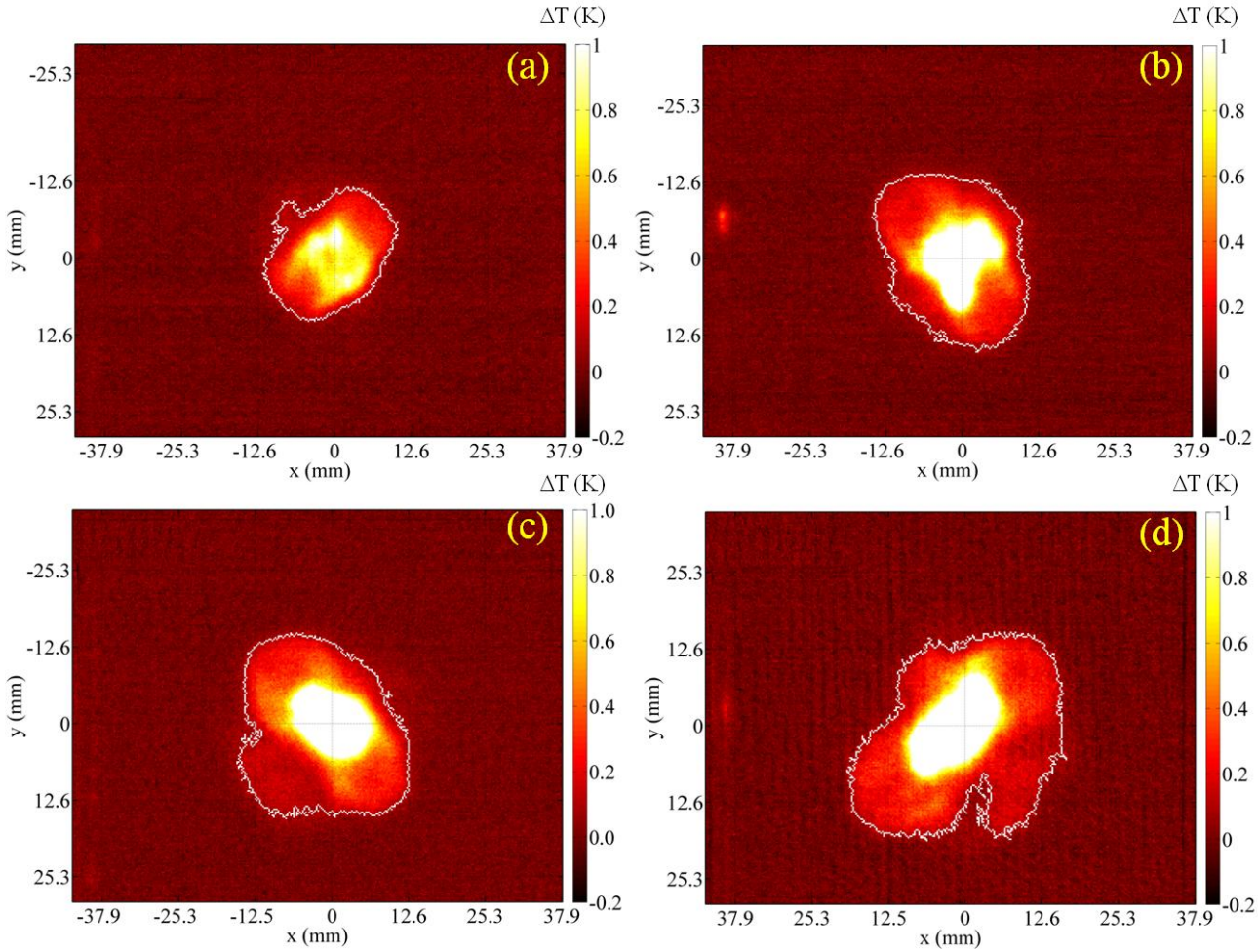

Fig. 5.47. Contoured warm area of specimen $CFRP_{FU}$ impacted at E = 10.5 J (a), E = 14 J (b), E = 18 J (c), E = 28.8J (d).

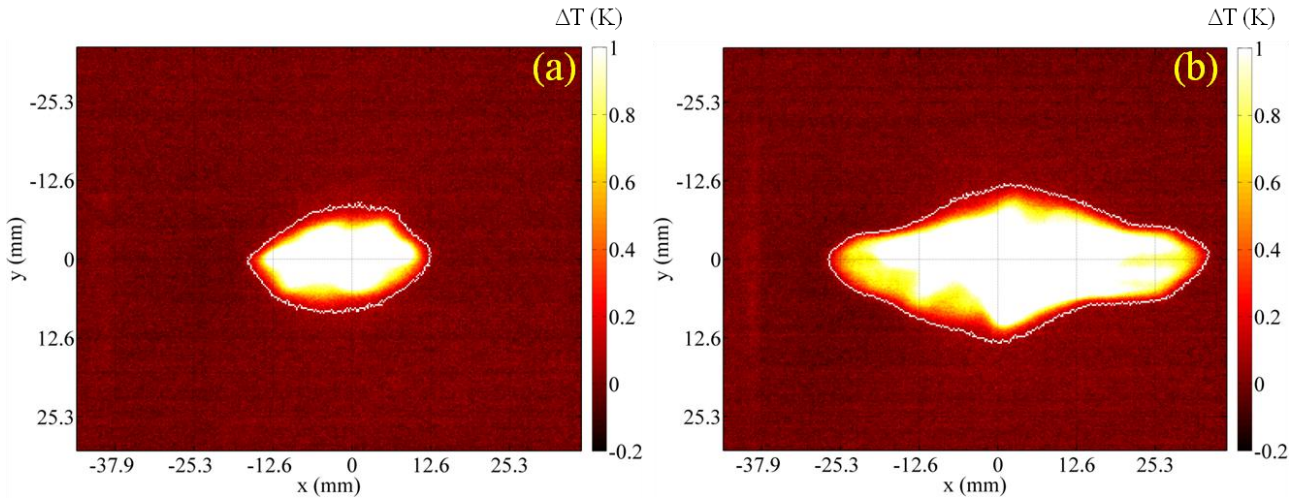

Fig. 5.48. Contoured warm area for $CFRP_{U}$ specimen impacted at E = 8.3 J (a), E = 11.7 J (b).

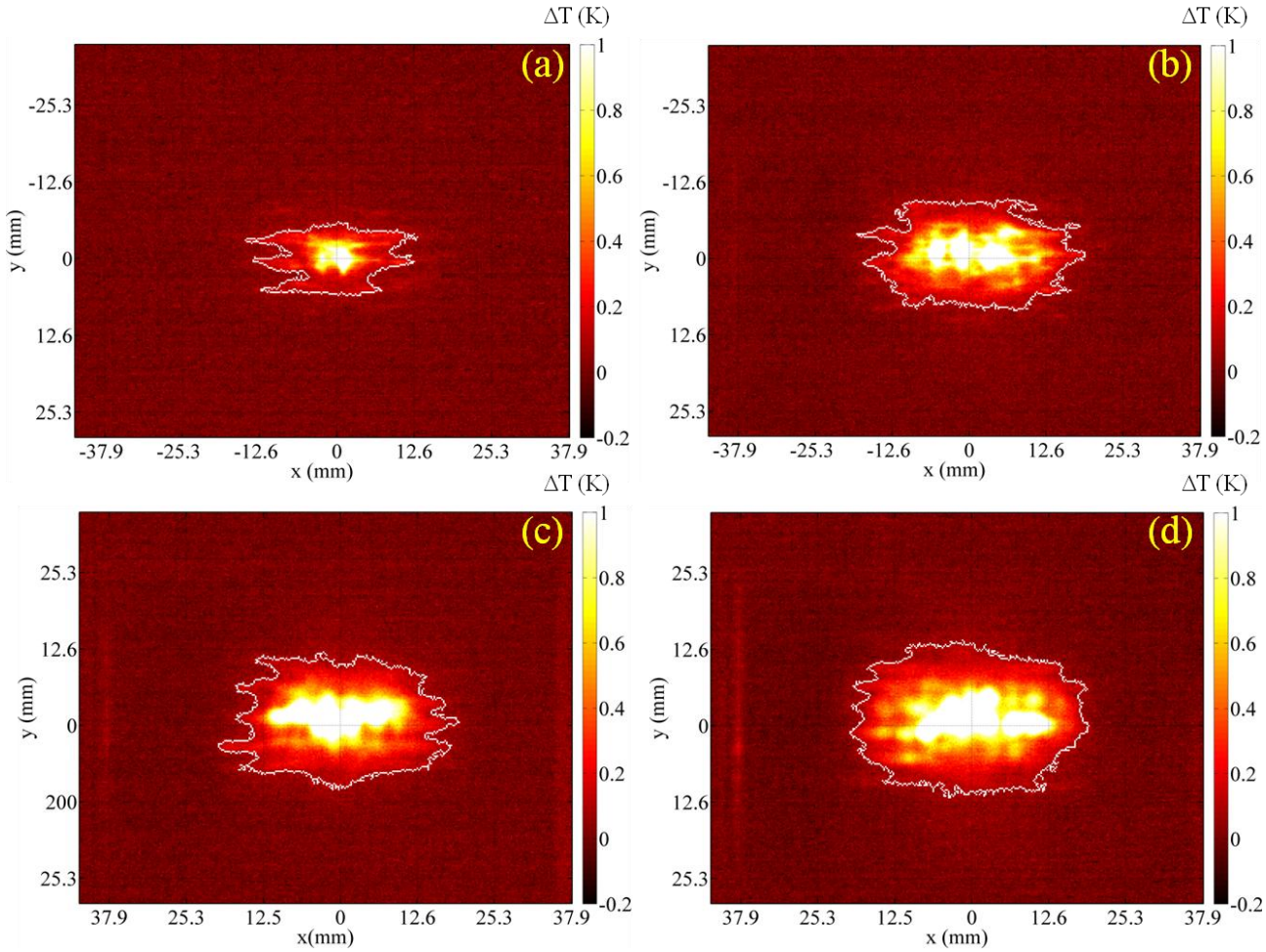

Fig. 5.49. Contoured warm area for GFRP specimen impacted at E = 2.8 J (a), E = 8.3 J (b), E = 12 J (c) and E = 15 J (d).

The results obtained for the $CFRP_{FU}$ at impact energy of 10.5 J, 14 J, 18 J and 28.8 J (Fig. 5.47) display the ability of the method to discriminate the small variations of ΔT and outline the overall extension of the warm area. In particular, it is possible to identify the quasi elliptical shape of the warm area with the mayor axis directed along the ±45° directions. This is in agreement with the well known damaging modes; however, mostly important is the possibility to discover also the secondary (lateral) structure that develops later (Fig. 5.47d), and is characterized by very small ΔT values, being deeper.

Looking at Fig. 5.48, the warm area assumes a quasi elliptical shape with its major axis directed along the 0° direction, even if the $CFRP_U$ specimen includes unidirectional fibres at 0°, 90° and ±45°. This because the fixture (Fig. 5.14) has a rectangular window with its longer side along the vertical direction. Considering that the longer side is two times the shorter one, it is evident that the specimen, under the impact, or pushing, force, is more constrained along the horizontal direction while is more free along the vertical direction. The different distribution of clamping force has a different effect, depending on the fibres direction, on the material deformation under impact. In general, the effect of the fixture rectangular shape is reduced in specimens involving woven fibres, which has a balancing effect on the clamping force leading the material to bow quite symmetrically in all directions.

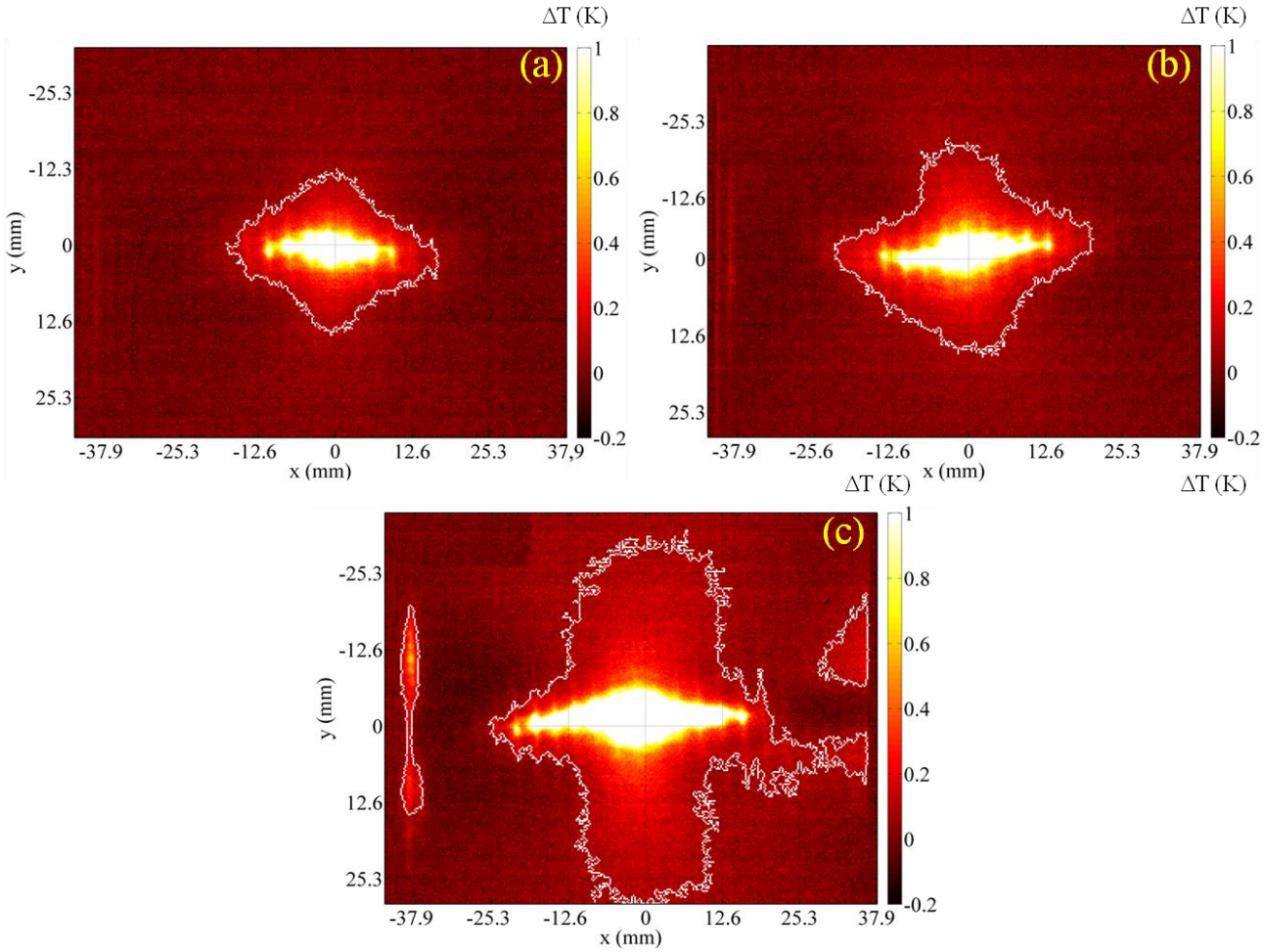

Fig. 5.50. Contoured warm area for PEF specimen impacted at E = 3 J (a), E = 5 J (b) and E = 12 J (c).

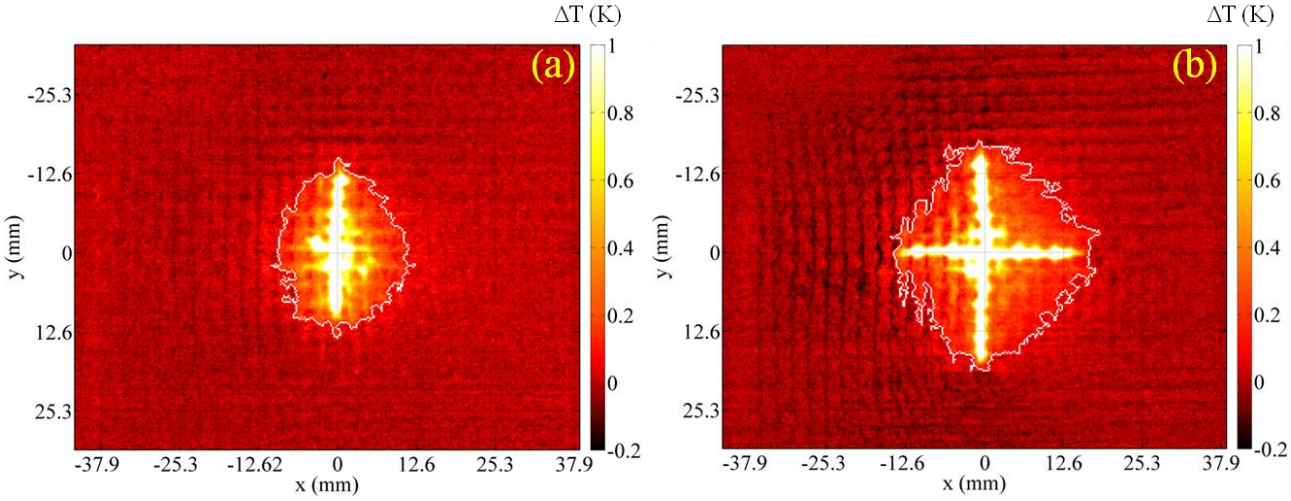

Fig. 5.51. Contoured warm area for PLAJ specimen impacted at E= 2 J (a) and E= 3 J (b).

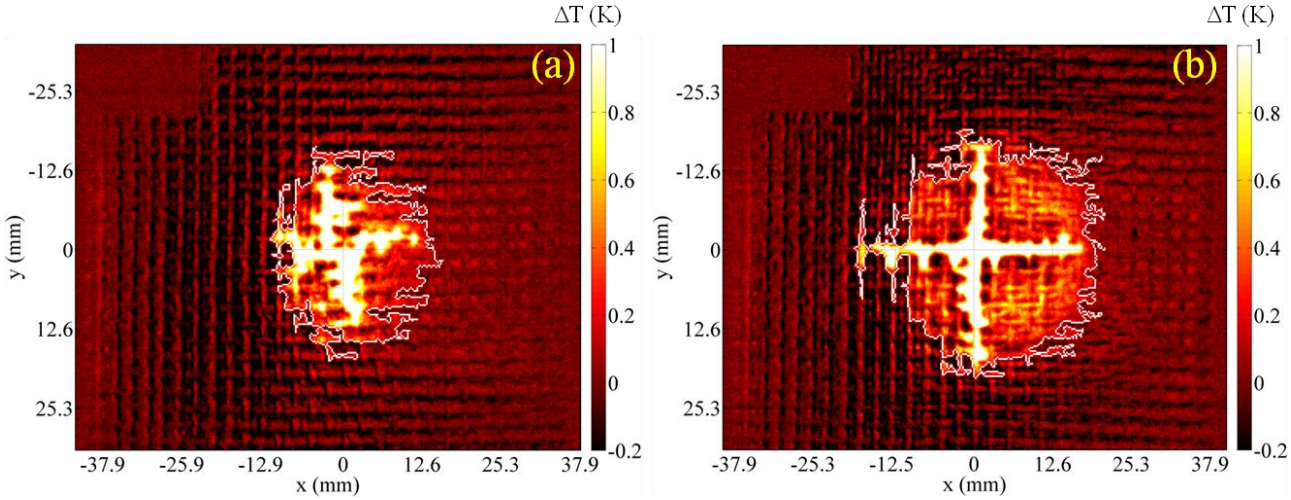

Fig. 5.52. Contoured warm area for PPJ specimen impacted at E = 2 J (a) and E = 3 J (b).

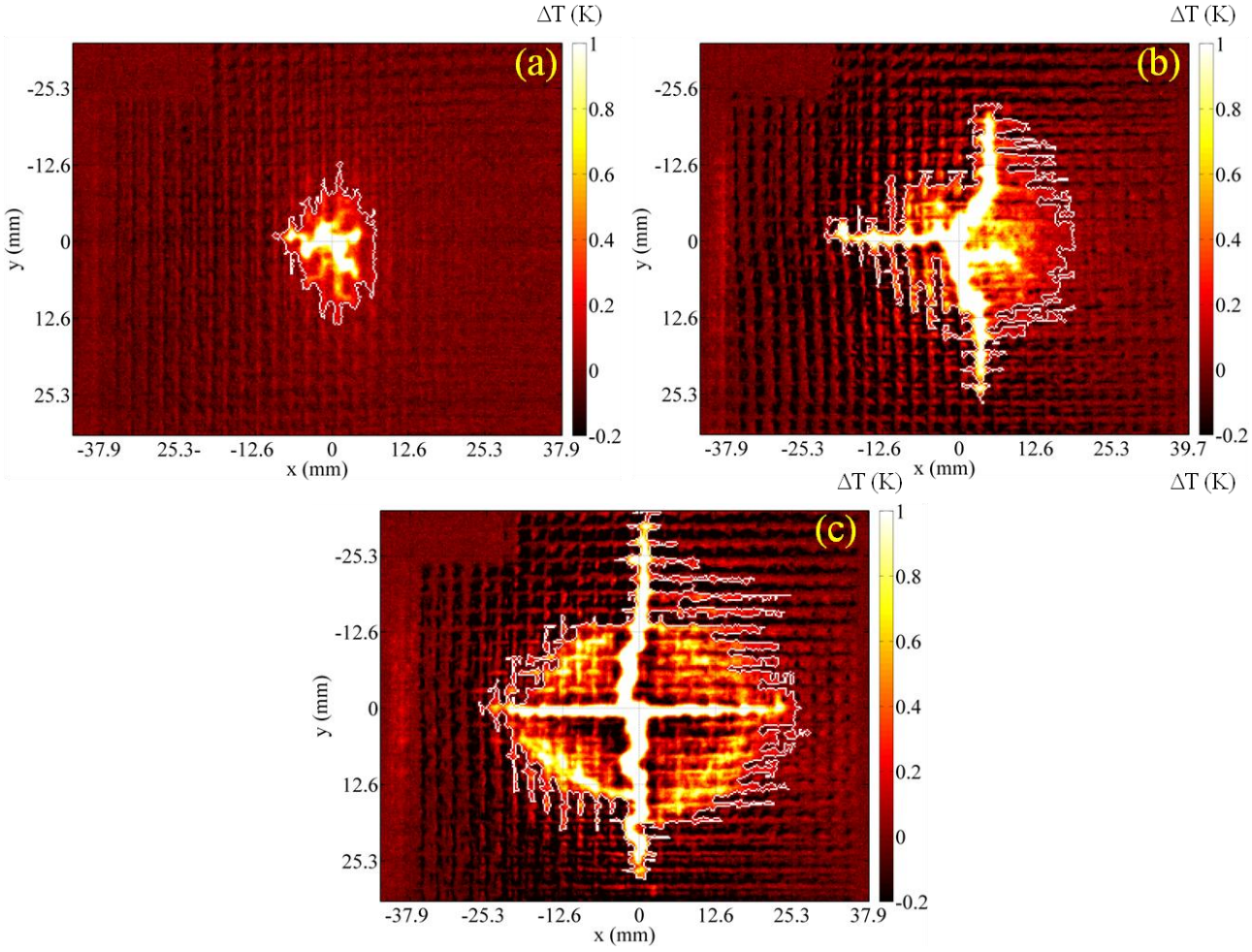

Fig. 5.53. Contoured warm area for PJC2 specimen impacted at E= 2 J (a), E = 3 J (b). and E = 5 J (c).

Particular attention must be given to the results obtained with the GFRP specimens (Fig. 5.49) since the warm area assumes a quasi rectangular jagged shape with some fibres tracts not enclosed in the contour. This can be explained by considering that these specimens come from a laminate made with the hand layup technology and cured at ambient temperature. This has caused fibres misalignment and porosity formation, which entailed, during impact, complex propagation of

delamination with associated very small temperature variations over fibres far from the impact site not connected to the central warmer region. The NCR method is effective in following the fibre direction connected with central damage, but cannot identify some very small and isolated hot points/stripes. Of course, it is possible to improve the method by optimizing the parameters of the MATLAB function bwareaopen used to eliminate the isolated warm small areas that does not contain a sufficient number of pixels (see Fig. 5.38).

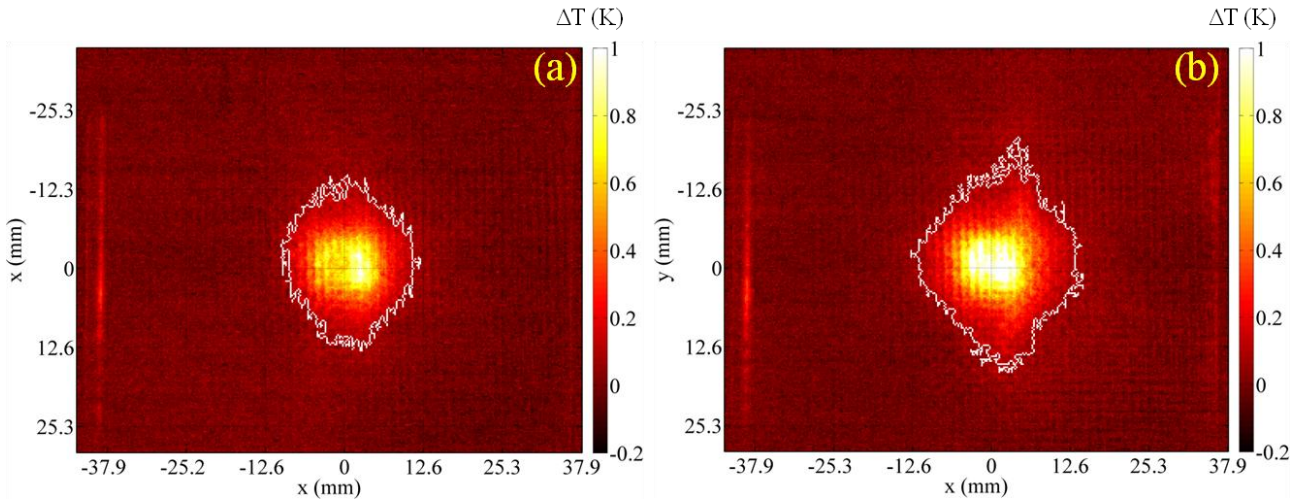

Fig. 5.54. Contoured warm area for PPG specimen impacted at E = 2 J (a) and E = 3 J (b).

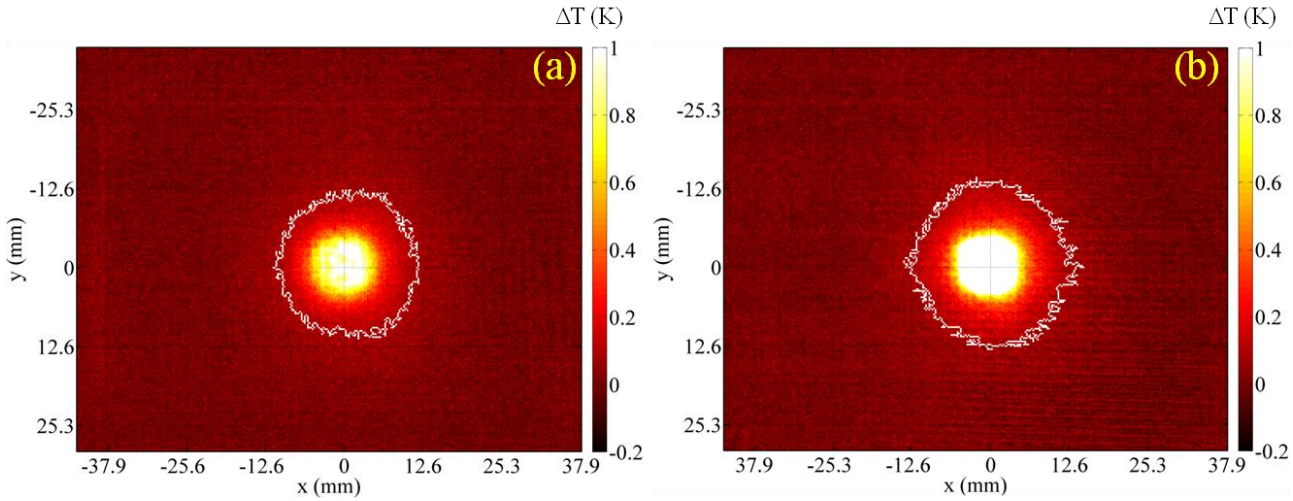

Fig. 5.55. Contoured warm area for PGC2 specimen impacted at E = 2 J (a) and E = 3 J (b).

From Fig 5.50, which refers to results obtained with the specimen PEF, involving flax fibres embedded in a polyethylene matrix, three warm areas far from the impact site are identified. These warm areas should not be considered as caused by the impactor, but mostly by the fixture. Indeed this is a phenomenon likely to occur and the distribution of the clamping force is a problem in impact tests. This phenomenon was not evidenced in other specimens because of the very small amount of pixels involved; they were very few and less than 1% of the total number of pixels contained in the image. However, these pixels are not enclosed in the A_h value (Eq.5.8), which is relative to only the central warm area region. Turning the attention to the central warm region, it is possible to see a particular shape with an oval central hotter zone surrounded by a lighter one,

which, by increasing the impact energy, enlarges vertically up. This happens for the same reasons before explained for the $CFRP_U$ specimen, but, in this case, the effect is more accentuated because the PEF specimen, differently from the $CFRP_U$ one, does not contain unidirectional fibres along the ±45° directions.

A different damaging mode is displayed by specimens involving jute fibres as can be seen from Figs. 5.51-5.53. In fact, all these specimens are characterized by sharp cuts along the main fibres directions (0° and 90°), which may display one vertical branch for lower impact energy like in Fig. 5.51a, or a well cross as in Fig. 5.51b. Of course, these cuts are surrounded by lighter damage, which sometimes may display a smoother (Fig. 5.51), or a jagged contour (Figs. 5.52-5.53).

Specimen	***E* (J)**	**A_h (mm^2)**	**E/A_h (J/mm^2)**
AFS	3.0	135	0.0222
AFS	8.3	950	0.0087
AFS	21.0	2340	0.0090
$CFRP_F$	18.0	82	0.2195
$CFRP_F$	24.0	426	0.0563
$CFRP_{FU}$	10.5	335	0.0313
$CFRP_{FU}$	14.1	564	0.0250
$CFRP_{FU}$	18.1	669	0.0271
$CFRP_{FU}$	28.8	884	0.0326
$CFRP_U$	8.3	363	0.0229
$CFRP_U$	11.7	950	0.0123
GFRP	2.8	206	0.0136
GFRP	8.3	467	0.0178
GFRP	12.0	580	0.0207
GFRP	15.0	743	0.0202
PEF	3.0	499	0.0060
PEF	5.0	766	0.0065
PEF	12.0	1602	0.0075
PLAJ	2.0	396	0.0051
PLAJ	3.0	730	0.0041
PPJ	2.0	556	0.0036
PPJ	3.0	942	0.0032
PJC2	2.0	225	0.0089
PJC2	3.0	791	0.0038
PJC2	5.0	1426	0.0035
PPG	8.3	390	0.0213
PPG	11.7	543	0.0215
PGC2	8.3	404	0.0205
PGC2	11.7	508	0.0230

Table 5.6. Measured values of warm area

As already said some quantitative results obtained by means of the NCR Method are collected in Table 5.6; in particular, impact energy E, warm area extension A_h and ratio E/A_h are reported. It is simple to see, for each material under investigation, an increase of A_h with the impact energy. Mostly important, it seems that the ratio E/A_h attains similar values for the same type of material, meaning that there exist a characteristic value of E/A_h for each material. This most probably because the damaging way of a material depends on its composition and architecture. However, some variations are observed probably due to any changes in the damage modality which occurs passing from lower to higher E values. Of course, more tests with a wider variation of materials characteristics are necessary to ascertain these observations.
At last, owing to the specimen PLAJ impacted at 3 J, a comparison between the Otsu's method and the NCR method is reported in Fig. 5.56. Again, it has to be stressed that the Otsu's method is able to identify only the region which contains the most important damage, in particular, only the cross appears encircled (Fig. 5.56b) which involves the greatest amount of energy dissipated in fibres rupture and pull out; conversely this method fails in detecting the overall extension of the warm area as does the NCR method (Fig. 5.56a).

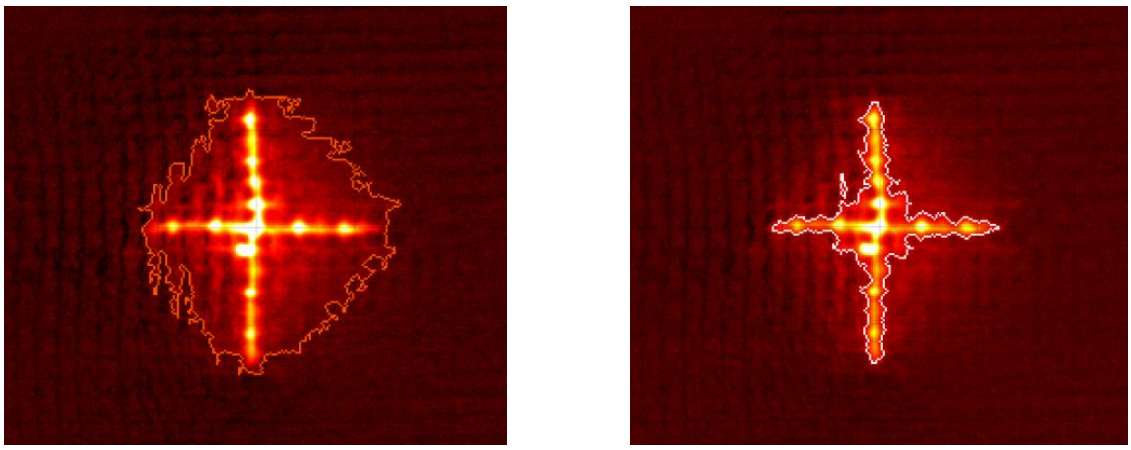

a) NCR b) Otsu

Fig. 5.56. A comparison between NCR and Otsu's methods.

5.9 Problems and future improvement of the NCR method

In the NCR method a feature that is worth attention regards the number of images post impact to be included in the average ΔT_{CW} image (Eq.5.10). In fact, the number of 50 ΔT images has been considered intuitively, owing to the specific materials under consideration, to be enough to account for the development of impact damaging related heat transfer mechanisms. In reality, this is a crucial aspect of great concern.
In the light of the development of a general and more accurate method to be applied with whatever material, it is important to, first of all, clear the meaning of the ΔT_{CW} image. While the ΔT_{CR} image simply represents the conditions before starting of the impact and it can be either chosen as a single image, or the average amongst a certain number of images without any physical implication . In fact the number of images chosen to calculate ΔT_{CR} has only a statistical influence in evaluating the material condition before the impact; then, the number of 100 consecutive images is certainly sufficient from a statistical point of view. The choice of the ΔT_W image is more critical and may

affect the final results. This implies the set of ΔT images used to calculate ΔT_W to be chosen owing to the material thermal diffusion time and its damaging way.
Owing to thermoset composites, in thick parts, the damage spreads out from the impact zone to the opposite one through the typical pine tree configuration; conversely, in thin laminates the damage starts from the rear surface (opposite to the impact) and evolves in the reversed pine tree pattern [64]. The damaging way has to be taken into account for the interpretation of the hot stain visualized over the viewed surface since it helps to be acquainted with what is responsible for formation and/or enlargement of such a hot stain.
In thin parts, surface and/or shallow damage is accompanied by sudden temperature rise on the opposite surface which is promptly captured by the infrared camera. Instead, surface temperature variations linked to internal damage appear with delay; this because the heat produced by the damage that branches through the thickness (reversed pine tree pattern) has to cross the thickness moving backward towards the viewed surface. Of course, such a delay depends on the location of the damage through the thickness and on the material characteristic diffusion time. Then, the warm stain starts to form first very small, but very hot, at the tip of the impact (on the opposite side) and after enlarges to cover the entire area affected by the reversed pine tree ramification. Unfortunately, heat does not travel straight in one direction alone but it diffuses in all directions; this entails losses and spreading with the consequence that the associated surface temperature (on the viewed side) appears weaker and spread over a larger area. In the meantime, over the viewed surface, there is lateral diffusion from hotter points/zones towards the colder ones. Of course, heat travels freely along unidirectional fibres, while it is hindered by the fabric, as well other complex fibres architecture. Then, for a specific material, it is important to know the characteristic diffusion time through the thickness and between contiguous points over the viewed surface.
In thick parts, the damage starts close to the impacted surface and spreads in the pine tree configuration. This would mean that the heat dissipated by the damage at the impact tip has to cross the entire thickness before any temperature variation is visualized over the viewed surface. Conversely, the outer damage branching in the pine tree pattern moves through the thickness towards the opposite (viewed) surface Then, it is likely that the entire warm area may appear outlined on the viewed surface sudden at the impact. Most likely, the warm area of a thicker part may be less affected by lateral diffusion effects and then it might be more easily and accurately outlined.
Thermoplastic matrix based composites behave differently under impact since they react to the impact with visible permanent modifications, like metals, displaying an indentation (a small concavity) on the impacted side and a protrusion on the rear one [39].
From these observations, the next step may be to find, for each material under investigation, a characteristic time which allows to choose the number of images to be used to evaluate ΔT_{CW} and the time after impact from which extract such images.

5.10 A summary to Chapter 5

The obtained results show that monitoring the thermal signatures induced by an impact event supplies information useful for the material characterization specifically for identifying initiation and propagation of the impact damage. Through post-processing of the recorded images, it is possible to get information useful for understanding more on the impact damaging mechanisms,

starting from the time interval the impactor remains in contact with the surface, the curvature experienced by the different composites, as well the occurred plastic deformations. In particular, from the time evolution of thermo-elastic effects it is possible to get information useful to establish the time interval the impactor remains in contact with the specimen surface and to derive knowledge about bending and deformation of the surface under the impactor pushing force. Besides, the temperature rise with its time history allows getting information about the instant the material starts to damage and the importance of the occurred damage. In addition, it was demonstrated that applying the proposed NCR method it is possible to encircle and evaluate the warm area, which accounts for the impact damaged area.

On the whole, as main findings, it has been shown that using infrared thermography it is possible to get in a fast way different types of information about impact damaging of composites (impactor peak contact, damage initiation and propagation, extension of delamination, etc.) which otherwise require many different tests.

References to Chapter 5

[1] M.O.W. Richardson, M.J. Wisheart, Review of low-velocity impact properties of composite materials. Composites Part A, 27, 1123-1131, 1996.

[2] R. Park, J. Jang, Impact behaviour of aramid/glass fiber hybrid composite: evaluation of four-layer hybrid composites, J Mater Sci, 36, 2359-2367, 2001.

[3] T.W. Shyr, Y.H. Pan, Impact resistance and damage characteristics of composite laminates, Compos Struct, 62, 193-203, 2003.

[4] S. Abrate, Impact on Composite Structures, Cambridge University Press, Cambridge, 1998.

[5] Baucom JN, Zikry MA. Low-velocity impact damage progression in woven E-glass composite systems, Composites Part A, 36, 658-664, 2005.

[6] R. Olsson, M.V. Donadon, B.G. Falzon, Delamination threshold load for dynamic impact on plates, Int. J. Solids Struct. 43, 3124-3141, 2006.

[7] D.J. Elder, R.S. Thomson, M.Q. Nguyen, M.L. Scott, Review of delamination predictive methods for low speed impact of composite laminates, Compos. Struct. 66, 677-683, 2004.

[8] G.A. Schoeppner, S. Abrate, Delamination threshold loads for low velocity impact on composite laminates, Compos. A 31, 903-915, 2000.

[9] W.J. Cantwell, Geometrical effects in the low velocity impact response of GFRP, Compos. Sci. Technol. 67, 1900-1908, 2007.

[10] T. Mitrevski, I.H. Marshall, R. Thomson, R. Jones, B. Whittingham, The effect of impactor shape on the impact response of composite laminates, Compos. Struct. 67, 139-148, 2005.

[11] H.S. Huang, R. Talreja, Effects of void geometry on elastic properties of unidirectional fiber reinforced composites, Compos. Sci. Technol. 65, 1964-1981, 2005.

[12] P.O. Hagstrand, F. Bonjour, J.A.E. Månnson, The influence of void content on the structural flexural performance of unidirectional glass fibre reinforced polypropylene composites, Compos. A 36, 705-714, 2005.

[13] L. Liu, B.M. Zhang, D.F. Wang, Z.J. Wu, Effects of cure cycles on void content and mechanical properties of composite laminates, Compos. Struct. 73, 303-309, 2006.

[14] S. Abrate, Modeling of impacts on composite structures, Compos. Struct. 51, 129-138, 2001.

[15] C. Meola, G.M. Carlomagno, Infrared thermography to evaluate impact damage in glass/epoxy with manufacturing defects, Int. J. Impact Eng. 67, 1-11, 2014.

[16] M. Ashby, A. Evans, N. Fleck, L. Gibson, J. Hutchinson, H. Wadley, Metal foams: a design guide, referex engineering. Butterworth-Heinemann, 2000.

[17] G. Petrone, V. D'Alessandro, F. Franco, S. De Rosa, Numerical and Experimental investigations on the acoustic power radiated by Aluminium Foam Sandwich panels, Composite Structure, 118, 170-177, 2014.

[18] V. D'Alessandro, G. Petrone, S. De Rosa, F. Franco, Modelling of aluminium foam sandwich panels, Smart Struct Syst, 13(4), 615–636, 2014.
[19] L.J. Gibson; M.F. Ashby, Cellular Solids, 2nd ed.; Cambridge University Press: Cambridge, UK, 1997.
[20] P. Feraboli, K.T. Kedward, A new composite structure impact performance assessment program, Composites Science and Technology, 66, 1336–1347, 2006.
[21] G.M. Carlomagno, P.G. Berardi, Unsteady thermotopography in non-destructivetesting, in: C. Warren (Ed.), Proc. III Infrared Inform. Exch, AGA, St. Louis, MO, pp. 33-40, 1976.
[22] G. Busse, Optoacoustic phase angle measurement for probing a metal, Appl. Phys. Lett. 35, 759-760, 1979.
[23] A. Letho, J. Jaarinen, T. Tiusanen, M. Jokinen, M. Luukkala, Magnitude and phase in thermal wave imaging, Electron. Lett. 17, 364-365, 1981.
[24] J.-L. Beaudoin, E. Merienne, R. Danjoux, M. Egee, Numerical system for infrared scanners and application to the subsurface control of materials by photothermal radiometry, Proc. SPIE 590, 287-292, 1985.
[25] G. Busse, D. Wu, W. Karpen, Thermal wave imaging with phase sensitive modulated thermography, J. Appl. Phys. 71, 3962-3965, 1992.
[26] V. Vavilov, Thermal nondestructive testing: short history and state-of-art, in:D. Balageas, G. Busse, G.M. Carlomagno (Eds.), Proceedings of the QIRT92,Eurotherm Series 27. EETI ed., pp. 179-193, 1992.
[27] X. Maldague, Introduction to NDT by active infrared thermography, Mater. Eval. 6, 1060-1073, 2002.
[28] C. Meola, G.M. Carlomagno Application of infrared thermography to adhesion science, Journal of Adhesion Science and Technology, 20(7), 589-632, 2006.
[29] O. Breitenstein, W. Warta, M. Langenkamp, Lock-in Thermography: Basics and Use for Evaluating Electronic Devices and Materials, Springer, 2nd. s.l., 2010.
[30] C. Maierhofer, P. Myrach, H. Steinfurth, M. Reischel, and M. Röllig, Development of standards for flash thermography and lock-in thermography, Proceedings of the QIRT conference 2014.
[31] P.G. Bison, S. Marinetti, E. Grinzato, Measurement of thermal diffusivity by lock-in thermography. Proc. QIRT 2000, 30-5, 2000.
[32] C. Meola, G.M. Carlomagno, A. Squillace, G. Giorleo, Non-destructive control of industrial materials by means of lock-in thermography, Meas. Sci. Technol. 13, 1583-1590, 2002.
[33] W.J. Parker, R.J. Jenkins, C.P. Butler, G.L. Abbott, Flash Method of Determining Thermal Diffusivity, Heat Capacity, and Thermal Conductivity, J. Appl. Phys., 32, 1679–84, 1961.
[34] C. Meola, C. Toscano, Flash thermography to evaluate porosity in carbon fiber reinforced polymer (CFRPs). Materials, 7, 1483–501, 2014.
[35] Standard Practice for Ultrasonic Testing of Flat Panel Composites and Sandwich Core Materials Used in Aerospace Applications ASTM E2580-07 2007.
[36] T.J. Batzinger, W. Li, R.S. Gilmore, E.J. Nieters, W.T. Hatfield, et al. Phased array ultrasonic inspection method for industrial applications US6789427 (2004).
[37] Olympus manual: advances in phased array ultrasonic technology applications.
[38] C. Meola, S. Boccardi, G.M. Carlomagno, N.D. Boffa, F. Ricci, G. Simeoli, P. Russo, Impact damaging of composites through online monitoring and non-destructive evaluation with infrared thermography, NDT&E International, 85, 34-42, 2017.
[39] S. Boccardi, G.M. Carlomagno, C. Meola, P. Russo and G. Simeoli, Infrared thermography to evaluate impact damaging of thermoplastic composites, Proc. QIRT 2014, Bordeaux, France, 7-11 July 2014. paper 214.
[40] C. Meola, S. Boccardi, N.D. Boffa, F. Ricci, G.M. Carlomagno Infrared thermography to evaluate impact damaging of composites, Proc. of ECCM16 Seville (Spain) 22-26 June 2014, Paper 0318, Program book: ISBN-10: 84-616-9798-7 and ISBN-13: 978-84-616-9798-4.
[41] C. Meola, S. Boccardi, G.M. Carlomagno, N.D. Boffa, E. Monaco, F. Ricci, Nondestructive evaluation of carbon fibre reinforced composites with infrared thermography and ultrasonics. Compos Structures, 134, 845–53, 2015.
[42] S. Boccardi, N.D. Boffa, G.M. Carlomagno, L. Maio, C Meola, F Ricci, Infrared thermography and ultrasonics to evaluate composite materials for aeronautical applications, Journal of Physics, Conference Series 658 (2015)

[43] L. Maio, V. Memmolo, S Boccardi, C. Meola, F. Ricci, N.D. Boffa, E. Monaco, Ultrasonic and IR Thermographic Detection of a Defect in a Multilayered Composite Plate, Procedia Engineering, 167, 71-79, 2016. doi: 10.1016/j.proeng.2016.
[44] C. Meola, S. Boccardi, N.D. Boffa, M. Di Palma, L. Maio, G.M. Carlomagno, Impact Damaging of Carbon Fibre-reinforced Composites: a Comparison between Infrared Thermography and Ultrasonics, Proc. 11th ECNDT, Prague (Czech Republic), 10p, 2014.
[45] C. Meola, G.M. Carlomagno, Infrared thermography to impact-driven thermal effects, Applied Physics A, 96, 759-762, 2009.
[46] C. Meola, G.M. Carlomagno, V. Lopresto, G. Caprino, Impact damage evaluation in composites with infrared thermography, 3rd European Conference for Aerospace Science EUCASS, Versailles (France) 6-9 July, 2009.
[47] C. Meola, G.M. Carlomagno, Health monitoring of composites with infrared thermography ESMC2009 7th EUROMECH Solid Mechanics Conference Lisbon (Portugal) 7-11 September, 2009.
[48] C. Meola, G.M. Carlomagno, Impact damage in GFRP: new insights with Infrared Thermography, Composites Part A, 41(12), 1839-1847, 2010.
[49] G.M. Carlomagno, C. Meola, F. Ricci, Infrared thermography and piezoelectric patches for impact damage detection in composite structures, IWSHM 2011 - International Workshop on Structural Health Monitoring 2011, Stanford University, Stanford, CA, September 13-15, 2011.
[50] C. Meola, G.M. Carlomagno, F. Ricci, V. Lopresto, G. Caprino, Investigation of Impact Damage in Composites with Infrared Thermography, 6th NDT in Progress, Prague (Czech Republic) 10-12 October 2011, Ed. P. Mazal, pp. 175-182, 2011.
[51] C. Meola, G. M. Carlomagno and F. Ricci, Monitoring of impact damage in Carbon Fibre Reinforced Polymers, QIRT 2012, Napoli, June 11-14, 2012, paper n. 374, pp.8.
[52] S. Abrate, Impact on laminated composite materials, Applied Mechanics Review, 44, 155-190, 1991.
[53] T.J. Kang, C. Kim, Impact Energy Absorption Mechanism of Largely Deformable Composites with Different Reinforcing Structures, Fibers and Polymers, 1, 45-54, 2000.
[54] C. Meola, S. Boccardi, N.D. Boffa, F. Ricci, G. Simeoli, P. Russo, G.M. Carlomagno, New perspectives on impact damaging of thermoset- and thermoplastic-matrix composites from thermographic images, Composite Structures, 152, 746-754, 2016.
[55] C. Meola, S. Boccardi, G.M. Carlomagno, N.D. Boffa, E. Monaco, F. Ricci, The added value of infrared thermography to impact damaging assessment of carbon fibre reinforced composites, NDT WORLD, 19, (3), 49-53, 2016
[56] N.K. Naik, Y. Chandra Sekher, Sailendra Meduri, Damage in woven-fabric composites subjected to low-velocity impact, Comp. Sci. Technol. 60, 731-744, 2000.
[57] N.K. Naik, R. Ramasimha, H. Arya, S.V. Prabhu, N. ShamaRao, Impact response and damage tolerance characteristics of glass–carbon/epoxy hybrid composite plates, Composites Part B: Eng., 32, 565–574, 2001.
[58] H.Y.T. Wu, F.K. Chang, Transient dynamic analysis of laminated composite plate subjected to transverse impact. Comput Struct. 31, 453–66, 1989.
[59] H.Y. Choi, H.Y.T. Wu, F.K. Chang, A new approach toward understanding damage mechanisms and mechanics of laminated composites due to low-velocity impact: part II—analysis. J Compos Mater. 25, 1012–38, 1991.
[60] H.Y. Choi, F.K. Chang, A model for predicting damage in graphite/epoxy laminated composites resulting from low-velocity point impact. J Compos Mater. 26, 2134–69, 1992.
[61] Z. Aslan, R. Karakuzu, B. Okutan, The response of laminated composite plates under low-velocity impact loading Comp. Struct. 59, 119–127, 2003.
[62] Y. Perrot, C. Baley, Y. Grohens, P. Davies, Damage resistance of composites based on glass fibre reinforced low styrene emission resins for marine applications. Appl Compos Mater 14, 67–87, 2007.
[63] G.P. Zhao, C.D. Cho, Damage initiation and propagation in composite shells subjected to impact. Comp. Struct 78, 91–100, 2007.
[64] S. Abrate (Editor) Impact Engineering of Composite Structures, Springer Wien New York (2011).

[65] C. Meola, S. Boccardi, G. Petrone, N.D. Boffa, F. Ricci, G.M. Carlomagno, Infrared thermography to an aluminium foam sandwich structure subjected to low velocity impact tests, Procedia Engineering, 167, 23-29, 2016.
[66] C. Meola, S. Boccardi, G.M. Carlomagno, Measurements of very small temperature variations with LWIR QWIP infrared camera, Infrared Physics & Technol. 72, 195-203, 2015.
[67] S. Boccardi, G.M. Carlomagno, C. Meola, The added value of infrared thermography in the measurement of temperature-stress coupled effects, Sensors & Transducers, 201(6), 43-51, 2016.
[68] S. Boccardi, G.M. Carlomagno, C. Meola, Basic temperature correction of QWIP cameras in thermo-elastic-plastic tests of composite materials, Applied Optics, 55(34), D87-D94, 2016.
[69] S.B. Vardeman, J.M. Jobe, Statistical Methods for Quality Assurance, second edition, Springer-Verlag, New York, 2016.
[70] S. Boccardi, G.M. Carlomagno, C. Meola, P. Russo, G. Simeoli, Monitoring impact damaging of thermoplastic composites, Journal of Physics: Conference Series 658 (2015).
[71] S Boccardi, GM Carlomagno, G Simeoli, P Russo, C Meola, Evaluation of impact-affected areas of glass fibre thermoplastic composites from thermographic images. Measurement Science &Technology, 27, 075602, 12p. 2016
[72] N. Otsu, A threshold selection method from gray-level histograms IEEE Trans. Syst. Man Cybern. smc-9 62–6, 1979.
[73] R.C. Gonzales, R.E. Woods, S.L. Eddins, Digital Image Processing Using MATLAB 2nd edn (USA: Gatesmark) 2009, ISBN 978-0-9820854-0-0.
[74] S.U. Lee, S.Y. Chung, R.H. Park, A comparative performance study of several global thresholding techniques for segmentation Comput. Vis. Graph. Image Process. 52, 171–90, 1990.
[75] S. Boccardi, G.M. Carlomagno, C. Meola, Post-processing of time-sequences acquired during impact tests with the aid of a reference area. Proc. QIRT 2016, Gdańsk (Poland), 126-134, 2016,

Conclusions

This thesis was concerned with the application of infrared thermography to monitoring composite materials subjected to either cyclic bending, or impact tests. These tests were applied to different types of composites involving either a thermoset, or a thermoplastic, matrix and different types of fibres as reinforcement.

The main encountered problem to be solved has been the evaluation of the very small temperature differences coupled with thermo-elastic and thermoplastic effects, which are at the edge of instrument sensitivity, so strongly affected by noise.

At least for the QWIP detector, mostly used within this thesis, this noise is mainly constituted by random jumps, which may completely disrupt the sinusoidal trend coupled with cyclic bending or the detection of feeble delaminations. A solution to this problem has been devised in the use of a reference specimen to account for temporal noise, which was successively eliminated from the recorded sequences of images. To this end, also some simple post-processing algorithms have been developed in the Matlab environment to handle the thermal images. This correction method, called *Reference Area Method*, has also been applied to other infrared cameras with ad hoc experimental tests, involving either a black body or a real surface, both kept at constant temperature.

In addition, some key parameters such as the dimension of the measuring area A, and of the reference area A_R, as well the influence of their relative positions have been considered; the obtained results are shown in term of plots and/or Tables in Chapter 3. In all the test cases, the Reference Area Method has proved its effectiveness in significantly reducing the temporal noise and in particular abrupt jumps, sinusoidal patterns, drift and external disturbances due to the environment. As an important result, it has been found that the Reference Area Method was able to restore the signal coming from different cameras equipped with any type of tested detector: QWIP, InSb and micro-bolometric.

Then, the Reference Area Method has been widely used coupled with both cyclic bending tests and impact tests.

In particular, cyclic bending tests (Chapter 4) have been the litmus test of this method. In fact, the Reference Area Method has been effective to restore the sinusoidal trend coupled with cyclic bending tests, which, at low bending frequency, was completely disrupted by the random jumps (e.g., Fig. 4.12).

Besides, the results obtained with the prototype machine setup (realized during doctorate and described in chapter 4) show that, through simple tests, it was possible to get information useful for the characterization of new composite materials, in particular, to discriminate the small variations of ΔT induced by any variation in the material such as the type of matrix, the reinforcement, or the percentage of compatibilizing agent.

Of course, the obtained data cannot be considered exhaustive to characterize the specific behaviour of the considered materials; other tests are required with also a comparison with conventional mechanical tests made on the same materials.

The topic of chapter 5 has been the monitoring of impact tests, at low velocity/energy, on different types of composites (different matrix, and/or reinforcement).

In particular, the efforts have been devoted towards two main aspects:

1. Get information about the impact dynamic through the analysis of image sequences acquired at high frame rate (960 Hz).
2. Define a general criterion to measure the overall extension of the impact damage.

In relation to point 1, the obtained results showed that monitoring the thermal signatures, induced by an impact event, supplied information useful for identifying, in a fast way, initiation and propagation of the impact damage. However, more information were derived from post processing of the recorded images, with ad hoc routines developed in the Matlab environment. In particular, it was possible to get information useful for understanding more on the impact damaging mechanisms, starting from the time interval the impactor remained in contact with the surface, the curvature experienced by the different composites, as well the occurred plastic deformations. In fact, from the time evolution of thermo-elastic effects, it was possible to get information useful to establish the time interval the impactor remains in contact with the specimen surface and to derive knowledge about bending and deformation of the surface under the impactor pushing force. Besides, the temperature rise with its time history allowed getting information about the instant the material started to damage and the importance of the occurred damage.
In addition, a procedure to measure the extension of the impact damage, from the warm area has been proposed.
Such a procedure consisted in comparing two average ΔT images (above a set of ΔT images) taken before and after impact and building a binary image, which highlighted the warm area. This approach, which is named NCR, encloses the reference sample noise correction method. The obtained results proved the capability of the NCR method to encircle the warm area accounting for the extension of the impact affected area also in presence of complex materials architecture. The effectiveness of the NCR method has been demonstrated also in comparison with the Otsu's method.
It is worth noting that the NCR method was effective in measuring the overall extension of the warmed area, but it still needs to be refined to get the real extension of the damaged area. In particular, the introduction of a material characteristic diffusion time appears necessary to account for heat diffusion related phenomena i.e. for a better choice of the number of thermal images to be considered.

Acknowledgments

Today, April 4th 2017, I am in the Laboratory of Gasdynamics of the Department of Industrial Engineering sat in front of the Desktop, which was with me along the Ph.D. adventure as a votary friend, and I'm going to write the last part of my thesis: the acknowledgments.
I don't know the opinion of who has the difficult task to judge my work and all the other activities performed in these 3 years Ph.D course, but just now, I need to thank all people who shared a little step of this journey with me and encouraged me to go on, especially when dealing with life problems, when deep sadness and despair obscure the brain and stop the heart.
My first thought goes, far away somewhere in the universe, to my mother Paola. Thanks Mom for everything, I'll never forget your love and life lessons taught to me and to our family. The strength, serenity and religious faith you have shown during the long illness and especially in your last days, when also the last hopes vanished, have been a great example for everybody and will inspire forever my life.
I want to thank my father Vincenzo, my brother Emanuele and in particular my young sister Nicoletta who has tolerated me and my frequent absence. A special thank to my love Daniela, to my brother's girlfriend Federica and to my aunts Maria and Silvana. Thanks to you all, without your moral and material help everything would have been more and more difficult. Special thanks to Antonio Rolfi for all the support he has given to me.
Rarely during the life, by chance, happens to meet uncommon people who have inside genius, humanity and something special that I cannot' exactly explain, qualities joined in only one person. I had the great luck to have as guides during the Ph.D travel two examples of this extraordinary persons (sometimes I think it has been too much for an ordinary person like me). Dear Ing. Meola and Prof. Carlomagno my only hope is having repaid at least a part of the trust you gave to me 3 years ago. Apart from your personal opinion about me and my activities, I want to tell you that I have put in this adventure all myself and I have done everything that I could in order to honour the opportunity you have offered to me. It is for you all my gratitude.
In particular, I thank you Carosena for all the time you have spent for me and for every single word of encouragement and hope. You have been a great example for me because what you have taught to me overcomes the pure academic activities and will remain forever in my *life luggage*. It is also thanks to you if I never gave up.
My heartfelt thanks to my colleague, co-author and friend Ing. Giorgio Simeoli. Giorgio, during these three years you have been as a big brother for me. Your advices about work and life problems have been very precious for me. Your constant presence especially in the worst times has been fundamental for me to keep on going on.
I thank Prof. Domenico Acierno and Pietro Russo who have made my Ph.D. possible and have provided me with funds and all the necessary support and ever more in order to perform the research activities.
I thank Prof. Michele Russo who has loaned me the electro-mechanical actuator to perform the cyclic bending tests.
A particular thank to Ing. Francesco Messa (FLIR Systems) and Roberto Rinaldi (Infrared Training Center) for the support in carrying tests with SC6800, X6540sc and T440 cameras and for fruitful discussion.

I would thank the Evaluators Prof. Christiane Maierhofer and Prof. Vladimir Vavilov who patiently read my work and supplied me fruitful and precious suggestions.
I thank all my co-authors, researchers and professors who have shared with me the experimental activities and experiences, in particular: Prof. Fabrizio Ricci, Ing. Natalino Daniele Boffa, Ing. Giuseppe Petrone and Ing. Leandro Maio.
I would say thank you to my colleagues, mates of adventure in the Gasdynamic Laboratory, for the leisure hours spent together which have made the work less hard and for their support: Ing. Giusy Castrillo, Ing. Carlo Salvatore Greco, Ing. Gerardo Paolillo, Ing. Cuono Massimo Crispo, Ing. Mattia Contino, Ing. Francesco Avallone, Ing. Gioacchino Cafiero and Dott. Giuseppe Sicardi.
At last, but not least, I'm grateful to God. I am sure that without his help nothing of what happened in my life till now would have been possible.

Naples, 04/04/2017

Simone Boccardi